Mechanisms and parameters affecting adhesion for titanium/ceramic interfaces created by cold spray

Sara Irene Imbriglio

Department of Mining and Materials Engineering
McGill University, Montréal
March 2020

A thesis submitted to McGill University in partial fulfillment
of the requirements for the degree of Doctor of Philosophy

Abstract

A study is conducted on the formation of Ti/Al_2O_3 and Ti/SiC metal/ceramic interfaces by cold spray. There is a focus on the Ti/Al_2O_3 interface given its better adhesion as compared to Ti/SiC. Independent variables in the cold spray process including the type of ceramic, the powder and substrate morphology and the powder particle impact velocity are considered. Interfaces are formed by cold spraying single metallic powder particles (i.e., splats) onto the ceramic substrates. Micromechanical testing by a splat adhesion test is conducted to determine splat adhesion strength.

The deposition of Ti powder particles onto a polished Al_2O_3 substrate is compared to the deposition, at identical spray conditions, onto SiC with a comparable surface roughness. For Al_2O_3, Ti powder particles bonded near the periphery of the splat by forming a continuous and strong bond. These results demonstrate the importance of the formation of a material jet at impact by adiabatic shear instabilities on bond formation with a ceramic. For deposition onto SiC, the presence of fragments of Ti in the periphery of the splat remaining on the substrate demonstrates that the material properties of the ceramic play a significant role in bond formation. In addition to the ceramic's intrinsic material properties, surface roughness also influences deposition. The deposition of Ti onto Al_2O_3 with a high surface roughness rendered a lower splat adhesion strength than when deposited onto a substrate with a lower surface roughness. Mechanical interlocking contributes to bonding onto the Al_2O_3 substrate with a higher surface roughness, while chemico-physical factors primarily contribute to bonding on the smooth substrate.

Large fluctuations in velocity for the same cold spray conditions are challenging when analyzing single splats. To isolate the effect of velocity on the deposition of single splats, a laser-induced projectile impact test (LIPIT) is used. By LIPIT, the impact velocity is recorded by a high-speed camera and is used to determine the critical velocity for deposition. The critical velocity for deposition of Ti onto Al_2O_3 is identified to be approximately 580 m/s. For deposited splats, velocity is correlated to the powder deformation. The deformation of splats is quantified by use of the flattening ratio. The effect of an increase in velocity beyond the critical velocity is investigated.

Splat adhesion strength decreases with increasing flattening ratio due to fracture in the ceramic and rebound forces.

The effect of powder morphology is investigated by splat adhesion testing and post-test characterization of spherical powder and irregular powder with a coral-like morphology. To reduce the effect of ceramic substrate surface morphology, smooth single crystal sapphire substrates are used. The transparent nature of single crystal sapphire substrates allows for the use of an *in situ* splat adhesion test. For the two spray conditions used, the spherical powder splat consistently has an interface pore in its center which acts as a crack initiation site. Several interface cracks are seen when depositing irregular powder at low velocity; tamping at higher velocities due to the shape of the powder significantly improves adhesion strength leading to a continuous interface.

The abovementioned work was useful in understanding the effect of independent variables in the process. To further understand bond formation between a metal and a ceramic by high-speed impact, high resolution transmission electron microscopy in addition to energy-dispersive X-ray spectroscopy and electron energy loss spectroscopy is used. An interfacial interaction layer with atomic intermixing and nanosized precipitates is identified.

Résumé

La formation d'interfaces Ti/Al_2O_3 et Ti/SiC métallocéramiques par pulvérisation à froid est étudiée. L'interface Ti/Al_2O_3 est priorisée vu que son adhésion est supérieure à celle de l'interface Ti/SiC. Les variables indépendantes, telles que le type de céramique, la morphologie de la poudre et du substrat et la vitesse d'impact de la particule poudreuse, sont étudiées. Des interfaces sont créées par pulvérisation à froid de particules individuelles de poudre métallique sur substrat de céramique. Des essais micromécaniques par des tests d'adhésion de particules sont effectués pour déterminer la force d'adhésion des particules.

Le dépôt de particules de poudre de Ti sur un substrat poli d'Al_2O_3 est comparé au dépôt, à des conditions de pulvérisation identiques, sur un substrat de SiC avec une rugosité comparable. Pour l'Al_2O_3, les particules poudreuses de Ti ont adhéré sur leur périphérie en formant une forte adhésion continue. Ces résultats démontrent l'importance de la formation d'un jaillissement matériel au moment de l'impact, causé par des instabilités de cisaillement adiabatiques, sur la formation d'une adhésion avec une céramique. Pour le dépôt sur du SiC, la présence de fragments de Ti en périphérie de la particule déposée sur le substrat démontre que les propriétés matérielles de la céramique jouent un rôle important dans la formation d'une adhésion. En sus des propriétés matérielles intrinsèques de la céramique, la rugosité surfacique influence également le dépôt. Le dépôt de Ti sur de l'Al_2O_3 rugueux a résulté en une force d'adhésion plus faible que le dépôt sur un substrat lisse. L'imbrication mécanique contribue à l'adhésion sur un substrat d'Al_2O_3 rugueux, alors que l'adhésion sur un substrat d'Al_2O_3 lisse est plutôt influencée par des facteurs physicochimiques.

La grande fluctuation des vitesses associées aux mêmes conditions de pulvérisation est problématique lors de l'analyse de particules individuelles. Pour isoler l'effet de la vitesse sur le dépôt de particules individuelles, un essai d'impact de projectile induit par laser est effectué. Lors de cet essai, la vitesse d'impact est recueillie par une caméra haute vitesse en vue de déterminer la vitesse critique nécessaire au dépôt. La vitesse critique pour le dépôt de Ti sur de l'Al_2O_3 est estimée à environ 580 m/s. Pour les particules déposées, la vitesse est proportionnelle à la déformation des particules, quantifiée à l'aide d'un ratio d'aplatissement. Lorsque ce ratio

augmente, la force d’adhésion des particules diminue en raison de fractures dans la céramique et des forces de rebond.

L’effet de la morphologie de la poudre est examiné à l’aide de tests d’adhésion de particule et de caractérisation post-test de poudres sphérique et irrégulière de morphologie corallienne. Ces poudres sont pulvérisées sur des substrats de saphir lisses et monocristallins. La transparence du substrat permet d’effectuer des tests d’adhésion de particules *in situ*. Pour les deux ensembles de conditions de pulvérisation, le centre de la particule issue de la poudre sphérique a une interface poreuse qui agit comme une amorce de fissure. Plusieurs fissures interfaciales sont observées lors du dépôt de poudre irrégulière à basse vitesse; en raison de la morphologie de la poudre, le pilonnage à des vitesses élevées augmente la force d’adhésion, résultant en une interface continue.

Les essais susmentionnés ont permis de mieux comprendre l’effet des variables indépendantes sur le processus. Pour mieux comprendre la formation d’une adhésion entre un métal et une céramique par impact à haute vitesse, la microscopie électronique à transmission à haute résolution, la spectroscopie de rayons X à dispersion d'énergie et la spectroscopie à perte énergétique d'électrons sont employées. Une couche de réaction interfaciale est identifiée avec un mélange interatomique et des précipités métastables nanométriques.

Table of Contents

Figures

Tables

Acknowledgements

Firstly, I would like to express my sincere gratitude to my advisor Prof. Richard Chromik for offering me the opportunity to take part in his research group's cold spray project and for the continuous support throughout my Ph. D. studies and related research. Prof. Richard Chromik helped in continuously improving my research through discussion of results, thorough and scrutinous reviews of this thesis and of research articles sent out for publication, in addition to offering constructive feedback on conference presentations. Prof. Richard Chromik also gave me the opportunity to explore new idea by allowing research freedom while also guiding me and organizing collaborations which significantly improved the quality of my work. I would like to also thank my co-supervisor, Prof. Raynald Gauvin, for providing expertise in the field of microscopy and for his continuous motivational feedback throughout my project.

At McGill University, special thanks are due to my friends and colleagues, Vamsi, Sima, Yinyin, Lisa, Nima, Pryadarshi, Aroba, Bruno, Sriraman, Evelin, Marianna, Rana, Konstantina, Luis, Mohsen, and others for their continuous motivation, support during difficult times, engaging discussions, assistance with various experiments and training. The technical support from Nicolas Brodusch must also be highlighted. Nicolas continuously made time for me despite his busy schedule and helped guide me in the most difficult part of my project. I also acknowledge the technical support of Florence Paray, Monique Riendeau, Robert Paquette, Alexandra Djuric, Stéphanie Bessette, Boris Nijikovsky, Weawkamol Leelapornpisit and David Liu. Acknowledgement and thanks are also due to Ms. Barbara Hanley for administrative assistance and continuous support and motivation. The administrative support of June Persaud and Leslie Bernier must also be recognized. June's, Leslie's and Barbara's respective smiles were always heartwarming.

I would also like to thank my collaborators at Polytechnique Montréal, Prof. Jolanta Klemberg-Sapieha, Dr. Thomas Schmitt and Francis Turcot, without whom this project would not have been possible. They provided access, training and repairs to the scratch tester used throughout most of

this research project. A special acknowledgement must also go to my collaborators at the national research council which include Maniya Aghasibeig, Phuong Vo, Jean-François Alarie and Caroline Hoang. A thank you is also due to my collaborators at the Massachusetts Institute of Technology, Prof. Christopher A. Schuh, Dr. Mostafa Hassani-Gangaraj, Dr. David Veysset, and Prof. Keith A. Nelson for access and technical support on the laser-induced projectile impact test. The experiments conducted through this collaboration would not have been possible without their support. Prof. Wayne Kaplan and Prof. Christina Scheu must also be recognised for their guidance on transmission electron microscopy sample preparation and on data analysis for these samples.

I am grateful for the funding sources and awards that have allowed for this project to take place. Funding sources and awards include the Natural Science and Engineering Research Council (NSERC) Strategic Grants Program, McGill Engineering Doctoral Award (MEDA), Rio Tinto Aluminum Fellowship Award, Hydro Quebec Master's in Engineering Award, Master's to Ph. D. Fast-track Award, Vadasz Doctoral Fellowship in Engineering, Hydro-Quebec Doctoral Fellowship in Engineering, Dr. Gérard T. Simon Award, Department of Mining and Materials Engineering Graduate Student Departmental Scholarship, the SEDTalks! Graduate Award and the graduate mobility award. I am also grateful to Tekna and Cristal Metals for providing some of the powder used in this project.

I am also grateful to the SEDTalks! Selection committee of 2018 for selecting me to take part in the SEDTalks!. The SEDTalks! gave me the unique opportunity to improve my communication skills. A special acknowledgement is required for Prof. Jeff Bergthorson, Stefanie Kibsey and Andrew Churchill for training me to be a better communicator. I am also sincerely grateful to Mr. Adam and Ms. Margo Koniuszewski and Prof. Marek Hebda for giving me the opportunity to take part in a student exchange at the Cracow University of Technology; an experience I will never forget.

I would also like to thank my family and friends for their continuous support, in particular, my husband, Marc Khalil, my mom, Rosina Mucci, my dad, Emilio Imbriglio, and my sister, Tina Imbriglio.

Contribution of Authors

The present thesis is manuscript-based and includes the work completed from September 2015 to January 2020 over the course of the author's Ph. D. at McGill University. The thesis includes three publications and one manuscript nearly ready for submission. The three publications found in Chapters 4, 5 and 6 were adapted to maintain the format of the thesis. Chapter 4 was published in the past tense while Chapters 5 and 6 were published in the present tense. While the format of each chapter was adapted to fit the thesis, the verb tense was not modified. A portion of the work was completed at Polytechnique Montréal, at the Massachusetts Institute of Technology and at the National Research Council of Canada. Particularly, splat adhesion testing reported in Chapters 4 and 5 and *in situ* splat adhesion testing reported in Chapter 7 were completed at Polytechnique Montréal. All experiments completed on the laser-induced projectile impact test as reported in Chapter 5 were completed at the Massachusetts Institute of Technology. All cold spraying was done at the National Research Council of Canada. Given abovementioned collaborations, several people from different research groups and universities contributed to the completion of each manuscript. Details regarding the contribution of each author within are provided below for each chapter.

Chapter 4: S.I. Imbriglio, N. Brodusch, M. Aghasibeig, R. Gauvin, R.R. Chromik, Influence of substrate characteristics on single Ti splat bonding to ceramic substrates by cold spray, J. Therm. Spray Technol. 27 (2018) 1011-1024.

S.I. Imbriglio prepared the cold spray samples with assistance from the equipment operator, completed all sample preparation for scanning electron microscopy (SEM) and some of the SEM images, performed the splat adhesion tests, completed all pre- and post-test characterization, performed the data analysis as well as wrote the manuscript. N. Brodusch assisted with SEM imaging, completed some of the SEM images and reviewed the manuscript. M. Aghasibeig assisted with cold spray deposition and reviewed the manuscript. R. Gauvin assisted with analysis

of SEM images and reviewed the manuscript. R.R. Chromik supervised the project, provided guidance regarding testing, analysis and manuscript format and edited the manuscript.

Chapter 5: S.I. Imbriglio, M. Hassani-Gangaraj, D. Veysset, M. Aghasibeig, R. Gauvin, K.A. Nelson, C.A. Schuh, R.R. Chromik, Adhesion strength of titanium particles to alumina substrates: A combined cold spray and LIPIT study, Surf. Coat. Technol. 361 (2019) 403-412.

S.I. Imbriglio completed all pre- and post-test characterization and analysis, completed deposition by cold spray with assistance from the equipment operator, performed the splat adhesion tests, wrote the MATLAB code to simulate the powder velocity and temperature in the cold spray system, captured all SEM images, assisted with the laser-induced projectile impact tests, analyzed the laser-induced projectile impact test data in comparison to the cold spray data and wrote the manuscript. M. Hassani-Gangaraj and D. Veysset performed the laser-induced projectile impact test and reviewed the manuscript. M. Hassani-Gangaraj also did post-test characterization of the laser-induced projectile impact test data to measure the impact velocity and rebound velocity and calculated the coefficient of restitution. M. Aghasibeig assisted with cold spraying of samples and reviewed the manuscript. R. Gauvin, K.A. Nelson, C.A. Schuh and R.R. Chromik supervised the project and edited the manuscript. R.R. Chromik provided valuable input in the characterization to correlate the cold spray data to the laser-induced projectile impact test data.

Chapter 6: S.I. Imbriglio, V.N.V. Munagala, T. Schmitt, R. Gauvin, J.E. Klemberg-Sapieha, R.R. Chromik, Failure dynamics of spherical and irregular shaped Ti splats deposited on sapphire by cold spray, Surf. Topogr. : Metrol. Prop. 27 (2019) 045002

S.I. Imbriglio completed deposition by cold spray with assistance from the equipment operator, completed all splat adhesion testing, completed pre- and post-test analysis, completed some of the SEM images and wrote the manuscript. V.N.V. Munagala assisted with pre- and post-test analysis, in particular, assisted with characterization of the irregular shaped powder as well as reviewed and edited the manuscript. T. Schmitt and J.E. Klemberg-Sapieha assisted with splat adhesion testing and reviewed the manuscript. R. Gauvin and R.R. Chromik supervised the project and edited the

manuscript. R.R. Chromik provided valuable feedback and ideas for the organization of the manuscript and data analysis.

Chapter 7: New insight on adhesion in Ti/Al_2O_3 interfaces created by cold spray, manuscript intended for publication

S. I. Imbriglio performed the cold spray deposition of coatings with assistance from the equipment operator, conducted splat adhesion testing, completed all data analysis and wrote the manuscript. N. Brodusch operated the SU9000 microscope for electron energy loss spectroscopy (EELS) data acquisition, provided useful feedback on sample preparation and assisted with EELS data analysis. B. Nijikovsky operated the Talos microscope and assisted in developing a methodology for sample preparation. B. Nijikovsky also provided valuable feedback on analysis of transmission electron microscopy (TEM) images. R. Gauvin and R.R. Chromik supervised the research, provided feedback on the data analysis and edited the manuscript.

Chapter 1

Introduction

1.1 General Background

The high strength, low thermal expansion coefficient, low conductivity, ability to withstand high temperatures and high melting point of ceramics make them interesting for various engineering applications in the aerospace, automotive, biomedical and electrical industries [1, 2]. In most industrial applications, ceramic parts require integration with surrounding metallic parts. Metal/ceramic joining remains an industrial challenge with implications in direct joining of parts, in deposition of metal coatings on ceramic substrates or of ceramic coatings on metal substrates, as well as in the development of metal matrix composites (MMC) with ceramic reinforcement among others [1, 3, 4]. While various techniques are available for joining metal and ceramic, cold spray has recently attracted attention for the deposition of MMC coatings in tribological applications [5] and for ceramic metallization with applications in electronics [6-10], in production of interlayers for brazing [11] and in electroding piezoelectric ceramics [12, 13]. Interest in cold spray for joining of metal and ceramic has emerged due to its eco-friendly characteristics, high speed, capacity to produce coatings with low porosity, lateral precision and high purity of final products [14].

Coating buildup by cold spray relies on the supersonic velocity of micron-sized particles accelerated towards a substrate. The high-speed impact leads to adhesion [15-17]. Since the

invention of the cold spray process, it has mainly been used for the application of metal coatings on metal substrates as deformation of both the powder and the substrate was considered one of the main requirements for adhesion [18-22]. Successful deposition of MMCs and metal coatings on ceramic substrates has intrigued researchers for several years. Adhesion of the ceramic phase in MMCs with ceramic reinforcements was widely believed to be purely mechanical in nature by particle embedding and entrapment [16, 23, 24]. Evidence of metal coatings adhesion to atomically smooth ceramic substrates with a higher bond strength than rougher substrates indicates that chemical bonding can occur by high-speed impact in metal/ceramic interfaces [8, 25-27]. Few researchers have investigated the potential for forming a chemical bond during the deposition of single powder particles to correlate its potential presence and influence in MMCs with ceramic reinforcements [10, 13, 28, 29]. Despite the growing interest in using cold spray as a metal/ceramic joining technique, there remain several unanswered research questions regarding process independent variables (i.e., substrates surface roughness, process gas temperature and pressure, type of ceramic substrate, powder size and powder morphology) and adhesion mechanisms.

The objective of this work is to investigate the effect of these process independent variables on bond strength as well as to investigate the adhesion mechanisms between a metal and a ceramic during high-speed impact. Metal/ceramic interfaces are studied by deposition of metallic single particles or full coatings onto ceramic substrates. The basis of coating buildup relies on single particle impact. Therefore, a significant portion of the work presented in this thesis was completed on single powder particles adhering to a substrate by cold spray rather than full coatings. The deposition of an MMC with ceramic reinforcement also occurs at the single splat level during impact of metal and ceramic powder. As such, knowledge acquired can also be used to gain a better understanding of MMC coatings deposited by cold spray. When depositing MMCs with ceramic reinforcements, metal/ceramic interfaces are formed by either metal impacting a ceramic or ceramic impacting a metal. Metal impacting a ceramic is studied here due to its potential for ceramic metallization. The deposition of full ceramic coatings is deemed rather complex as the impact of ceramic onto ceramic typically results in fracture. There are few publications addressing the potential of spraying full ceramic coatings, but these require deposition under vacuum conditions and fine powder particles [30, 31].

In this work, the ceramic substrates used include Al_2O_3 and SiC, ceramics commonly used in metal matrix composites deposited by cold spray [23, 24, 32-34]. In early work, Al, Cu and Ti metallic powder particles were used, but the significantly higher bond strength obtained in Ti/Al_2O_3 interfaces became the primary focus of the work. On the one hand, the above-mentioned independent processing conditions were studied in the context of their effect on the adhesion strength of single metallic powder particles deposited onto the ceramic substrate. These deposited single particles are referred to as splats. The adhesion strength of single splats is measured by a technique called the splat adhesion test [35, 36]. Post-test characterization by scanning electron microscopy (SEM) and light optical microscopy (LOM) images or *in situ* observation during testing are used to explain splat adhesion strength measurements. On the other hand, the adhesion mechanism is studied by transmission electron microscopy (TEM) combined with electron energy loss spectroscopy (EELS) and energy-dispersive X-ray spectroscopy (EDS) in scanning transmission electron microscopy (STEM).

1.2 Organization of Thesis

The work presented in this thesis is divided into eight chapters. The current chapter includes an introduction to the industrial applications of ceramics and the importance of metal/ceramic interfaces, the cold spray process, metal/ceramic interfaces created by cold spray, the background of the project undertaken, a brief description of the project and outline of the thesis.

Chapter 2 presents the relevant literature to the project undertaken. The literature review includes five parts. The first part presents metal/ceramic interfaces and techniques used to produce them as well as a review of the adhesion mechanisms. The second part is an overview of the cold spray process, addressing the adhesion mechanism and the influence of relevant independent variables as they are currently understood for metal/metal interfaces. In the third part, metal/ceramic interfaces produced by cold spray are introduced. Firstly, an overview of metal matrix composites with ceramic reinforcements is presented with a brief discussion on the advantage of including a ceramic phase in the coating. Secondly, current studies on the adhesion mechanism during ceramic

metallization by cold spray are summarized. The fourth part reviews the methods typically used to test the adhesion of coatings by cold spray outlining the advantages and disadvantages of the various techniques. Finally, a summary of the literature is provided to further contextualize the project.

Chapter 3 includes details on the experimental techniques used in the project which are not presented within individual manuscripts. A justification and characterization of materials used in the project are initially presented. Then, an overview of the cold spray process, the spray conditions and methodology for numerical simulation of powder velocity and temperature is provided. Details regarding the laser-induced projectile impact test are presented in addition to the methodology for determining impact and rebound velocity. Following a description of the sample preparation techniques, the testing and characterization methodologies are further explained. Testing methodology includes splat adhesion testing and *in situ* splat adhesion testing. Characterization techniques include SEM and TEM with a section clarifying sample preparation.

Chapters 4, 5 and 6 are published chapters that address the effect of different independent variables on the cold spray process.

In **Chapter 4**, a single spray condition is used to deposit Ti on Al_2O_3 and SiC. Given differences in surface roughness between the two ceramics in their as-received states, the Al_2O_3 substrate is polished to a level more comparable to SiC. Within this chapter, deposition onto Al_2O_3 and SiC is compared in the context of splat adhesion strength as measured by the splat adhesion test. The effect of surface roughness is also investigated for the Al_2O_3 substrate. Single splats of different sizes deposited onto each substrate are also tested to determine the effect of powder size. Characterization by SEM is completed to further explain the results.

Given the high bond strength between Ti and Al_2O_3 reported in Chapter 4, all other chapters focus on characterizing this particular interface.

In **Chapter 5**, the laser-induced projectile impact test (LIPIT) is used to determine the critical velocity for deposition of Ti onto Al_2O_3. Beyond the critical velocity, splats are studied to

determine the effect of increasing velocity on splat adhesion strength. Splats deposited by LIPIT are characterized to determine the effect of velocity on splat morphology (i.e., flattening ratio). Given a linear dependence between flattening ratio and velocity, flattening ratio is used to represent a relative velocity of single splats deposited by cold spray to determine the effect of velocity on splat adhesion strength. To achieve a wide range of velocities, two nozzle geometries are used during cold spraying. The thermal effect in cold spray when using these two nozzle geometries due to more or less preheating of the gas is also investigated by numerical modeling the temperature of powder particles. Furthermore, local heterogeneity in the substrate allows for further characterization of the influence of surface roughness on splat adhesion strength. Post-test characterization is completed by use of SEM of failed interfaces.

In **Chapter 6**, the effect of powder morphology is isolated by using smooth single crystal sapphire windows rather than polycrystalline sintered ceramics as done in Chapters 4 and 5. The use of smooth single crystal sapphire windows eliminated substrate heterogeneity. The effect of powder morphology and microstructure is studied in terms of its effect on splat adhesion strength. The transparency of the substrate allowed for *in situ* testing which enhanced characterization. Further characterization was completed by post-test imaging of failed interfaces by SEM.

The previously mentioned chapters focus on deposition while Chapter 7 focuses primarily on the adhesion mechanism. Chapter 7 includes new results regarding adhesion in metal/ceramic interfaces.

In **Chapter 7**, the adhesion mechanism is investigated on two fronts. Firstly, since heteroepitaxy is believed to significantly contribute to adhesion in metal/ceramic interfaces in the literature, single splats are deposited onto three crystallographic orientations of single crystal sapphire substrates to determine the effect of crystallographic orientation on adhesion strength. Secondly, given the more prominent use of polycrystalline ceramics in metal/ceramic interfaces, full coatings of Ti are deposited onto a rough polycrystalline Al_2O_3 substrate for investigation of the adhesion mechanism by TEM imaging as well as by EELS and EDS in STEM.

Chapter 8 includes a global discussion addressing comparisons which were not made in the standalone manuscripts included in Chapters 4, 5, 6 and 7. The discussion further elaborates on the possible reasons behind the low bond strength obtained in the Ti/SiC interface by drawing on the new findings regarding the Ti/Al_2O_3 interface. Furthermore, overall recommendations for deposition of metal/ceramic interfaces are provided based on current findings. Then, global conclusions for the work presented in this thesis, a description of the contribution to original knowledge as well as suggestions and future work are presented.

The thesis also contains one appendix including the MATLAB script written to estimate the particle velocity and temperature in cold spray for Chapter 5.

Chapter 2

Literature Review

2.1 Fundamentals and Terminology in the Study of Interfaces

An interface is an area delimiting materials which differ in physical state, chemical composition, structure and/or crystallographic orientation [37, 38]. Often, of interest in the study of interfaces are their mechanical properties. It is important to distinguish between the various terms used to define the mechanical properties of an interface. Adhesion refers to phenomena occurring between atoms, molecules or ions in the interfacing materials. Adhesion encompasses the various types of interatomic forces, which can also be referred to as bonding forces, in addition to mechanical bonds, a term used to define interlocking (or anchoring) of rough surfaces by their mutual interpenetration [37]. There are two categories of bonding forces: primary and secondary bonds. A primary bond is strong and relies on valence electrons. Primary bonds include metallic, ionic and covalent bonds. A secondary bond, such as Van der Waals and hydrogen bonds, is a weaker type of bond typically caused by atomic or molecular dipoles [39].

Adhesion results from the advantageous reduction of free energy which occurs by forming the interface [40]. From a thermodynamics perspective, the work of adhesion (W_{ad}) represents the reversible work required to break the bonds formed between the two materials at the interface and form new surfaces. Work of adhesion is calculated by Dupré's equation (Eq. 2.1) [37, 41].

$$W_{ad} = \gamma_1 + \gamma_2 - \gamma_{12} \qquad \text{Eq. 2.1}$$

Where γ_1 and γ_2 represent the surface free energies of each material in the interface (1 and 2) and γ_{12} represents the interfacial free energy following the formation of primary or secondary bonds. Therefore, interatomic bonds resulting in a lower interface free energy are associated with better adhesion [37, 41].

The work of adhesion equation (Eq. 2.1) provides useful information but its application, in practice, is limited by the difficulties of measuring both surface free energy in a solid and interface free energy [4, 37, 38, 42]. Only in the case of a liquid/solid interface, work of adhesion can be experimentally measured by use of a sessile drop experiment. A liquid drop with known surface area is placed on a solid surface. As the drop is placed on the substrate gravity and bonding forces will act on the drop until it comes to rest. At rest, the contact angle (θ_0) shown in Figure 2.1 is used to analyze the wettability of the liquid drop on the surface. For the liquid/solid interface, surface energies are related by the Young equation (Eq. 2.2) and, as such, the work of adhesion equation is simplified to the form presented in Eq. 2.3. A lower contact angle is related to a higher work of adhesion. By this simplification, the surface energy of the solid and the interface free energy are no longer required [1, 41].

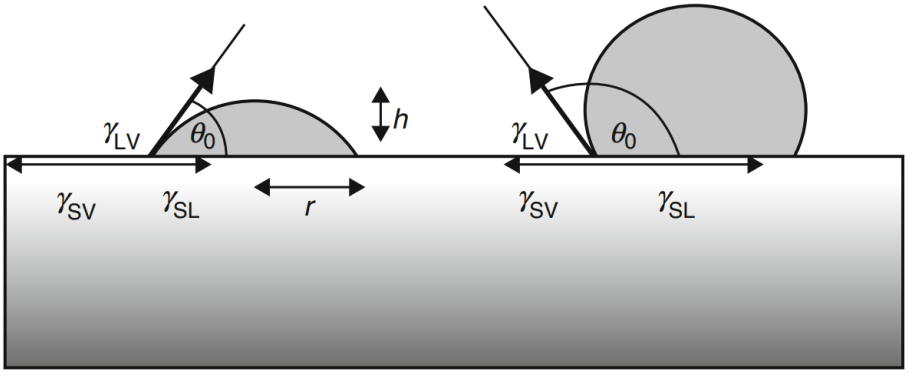

Figure 2.1 Schematic of a sessile drop with low (left) and high (right) contact angle with surfaces energies identified [41].

$$\gamma_{interface} = \gamma_{solid} + \gamma_{liquid} \cos\theta_0 \qquad \text{Eq. 2.2}$$

$$W_{ad} = \gamma_{liquid}(1 + \cos\theta_0) \quad \text{Eq. 2.3}$$

Adhesion measurements by the sessile drop experiment provide useful information regarding the strength of the bonds which contribute to the formation of an interface between specific material combinations, but results rarely directly equate to the strength of a solid/solid interface, even when measuring adhesion on a solidified sessile drop [1, 37]. Sessile drop experiments are often highly influenced by environment, as well as by the composition and state of the materials [40]. Also, mechanical tests used to characterize the strength of solid/solid interfaces involve the application of an external load which induces dissipative forces. Dissipative forces include plasticity, roughness, crack propagation, failure mode mixity and interfacial defects among others [37, 42]. The work required to physically separate the interfacing materials including dissipative forces is referred to as adherence, also informally known as "practical work of adhesion". Nevertheless, it is generally acceptable to assume proportionality between adhesion and adherence [37]. As described by Evans and Dalgleish, the proportionality between fracture resistance of the interface and work of adhesion is more pronounced for brittle failure than ductile failure [43]. These terms are frequently used interchangeably in the literature and hereafter in this thesis.

An added complexity in the study of interfaces is that there is rarely an abrupt change in physical and chemical characteristics. Practical solid/solid interfaces generally have a certain thickness which cannot be evaluated through a sessile drop experiment, but which contribute to adhesion and adherence [37]. Interactions between the interfacing materials cause disruptions in structure and composition of each material approaching the interface. In the interface, due to the presence of another material, atoms or molecules are exposed to interaction stresses with differ from those in their respective bulk materials. These interaction stresses may lead to atomic reconstruction in the interface which may modify the crystallography. Disrupted regions are referred to as diffuse interfaces. These diffuse interfaces may be heterogenous due to mechanical interlocking, interdiffusion and/or the presence of intermediate layers, interphases or intermetallics caused by solid state reactions at the interface [37]. Excluding mechanical interlocking, adhesion mechanisms such primary and secondary bonds, in addition to solid state reactions and diffusion, are frequently referred to as chemical bonds or chemical bonding mechanisms. Specifically for

metal/metal interfaces, all mechanisms leading to the formation of a permanent joint, excluding mechanical interlocking, are frequently referred to as metallurgical bonds [44].

2.2 Metal/Ceramic Interfaces

2.2.1 Interest and Applications

Metal/ceramic joints have numerous industrial applications. From an engineering perspective, ceramics are typically selected for use in severe operating conditions. Because ceramics offer low thermal expansion and high strength at high temperatures, they are used in the aerospace industry as structural components in gas turbine engines where higher operating temperatures lead to higher efficiency [1]. In automotive vehicles with reciprocating engines, ceramics are also used for their high strength, wear resistance and low thermal conductivity [1]. Yet, there are physical limitations in the production of complex ceramic parts due to their inherent material properties. Joining metals and ceramics is fundamental for their widespread industrial use [1, 2, 45-47].

Although they have interesting industrial applications, producing durable metal/ceramic joints remains a challenge. Bulk metal and ceramic components are commonly joined by adhesives and mechanical fasteners or by direct joining techniques. Adhesives and mechanical fasteners are inexpensive and widely used but are limited in operating temperature and strength. Direct metal/ceramic joining techniques help mitigate these problems. Some direct metal/ceramic joining techniques include welding, brazing, soldering, hot pressing, fusion welding and diffusion bonding [1, 46].

Beyond joining bulk metal and ceramic parts, these interfaces are also created to modify surface characteristics of materials for specific applications through coatings. Two particularly interesting types of coatings include metal coatings on ceramic substrates and metal matrix composite (MMC) coatings. Firstly, ceramic metallization typically involves the deposition of a thin metal layer on the surface of a ceramic. The electronics industry relies on ceramic metallization for circuitry and electronic packaging [6, 9, 48, 49]. Thin layers can also act as a bonding surface for the bulk metal

part. Metallization of the ceramic part can be done by using techniques such as electroplating, sintered metal powder techniques, physical vapor deposition (PVD) and chemical vapor deposition (CVD) [1]. Secondly, MMCs involve the deposition of a coating composed of both metal and ceramic on various materials. These coatings offer improved tribological properties [5]. Tribology is the study of all aspects relating to bodies in relative motions such as friction, wear and lubrication [50]. Poor tribological properties have adverse environmental and economic impacts. High wear rates are associated with reduced lifetime of components leading to waste, with resulting debris emitted as pollutants [51]. Friction also leads to increased energy consumption [51-53]. As reported by Holmberg and Erdemir in 2015, industry and transportation consume respectively 29% and 27% of the global energy supply, these represent some of the highest energy consumers. Yet, 30% of that energy for transportation and 15-20% for industry is lost in overcoming friction [53]. Lubricants are an option for reducing frictions but many are environmentally hazardous, making MMCs a more viable and environmentally responsible option [51].

Recently, cold spray has been investigated as a relatively novel alternative direct metal/ceramic joining technique for both the deposition of ceramic particulate reinforced MMCs and metal coatings on ceramic substrates (Figure 2.2) [5, 25]. In fact, it has been suggested that a cold sprayed metallic interlayer for brazing metal and ceramic parts is stronger than directly brazed parts [11]. However, to date, there is no generalized understanding of the process independent variables allowing for deposition of a well-adhering coating, nor is the bonding mechanism during high strain rate plastic deformation well understood [25].

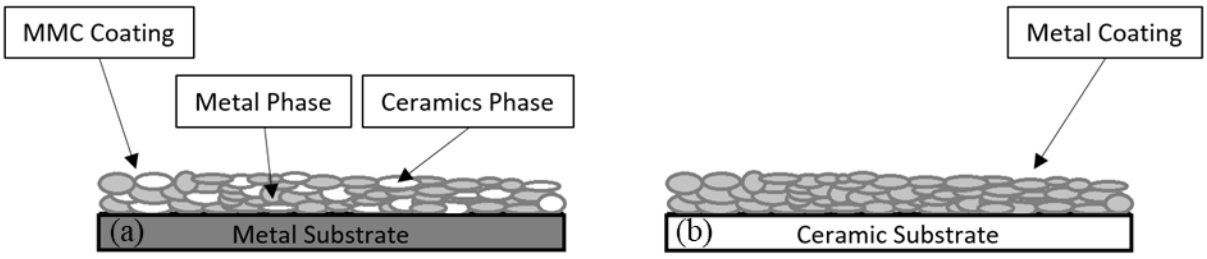

Figure 2.2 Schematic of metal/ceramic interfaces created by cold spray where (a) an MMC coating is applied on a ceramic substrate and (b) a metal coating is applied on a ceramic substrate.

2.2.2 Adhesion in Metal-Ceramic Interfaces

Direct joining of metals and ceramics by any process is difficult to achieve and to predict due to differences in chemical and physical states between the two materials and due to defect structures [54, 55]. Difficulties in joining are largely related to the inherent material properties of ceramics. For instance, due to the restricted motion of electrons in ionic and covalent bonds between atoms forming ceramics, these are more stable than metallic bonds which have delocalized electrons. The inherently more stable bonds in ceramics reduce surface interactions which are required to adhere with metal and form an interface. Interfaces are also characterized by an abrupt change in the type of bond [54, 56]. In addition, the thermal expansion coefficient of ceramics is significantly lower than that of metals, causing a large thermal expansion mismatch in the joint created by processes in which the interface is exposed to heat. Interfacial stresses associated with this thermal expansion mismatch can induce interfacial cracks or weaken the joint. Interfacial cracks may also result from the low thermal conductivity of ceramics, making them susceptible to thermal shock. Low temperature joining processes with controlled heating and cooling rates are therefore sought but not always achievable [54]. From a theoretical point of view, ab initio methods such as density function theory can be used to predict the strength of the metal/ceramic joint [42]. However, theoretical predictions do not include defect concentrations and defect dynamics which, for a metal/ceramic joint, seem to highly influence mechanical properties [42, 55]. Interface defects may include reaction layers, interfacial gaps, microcracks or high stress concentrations associated with the thermal expansion mismatch [55].

While ab initio techniques are improving to better understand and predict the behaviours of metal/ceramic interfaces, qualitative and quantitative characterization still highly relies on empirical correlations. The sessile drop experiment has been the most frequently used to understand the role of specific metal and ceramic material properties in forming a joint [42, 55]. While the wetting behaviour is considered qualitative at best, it remains a relatively simple way to characterize initial interactions at the interface and correlate material properties with the ability to form bonds between specific metal/ceramic pairs at initial contact [42].

Two examples of empirical correlations by the sessile drop experiment include the effect of ceramic ionicity and the formation of crystallographic orientation relationships at the interface [40]. Highly ionic ceramics are reported to form weaker bonds with metals than highly covalent ceramics. This correlation is explained by looking into the behaviour of electrons within each type of bond. Ionic bonds are characterized by the transfer of a valence electron from the metallic component to the non-metallic component. This results in electrons which are highly localized and stable. In a covalent bond, atoms share electrons. This type of bond displays characteristics of both ionic and metallic bonding (i.e., it is less stable than ionic but more stable than metallic). The similarities between metallic and covalent bonds are believed to explain the reduced discontinuities at the interface, causing ceramics with higher covalency to be more easily wetted by metal [39, 40, 56]. Comparing the bond strength of various metals interfacing alumina (63% ionic) and silicon carbide (12% ionic) was useful in establishing this relationship [40, 47, 57]. Additionally, in many metal/ceramic interfaces, crystallographic orientation relationships between the metals and ceramics play an important role. Higher work of adhesion is found if close packed planes are aligned. When the ceramic is not oriented to have its close packed plane exposed to the interface, other orientation relationships have been observed and are also motivated by the reduction of interfacial energy and symmetry in the crystallography [40]. These orientation relationships occur to reduce the number of broken bonds in the interface, which inherently reduces the interface free energy [38]. Differences in lattice parameters may be compensated by misfit dislocations to ensure semi-coherence at the interface [40, 58].

It appears that the abovementioned empirical correlations only consider charge transport between the interfacing atoms, but mass transport may also occur in the form of a chemical reaction causing an interfacial reaction layer [40]. The occurrence of a chemical reaction is highly dependent on various variables including the environment, the nature and state of the materials in the interface, conditions used to create the interface, and reaction kinetics for which very little data is available [4, 59]. Making generalized statements regarding the formation of metal/ceramic joints is therefore difficult. Nevertheless, these empirical correlations can be used as a starting point in understanding and analysing new joining techniques.

While empirical correlations are frequently made for liquid/solid interfaces by the sessile drop experiment, of interest for this thesis is metal/ceramic interfaces formed in solid state. In both solid state and liquid state joining, interface atoms are brought in intimate contact and the driving force for bond formations remains the reduction in free energy at the interface. On the one hand, intimate contact in a solid/liquid interface is achieved by wetting and penetration of the liquid into surface irregularities. On the other hand, in a solid/solid interface, intimate contact is typically achieved by the application of pressure and heat [1, 4]. Lower atomic mobility in solid-state renders the joining process more difficult [4]. Joining of metals and ceramics in solid state occurs over a two or three step process. As the two materials are brought in contact, the metal deforms and conforms to the shape of the ceramic's asperities to achieve intimate contact. Sharp grooves may not be filled, resulting in interfacial voids. To achieve a void free interface, vacancy diffusion through the metal is required. Once intimate contact has been achieved, bonds form to reduce interfacial free energy. In addition, there may be a chemical reaction at the interface. When bonds are formed between metals and ceramics, factors such as their respective diffusion rates and complex interfacial chemistry may encourage the formation of non-equilibrium structures [4]. As such, predicting the behaviour of metal/ceramic interfaces in intimate contact remains a challenge. There is an added complexity in understanding and predicting the behaviour of solid-state metal/ceramic interfaces formed under high strain rate conditions because they may also experience significant local changes in a short period of time. This difficulty applies to the cold spray process which will be explained in the following section. The thermodynamics and chemistry of these solid-state interactions are typically evaluated on a case-by-case basis.

Given the abovementioned challenges, adhesion is typically studied by mechanical testing correlated to microscopic and nanoscopic interface features or by modeling. Microscopic features include interface cracks and residual stresses which can influence interface strength and are studied by light optical microscopy (LOM) or SEM [43, 60]. Nanoscopic features include the level of atomic coherence (coherent, semi-coherent and incoherent), misfit dislocations, new compounds formed by chemical reaction, atomic steps due to surface roughness and impurities. These nanoscopic features are typically studied by transmission electron microscopy (TEM) [42, 55, 58,

60-63]. Atomic bonding is studied by various spectroscopy techniques like electron energy loss spectroscopy (EELS) and auger electron spectroscopy (AES) [42, 55]. Additional work in the field correlating bond strength with macroscopic, microscopic and nanoscopic defects is required to help explain bond formation, defects, chemical reactions and other interface characteristics to better understanding the influence of material properties as well as process parameters.

2.3 Introduction to the Cold Spray Process

2.3.1 Overview of the Process

The cold spray process is considered an environmentally friendly technique with little wasted material and low energy consumption. The main components of the process are compressed gas, a powder feeder, a converging/diverging nozzle and a gas heater. Coatings are formed by plastic deformation of solid powder particles accelerated towards the substrate [15-17]. For powder particles to adhere, they must travel above a critical velocity (details on critical velocity are discussed in Section 2.2.2.1) [18, 19, 64-66]. Achieving the critical velocity typically requires a supersonic gas flow. The converging-diverging nozzle allows supersonic flow in the diverging section if the flow at the throat is choked (i.e., at Mach 1). The pressure difference at the inlet and exit of the nozzle allows for a flow and the decrease in cross-sectional area in the converging section of the nozzle causes acceleration of the gas due to conservation of mass. If the critical pressure ratio between the exit and inlet pressures for supersonic flow is respected, the expansion of gas in the diverging section of the nozzle will cause supersonic velocities [16, 19, 67]. The compressed gas can be heated to increase the local speed of sound in the nozzle, which results in an overall increase in velocity given a fixed Mach number as governed by the local-to-throat area ratio along the length of the nozzle. While the compressed gas is heated, the temperature of the gas is maintained below the melting temperature of the powder [16]. To further increase the velocity, gases with a lower molecular weight are generally sought. Options of compressed gas generally include air, He or N. Commonly, to achieve adequate velocities, N is used. He is often considered prohibitively expensive and only used for specific materials requiring higher

velocities [16]. The powder particles, injected into the gas stream, are accelerated by the drag force acting on them. Injection of powder particles occurs either upstream or downstream of the nozzle depending on the cold spray system used [16]. Figure 2.3 includes a schematic representation of the cold spray process with powder injection upstream of the nozzle.

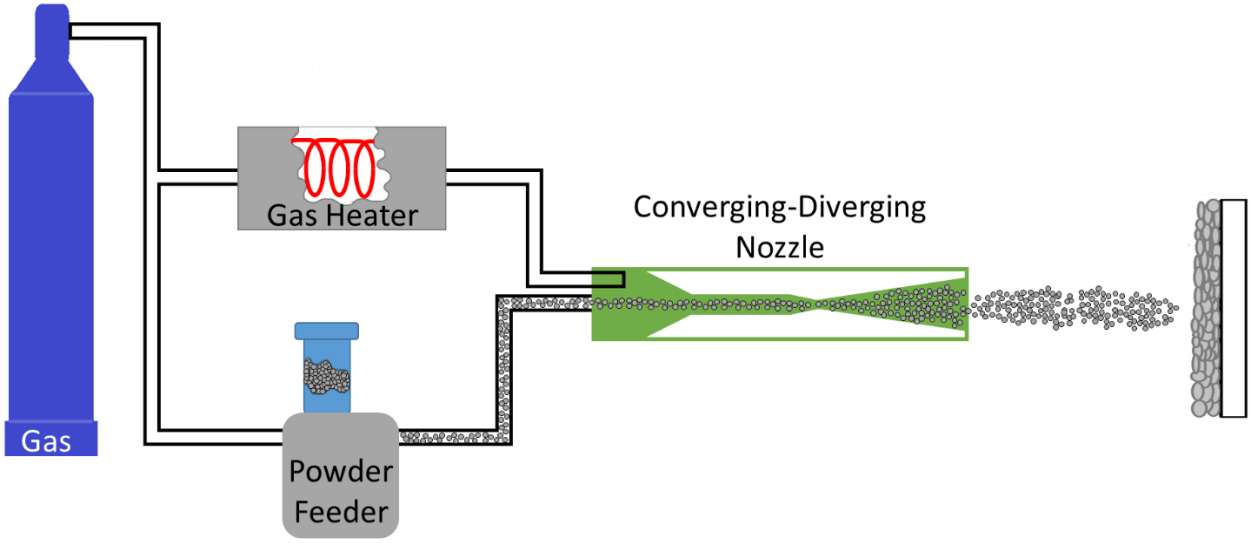

Figure 2.3 Schematic representation of the cold spray process.

A basic understanding of gas and powder temperature as well as velocity can be achieved by a simple one-dimensional numerical approximation using a numerical computing system like MATLAB. The simplified numerical model assumes a quasi-one-dimensional isentropic flow and the use of spherical powder at a uniform temperature [16, 19, 67].

Coating deposition by means of high-speed impact, by cold spray, has many advantages as compared to a thermal spray process where powder particles are melted. There are both manufacturing advantages and enhanced coating properties. For instance, grain growth, phase changes and oxidation of the powder are typically avoided during deposition [20, 68]. Also, no masking is required as the particle bonding area is proportional to the diameter of the nozzle. Overspray particles do not tend to adhere to the surface [68]. This is particularly interesting for the electronics industry as customized circuits can be manufactured by cold spraying conductive

metals on ceramic substrates [10]. Moreover, particles and substrates of dissimilar materials have been shown to bond adequately [68]. In recent years, many have experimented with various new material combinations such as metal-to-polymer [24, 69-74], metal-to-ceramic [6-8, 10, 12, 13, 24, 75] and MMC-to-metal interfaces [5, 23, 24, 33, 34, 76-82], significantly widening the realm of applications for this process. However, to this point, most available literature regarding the bonding mechanism and required deposition conditions in cold spray is limited to metal/metal interfaces. Additional work is required to fully expand this technology to other material systems.

Independent variables in the system need to be understood and optimized for each new material combination to form of strong interface. From the processing point of view, input variables include the gas temperature, gas pressure, standoff distance, gun traverse speed and feed rate. While the latter all influence coating deposition, most works focus on determining optimal gas temperature and gas pressure, which directly affect particle impact velocity [19, 36, 64-66]. From the materials point of view, for a selected material combination, some crucial parameters to consider are the powder's morphology and microstructure in addition to the substrate's morphology and surface roughness. The effect of material properties on critical velocities, powder morphology and microstructure, as well as substrate morphology and surface roughness are therefore summarized. While this thesis focuses primarily on metal/ceramic interfaces, current literature on the abovementioned independent variables is mostly limited to metal/metal interfaces and as such the description of each variable in the following sections generally highlights examples of these interfaces. A preliminary understanding of metal/ceramic interfaces comes from understanding soft metallic particles sprayed onto hard metallic substrates.

2.3.2 The Window of Sprayability

Each material combination has a window of sprayability delimited by a minimum critical velocity for deposition and a maximum critical velocity when erosion occurs. Critical velocity and erosion velocity are influenced by the material properties of both the powder and the substrate as well as the particle impact temperature [22]. To control powder velocity, processing parameters include gas preheat temperature and initial gas pressure when using a single nozzle geometry and type of

gas. Gas preheat temperature and initial pressure are modified to ensure that the powder particles are traveling at sufficiently high velocities to deform and adhere to the substrate by reaching the minimum critical velocity for deposition [20, 68, 83]. Powder velocity and impact temperature cannot be dissociated from one another rendering the selection of processing parameters difficult. Figure 2.4 outlines the relationship between impact velocity and particle temperature while also outlining the window of sprayability and how it varies with variations in the latter parameters [6, 22]. When working with brittle materials like ceramics, fracture is also a concern and limits the window of sprayability as Figure 2.4 also outlines for the use of an Al_2O_3 substrate [6].

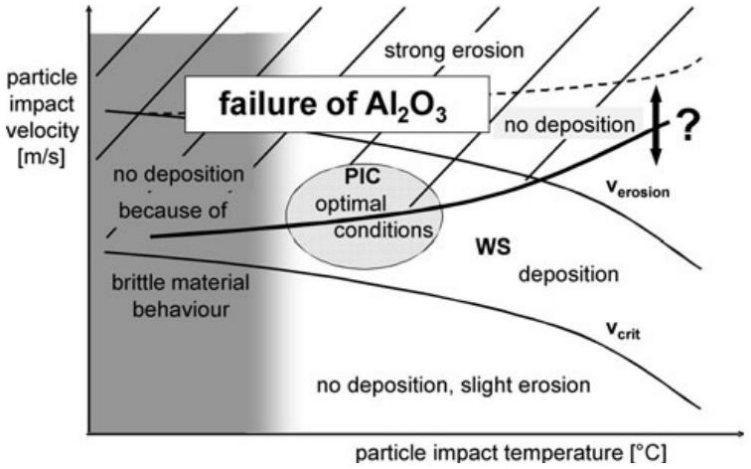

Figure 2.4 Schematic of the relationship between particle impact velocity and particle impact temperature outlining the window of sprayability delimited by the critical velocity and the erosion velocity for a metal/metal interface. If the substrate is replaced by a ceramic (e.g., Al_2O_3), failure of the ceramic would reduce the window of sprayability as illustrated by the area with a diagonal hatch pattern. [6, 22].

To understand the concept of critical velocity, adhesion and rebound energies must be considered [84, 85]. At impact, the interfacing materials deform plastically and elastically. Rebound energy is related to elastic recovery immediately after impact. Adhesive energy is associated with both mechanical interlocking and any type of interatomic bonding whether there be a chemical reaction or not. For a particle to adhere to the substrate, adhesive energy must be higher than rebound energy. The rebound energy scales with the square of the powder particle

impact velocity [84, 85]. The relationship between impact velocity and adhesion energy is not as straight forward and, neglecting mechanical interlocking, is related to the fraction of atoms which form a bond per unit area [84, 85]. To illustrate variations in adhesion and rebound energy with respect to particle velocity, the work by Wu et al. for Al-Si powder deposited onto mild steel substrates is shown in Figure 2.5.

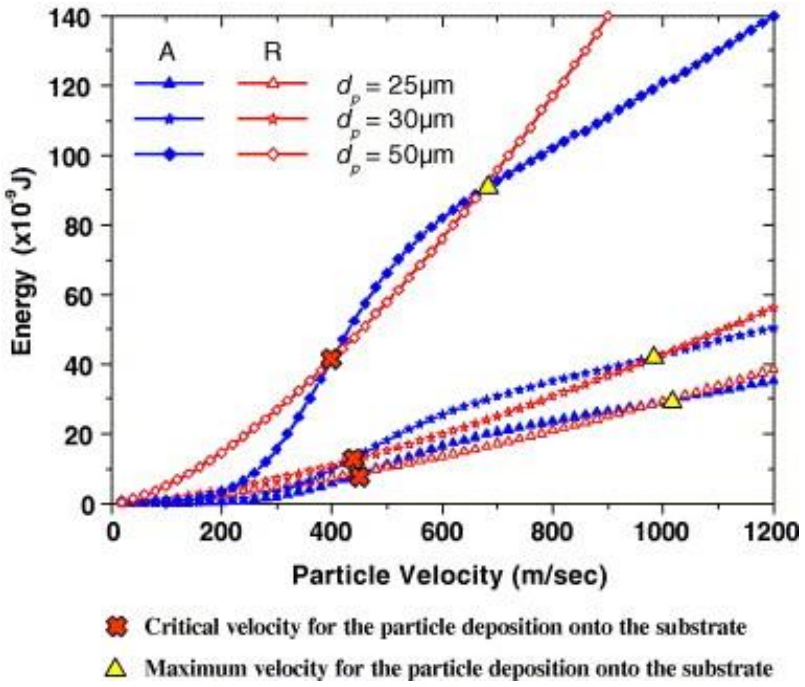

Figure 2.5 Adhesion energy (A) and rebound energy (R) for deposition of Al-Si powder onto mild steel substrates at various velocities [85].

From Figure 2.5, it can also be noted that the adhesion energy surpasses the rebound energy by a varying amount through the window of sprayability. For example, for a powder diameter of 50 μm, the difference in energies at 450 m/s is smaller than at 550 m/s. Therefore, each material not only has a window of sprayability but it also has an optimal velocity. This concept of optimal velocity is generally overlooked in the literature and coatings are often simply deposited above the critical velocity. This approach is acceptable for the deposition of like-material interfaces but becomes a greater concern when depositing dissimilar material interfaces. The work by Manap et al. (Figure 2.6) [84] shows the rebound energy (Er) divided by the adhesion energy (Ed) with respect

to velocity for different powder/substrate material combinations (soft/soft, hard/hard, hard/soft, soft/hard) within the window of sprayability delimited by minimum and maximum critical velocities. For the curves shown in Figure 2.6, adhesion energy remains higher than rebound energy, but the ratio fluctuates especially for dissimilar material combinations. If adhesion energy is significantly higher than rebound energy, the ratio decreases, and adhesion strength of the particle increases. For like-material interfaces, ratio fluctuations are minimal showing that, throughout the window of sprayability, deposition conditions will remain relatively comparable. A soft material (Al) deposited on a hard material (mild steel) is the most prone to variations in adhesion strength due to the rebound phenomenon [84]. These results suggest that for metal particles deposited on ceramic substrates which are comparable to a soft/hard interface, the rebound phenomenon would play an important role. Critical velocities for deposition in metal/ceramic interfaces have not been identified nor has the effect of an increase in velocity beyond the critical velocity been investigated. Further work is required to confirm the role of the rebound phenomenon in these interfaces.

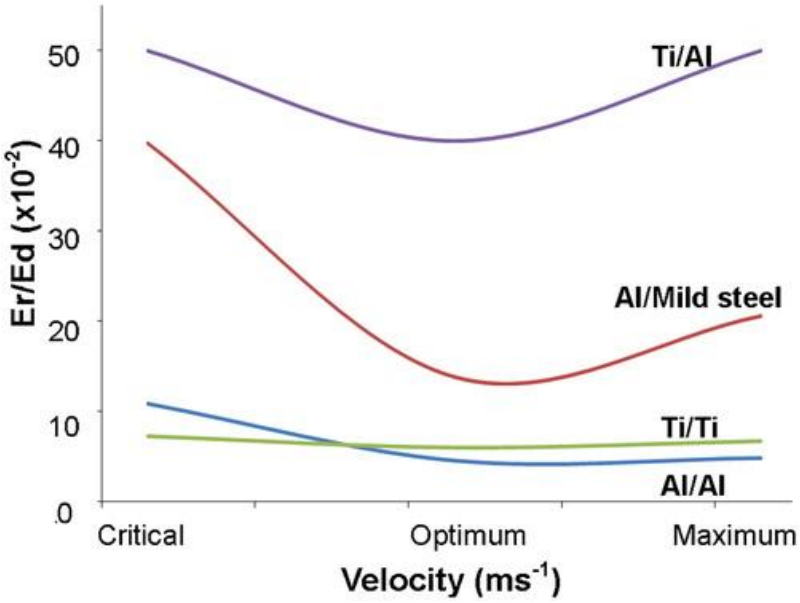

Figure 2.6 Ratio of rebound to adhesion energies (Er/Ed) with respect to velocity for Ti/Al, Al/Mild steel, Ti/Ti and Al/Al interfaces [84].

The rebound phenomenon provides a means of explaining the window of sprayability and the effect of different material combinations, but it is rarely used to determine the critical velocity for cold spray deposition. Rather, approximations are made by numerical modeling or experimentally by comparison of deposition efficiency under different spray conditions or by analysis of single splats [68]. Through modeling, Assadi et al. [18] found an empirical equation (Eq. 2.4) which associates critical velocity to material properties such as density (ρ), melting temperature (T_m), ultimate tensile strength (σ_u) and the particle impact temperature (T_i). However, this equation is limited to cold spray of identical powder and substrate material with mechanical properties similar to copper. For adhesion between dissimilar metallic materials, critical velocity is rather affected by differences in hardness and density [25, 86]. For metal/ceramic interfaces, no clear correlations have been agreed on.

$$v_{cr} = 667 - 14\rho + 0.08T_m + 0.1\sigma_u - 0.4T_i \qquad \text{Eq. 2.4}$$

Recently Hassani-Gangaraj et al. suggested a new technique to directly measure the critical velocity for deposition. By this technique, a laser pulse is used to accelerate single powder particles from a launch pad at velocities comparable to those in cold spray. The impact of the accelerated single particles is captured by a high-speed camera. Both impact velocity and rebound velocity are measured by knowing the distance traveled and the inter-frame time. The coefficient of restitution, which is the rebound velocity divided by the impact velocity, can be plotted with respect to impact velocity to identify the critical velocity for deposition as shown in Figure 2.7. However, the effect of temperature has not yet been considered and only identical material counterparts have been tested by the laser-induced projectile impact test [87].

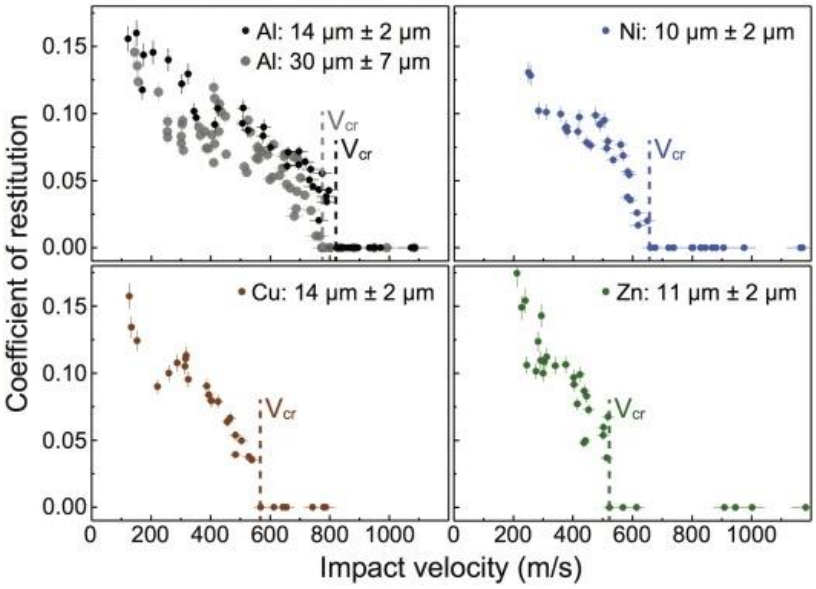

Figure 2.7 Coefficient of restitution with respect to impact velocity for Al, Ni, Cu and Zn as determined by the laser-induced projectile impact [87].

2.3.3 Particle Impact Dynamics and Adhesion

2.3.3.1 Particle Impact and Jetting

To understand coating adhesion by cold spray, it is necessary to understand the impact dynamics leading to adhesion. When a particle is sprayed above a certain critical velocity, bonding between the splat and substrate occurs by severe plastic deformation of the powder and/or the substrate [18, 21, 83]. Severe plastic deformation is observable through the viscous flow of material, also referred to as 'jetting' and shown in Figure 2.8 [18]. Many have proposed that the formation of a material jet is due to adiabatic shear instabilities (ASI) occurring when, as a result of plastic deformation, effects of thermal softening prevail over strain hardening [18, 20, 21, 24, 68]. Severe plastic deformation at the interface is accompanied by a drastic rise in temperature. During high strain rate plastic deformation, heat is released due to dislocation avalanches occurring when dislocation pile-ups break through high strength obstacles in the material [88]. The released temperature causes thermal softening of the interfacing materials. Recently, it has been argued that jetting may not be caused by ASI but rather by a release of hydrodynamic pressure [89]. While the cause of

jetting in cold spray may be debated, all agree that jetting is associated with the formation of a well-adhering coating in a metal/metal interface [18, 20, 21, 24, 68]. Many have also correlated critical velocity with the onset of jetting [18, 21, 24, 87, 90].

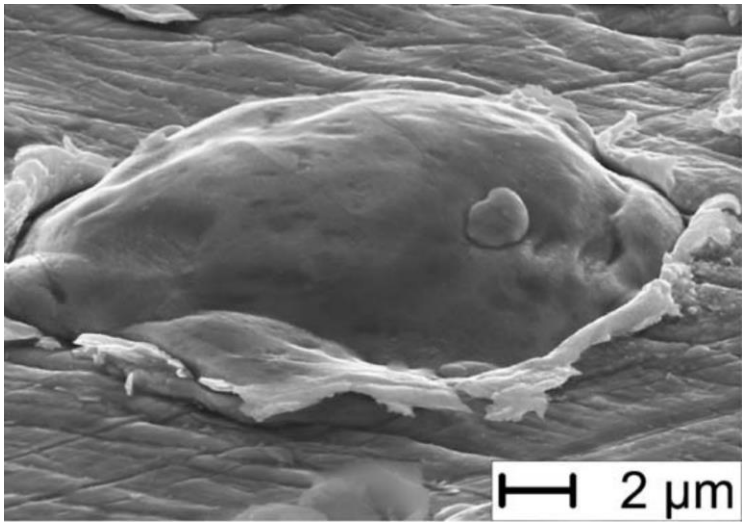

Figure 2.8 Typical flow of material around particles following impact with substrate in cold spray; Image includes a copper-to-copper interface [18].

Jetting is also necessary for bonding in explosive welding, a technique to which cold spray is often compared [25]. As known for explosion welding, jetting is not only dependent on impact velocity but also impact angle. A normal impact does not result in jetting despite being exposed to the highest hydrostatic pressure. A shear contact is required to promote jetting [25]. This behavior is also observed in cold spray at the single splat level using spherical powder for many interface combinations. Above the critical velocity, adhesion occurs at the periphery of the splat where an appropriate angle is encountered between the interfacing materials and where jetting occurs [25, 28]. A gap in the center is often observed as the parallel contact prevents viscoplastic deformation as observed in Figure 2.9 (a), (c) and (e) for different material interfaces [25, 28].

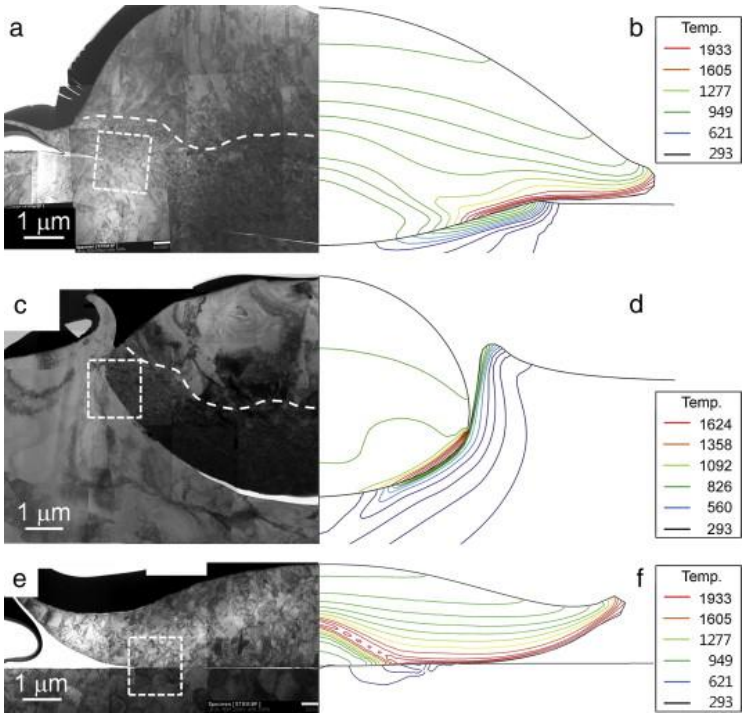

Figure 2.9 STEM images of the deformation behaviour of cold sprayed titanium powder particles deposited onto (a) titanium, (c) aluminum and (e) zirconia alongside the temperature distribution as modeled for the (b) titanium/titanium, (d) titanium/aluminum and (f) titanium/zirconia interface [28].

Therefore, a material's resistance to viscoplastic jetting will influence critical velocity. This resistance is directly related to the material properties of the interfacing materials. For instance, materials with a face-centered cubic (FCC) crystal structure will deform with more ease, requiring lower velocities than those with a body-centered cubic (BCC) or hexagonal close-packed (HCP) crystal structure, as they have more slip systems to accommodate the motion of dislocations [39, 68]. Despite the importance of deformability in deposition, metal has been deposited onto ceramic with success at velocities comparable to those required for metal/metal interfaces. Ceramics do not show any deformation. Interestingly, jetting in the metallic powder particle appears to be critical to adhesion with the ceramic as well [10, 28]. The role of jetting in metal/ceramic interfaces has yet to be fully clarified. Some theories have been put forth regarding the adhesion mechanisms in play between the metal and ceramic but there is no consensus. These theories will be discussed in Section 2.4.2.3.

2.3.3.2 Jetting and Adhesion

To understand the role of jetting on deposition in cold spray, interfacial changes associated with jetting must be considered. Firstly, the formation of a jet at the interface allows the two interfaces to conform to one another allowing for mechanical interlocking [20, 68, 91, 92]. Also, as the particle impacts the substrate, the severe plastic deformation causes a breakdown of the oxide layer on both the powder and the substrate. A portion of the broken oxide layer may be removed from the interface due to jetting which leaves a clean interface for bonding. Some portions of fragmented oxides may remain in the interface, but intimate contact between the materials is achieved around them as shown schematically in Figure 2.10 [25]. Tamping from later impacting particles can also assist in the breakdown of interface oxides to promote intimate contact [93]. Intimate contact between two materials, as described in Section 2.2.2, leads to atomic interactions to reduce interfacial free energy [4]. While this was previously discussed in the context of a metal/ceramic joint, it applies to all material combinations [37].

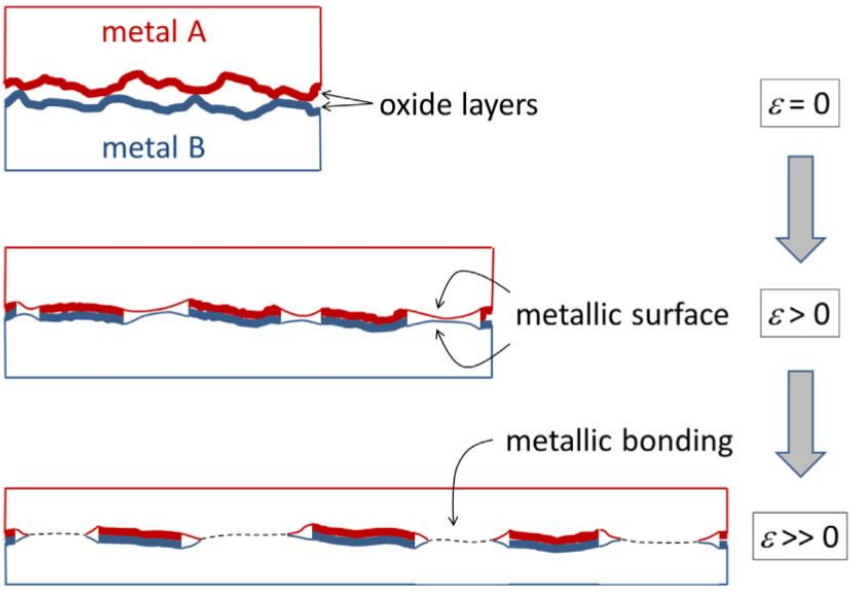

Figure 2.10 Schematic of breakdown of oxides at the coating/substrate interface resulting in clean portions of metal which form a metallic bond with increasing strain (ε) as a result of plastic deformation [25].

Additionally, as shown in Figure 2.9 (b), (d) and (f) where jetting occurs in the material, temperature is at its highest [28]. Higher temperatures in the jetting region is frequently reported for cold sprayed splats [18, 21, 28, 94]. This rise in temperature may promote atomic mobility for various thermally activated mechanisms enhancing adhesion, such as alignment of atoms in a specific orientation relationship to promote coherence or chemical reactions at the interfaces [37, 95]. Local orientation relationships have been identified in some interfaces as well as interaction layers or intermetallic layers [8, 26, 27, 75, 96-104]. Because of this rise in temperature, some have also observed interfacial melting which may contribute to the joint formation [29, 101, 105-108].

In interfaces with no evidence of melting, many believe that atomic diffusion is not solely responsible for adhesion [21, 97, 101, 109]. Given the short contact time at impact and low diffusions rates, the diffusion distance would be significantly lower than those measured [101]. However, it must be considered that under severe plastic deformation, diffusion rates are significantly increased [110]. Increased diffusion rates are due to increased atomic mobility, which, in turn, is caused by boundary diffusion, lattice diffusion and dislocation assisted lattice diffusion [111]. Jetting also causes an ultrafine grain microstructure near the interface [22, 25, 112, 113]. A high dislocation density induces the formation of elongated subgrains, which successively leads to the formation of ultrafine grains. Such grains may also form due to dynamic recovery and recrystallization [112, 114]. This microstructural evolution was explained by Zou et al. [114] and represented schematically (Figure 2.11) for Ni but has been observed for many material systems [113, 115-118]. The fine grains formed at the interface may promote bonding by the formation of new grain boundaries between the interfacing materials but also may reduce the atomic transport distance causing a further increase in diffusion rates which scale with grain size [111, 113].

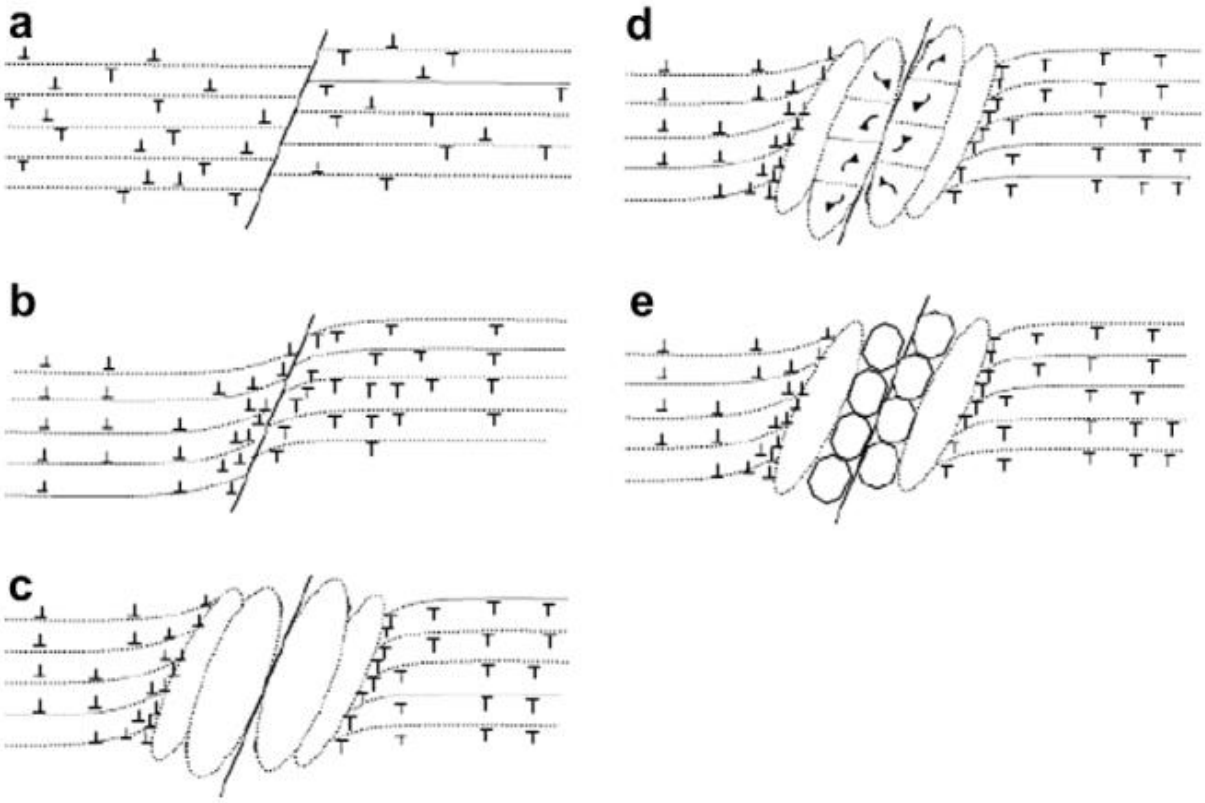

Figure 2.11 Microstructural evolution of cold spray splats from its (a) initial state with a low dislocating density to impact and formation of a material jet which causes (b) an increase in the dislocation density and a rotation of the lattice. The continuous accumulation of dislocations during the impact process causes (c) elongated sub-grains, which eventually (d) divide into equiaxed substrates, rotate due to additional deformation and form (e) misoriented grains in combination to the equiaxed grains [114].

In addition to accelerated interdiffusion, severe plastic deformation has been associated with interfacial supersaturated solutions, dissolution of precipitates and amorphization [119-131]. Particularly, evidence of dynamic amorphization has been reported for cold sprayed samples [97, 99, 132-134]. Ko et al. suggested that impact induced amorphization may lead atomic intermixing [134]. Atomic intermixing may explain adhesion in some metal/metal interfaces and metal/ceramic interfaces [133, 134].

2.3.4 Selection of Powder

There exist various manufacturing techniques for producing metal powders which are categorized as physico-mechanical or physico-chemical. Physico-mechanical methods do not involve changes in chemical composition and include various techniques for pulverization like ball-milling, as well as techniques for atomisation in which droplets are created from a melt and solidify to form the powder. Physico-chemical methods involve chemical changes to the powder as compared to the initial material and includes techniques like reduction and electrolysis [135]. Most of the powder used for cold spray is currently manufactured by gas or water atomization [68].

Each powder manufacturing technique results in powder with varying properties [135]. In cold spray, several powder characteristics are preserved in the coating and should therefore be carefully selected. Some critical properties to consider for cold spray deposition, assuming the material is fixed, include flowability, apparent density, size, morphology and microstructure [68].

Flowability, or the ability of a powder to flow under certain conditions, is considered critical to cold spray because it affects transport of powder through the converging-diverging nozzle and, in consequence, acceleration towards the substrate [68, 136]. High flow rates result in nozzle clogging due to a buildup of powder at the throat. Low flow rates cause intermittent feeding and inconsistent coating properties [68]. Similarly, apparent density, which is a characteristic of a powder's mass with respect to its volume including porosity, affects feed rate. Both flowability and apparent density are largely dependent on the morphology of the powder. Powder morphology includes both external and internal characteristics [68].

Spherical powder has long been the powder of choice due to its good flowability as compared to other powder morphologies allowing it to travel through the nozzle with ease [68]. However, the use of spherical powder is not always considered the best option for all materials systems [68, 137]. More recently, the use of powder with an irregular morphology has been studied [137-143]. A commonly reported advantage of irregular shaped powder is their higher velocities as compared to spherical powders under the same spray conditions. Irregular powder travels faster due to a

greater drag force acting on them. Therefore, irregular powder requires less energy to reach its critical velocity and higher deposition efficiencies can theoretically be achieved [68, 138-140].

Regarding the performance of irregular shaped powder, conflicting opinions have been put forth which may in part be due to significant differences in morphology and microstructure when reporting the use of 'irregular powder'. Jodoin et al. [138] reported more porosity in coatings deposited with cryomilled nanocrystalline irregular shaped Al 2618 powder onto an Al 6061 substrate when compared to spherical gas atomized Al 2618 powder under the same spray conditions. Despite the higher velocity of the irregular shaped powder, their nanocrystalline microstructure imparts them higher hardness which prevents proper deformation at impact. Wong et al. [142] investigated the effect of morphology using spherical powder in comparison to non-spherical powders. The non-spherical powders were referred to as 'sponge' and 'irregular'. While both powders have an irregular shape, they perform differently, further emphasizing the importance of proper characterization of the particular powder used. The sponge powder renders more porous coatings as compared to the irregular powder. The high level of porosity in coatings deposited with sponge powder is associated with the internal porosity of the powder. Potentially, the microstructure may contribute to these differences in performance, but microstructure was not characterized in the work by Wong et al. [142]. These results show that both external and internal porosity as well as microstructure are critical in cold spray deposition. For some irregular shaped powders, during impact, at sufficiently high velocities, there is a collapse of the internal porosity. Powders with a high internal porosity are believed to have lower yield stress and lower elastic modulus, which results in more plastic deformation, thereby resulting in lower rebound energies which is advantageous to deposition. Some irregular powder particles therefore result in more dense coatings than spherical powder particles [144].

A new type of irregular shaped powder showing promising results has a coral-like morphology and is manufactured by the Armstrong process [145]. To date, the advantageous properties of Armstrong powder have only been investigated for Ti [139] and Ti6Al4V [140, 141]. For Ti powder, it was reported that the particular morphology of the powder leads to anchoring and flattening resulting in high deposition efficiency (90%) and dense coatings (1.1% porosity) [139].

Yet, these powder particles have poor cohesion as the deformation mechanism is not accompanied by ASI at velocities lower than the critical velocity for Ti. A 3-hour heat treatment was found to substantially improve coating properties. Higher velocities may also lead to better cohesion [139]. The high deposition efficiency and coating density are also reflected in Ti6Al4V coatings deposited with Armstrong powder. The high yield strength of Ti6Al4V makes it difficult to deposit by cold spray, yet coatings with 0.3 ± 0.1% porosity are achieved with Armstrong powder, which is significantly lower than the 13.0 ± 2.0% porosity achieved using plasma gas atomized spherical powder (Figure 2.12) [140].

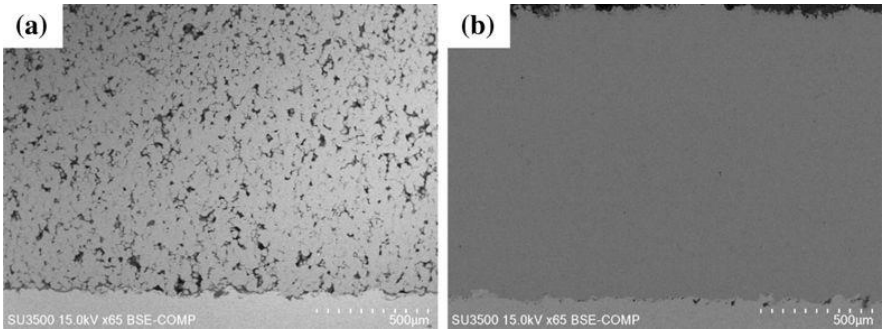

Figure 2.12 Ti6Al4V coating deposited using (a) plasma gas atomized spherical powder and (b) Armstrong irregular powder [140].

Ti6Al4V Armstrong powder has an equiaxed microstructure and is therefore softer than spherical powder which is typically manufactured by plasma gas atomization and has a martensitic microstructure. Therefore, the combined effect of a deformable morphology and microstructure leads to more dense coatings despite the high yield strength of Ti6Al4V [140]. In addition to an improvement in coating density and deposition efficiency when using Armstrong powder, the Armstrong process is significantly less expensive allowing for manufacturing powder at a fraction of the cost of plasma gas atomization [139]. Unfortunately, reports on powder manufactured by the Armstrong process applied in cold spray are limited so it remains unclear how other materials would perform if manufactured by the same process and how they would perform in other interfaces such as in a metal/ceramic interface. Nevertheless, the abovementioned works emphasize the importance of both morphology and microstructure in cold spray deposition.

In addition, the size of powder particles is critical to cold spray. While powders can be manufactured with a size ranging from 0.1 μm to several millimeters, there is a specific size range to be used due to the importance of jetting in adhesion of cold sprayed splats. Under the assumption that ASI leads to jetting, thermal diffusion in small powder particles would not permit localized heating at the interface required for ASI. Also, fine powder particles may be more affected by the bow shock as the gas reaches the substrate [22]. The optimal size range is around 45 ± 10 μm. Larger powder particles having a low deposition efficiency and rendering coatings with high porosity [22].

2.3.5 Selection of Substrate Morphology

Mechanical bonding in cold spray is believed to be of critical importance. In fact, in some cases, it has been shown to be responsible for the majority of the adhesion strength [90, 92, 101]. In like-material interfaces, there is mutual deformation of the counterparts which allows them to conform to each other. To further promote mechanical interlocking, substrate surfaces can be roughened [101]. For soft powder deposited on a hard substrate, like in metal/ceramic interfaces, mechanical interlocking occurs by powder material seeping into the cavities on the substrate as shown for a Ti coating on an Al_2O_3 substrate in Figure 2.13 [26].

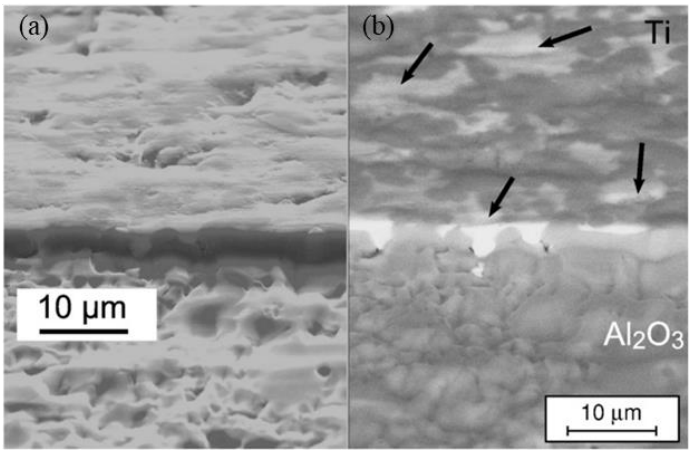

Figure 2.13 Evidence of mechanical interlocking between a cold sprayed titanium coating on an alumina substrate. Image (a) captured with a secondary electron (SE) detector and (b) captured with a backscattered electron (BSE) detector [26].

As such, substrate morphology and roughening are particularly important to achieve mechanical interlocking, as the hard phase may not sufficiently deform to conform to the shape of the splat. A roughened surface also promotes further deformation, as the peaks cause a reduced contact area at impact, which in turn causes higher pressure in localized section of the powder. The higher pressure allows for more plastic deformation [146]. In fact, mechanical interlocking also occurs when splats conform to the shape of the substrate, as can be seen for Al splats deposited onto Al_2O_3 substrate in Figure 2.14 [75]. However, a gap is notable in Figure 2.14 (b) between the splat and the substrate. This gap was found to disappear due to tamping as subsequent powder particles are sprayed to produce a full coating [75].

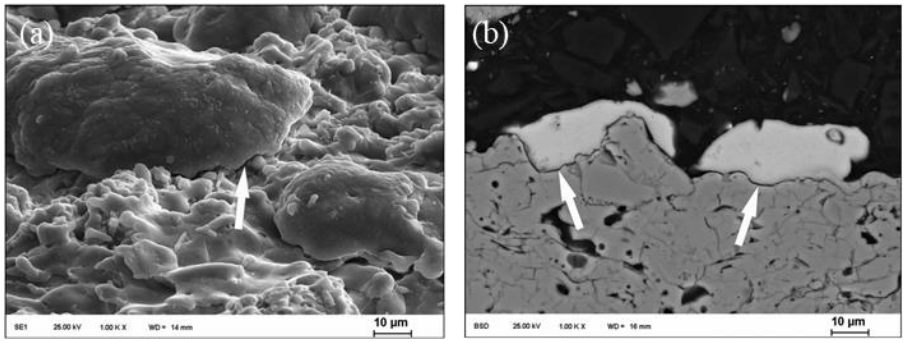

Figure 2.14 Mechanical clamping of Al splats on Al_2O_3 substrate identified in (a) top view and (b) cross-section. Arrows in (a) identify regions in which the powder particle conforms to the substrate morphology and in (b) interfacial gaps observed at the splat level [75].

Nevertheless, the advantages of surface roughening have been frequently debated. Some have suggested that higher surface roughness allows for more deformation, higher overall contact area and mechanical interlocking, and is thus advantageous to deposition [147-149]. Others found contradicting results suggesting that, under certain spray conditions, smoother surfaces have better adhesion than rougher surfaces in cases with metallic counterparts but also for metal/ceramic interfaces [8, 10, 26, 75, 150-152]. These contradicting results can be attributed to two main reasons. Firstly, Hussain et al. suggested that surface roughening promotes mechanical interlocking at the detriment of atomic interactions occurring through intimate contact between the splat and the substrate due to entrapment of surface oxides by reduced jetting [92]. Therefore, the

mechanisms leading to adhesion on smooth and rough substrates may be different. Secondly, it appears that each material combination has an optimal surface roughness which leads to the highest deposition efficiency [149, 153]. In the same way as mechanical properties of soft/soft, hard/hard, soft/hard and hard/soft interfaces influenced jetting [94] and rebound behaviour [84], substrate surface roughness may also affect deposition differently in each case. Kumar et al. found that, on average, protrusions and valleys should be smaller than the particle size to enhance bonding for the soft/soft, hard/hard and soft/hard cases [153]. In the hard/soft case, the substrate is significantly deformed at impact and, in consequence, surface roughness has a minimal effect [153].

2.4 Metal/Ceramic Interfaces by Cold Spray

2.4.1 Challenges & Outlook

As mentioned in the previous section, there has been successful deposition of metal/ceramic interfaces by cold spray. The advantages of these interfaces were overviewed in Section 2.2.1. However, several challenges must still be overcome. The most researched metal/ceramic interface is in the form of an MMC. The deposition of ceramic reinforced MMCs by cold spray can be achieved in various ways. Most commonly, the particles are admixed into one powder feeder [154-156]. Other options include pre-alloyed powders or the use of a dual-powder feeder [33, 68, 157-161]. However, one of the biggest challenges in depositing MMCs is increasing the amount of retained ceramic powder in the coatings. The highest achievable concentration of retained ceramic in the coating is approximately 40 vol% using any of the available techniques [68]. How to improve upon the currently low deposition efficiency of the ceramic phase in MMCs remains a critical research question to address and is a significant motivating factor contributing to the work presented in this thesis. To date, mainly oxides and carbides have been used in combination to various metals to form MMCs [24]. Some common reinforcing hard phases include alumina and silicon carbide [23, 32].

Due to a poor understanding of interactions leading to adhesion between metal and ceramic, there is also a limited understanding of the effect of cold spray process parameters to achieve higher

deposition efficiencies. Some researchers have attempted to increase deposition efficiency by simply increasing the concentration of ceramic in the feedstock powder, but this increase in sprayed ceramic did not always result in an increase in deposited ceramic. The impact of a ceramic particle onto a previously embedded ceramic particle results in fracture or removal of the embedded particle. This ceramic-to-ceramic interaction highly contributes to the low deposition efficiency of the ceramic phase in MMC coatings [80, 162]. Rather, the increase in the concentration of sprayed ceramic results in additional ceramic-to-ceramic interaction, leading to a potential reduction of ceramic in the coating [80, 162]. There is an optimal concentration of ceramic in the coating beyond which there is a reduction in deposition efficiency [80]. Other researchers have varied the spray conditions or powder morphology to achieve higher deposition efficiencies and have been successful. For instance, the use of angular [161] or finer [34] ceramic powders has shown improvements in ceramic retention in MMC coatings. Nevertheless, the parameters affecting deposition efficiency remain difficult to characterize without a proper understanding of adhesion mechanisms between the metal and ceramic phases.

Adhesion between metal and ceramic particles is typically attributed to mechanical interlocking of the ceramic phase by the deformable metal phase [23, 80, 154]. Under this assumption, all ceramic particles would behave in the same way at impact. These effects are difficult to examine during the deposition of MMCs given a wide range of impact conditions. Impact conditions include different material interfaces (metal-to-metal, ceramic-to-ceramic or metal-to-ceramic), variations in particle speed and variations in local morphology. To better understand the effect of process parameters on metal/ceramic interactions, metal/ceramic interfaces should be isolated and studied. One way of doing this is by analyzing the interface between metal splats or coatings deposited on ceramic substrates. Some research has been done on the latter for the study of ceramic metallization by cold spray. Available research is mostly limited to Al deposited on various ceramics [8-10, 26, 27, 75, 100, 150]. In the deposition of metal coatings on ceramic substrates, it has been shown that interfacial strength varies with the type of ceramic used for a particular metal, and higher strengths are frequently reported on smoother ceramics [8, 26, 100]. These results do not support the assumption that metal/ceramic joints by cold spray are solely attributable to mechanical

interlocking. Rather, adhesion appears to have a component attributed to atomic bonding (with or without mass transfer) or chemical reaction at the interface requiring further investigation.

Additional work is therefore required to identify the effects of the various independent variables described in Section 2.3.1 on bond formation, as well as to understand the bonding mechanism in metal-to-ceramic interfaces. For example, with regards to process parameters, the critical velocities leading to adhesion in specific metal/ceramic interfaces should be identified. The effect of an increase in velocity beyond the critical velocity is also important to evaluate to select appropriate deposition conditions. With a better understanding of chemico-physical factors leading to adhesion, the effects of the abovementioned process parameters would ideally be correlated with material properties as was done for metal/metal interfaces.

2.4.2 Observations and Concepts of Adhesion

Available research on ceramic metallization primarily focuses on understanding the mechanisms leading to adhesion, the effect of temperature on adhesion (e.g., heat treatment or preheated substrate) and the effect of material properties on adhesion. However, it must be noted that the vast majority of available literature on ceramic metallization by cold spray focuses on Al interfaces with various ceramics [8, 26, 27, 100, 150, 163]. Only few researchers address the deposition of other metals [10, 26]. To investigate the effect of material properties on adhesion, the interfacial strength of various metal/ceramic interfaces, to date, have been tested and compared by use of a coating tensile test. The typical testing methodology for a cold spray coating involves subjecting the coating to a tensile test normal to the plane of application. The tensile sample is prepared by spraying the top face of a cylindrical fixture and fixing the coating to an identical counterpart using epoxy [35, 75, 80]. By this technique, failure occurs either in the interface which provides a measure of the interfacial strength, or in the epoxy limiting the measurement to a minimal strength of the interface.

2.4.2.1 Effect of Temperature on Adhesion

Interfacial temperature and heat treatment have a significant effect on tensile adhesion strength for some material combinations, while it has a minimal effect for other material combinations [6, 8, 26, 75]. For instance, as shown by Drehmann et al. in Figure 2.15 (a), for Al interfacing MgF_2, adhesion only occurred with a substrate preheat temperature of 300 °C, the Al_2O_3 and AlN substrates also showing an increase in adhesion strength with an increase in temperature, while adhesion strength was not influenced by substrate temperature in interfaces with Si_4N_4 and SiC [100]. The inconsistent behavior of Si_3N_4 and SiC with an increase in temperature is not fully understood. For SiC, failure mostly occurred in the ceramic, resulting in inconsistent results due to a poorly adhering interface or defects in the ceramic [100]. Differences observed with the Si_3N_4 substrate are believed to be caused by a larger coefficient of thermal expansion mismatch with Al as compared to the other substrates [8, 100]. An increase in adhesion strength with temperature was also observed by Ernst et al. for Cu on Suspension High Velocity Oxygen Fuel (S-HVOF) sprayed Al_2O_3 [10].

Some suggested reasons for this increase in adhesion strength with temperature include an increase in atomic mobility at the interface and relaxation of residual stresses in the interface [8, 75, 100, 150]. As described in Section 2.2.2, the reduced atomic mobility in solid state joining techniques is believed to make the joining process more difficult. Therefore, increased atomic mobility can assist in promoting chemical bond formation [8, 75, 100, 150]. In addition, Ernst et al. suggested that the improvement in adhesion strength by increasing substrate temperature can promote desorption of surface contaminants, interfacial diffusion and modification of the substrate's mechanical properties [10]. Furthermore, some ceramics like Al_2O_3 present an increase in fracture toughness with an increase in temperature, hereby preventing cracking and better absorbing the shock of the impacting particle [10]. However, while an increase in substrate temperature has widely been considered to be advantageous to coating performance, Ernst et al. observed oxidation between cold sprayed layers on high temperature substrates [10]. Another potential issue which may become prominent when cold spraying on heated substrates is the thermal stress as a consequence of thermal expansion mismatch [10].

Figure 2.15 (b) shows the effect of annealing at different temperatures on adhesion strength. For Al_2O_3 and AlN, this translates to an increase in adhesion strength, while in SiC and Si_3N_4 are minimally affected by the annealing process, similarly to the increase in substrate temperature. The abovementioned reasoning for the trends concerning substrate temperature applies to annealing as well [100]. Other researchers have also reported an increase in adhesion with an increase in annealing temperature and time [10, 75, 100, 150]. The advantage of annealing is mostly believed to be a consequence of recovery and recrystallization leading to a reduction in interfacial residual stresses [10, 100].

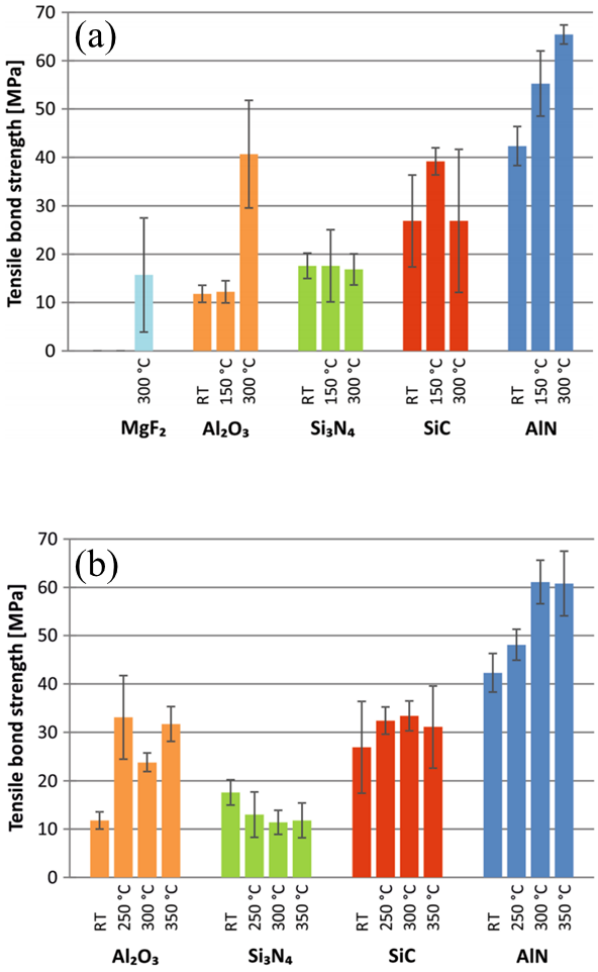

Figure 2.15 Tensile strength of Al coatings applied on (a) MgF_2, Al_2O_3, Si_3N_4, SiC, AlN at different substrate temperatures and on (b) Al_2O_3, Si_3N_4, SiC and AlN at room temperature and annealed at different temperatures [100].

2.4.2.2 Effect of Type of Ceramic on Adhesion

A better understanding of the effect of changing the metal or the ceramic on bond formation is also required. Some work has been done to investigate the effect of ceramic type when depositing Al as shown in Figure 2.15 [100]. As discussed in Section 2.2.2, the strength of the bonds formed in metal/ceramic interfaces can be correlated to their work of adhesion suggesting that higher bond strengths should be achieved for more covalent ceramics [8, 40, 150]. Per this theory, by comparing the ionicity of the types of ceramics presented in Figure 2.15, AlN (40%) and Al_2O_3 (63%) should have lower adhesion strength than Si_3N_4 (30%) and SiC (12%), however this is not the case [8, 100]. While the results by Drehmann et al. [100] show higher adhesion between Al and AlN in comparison to the Al/Al_2O_3 interface, Kümmel et al. [150] reported a higher adhesion strengths for Al coatings on an Al_2O_3 substrate. These seemingly diverging results require further investigation. This divergence may be due to differences in substrate surface roughness or processing conditions. Kümmel et al. suggested that, despite higher ionicity, the higher bond strength between Al and Al_2O_3 occurred due to Al's high oxygen affinity [150]. On the other hand, Drehmann et al. used the comparison of the four previously discussed ceramics to conclude that, in addition to ionicity, hardness and thermal expansion mismatch do not influence the mechanical properties of the metal-ceramic interface [8, 100]. Rather, coating adhesion strength for an Al coating on various ceramics is dependent on the thermal conductivity of the ceramic. A higher thermal conductivity correlates to a lower contact temperature. The lower contact temperature reduces the cool down gradient, which affects the residual stresses in the coating/substrate interface [100]. Furthermore, a higher thermal conductivity is positively correlated with atomic mobility, which is believed to promote bond formation [8, 100].

Given that little research has been completed to compare the influence of various ceramic substrate materials, given that conflicting results have been put forth, and given these effects have only been investigated for the deposition of Al powder, additional work is required to understand how metal-ceramic interfaces form and how both the powder's and substrate's respective properties influence adhesion strength.

2.4.2.3 Mechanisms Contributing to Adhesion

Literature on metal/ceramic interfaces deposited by cold spray suggests that adhesion occurs by a combination of mechanical interlocking and chemico-physical interaction at the interface. In the presence of a rough surface, as addressed in Section 2.3.5, mechanical interlocking significantly contributes to adhesion by metal infiltration within the surface porosity of the ceramic [10, 26, 75]. However, mechanical interlocking is not necessary for adhesion in metal/ceramic interfaces. Many have observed adhesion between metal coatings and smooth ceramic substrates suggesting that a chemico-physical interaction at the interface may also be at play [8, 10, 26, 75, 150]. These chemico-physical interactions remain poorly understood, as they do not follow trends observed in wetting as discussed in the previous section.

Some have shown that jetting is important for adhesion, but this concept has not fully been elaborated [10, 28]. The interfacial impact dynamics as a result of jetting, discussed in Section 2.3.3, are also likely critical for adhesion in metal/ceramic interfaces. Jetting was presented as beneficial as the plastic deformation allows surfaces to conform to each other, allows intimate contact due to the breakdown of oxides and surface contaminants and a drastic rise in temperature as a result of plastic deformation increases atomic mobility [18, 20, 21, 25, 28, 68, 91, 92, 94]. In an interface with a smooth ceramic substrate, due to limited deformation in the ceramic, surfaces will not conform to each other as observed for metal/metal interfaces to lead to mechanical interlocking. Mechanical interlocking can only be achieved on a rough surface where jetting becomes important enough to allow the metal powder to penetrate within the ceramic substrate's surface porosity.

Chemico-physical factors are likely a result of intimate contact between the metal/ceramic surfaces occurring through jetting. As presented in Section 2.2.2, metal/ceramic interfaces in intimate contact form interfacial bonds to reduce their interfacial free energy. However, in solid interfaces, there is typically limited atomic mobility; this renders bond formation more difficult [1, 4]. Atomic mobility is significantly increased during the severe plastic deformation accompanying jetting, due to the associated grain reduction and elevated temperatures [26, 27, 100]. In fact, an increase in

substrate temperature, as discussed in Section 2.4.2.1 may further promote this atomic mobility [8, 100]. Due to this increased atomic mobility, several researchers have reportedly observed interfacial orientation relationships (i.e, heteroepitaxy) through high-resolution transmission electron microscopy (HRTEM) in Ti/Al_2O_3, Al/Al_2O_3 and Al/AlN interfaces [8, 26, 27, 75, 100]. Figure 2.16 (b) shows schematically, the symmetry between the (111) lattice plane of Al and the (0001) lattice plane of Al_2O_3. This orientation relationship is found in HRTEM images of cold sprayed Al/Al_2O_3 interfaces as shown in Figure 2.16 (a) [75].

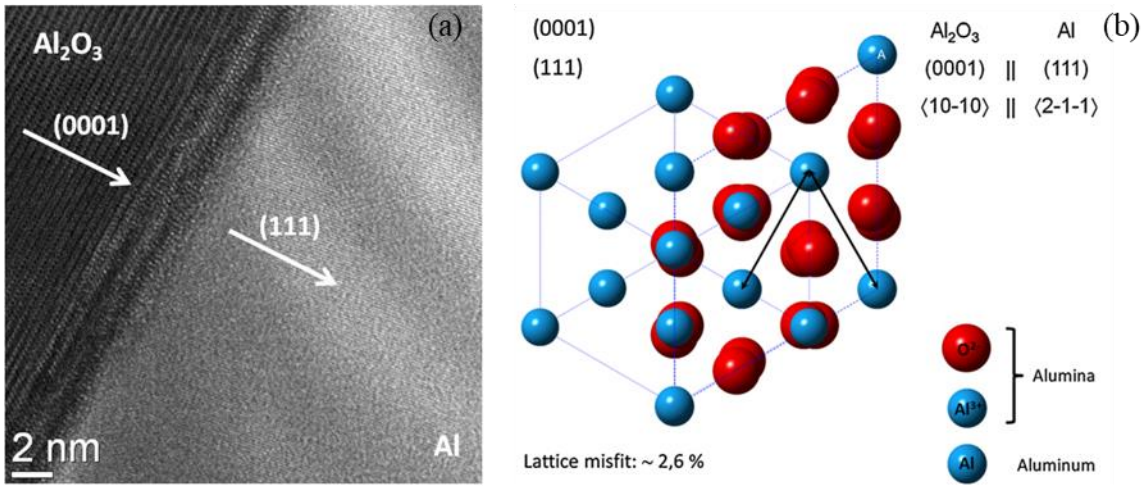

Figure 2.16 (a) Cold sprayed Al/Al_2O_3 interface showing a relationship between the (0001) crystallographic orientation of Al_2O_3 and the (111) orientation of Al. (b) Schematic representation of atomic rearrangement in heteroepitaxy of Al and Al_2O_3 [8, 75].

As addressed in Section 2.2.2, interfacial free energy is further reduced by forming interfacial orientation relationships in which there is a crystallographic symmetry with minimal misfit to reduce the number of broken bonds [38]. Therefore, the observation of orientation relationships at the interface is an indication of strong bonding leading to a higher work of adhesion. Heteroepitaxy is the most widely accepted factor contributing to a strong bond for metal particles cold sprayed onto smooth ceramic substrates [8, 26, 27, 75, 100]. These orientation relationships have also been found for Al coatings deposited onto rough AlN substrates, demonstrating that chemico-physical factors are also at play in mechanically interlocked interfaces [27]. However, electron backscatter

diffraction (EBSD) results have also shown that the grain size of various metals near the interface was reduced to a few nanometers due to dynamic recrystallization resulting from an increase in dislocation density during severe plastic deformation [9, 26, 75], which is consistent with results for metal/metal interfaces [22, 25, 112, 113]. Given the polycrystalline nature of the metal powder particle, heteroepitaxy is likely not generalized over the entire interface and, as such, is likely not the sole contributing factor to adhesion. Other possible adhesion mechanisms include chemical reactions or diffusion. The fact that metal/ceramic interfaces deposited by cold spray do not follow trends observed during wetting may also be an indication of additional interfacial phenomena leading to adhesion, in addition to the fact that certain ceramics may promote favorable conditions for adhesion through higher conductivity or chemical affinity to the metal. An additional mechanism which may contribute to adhesion, as suggested by Ko et al., is atomic intermixing as a result of amorphization during extreme plastic deformation[133] which was further discussed in Section 2.3.3.

2.5 Interfacial Adhesion Testing for Cold Sprayed Samples

The tensile test typically used for cold spray coatings was presented in Section 2.4.2. However, this testing methodology has several drawbacks. For instance, there is a need for a relatively large quantity of material and there are limitations in the maximum measurable strength due to epoxy failure. These drawbacks led to the development of techniques which focus particularly on bonding at the splat level. Two particularly interesting techniques are the splat adhesion test, proposed by Chromik et al. [35], and the cavitation test per ASTM G32-10 [164, 165]. These techniques can be used to investigate the splat-to-substrate interface bond strength and bonding mechanism as bonding normally occurs at this local interface [35, 164]. Single splats are sprayed by increasing the gas travel speed and decreasing the feed rate; this is referred to as a wipe test.

By splat adhesion testing, single splats are removed from the substrate with a stylus having a semicircular cross-section. This test is conducted on a scratch tester which has the ability to record

the tangential force applied on the stylus [35, 36]. A schematic of the stylus, test setup and results are shown in Figure 2.17 [36].

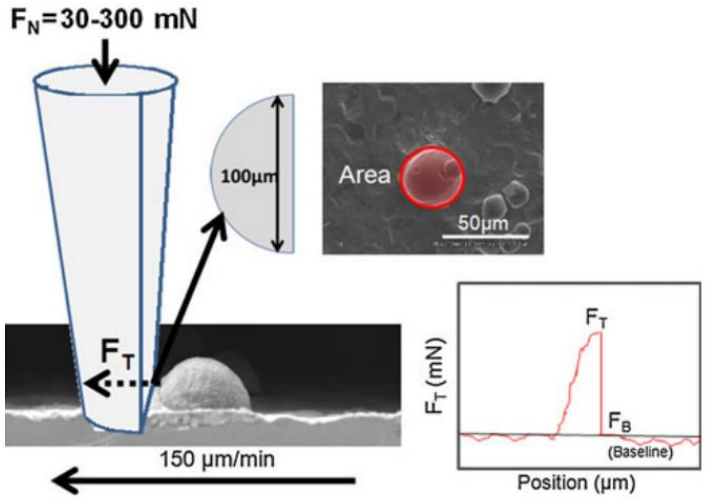

Figure 2.17 Schematic representation of the splat adhesion test [36].

The recorded tangential force versus position results typically show a baseline force due to friction and a peak force as the splat is removed from the substrate. By subtracting the baseline force from the peak force and dividing by the projected splat area (identified as 'Area' in Figure 2.17), adhesion strength of the splat on the substrate is evaluated [35, 36].

The splat adhesion test has been used to study the bonding interface between Ti and Ti6Al4V powder cold sprayed on Ti and Ti6Al4V substrates. As shown in Figure 2.18, three different shearing regimes were observable when analyzing failed interfaces. When the powder was sprayed below its critical velocity (Regime 1), a small peak in the tangential force with a width smaller than the diameter of the sprayed powder particle was found. The remaining interface showed no evidence of shear tracks which means that a weak bond was formed. When the powder was sprayed at the critical velocity (Regime 2), the peak was almost comparable to the width of the powder, however, there was still a sudden drop in tangential force following the shearing event. The shear tracks observed in Regime 2 were in the shape of a ring showing ductile fracture where ASI were formed. When powder was deposited above the critical velocity (Regime 3), shear tracks were

observable over the entire surface of the removed splat. In Regime 3, the drop in tangential force was smooth contrarily to the other two regimes [36].

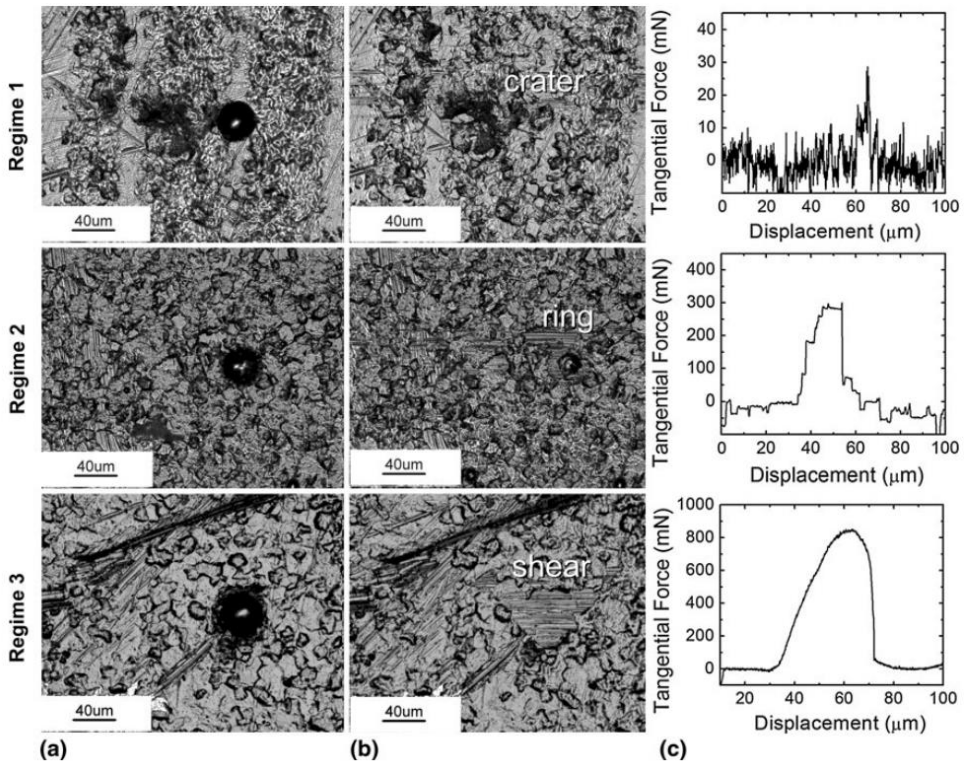

Figure 2.18 The three regimes observed during splat adhesion testing (a) pre-test, (b) post-test and (c) the associated tangential force verses displacement curve [36].

By the cavitation test, the sample is placed into distilled water and a sonotrode is used to expose the splats to ultrasonic vibrations which erode the surface. These ultrasonic vibrations cause the splat/substrate interface to fail after a certain amount of exposure time [164, 165]. The comparison of cavitation test time provides insight regarding better or worse adhesion [164]. This technique is more qualitative than the splat adhesion test which allows for the measurement of splat adhesion strength. Like the splat adhesion test, analysis of the failed interface allows for greater understanding of the bonding mechanism. Post-test images of the Ti substrate surface and of the previously adhered side of a failed Ti6Al4V splat is shown in Figure 2.19. In Figure 2.19 (b), the

region in the periphery of the splat (B), where ASI occur, shows failure of well-bonded material [164].

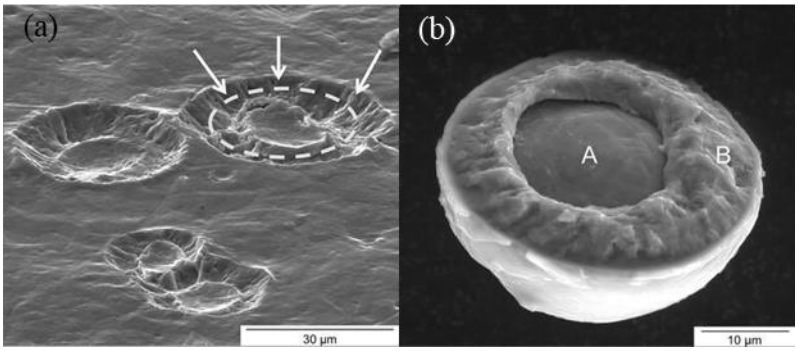

Figure 2.19 (a) Surface of the Ti Grade II substrate after removal of the splats and (b) the Ti6Al4V splat after removal from the substrate following the cavitation test. In (b), the region in the center of the splat (A) shows no bond, while the region in the periphery of the splat (B), where ASI occur, shows failure of well-bonded material [164].

Post-test characterization of single splats removed by splat adhesion testing or cavitation testing provide useful qualitative information regarding the bonding mechanism crucial to understanding coating buildup. Although the splat adhesion test also provides quantitative measurements of splat adhesion, these values should not be used to quantify full coatings. The objectives of these tests are to compare different characteristics leading to adhesion. The tensile test remains the best technique to test full coating behaviour.

2.6 Summary

There are several interesting industrial applications for metal/ceramic interfaces deposited by cold spray given their advantageous properties. However, for industrialized use of these interfaces, there remain many unanswered research questions. Various process independent variables affecting cold sprayed coatings have been fully characterized for metal coatings on metal substrates. These independent variables include, for instance, the effect of spray conditions and velocity in addition to the effect of surface roughness and powder morphology. Yet, to date, there

is very little literature which investigates the effects of these independent variables on metal/ceramic interfaces deposited by cold spray. The available literature is mostly limited to Al coatings deposited on various ceramics for which deposition conditions have not yet been optimized for the individual interfaces. Notably, there is a need to determine the effect of substrate morphology and type of ceramic for other metals than Al, to identify the appropriate deposition conditions, and to evaluate the effect of velocity and powder morphology on deposition. Furthermore, regarding mechanisms leading to adhesion in metal/ceramic interfaces, literature is also limited to few material interfaces and presents incomplete or conflicting theories which can only be better understood by the study of the interfacial adhesion strength of different material combinations.

Provided these limitations in the literature, this work is intended to further the understanding of metal/ceramic interfaces deposited by cold spray with a particular focus on Ti/Al_2O_3 interfaces. Comparisons are also made with Ti/SiC interfaces. The abovementioned independent variables are addressed to further understand their role on adhesion strength and deposition in cold sprayed metal/ceramic interfaces. Mechanisms leading to adhesion are also investigated for the Ti/Al_2O_3 interface.

Chapter 3

Experimental Techniques

3.1 Initial Material Selection

Regarding the study of metal/ceramic interfaces deposited by cold spray, only few material combinations have been characterized within the literature. Therefore, in early stages of the project, six material combinations were selected for preliminary investigation. Material combinations included Al, Cu and Ti to be deposited onto Al_2O_3 and SiC. Al_2O_3 and SiC are frequently used in MMC and were therefore the ceramics of choice for this study.

3.1.1 Powder Particles

The metals selected for preliminary investigation were chosen as they are frequently successfully deposited by cold spray due to their low-temperature ductility [68]. Interestingly, the deposition of Ti onto Al_2O_3 had particularly high splat adhesion strength as compared to all other material combinations orienting the work included in this thesis. For reference, the average adhesion strength measured at different spray conditions for Al and Cu are included in Figure 3.1 and Figure 3.2, respectively. Adhesion strength was measured at the splat level by the splat adhesion test described in Section 3.4. The highest average splat adhesion strength for the Al/Al_2O_3, Al/SiC, Cu/Al_2O_3 and Cu/SiC interfaces were 68 ± 34 MPa, 33 ± 15 MPa, 78 ± 34 MPa and 73 ± 41 MPa respectively, which is significantly lower than the splat adhesion strength measured in Ti/Al_2O_3 interfaces of 237 ± 47 MPa on the as-received substrate. During preliminary investigation, spray

conditions had been selected based on literature for metal/metal interfaces with varying temperature and pressure to determine their respective effects on adhesion strength. For Al, additional spray conditions were tested but these resulted in weak or no bonding and have not been included in Figure 3.1. A difference in the temperature range tested for Al, Cu and Ti is notable. This difference was necessary to avoid nozzle clogging during the deposition of Al at high temperatures. Due to difference in spray conditions, it is difficult to directly compare the materials. Yet, the impressive performance of Ti/Al_2O_3 stands out.

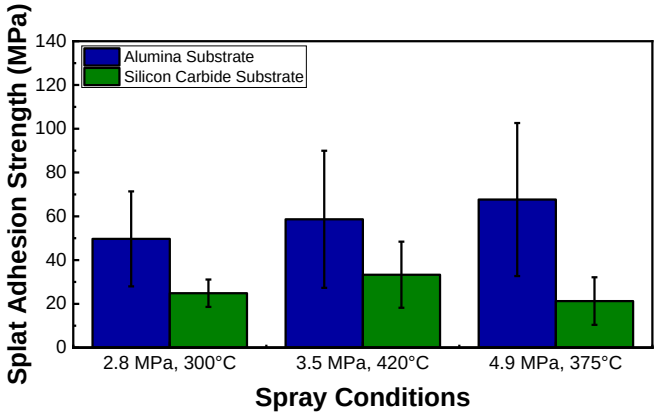

Figure 3.1 Splat adhesion strength for Al/Al_2O_3 and Al/SiC interfaces.

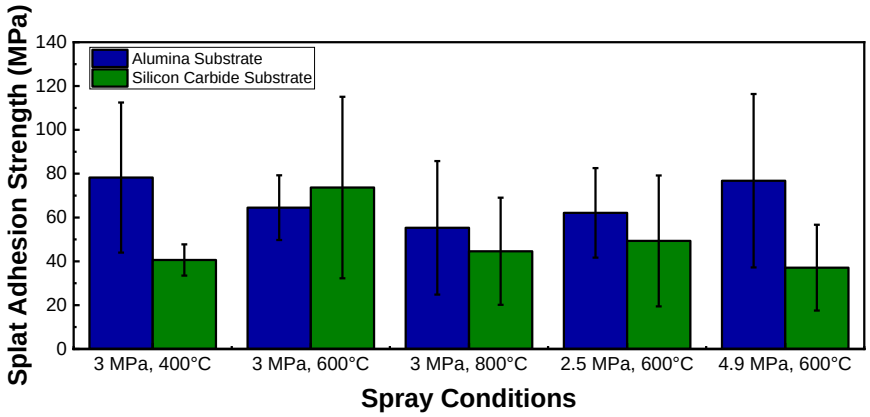

Figure 3.2 Splat adhesion strength for Cu/Al_2O_3 and Cu/SiC interfaces.

Spherical and irregularly shaped commercially pure Ti powder are used. The spherical powder (Grade 1, AP&C, Quebec, Canada) is manufactured by plasma gas atomization resulting in a martensitic microstructure (Figure 3.3 (a)). The mean size of the powder is 29 μm. By plasma gas atomization, powder particles are formed using a plasma torch which melts and separates raw material fed in wire form. Solidification is delayed by maintaining high temperatures in the chamber. This delay promotes spheroidization of the powder particles due to surface tension. The process occurs in an argon environment to maintain the purity of the material and avoid gaseous reactions [166].

The irregular shaped powder (Cristal metals, Illinois, USA), manufactured by the Armstrong process, has a coral-like morphology with an average size of 66 μm. The irregular shaped powder has an equiaxed microstructure with grains varying from hundreds of nanometers to few microns within a single powder particle (Figure 3.3 (b)). Manufacturing Ti powder by the Armstrong process involves injecting $TiCl_4$, in gaseous form, into a liquid stream of Na. Under the right conditions, the $TiCl_4$ and Na react to form solid Ti powder particles and NaCl. The Ti powder is then rinsed to remove NaCl [145].

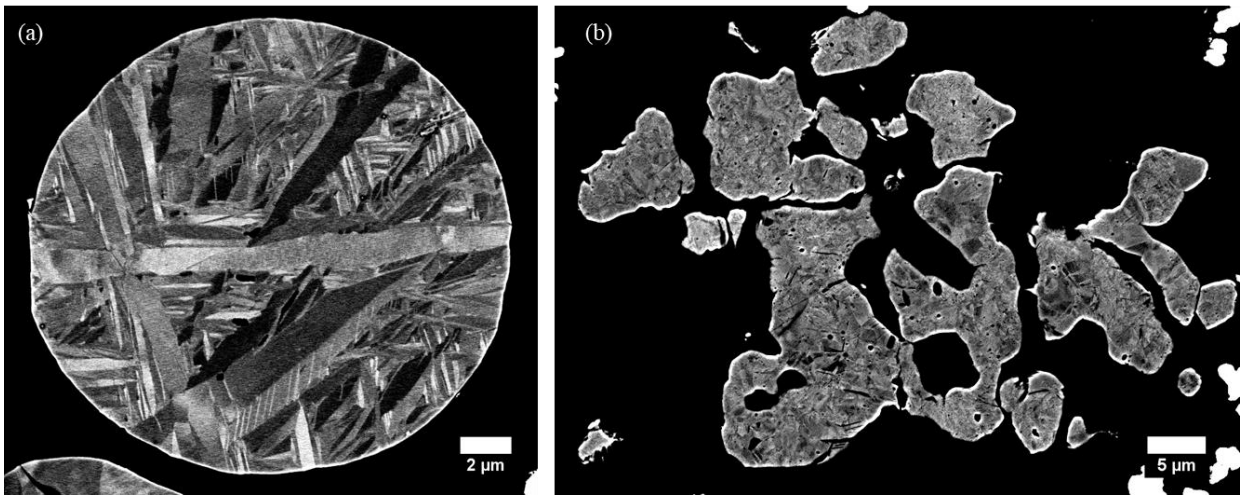

Figure 3.3 The microstructure of the (a) spherical and (b) irregular shaped Ti powder.

3.1.2 Substrate Materials

As substrates, polycrystalline Al_2O_3 and SiC (AD-995, SC-30, CoorsTek, Arkansas, USA) are used to compare adhesion strength of single splats with a change in ceramic composition. The purity and mechanical properties provided by the manufacturer for these substrates are shown in Table 3.1.

Table 3.1 Purity and mechanical properties of the polycrystalline Al_2O_3 and SiC substrates provided by the manufacturer.

Properties	**Units**	**Test**	**Al_2O_3**	**SiC**
Purity	%	Not Specified	99.5	> 99
Density	g/cm^3	ASTM-C20	3.90	3.15
Flexural Strength (MOR) at 20°C	MPa	ASTM-F417	379	480
Elastic Modulus at 20°C	GPa	ASTM-C848	370	410
Poisson's Ratio at 20°C	-	ASTM-C848	0.22	0.21
Compressive Strength at 20°C	MPa	ASTM-C773	2600	3500
Tensile Strength at 25°C	MPa	ACMA TEST #4	262	-
Fracture Toughness	$MPam^{1/2}$	NOTCHED BEAM	4-5	4.0
Thermal Conductivity at 20°C	W/m K	ASTM-C408	30.0	150.0
Coefficient of Thermal Expansion at 25-1000°C	1X 10-6/°C	ASTM-C372	8.2	4.4
Specific Heat at 100°C	J/kg*K	ASTM-E1269	880	800

Given the particularly high adhesion strength measured in the Ti/Al_2O_3 interface, most of the thesis focuses on this interface. Some of the Al_2O_3 polycrystalline substrates are ground to a final grinding step using a 60 μm grinding disk (Buehler, Illinois, USA) and some to a final polishing step of 1 μm diamond suspension (Buehler, Illinois, USA). The 60 μm diamond grinding disk and 1 μm diamond suspension rendered a reduced peak height value (R_{pk}) of 0.33 ± 0.07 μm and 0.16 ± 0.03 μm respectively. The as-received polycrystalline Al_2O_3 substrates have a surface roughness of 0.78 ± 0.38 μm. The as-received, ground and polished substrates are used to investigate the effect of surface roughness on splat adhesion strength. Additionally, single

crystalline Al_2O_3 substrates (Meller optics, Rhode Island, USA and GT Advanced Technologies, Massachusetts, USA) are also used for *in situ* testing given their transparent nature and for investigating the effect of crystallographic orientation on splat adhesion strength. For clarity the abovementioned substrates, used throughout the thesis, are summarized in Table 3.2 with the respective chapter(s) they are used in.

Table 3.2 Summary of substrates used throughout the thesis

Substrate	Post-processing	Chapter
Sintered Al_2O_3	None	4, 5, 7
Sintered Al_2O_3	Ground with 60 μm diamond grinding disk	4
Sintered Al_2O_3	Polished with 1 μm diamond suspension	4
Sintered SiC	None	4
Sapphire C-Plane (001)	None – Pre-polished	6, 7
Sapphire A-Plane (110)	None – Pre-polished	7
Sapphire R-Plane ($\mathbf{1\bar{1}2}$)	None – Pre-polished	7

3.1.3 Material Characterization

Prior to deposition, the materials used are characterized by various techniques. Powder morphology is analyzed by SEM (SU3500 and SU8000, Hitachi, Tokyo, Japan) by fixing a small quantity of powder on carbon tape. Powder cross-sections are also analyzed by SEM. For cross-sectioning, powder particles are mounted in copper-based Technovit 5000 epoxy (ANAMET, Quebec, Canada) then ground and polished to 0.05 μm colloidal silica (ANAMET, Quebec, Canada). Powder size distribution is analyzed using a laser diffraction particle size analysis (LA-920, Horiba, Kyoto, Japan). In addition to powder characterization, the substrates are analyzed by SEM (SU8230, Hitachi, Tokyo, Japan) for morphology and by energy-dispersive X-ray spectroscopy (EDS) for composition. The surface of the polycrystalline Al_2O_3 has contaminants including calcium, magnesium, chlorine, sodium and sulfur in localized locations mainly between grains (Figure 3.4). The SiC have mainly traces of boron and regions of higher carbon content which may be due to the sintering process since free carbon and boron are used as sintering aids

(Figure 3.5) [167]. Minor traces of aluminum and oxygen are also found on the surface of SiC. Surface roughness is investigated using an interferometer profiling system (ZYGO, Connecticut, USA) on 12 spots on 3 randomly selected substrates at a magnification of 25X and 100X. The analysis of surface roughness at different magnifications is required to have a proper understanding of overall surface conditions but also conditions at the splat level. Also, by analysis of surface roughness at different positions along the substrate, it is possible to identify the extent of local heterogeneity in the substrate which was ultimately found to significantly affect the adhesions strength results.

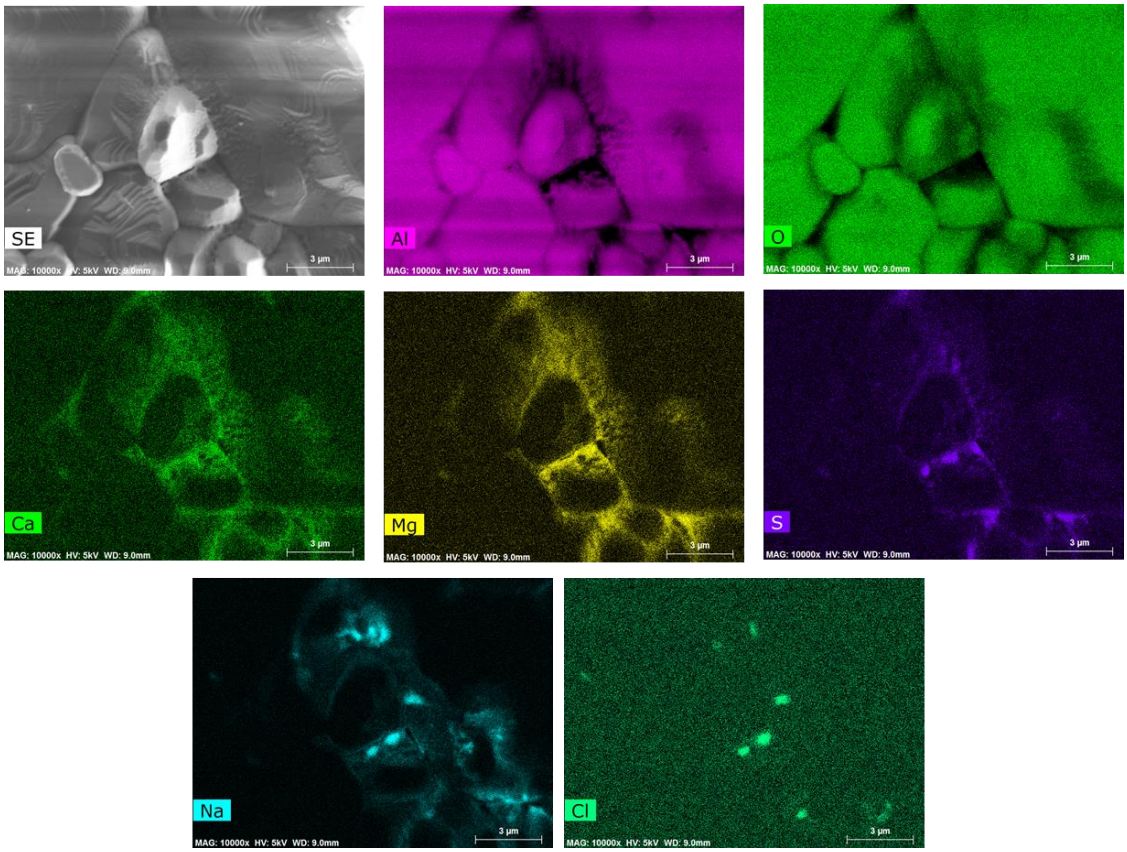

Figure 3.4 SE and EDS results for the surface of the polycrystalline Al_2O_3.

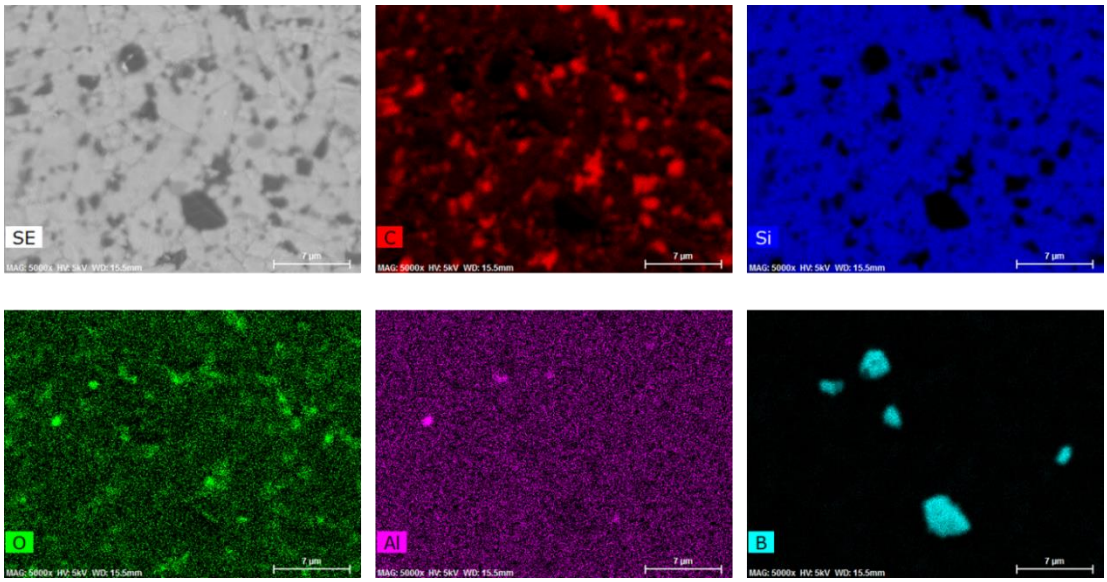

Figure 3.5 EDS results for the surface of the polycrystalline SiC.

3.2 Cold Spray

The Plasma Giken PCS-800 system (Plasma Giken, Saitama, Japan) is used for cold spray with nitrogen as the carrier gas. The equipment is located at the McGill Aerospace Materials and Alloys Design Center (MAMADC) at the National Research Council of Canada (NRC) in Boucherville, Quebec, Canada. The majority of deposits are done using the PG PNFC2-010-20S nozzle (Plasma Giken, Saitama, Japan) but in Chapter 5, where a wide range of velocities are required, the PG PNFC-012-30 nozzle (Plasma Giken, Saitama, Japan) is also used. The PG PNFC-012-30 nozzle has a specialized geometry which allows the gas and the powder to reach higher velocities at lower temperatures and gas pressures. By use of this nozzle, velocities which could not be achieved with the PG PNFC-012 are reached. With both nozzle configurations, nitrogen is used as the carrier gas. Prior to deposition, for some spray conditions, a time-of-flight particle diagnostic system (DPV 2000, Coldspraymeter, Tecnar Automation, Quebec, Canada) is used to measure particle velocity.

Most of the work conducted is on single splats. To ensure the deposition of single splats, the powder feed rate used is 1 to 2 g/min and the gun traverse speed is 1 m/s [35, 36]. The standoff

distance for all tests is fixed to 30 mm away from the substrate. When comparing Al_2O_3 to SiC at identical spray conditions, the two substrates are clamped side by side to ensure that conditions are truly comparable (Figure 3.6 (a)). For deposition onto the sapphire windows, a specialized holder was manufactured given their small size (Figure 3.6 (b)).

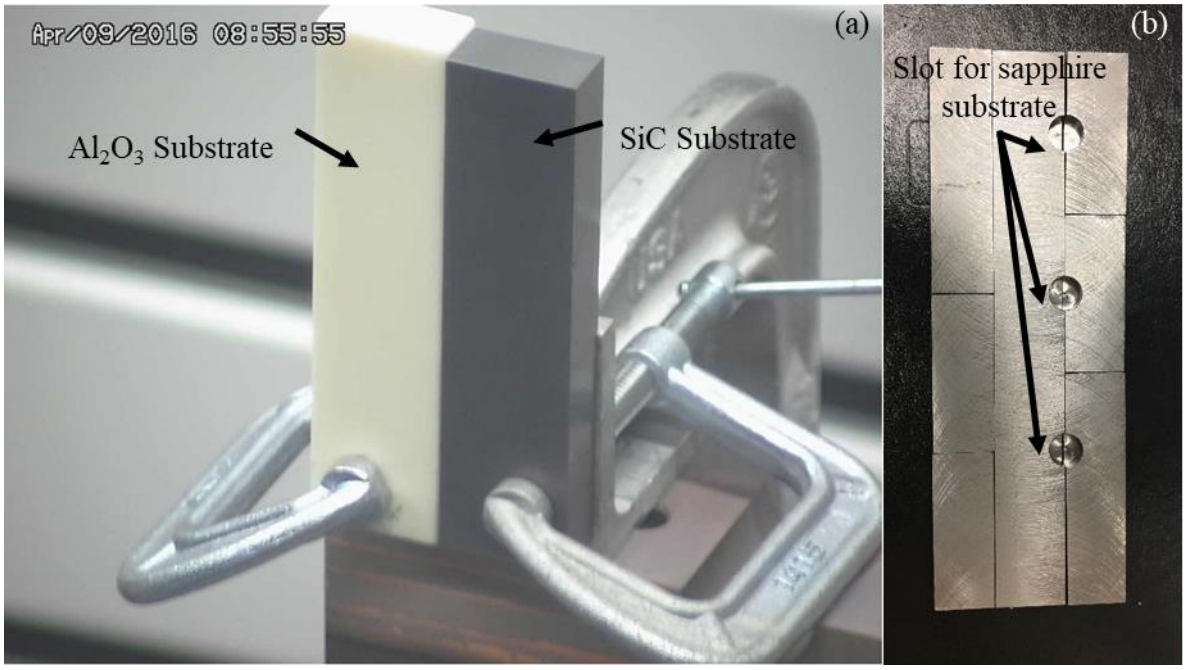

Figure 3.6 Substrate setup for cold spray (a) polycrystalline Al_2O_3 and SiC and (b) sapphire substrates.

3.2.1 Spray Conditions

Prior to this work, successful deposition of Ti onto Al_2O_3 was only reported by Rafaja et al. [26] who did not include a study on optimization of spray conditions. In metal/metal interfaces critical velocity for Ti deposition has been approximated to be between 700 m/s and just under 900 m/s [22]. Initial tests (Chapter 4) are completed at spray conditions of 4 MPa and 800ºC rendering a velocity of 692 ± 133 m/s; the velocity is relatively close to the critical velocity range reported for Ti and rendered successful deposition of single splats onto both polycrystalline Al_2O_3 and SiC. As such, the Ti/Al_2O_3 and Ti/SiC interfaces are compared under this spray condition.

To determine the critical velocity for deposition of Ti onto Al_2O_3 and SiC, a laser-induced projectile impact test (LIPIT) (described in Section 3.3) is used. Unfortunately, limitations in laser power did not allow for many particles to deposit onto SiC. Preliminary results obtained by LIPIT showed a critical velocity near 800 m/s (Figure 3.7 (b)), a value significantly higher than that obtained for the Ti/Al_2O_3 interface, which was around 580 m/s (Figure 3.7 (a)). Unfortunately, working with such high velocities made it difficult to get repeatable data in both cold spray and by LIPIT for the Ti/SiC interface given equipment limitations. Therefore, exact critical velocity and the effect of velocity on adhesion strength are only investigated for the Ti/Al_2O_3 interface (Chapter 5). Some details regarding the comparison between Al_2O_3 and SiC are addressed in the global discussion (Chapter 8).

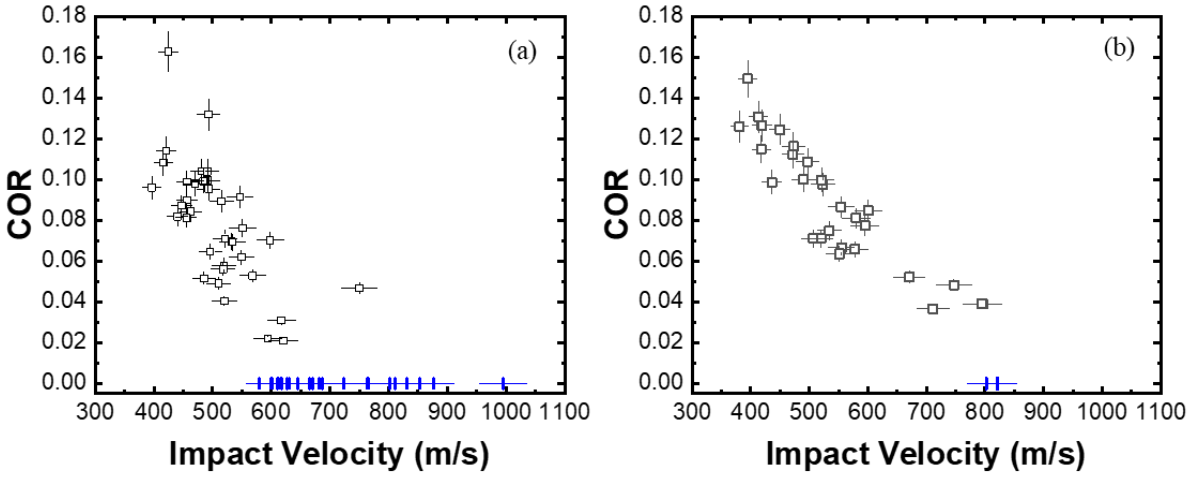

Figure 3.7 Coefficient of restitution and critical velocity for (a) Ti/Al_2O_3 and (b) Ti/SiC interfaces. Squares are used to represent rebounded powder particles while blue markers are used to represent adhering splats.

To investigate the effect of deposition velocity on adhesion strength, five different cold spray conditions and two nozzle geometries were used. Deposits with the PG PNFC2-010-20S nozzle at 4 MPa and 800ºC and with the PG PNFC-012-30 nozzle at 4.9 MPa and 450ºC are used to investigate the effect of changes in gas temperature on adhesion strength as identical velocities are achieved at significantly different temperatures using the two nozzle configurations. The use of

two different nozzle configurations led to concerns regarding the effect of temperature. The amount of heat absorbed by the powder is therefore approximated by a numerical model described in Section 3.2.2.

When depositing on sapphire, the primary focus is the effect of powder morphology given the importance of ASI when depositing on smooth substrates (Chapter 6). Therefore, a complete study of the effect of spray conditions on the smooth substrate is not repeated. Nevertheless, since the required deposition conditions on sapphire for spherical and irregular powder are unknown, Ti is deposited at 4 MPa and 400ºC as well as 4 MPa and 800 ºC using the PG PNFC2-010-20S nozzle. While the use of two nozzle geometries could have allowed us to investigate a wider range of velocities on sapphire, issues regarding changes in temperature, which may be more significant with the irregular powder as it has a larger surface area, are avoided by using one nozzle geometry throughout this set of experiments. The spray conditions used throughout the thesis are summarized in Table 3.3.

Table 3.3 Summary of spray conditions and powder morphology used throughout the thesis

Nozzle	Powder Morphology	Gas Pressure (MPa)	Gas pre-heat temperature (°C)	Chapter
PG PNFC2-010-20S	Spherical	4.0	400	5, 6, 7
PG PNFC2-010-20S	Coral-like	4.0	400	6
PG PNFC2-010-20S	Spherical	4.0	600	5
PG PNFC2-010-20S	Spherical	4.0	800	4, 5, 6
PG PNFC2-010-20S	Coral-like	4.0	800	6
PG PNFC-012-30	Spherical	4.9	450	5
PG PNFC-012-30	Spherical	4.9	800	5

3.2.2 Numerical Simulation of Powder Temperature in Cold Spray

When using the two different nozzle configurations (Chapter 5), a major concern is the effect of powder temperature on the reported results given that the PG PNFC-012-30 nozzle renders higher velocities at lower gas temperatures. As described in Section 3.2.1, two spray conditions rendering

identical powder velocities were used to compare the two nozzles and ensure that nozzle configuration and gas temperature do not significantly contribute to adhesion strength. However, the PG PNFC-012-30 nozzle is longer and will result in a longer contact time between the powder and the gas, which can ultimately promote more heat transfer. It is therefore important to approximate the temperature of the powder traveling through the nozzle to ensure that adequate conclusions and comparisons are made.

To investigate the effect of temperature, a simplified two-dimensional numerical model is used (MATLAB script available in Appendix A). A two-dimensional model with a gas flow modeled to be in a quasi-one-dimensional isentropic semi-perfect state is often used in cold spray literature to investigate the effect of nozzle dimensions on gas velocity, temperature and pressure along the length of the nozzle as a first step to approximating powder velocity and temperature along the length of the nozzle [19, 67, 168-171]. Variables used in the model equations are summarized in Table 3.4.

Table 3.4 Variables used in the model equations.

Variable	Description
A	Nozzle area
A*	Nozzle area at throat
M	Mach number
γ	Ratio of gas specific heat
p	Pressure
p_o	Stagnation/initial pressure
T	Temperature
T_o	Stagnation/initial temperature
U_g	Gas velocity
U_{gi}	Initial gas velocity
R	Specific gas constant
U_p	Powder particle velocity
C_d	Drag coefficient
ρ_g	Gas density
D_p	Powder particle diameter
ρ_p	Powder particle density
x	Axial position of the powder particle
T_p	Powder particle temperature
h	Powder particle heat transfer coefficient
C_p	Gas heat capacitance at constant pressure
D	Drag force on a particle
m	Mass of the particle

The first step is to determine the local Mach number (Eq. 3.1) given the local area ratio (local-to-throat) along the length of the nozzle. A system of linear equations is used to define the radius of the nozzle at different positions in the nozzle using the inlet, throat and exit radius which is then used to solve for the area ratio at specified points along the nozzle. Then, local gas temperature (Eq. 3.2) and gas pressure (Eq. 3.3) are calculated using the local Mach number.

$$\frac{A}{A^*} = \left(\frac{1}{M}\right)\left[\left(\frac{2}{\gamma+1}\right)\left(1+\frac{\gamma-1}{2}M^2\right)\right]^{\gamma+1/[2(\gamma-1)]} \quad \text{Eq. 3.1}$$

$$\frac{T}{T_o} = \left(1+\frac{k-1}{2}M^2\right)^{-1} \quad \text{Eq. 3.2}$$

$$\frac{p}{p_o}\left(1+\frac{k-1}{2}M^2\right)^{\frac{-k}{k-1}} \quad \text{Eq. 3.3}$$

Once the local gas pressure along the length of the nozzle is known, the gas velocity along the length of the nozzle can also be solved for by Eq. 3.4.

$$U_g=\sqrt{2\frac{\gamma}{\gamma-1}RT_o\left[1-\left(\frac{p}{p_o}\right)^{\frac{\gamma-1}{\gamma}}\right]+U_{gi}^2} \quad \text{Eq. 3.4}$$

With the gas velocity known, the powder velocity is found by Eq. 3.5.

$$\frac{dU_p}{dt}=\frac{3}{4}\frac{C_d\rho_g}{D_p\rho_p}\left(U_g-U_p\right)\left|U_g-U_p\right| \quad \text{Eq. 3.5}$$

By the Euler method, dU_p and dx can be rewritten as $U_{p,\,x}-U_{p,\,x-1}$ and $x_{p,\,x}-x_{p,\,x-1}$ (Δx_p). Also, using kinematics, Eq. 3.6 is used assuming that over the step size along the length of the nozzle, the acceleration is constant [169, 171]. Therefore, Eq. 3.5 is further rearranged to solve for gas velocity as shown in Eq. 3.7 [169, 171]. In the model, the particle specific heat (c_p), density (ρ_p) and particle diameter (D_p) are 472 J/(kg K), 4540 kg/m^3 and 29 µm respectively [42].

$$U_{p,x}^2=U_{p,x-1}^2+2\frac{dU_p}{dt}\Delta x \quad \text{Eq. 3.6}$$

$$U_{p,x}=\sqrt{U_{p,x-1}^2+\frac{3}{2}\frac{C_d\rho_g\Delta x_p}{D_p\rho_p}\left(U_{g,x}-U_{p,x-1}\right)\left|U_{g,x}-U_{p,x-1}\right|} \quad \text{Eq. 3.7}$$

Particle temperature (T_p) at the exit of the nozzle is estimated by Eq. 3.8. The differential equation is simplified by the same technique used for the velocity equation. Eq. 3.8 is rewritten as shown in Eq. 3.9.

$$\frac{dT_p}{dt}=\left(T_g-T_p\right)\frac{6h}{c_p\rho_pD_p} \quad \text{Eq. 3.8}$$

$$T_p = \sqrt{T_{p,x-1}^2 + 2\Delta x \left[T - T_{p,x-1} \frac{6h}{C_D \rho_p D_p}\right]} \quad \text{Eq. 3.9}$$

Additional details to solve for the heat transfer coefficient and drag coefficient are available in [67, 169, 170]. To validate the model, the particle velocity and particle temperature were compared to modeled values in [19, 67] using nozzle and particles properties provided within the references.

3.3 Laser Induced Projectile Impact Test

The LIPIT platform is intended to simulate microscale ballistic impact and was built in-house at the Massachusetts Institute of Technology. A schematic of the test platform, as shown by Hassani-Gangaraj et al. [87], is shown in Figure 3.8. A laser pulse (Nd:YAG laser pulse of 10 ns and 532 nm wavelength) is used to accelerate micron-size powder particles towards a substrate by use of a launching pad. The launching pad consists of a 210 μm thick glass substrate sputter-coated with 60 nm of gold, then coated with an elastomeric polyurea coating about 30 μm thick [87]. Micron-sized powder particles are placed onto the launching pad in an ethanol suspension, spread using a lens cleaning paper, and left to dry [87]. When the laser pulse is focused on the launching pad, ablation of the gold film and rapid expansion of the polymer occurs. This expansion causes the micron-sized particles to be accelerated towards the substrate positioned beneath [87]. Smaller particles are lighter and reach higher velocities. To ensure that velocities comparable to cold spray are reached, the powder particles selected for impact need to have an average diameter of 10 ± 1 μm. Appropriate particles are specifically selected using a secondary charge-coupled device (CCD) camera. The substrates, onto which the particles are accelerated, must be cut to dimensions of 2-3 x 12.5 x 10 mm^3. Deposition occurs on the edge of 2-3 mm to ensure proper visibility for *in situ* observation of impact.

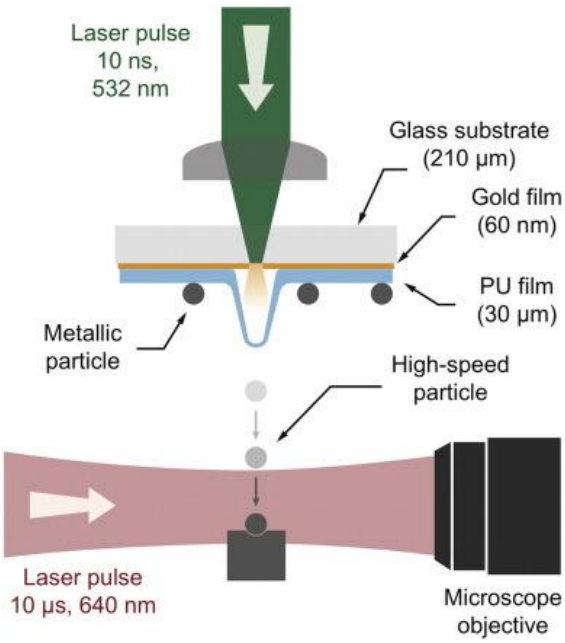

Figure 3.8 Schematic of LIPIT platform [87].

In situ observation of impact can be achieved by use of a 16-frame high-speed camera (SIMX 16, Specialised Imaging) as the particle approaches the substrate. The sample is illuminated by a synchronized quasi-continuous-wave laser imaging pulse (30 µs duration, 640 nm wavelength SI-LUX640, Specialised Imaging) while the frames are captured [87]. The 16 frames show the position of the particle with respect to time as it approaches the substrate given that interframe time is known. For example, in Figure 3.9, the distance recorded in the sixth frame is 65 µm from the edge while in the eighth frame it is 202 µm. The particle has therefore traveled 137 µm in 300 ns (457 m/s). This task is made simple using the SIM Control software which is provided with the high-speed camera as velocity is automatically calculated when selecting the position of the particle in different frames.

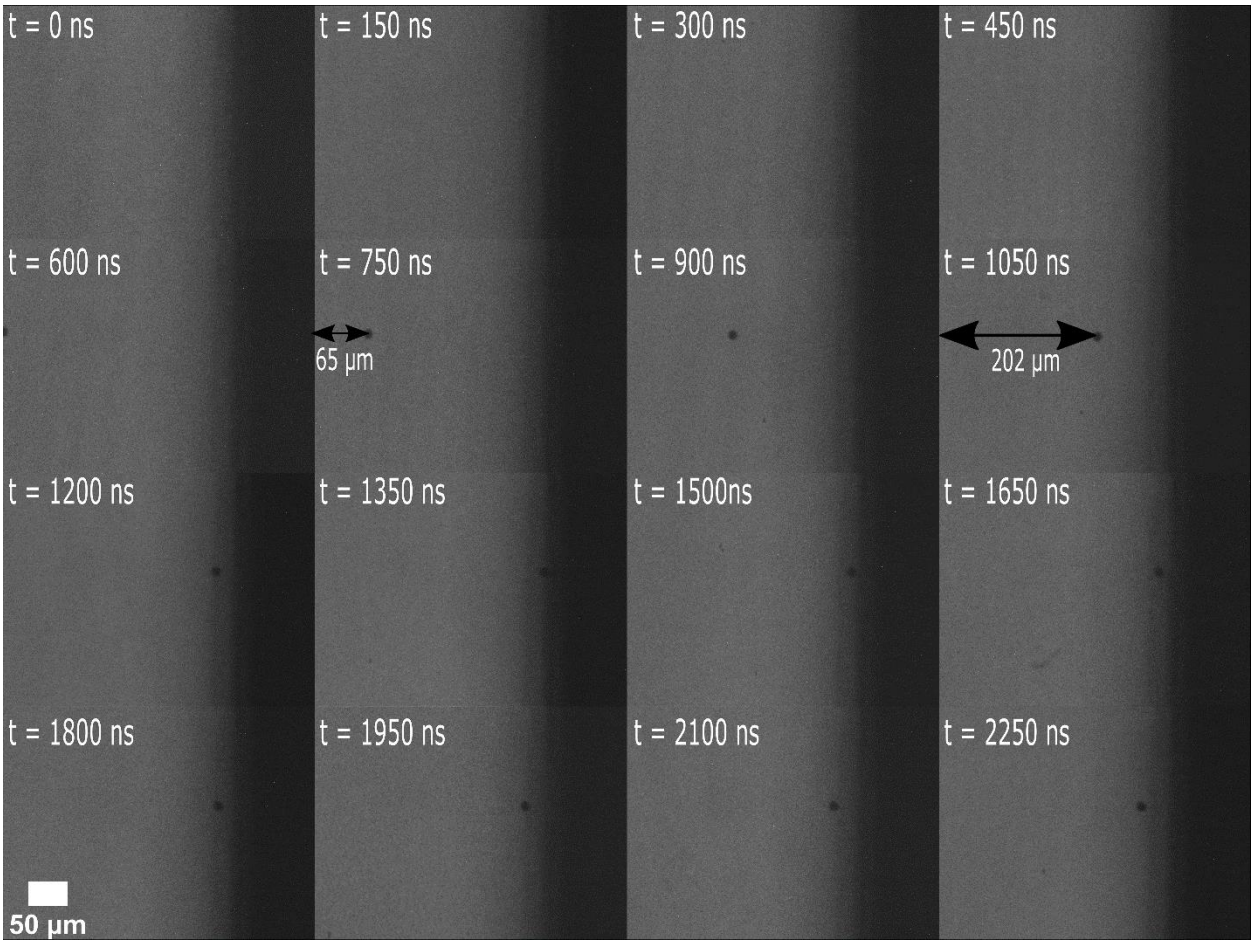

Figure 3.9 16 frames captured by the high-speed camera for a single particle of Ti accelerated towards and Al_2O_3 substrate annotated to emphasize the interframe time and distance traveled in 2 frames.

3.4 Splat Adhesion Test

Splat adhesion[1] testing is conducted using the Micro-Combi Scratch Tester (Anton Paar, Graz, Austria) to determine the splat adhesion strength of the single Ti splats deposited onto all substrates

[1] For consistency with the literature, the term "adhesion" is used throughout the thesis while, in theory, these tests would render a value of "adherence" as defined in Section 2.1.

and at all spray conditions. The equipment is calibrated to allow easy stage displacement from the light optical microscope (LOM) to the center of the tip. Therefore, positioning for the test is done under the LOM. The cursor is to be placed at the position of initial step down of the tip, that is, more than 50 μm from the splat. By positioning the tip at a distance of approximately 50 μm, contact with the splat is ensured to be within the test while recording a sufficiently large baseline. For all splat adhesion tests, the scratch speed is set to 150 μm/min. The tip has a semicircular geometry with a 100 μm flat edge. The flat edge is used to remove the splat during the scratch. The normal force and scratch length are varied depending on the test conditions. In cases where the splats are highly adhering, a higher normal load is required to ensure that the tip does not travel above the splat. The scratch length is often dependent on the distance available between splats.

During setup, it is important to ensure that only a single splat will be impacted by the tip during the test for accurate results. The tip has a diameter of 100 μm, therefore, there cannot be any additional splats 50 μm above or below the splat to be analyzed. Furthermore, given the large size of the tip with respect to the scratch length, it was determined that there should be no additional splats 100 μm before and 130 μm after the evaluated splat respectively. Images of the studied splat are to be taken with 5X, 10X and 20X magnification before and after the test to adequately correlate the results with observations. Prior to conducting the test, the diameter and height of the splat must also be measured. The position of the splat is also noted with respect to two edges to ensure that it can be relocated for further examination in the SEM.

During the splat adhesion test, the tangential force applied on the tip is recorded. As the tip encounters the splat, this results in a peak in the tangential force plot with respect to position. The peak ($F_{T\ Peak}$) is subtracted from the baseline tangential force ($F_{T\ Baseline}$) to calculate the force required to remove the splat. Splat adhesion strength is then measured by dividing the force by the projected area of the splat (Eq. 3.10) [35].

$$Splat\ adhesion\ strength\ [MPa] = \frac{F_{T\ Peak}\ [mN] - F_{T\ Baseline}[mN]}{Projected\ Splat\ Area\ [\mu m^2]} * 1000 \qquad \text{Eq. 3.10}$$

where the projected splat area can be measured by Eq. 3.11 [35].

$$Projected\ Splat\ Area\ [\mu m^2] = \pi\left(\frac{w\ [\mu m]}{2}\right)^2 \quad \text{Eq. 3.11}$$

where w is the splat diameter measured on LOM images captures prior to the test using two diagonals.

In Chapter 6, adhesion energy was also required and can be calculated by Eq. 3.12 by using the area under the peak of the tangential force with respect to position graph following subtraction of the baseline. The area under the peak is found using the quick peaks gadget in Origin.

$$Splat\ adhesion\ energy\ [KJ\ m^{-2}] = \frac{\int_{Contact}^{Failure}[F_T(x) - F_{T\ Baseline}]dx\ [mN.\mu m]}{Projected\ Area\ [\mu m^2]} \quad \text{Eq. 3.12}$$

3.5 *In Situ* Splat Adhesion Test

In situ splat adhesion testing is performed on an in-house modified Micro-Scratch tester (CSM Instruments, Graz, Austria). The modified Micro-Scratch Tester is located at Polytechnique Montréal. The test conditions and the procedure are identical to the conventional tests performed on the Micro Combi Scratch tester as described in Section 3.4. The only difference is that the microscope is positioned directly under the tip and a CCD camera can be used to record the test through the microscope lens. This testing technique can only be used if the substrate/sample is transparent. A schematic of the test platform is shown in Figure 3.10 [172].

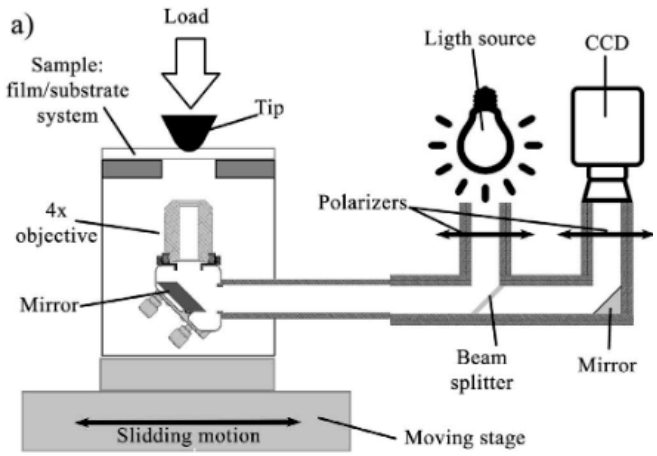

Figure 3.10 Schematic of *in situ* splat adhesion test platform [172] [sic].

3.6 Microscopy

3.6.1 Scanning Electron Microscopy of Metal/Ceramic Interfaces

SEM is used for evaluating the morphology of the splats, the powder cross-sections, the substrate morphology and compositions, the cross-section of interfaces and for post-test characterization following splat adhesion testing. For sample cross-sections, samples are cut using the Buehler Isomet 5000 and a Buehler diamond wafering blade. The cut samples are ground using 70, 45, 15 and 6 μm diamond grinding disks and polished with 9 and 3 μm diamond suspension followed by 0.05 μm colloidal silica mixed with 10 ml of diluted H_2O_2. For cross-sectioning of irregular shaped powder deposited on sapphire, focused ion beam milling (FIB) is used and imaging of cross-sections is done within the FIB (FEI Helios NanoLab 660, Massachusetts, USA).

When imaging nonconductive samples in the SEM, there is a large negative potential created between the sample and the stage, as the sample cannot discharge through the stage; this effect is referred to as charging of the sample. When charging, the sample appears very bright and a clear image cannot be captured. Therefore, to investigate metal/ceramic interfaces in the SEM, the variable pressure mode is often used to prevent charging effects. When gas is introduced into the

chamber, secondary electrons (SE) ionize the gas to produce positive and negative ions. The positive ions neutralize the negatively charged sample. Given the interaction between the SE and the gas, when using the variable pressure mode, the SE detector cannot be used [173]. The ultra-variable pressure detector (UVD), which produces an image by detecting photons produced during ionization, is therefore used. The image generated by a UVD detector shows topography and some composition similarly to a SE detector [174]. The use of the variable pressure mode is particularly important when analyzing samples with a large amount of ceramic such as during post-test characterization or evaluation of splat and substrate morphology. At McGill, only the SU3500 microscope (Hitachi, Tokyo, Japan) is equipped with the variable pressure mode and is used for analysis of the above-mentioned samples. Cross-sectional samples have a lot less ceramic. A gold coating of 4 nm is sputter coated on the samples to reduce charging. Imaging of metal/ceramic cross-sections and powder cross-sections is done on a cold field emission SEM (SU8000 or SU8230, Hitachi, Tokyo, Japan). Imaging in cold field emission microscopes has a higher resolution which allows for electron channeling contrast imaging (ECCI) of ultrafine grains [173].

3.6.2 Transmission Electron Microscopy (TEM) and Scanning Transmission Electron Microscopy (STEM)

For higher-resolution imaging of microstructure and to understand how a bond is formed by high-speed impact between a metal and a ceramic, cross-sections of the Ti/Al_2O_3 interface are analyzed by TEM (Talos, Thermo Scientific, Massachusetts, USA) and STEM at 200 kV (Talos, Thermo Scientific, Massachusetts, USA) and 30 kV (SU9000, Hitachi, Tokyo, Japan). TEM is used for high-resolution imaging, STEM at 200 kV is used for EDS and STEM at 30 kV is used for electron energy loss spectroscopy (EELS). TEM and STEM samples must be electron transparent and therefore have a thickness of less than 100 nm [175]. A thin lamella is created within the FIB (FEI Helios NanoLab 660, Massachusetts, USA). The *in situ* lift-out technique is used. Prior to milling, a protective Pt coating is applied to the region of interest (ROI). For one sample, a C coating is applied prior to deposition of the Pt coating for calibration in the TEM. By the lift-out technique, both sides of the ROI are ion milled until the lamella is approximately 1 μm thick. Extraction is

done by ion milling an L-shaped groove around the sample. The sample is then attached to the extraction needle using a Pt coating. The final edge of the sample is ion milled and the sample is lifted out. The lamella is mounted onto a Mo or Cu TEM grid using a Pt coating and separated from the extraction needle. Final thinning is completed with the sample on the TEM grid [176]. Several issues were encountered during final thinning of TEM samples which caused amorphization of the top surface of the cross-section and contamination. To avoid these issues, the ion voltage, current and incident ion angle suggested by Baram and Kaplan [176] during final thinning are used. That is, an ion voltage, current and incident ion angle of 30 kV, 93 pA and ±1° until a lamella thickness of 500 nm and 5 kV, 16 pA and ±1° until a lamella thickness under 100 nm. For HRTEM images, the sample is positioned in a zone axis of Al_2O_3 given that the Ti is polycrystalline with nanosized grains. TEM images are analyzed by use of the Digital Micrograph software which generates the local FFTs in the image. FFTs are indexed using both the CrysTBox software and the JEMS software to determine the phase.

Chapter 4

Influence of Substrate Characteristics on Single Ti Splat Bonding to Ceramic Substrate by Cold Spray

Sara I. Imbriglio · Nicolas Brodusch · Maniya Aghasibeig · Raynald Gauvin · Richard R. Chromik

Adapted from a paper of the same title published in the *Journal of Thermal Spray Technology*, 2018. **27**(6): p. 1011-1024

4.1 Abstract

The cold spray technique may be used to fabricate metal matrix composites and to metallize ceramics. Both applications involve the creation of metal/ceramic interfaces, which are well researched for other processes but not nearly as much for cold spray. Here, the effect of ceramic substrate composition and surface roughness on adhesion strength of metallic splats is investigated. Splat adhesion testing was performed on Ti splats deposited on Al_2O_3 substrates with varying average reduced peak height roughness (R_{pk}) values. Ti splats sprayed onto Al_2O_3 with the lowest surface roughness had a higher bond strength (305 ± 87 MPa) than splats deposited on the higher surface roughness Al_2O_3 (237 ± 47 MPa). Failed interfaces revealed that the bonding mechanism

for substrates with higher surface roughness is predominantly mechanical interlocking. Adhesion to the Al_2O_3 substrate with low surface roughness is predominantly along the periphery of the particle where jetting occurs. Splat adhesion testing was also performed on Ti splats deposited on SiC. Ti splats had a significantly higher bond strength to all Al_2O_3 substrates than to SiC. Post-test observations of SiC substrates showed little evidence of bonding. Several rebounded or detached splats left traces of Ti along the periphery of the impacted particle.

Keywords adhesion · alumina · cold spray · interface · silicon carbide · titanium

4.2 Introduction

High-pressure cold spray is a coating deposition technique by which powder is fed into a heated high-pressure gas flow and accelerated to supersonic velocities by a de Laval nozzle. The powders, accelerated to high velocity, impact on a substrate and if bonded create a 'splat'. The gas temperature is maintained below the melting temperature of the powder [68, 83]. Thus, for metal/metal interfaces, solid-state bonding between the powder and substrate occurs by extreme plastic deformation and the formation of adiabatic shear instabilities (ASI). Mechanical clamping and metallurgical bonding are reported for these interfaces [18, 19, 21]. While a significant amount of work has been done to understand adhesion in metal/metal interfaces by cold spray, metal/ceramic interfaces are not well understood given the low deformability of the ceramic [23-25].

Two types of metal/ceramic interfaces created by cold spray are addressed in the literature. Metal matrix composites (MMC) with ceramic reinforcements have been deposited to improve adhesion, increase hardness, reduce porosity and improve tribological properties, among other advantages [5, 24, 68]. Ceramic metallization by cold spray is investigated for various applications

such as in the electronics industries [6, 9, 10, 27]. These coatings can also be interesting for the biomedical industry as Ti coatings on Al_2O_3 orthopedic implants can be specially engineered to counter issues involving the low toughness of the ceramic [177, 178].

In the deposition of MMCs, it is generally agreed that ceramic particles are embedded in coatings by the deforming metal phase with no chemical interaction [23, 68, 179]. However, for metallic coatings deposited on ceramic substrates, the bonding mechanism cannot be solely attributed to mechanical clamping. Strong bonds are observed between Ti and Al coatings deposited on atomically smooth Al_2O_3 in addition to Al coatings deposited on AlN substrates [8, 26, 27]. Local heteroepitaxy was concluded to play a role in bonding between these heterogeneous materials. The kinetic energy of splats is converted to heat during plastic deformation, leading to increased atomic mobility and potential for hetero-epitaxial growth [8, 26, 27, 75]. Atomic mobility and intermixing of atoms at the interface have also been attributed to amorphization at the interface during plastic deformation [133]. Increased substrate temperature has been found to increase adhesion strength in metal/ceramic interfaces as it reportedly allows for a stronger chemical bond [6, 8, 10, 75, 150]. However, while adhesion strength varies for different types of ceramics, the influencing parameters have not been fully identified. Drehmann et al. showed that traditional trends observed between bond strength and ionicity when wetting ceramics by metals are not respected in cold spray [8]. Also, the coefficient of thermal expansion mismatch was not found to directly influence bond strength. Rather, a higher thermal conductivity and thermal effusivity of the substrate were assumed to have a positive effect as the interface contact temperature is lower. With a lower contact temperature, negative effects induced by the coefficient of thermal expansion mismatch between the metal and ceramic and tensile residual stresses are reduced [100]. It is still unclear how substrate surface roughness will influence the chemical interaction in these metal/ceramic interfaces as mechanical clamping can also occur and if strong bonds are formed at a single site of impact or if adhesion is promoted by further compaction from the impact of succeeding splats. On the one hand, cross-sectional micrographs have shown gapping in the interface of single Al splats deposited on APS-sprayed Al_2O_3 substrates but full Al coatings on sintered Al_2O_3 appeared

continuous [75]. On the other hand, single Ti splat deposited on zirconia only showed gapping near the center of the particle and bonding near the edge [28].

In this work, single splats of Ti are deposited on Al_2O_3 and SiC substrates. Ti has previously shown promising dense coatings with good adhesion to Al_2O_3 deeming further investigation [26]. The ceramics were selected as they are commonly found in MMCs [23, 24, 32-34]. The effect of substrate composition on adhesion strength is addressed, and the influence of surface roughness on adhesion in the Ti/Al_2O_3 interface is investigated.

To measure bond strength, a splat adhesion test is used. This test, also referred to as a modified ball bond shear test, was introduced by Chromik et al. and later used by Goldbaum et al. [35, 36]. Traditional testing techniques, such as DIN EN 582 or ASTM C-633-99, focus on full coating adhesion [35, 75]. The splat adhesion test was designed for analysis of bonding at the first site of impact in the splat/substrate interface. By splat adhesion testing, significantly less material is used and fracture of the ceramic as well as the epoxy under tension is avoided [35, 36]. Following splat adhesion testing, the failed interface was analyzed through light microscopy and scanning electron microscopy (SEM) to understand the bonding mechanism and the influence of the ceramic surface characteristics. Splat/substrate cross-sections were also studied to understand the interface morphology and bond formation.

4.3 Experimental Procedure

Single splats of spherical, commercially pure, Ti (Grade 1, AP&C, Quebec, Canada) were deposited onto high-purity sintered Al_2O_3 and SiC (AD-995, SC-30, CoorsTeK, Arkansas, USA) substrates. The CP-Ti powder has a size distribution of 0 to 45 μm. Figure 4.1 (a) and (b) show the powder size distribution and morphology. By laser diffraction particle size analysis (LA-920, Horiba, Kyoto, Japan), the mean particle size is 29 μm. The Ti powder is dense with a martensitic microstructure as shown through electron channelling contrasts (ECC) (Figure 4.1 (c)).

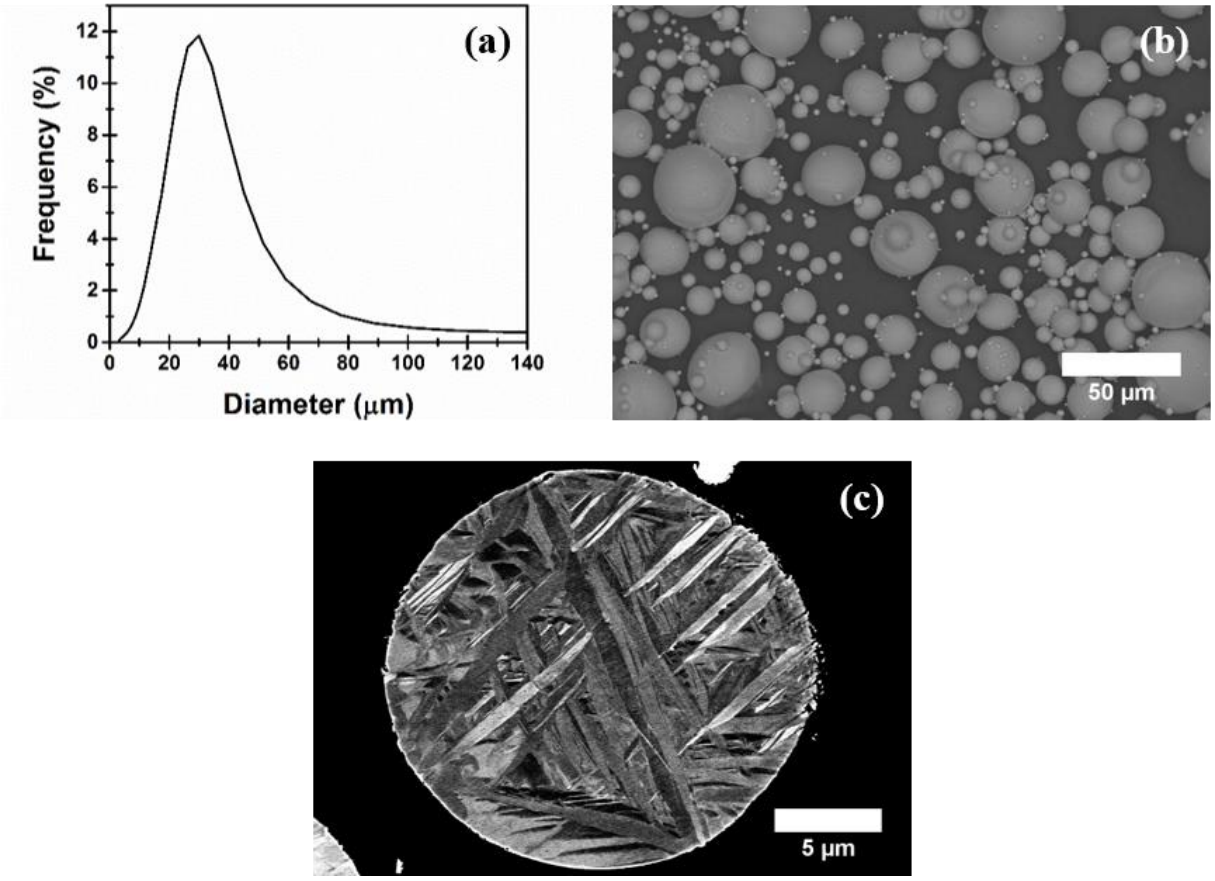

Figure 4.1 The (a) powder size distribution, (b) powder morphology and (c) microstructure of the Ti powder.

The polycrystalline and sintered Al_2O_3 and SiC substrates had a thickness of approximately 12.7 mm. Figure 4.2 shows the as-received surface morphology of the substrates. Both substrates have a significant variation in grain size and grain morphology. The grains used in the sintering of SiC substrates are mostly smaller than those used to produce the Al_2O_3 substrates. Data from the manufacturer showed an average crystal size of 6 μm for the Al_2O_3 and 3 to 10 μm for the SiC samples.

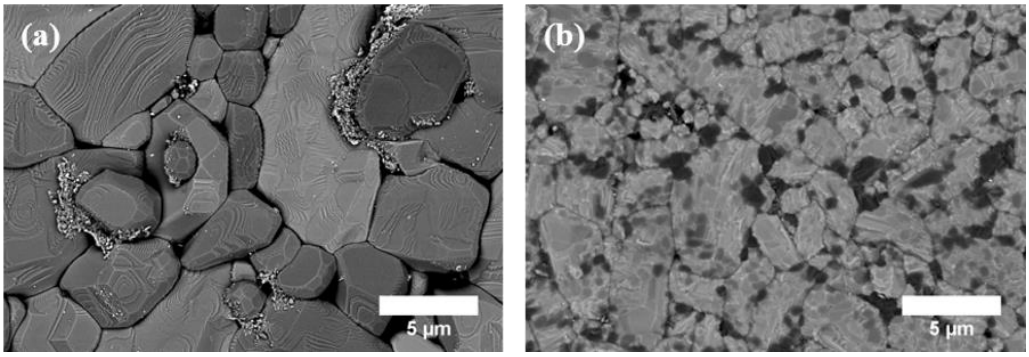

Figure 4.2 A representative backscattered SEM image of the morphology and grain size of the as-received (a) Al_2O_3 and (b) SiC substrates.

The chemistry of the substrates was characterized through energy-dispersive X-ray spectroscopy (EDS) in the SEM (SU-8230, Hitachi, Tokyo, Japan). Charging effects were reduced by using low accelerating voltages of 3 to 5 kV. A 3D Optical Surface Profiler (ZYGO, Connecticut, USA) was also used to measure surface roughness on 3 x 3 mm^2 and 87 x 87 μm^2 surface areas. Measurements were taken at two magnifications to determine the average roughness of the substrates and the local roughness at a length scale more similar to the size of a single splat. The reduced peak height value (R_{pk}) was used to characterize surface roughness as it is a better measure for sintered materials than R_a or R_k to reduce the effect of porosity. R_{pk} is the average height of peaks above the height of the core surface (R_k value) [180]. Twelve areas on three as-received Al_2O_3 and SiC substrates were analyzed to determine the average surface roughness of the substrates used. Given a relatively high surface roughness of Al_2O_3 in comparison to SiC (Table 4.1), six halves of the Al_2O_3 substrates were polished to a final step of 60 µm diamond grinding disk and the other six halves were polished to a final step of 1 µm diamond suspension. Twelve areas on the six ground and polished substrates were analyzed to obtain the average R_{pk} value for these processed substrates. Average R_{pk} values measured by optical profilometry and sample identification used in the following sections of this work are shown in Table 4.1.

Table 4.1 Sample roughness and identification.

Sample	R_{pk}, µm	Identification
As-received Al_2O_3	0.78 ± 0.38	Al_2O_3 (0.78)
60 µm diamond grinding of Al_2O_3	0.33 ± 0.07	Al_2O_3 (0.33)
1 µm diamond suspension polishing of Al_2O_3	0.16 ± 0.03	Al_2O_3 (0.16)
As-received SiC	0.39 ± 0.06	SiC

The Ti powder was deposited on both ceramics by cold spray (PCS-800, Plasma Giken, Saitama, Japan). Nitrogen was used as the carrier gas with a pressure of 4 MPa and a temperature of 800 °C. To deposit scattered single splats, the gun traverse speed was 1 m/s. The standoff distance was set to 30 mm. Once the feed rate was stable, the powder feeder was shut before scanning the surface of the substrate by the cold spray gun mounted on a robotic arm. As a result, only the powder that remained in the gas stream was available for deposition. This was done to ensure a population of splats that was appropriate for splat adhesion testing. Splats must be sufficiently far from one another in order to scratch single splats during splat adhesion testing.

Splat adhesion testing was conducted using a Micro-Combi Scratch Tester (CSM Instruments, Inc, Massachusetts, USA) in accordance with the testing methodology described by Chromik et al. and Goldbaum et al. [35, 36]. In this test, the flat face of a semicircular stylus, 100 µm long, is used to shear single splats (Figure 4.3). A normal force between 30 and 100 mN is applied to maintain contact between the stylus and the substrate. In a small number of tests, the stylus traveled fully or partially above the splat and these tests were disregarded in the analysis. A scratch length of 130 µm or 100 µm was used depending on the available space between splats. The splat is positioned approximately at the center of the scratch length. The scratch speed was set to 150 µm/min.

The splat adhesion test outputs a plot of tangential force applied on the stylus with respect to the scratch length. Baseline tangential force due to friction along the substrate and a peak tangential force due to the removal of the splat are recorded. Some Ti splats deposited on SiC rendered no distinguishable peak. A schematic of the test and an example plot of a test with a peak and one with no distinguishable peak are shown in Figure 4.3.

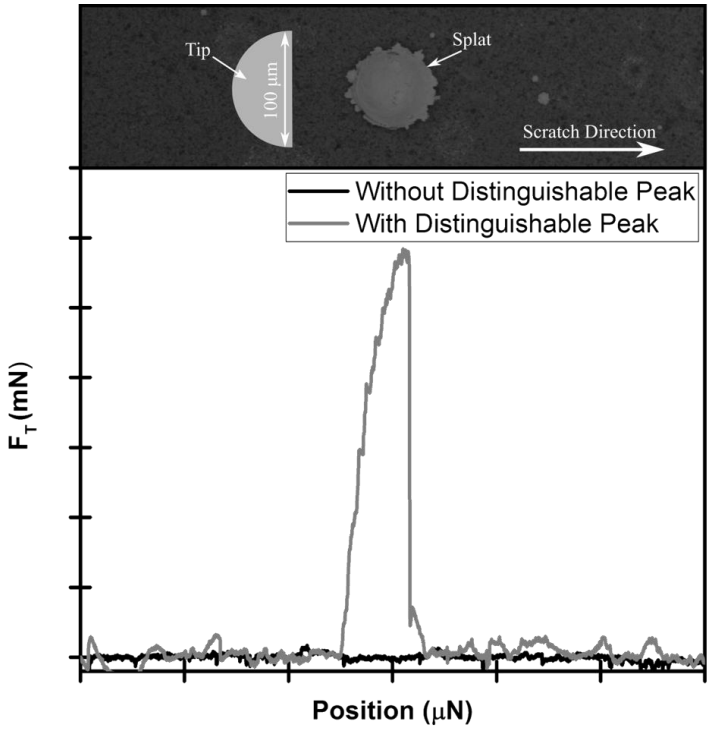

Figure 4.3 Schematic of the splat adhesion test and output graph. The output graph shows a typical tangential force versus position graph with and without distinguishable peak.

To process the splat adhesion test data, the baseline tangential force is subtracted from the peak. The baseline was subtracted in OriginLab using the 2nd derivative method and fit with a spline. Adhesion strength is then measured by Eq. 4.1 [35, 36].

$$Adhesion\ Strength\ [MPa] = \frac{F_{T\ Peak}\ [mN] - F_{T\ Baseline}[mN]}{Projected\ Splat\ Area\ [\mu m^2]} * 1000 \qquad \text{Eq. 4.1}$$

where the projected splat area can be measured by Eq. 4.2.

$$Projected\ Splat\ Area\ [\mu m^2] = \pi \left(\frac{w\ [\mu m]}{2}\right)^2 \quad \text{Eq. 4.2}$$

where w is the splat diameter measured using the light optical microscope (LOM) on the scratch tester prior to testing.

To determine the approximate equivalent powder diameter prior to deposition, Eq. 4.3 is used [36, 181]. FR is the flattening ratio which can be calculated by dividing the diameter of the splat by its height [36]. The height of the splat is measured by subtracting the height of the microscope when focusing on the substrate from the height of the microscope when focusing on the top of the splat [35, 36].

$$d[\mu m] = \left(\frac{w^3}{FR}\right)^{\frac{1}{3}} \quad \text{Eq. 4.3}$$

At least 35 splats were tested for each material combination studied over a wide range of powder sizes. To compare the effect of surface roughness and composition on adhesion strength, measurements are averaged for powder with an equivalent powder diameter between 20 and 40 μm given an average powder size of 29 μm.

The splat adhesion test was developed as a micromechanical test to measure the adhesion or bond strength of cold-sprayed splats to substrates. The test is in shear and generally measured values range from zero up to the theoretical shear strength of the metal splat. When the measured value from the splat adhesion test is low, it means that there is a significant lack of adhesion or metallurgical bonding. When the value is high, close to the shear strength of the metal splat, it means the adhesion is high and the test is shearing through the splat rather than failure occurring at the interface. To make best use of this test and to have proper interpretation of results, post-characterization is required to understand failure mechanisms at the bonded interface. Past studies

have demonstrated the efficacy of this technique for measuring splat adhesion strength of cp-Ti and Ti6Al4V splats [36].

LOM images of failed interfaces were used to investigate the percentage of Ti remaining on the substrate with respect to the projected area of the splat. The area of the remaining Ti on the substrate was measured using color thresholding in ImageJ. The failed interfaces following splat adhesion testing were also analyzed using the variable pressure mode of the SEM (SU-3500, Hitachi, Tokyo, Japan) at an accelerating voltage of 5 kV and a 40 Pa air pressure to reduce charging effects from the bulk ceramic substrate. Metal/ceramic interfaces were cross-sectioned by mechanical grinding and polishing with 0.05 μm colloidal silica mixed with 30% hydrogen peroxide. Polished interfaces were sputter-coated with chromium to reduce charging effects in the high-pressure SEMs (SU-8000, Hitachi, Tokyo, Japan). The low accelerating voltage of 5 kV was maintained.

4.4 Results

4.4.1 Characterization of Ceramic Substrates

Through EDS analysis, traces of elemental contaminants were found at the surface of both substrates. For Al_2O_3, the contaminants were mainly found between grains (Figure 4.2 (a)). The main elements detected were calcium and magnesium with traces of chlorine, sodium and sulfur. These surface contaminants do not seem to influence the results, as backscattered electron (BSE) splat/substrate cross-sectional images do not show changes in contrast near the interface. Therefore, no contaminants are found in the interfaces. Figure 4.2 (b) shows grains with a dark contrast distributed throughout the surface of the SiC. EDS results showed that these darker grains contained boron. Furthermore, areas with a higher concentration of carbon were observed. Free carbon and boron are used as sintering aids for SiC to improve densification [167].

The average R_{pk} values of each sample are shown in Figure 4.4 (a) for two magnifications. For all samples, the standard deviation is larger when measured at a higher magnification. Positioning of grains and pores does not significantly influence roughness at lower magnifications. Higher-magnification measurements on a 87 x 87 μm^2 surface area are indicative of the local heterogeneity encountered by splats. High standard deviations in surface roughness measurements may be reflected in variability found in the splat adhesion tests. Single splats encounter various substrate morphologies. Figure 4.4 (b)-(e) shows representative surface topographies of each substrate on a 87 x 87 μm^2 surface area. The as-received substrates are characterized by a series of fine peaks and valleys due to the morphology of the sintered grains. Polished substrates show minimal fine peaks with valleys caused by porosity.

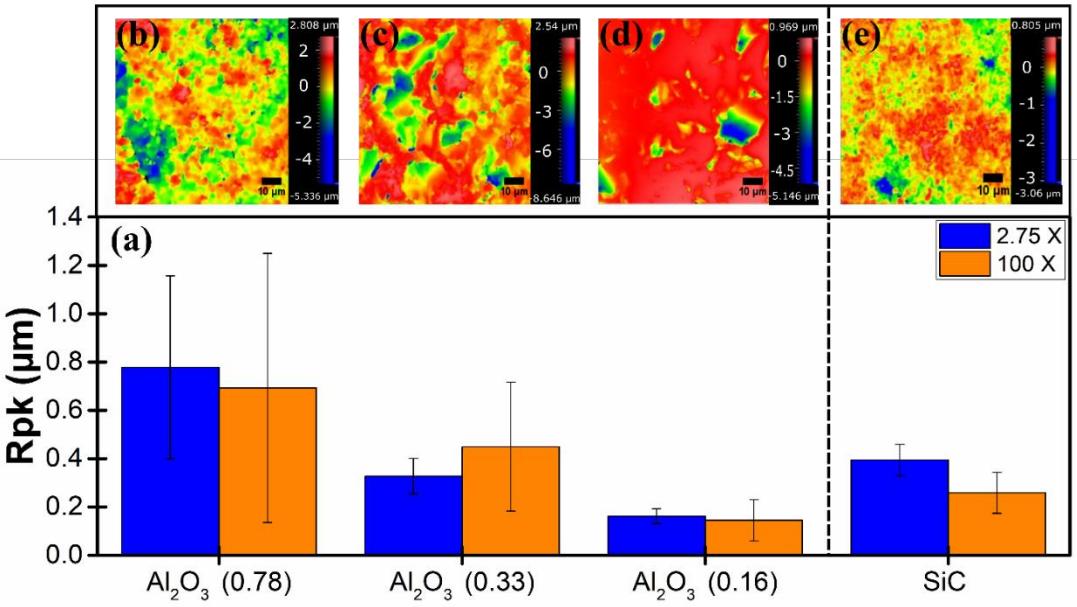

Figure 4.4 (a) Surface roughness of Al_2O_3 and SiC substrates in addition to the surface morphology of (b) Al_2O_3 (0.78), (c) Al_2O_3 (0.33) and (d) Al_2O_3 (0.16) and (e) SiC.

4.4.2 Splat Adhesion Testing

4.4.2.1 Adhesion Strength

Splats with an equivalent powder diameter between 10 μm and 40 um were tested by splat adhesion testing (Figure 4.5). For the Al_2O_3 substrates, there is a decrease in bond strength with increase in powder diameter (Figure 4.5). Similar trends were observed for splat adhesion testing of Ti splats deposited on Ti substrates [36]. Finer powder particles have higher impact velocities than larger powder particles. The higher impact velocities cause higher adhesion strengths [22, 36, 182]. For the SiC substrate, there are 18 splats that resulted in no distinguishable peak. The adhesion strength for these cases was assumed to be zero. From Figure 4.5 (d) null results for the Ti/SiC interface were seen throughout the size distribution. No particular trend or relationship between powder size and probability of a null result was observed for the Ti/SiC interface. For measurable adhesion strengths in the Ti/SiC interface, average adhesion strength appears to be slightly higher than for finer powder particles in the range of 10-20 μm. However, there was no trend of adhesion strength with powder diameter for the Ti/SiC interfaces, which was different from the Ti/Al_2O_3 interfaces.

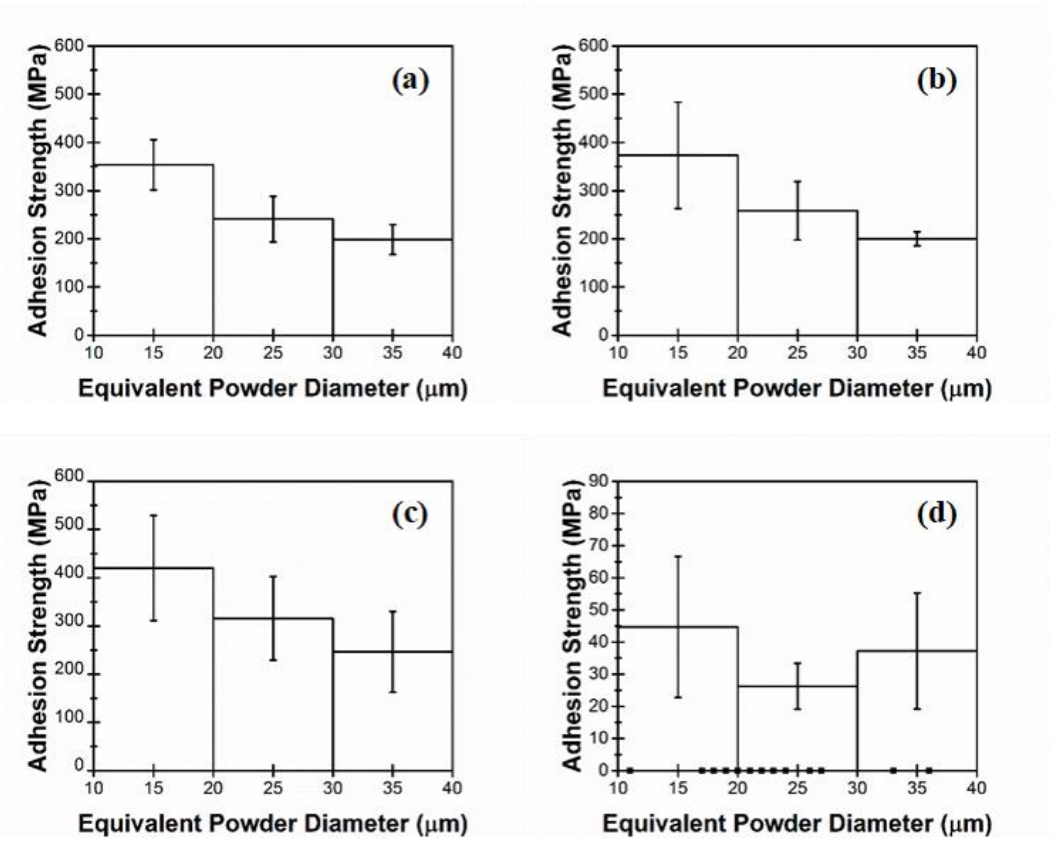

Figure 4.5 Effect of equivalent powder diameter on adhesion strength between Ti and (a) Al_2O_3 (0.78), (b) Al_2O_3 (0.33), (c) Al_2O_3 (0.16) and (d) SiC. (d) includes null results for the Ti/SiC interface as points along the x-axis.

Given the average powder size of 29 μm and the powder size distribution, averages are compared for an equivalent powder diameter between 20 and 40 μm (Figure 4.6). Splat adhesion test results showed significantly higher adhesion between all Ti and Al_2O_3 substrates than between Ti and SiC substrates. Thirteen of the 26 tests conducted for the Ti/SiC interface, in this size range, resulted in a null adhesion strength. These results were not included to measure the average adhesion strength.

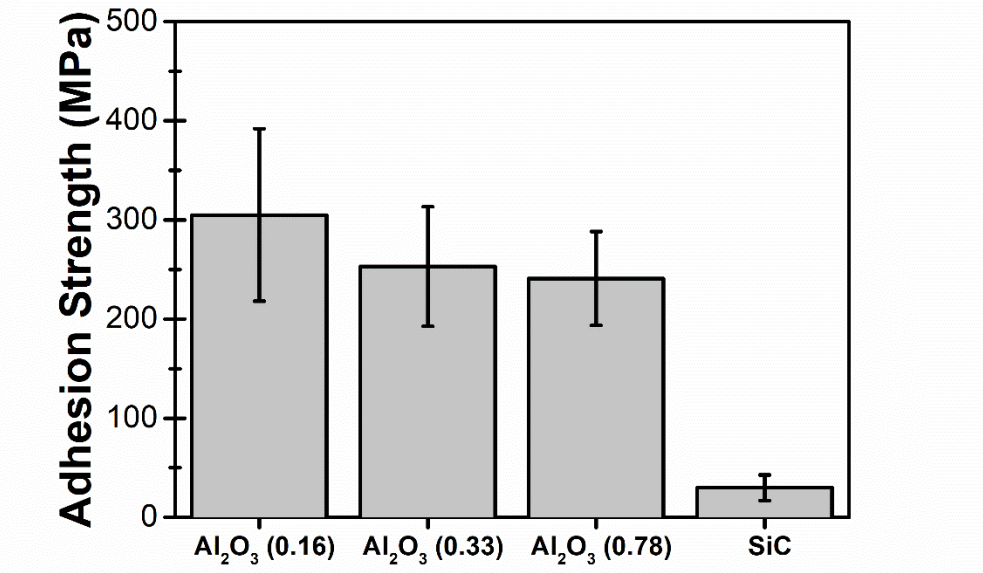

Figure 4.6 Average adhesion strength by splat adhesion testing for powder diameters varying from 20 μm to 40 μm deposited on all substrates with the standard deviation as the error bar.

Al_2O_3 (0.16) had the highest bond strength. A Student t-test[2] was used to validate if the bond strength measurements are significantly different with decreasing surface roughness. The difference between Al_2O_3 (0.33) and Al_2O_3 (0.78) was not significant. The difference between Al_2O_3 (0.16) and the two other substrates was significant.

4.4.2.2 Splat Morphology

Figure 4.7 shows the top view of a single splat deposited on Al_2O_3 (0.78), Al_2O_3 (0.16) and SiC. Splats typically show jetting along the edges of the powder due to ASI as commonly observed in cold spray [18, 21]. Losses in kinetic energy required to adapt to the rougher substrate morphology

[2] A two-tailed t-test was used given that the number of tests and the variance for each test conditions was not equal. The null hypothesis, that is the hypothesis that there is no difference between the means, was rejected if the P-value was smaller than 0.05. Therefore, a statement can be made that, despite the standard deviation in the data, the means are statistically different with at least a 95% level of confidence when the null hypothesis is rejected.

do not cause reduced jetting in the Ti/Al_2O_3 interface (Figure 4.7 (a)). Also, differences in adhesion strength cannot be identified through splat morphology. Single Ti splats deposited on SiC also show a similar morphology to those deposited on Al_2O_3, despite their significantly lower adhesion strength (Figure 4.7 (c)).

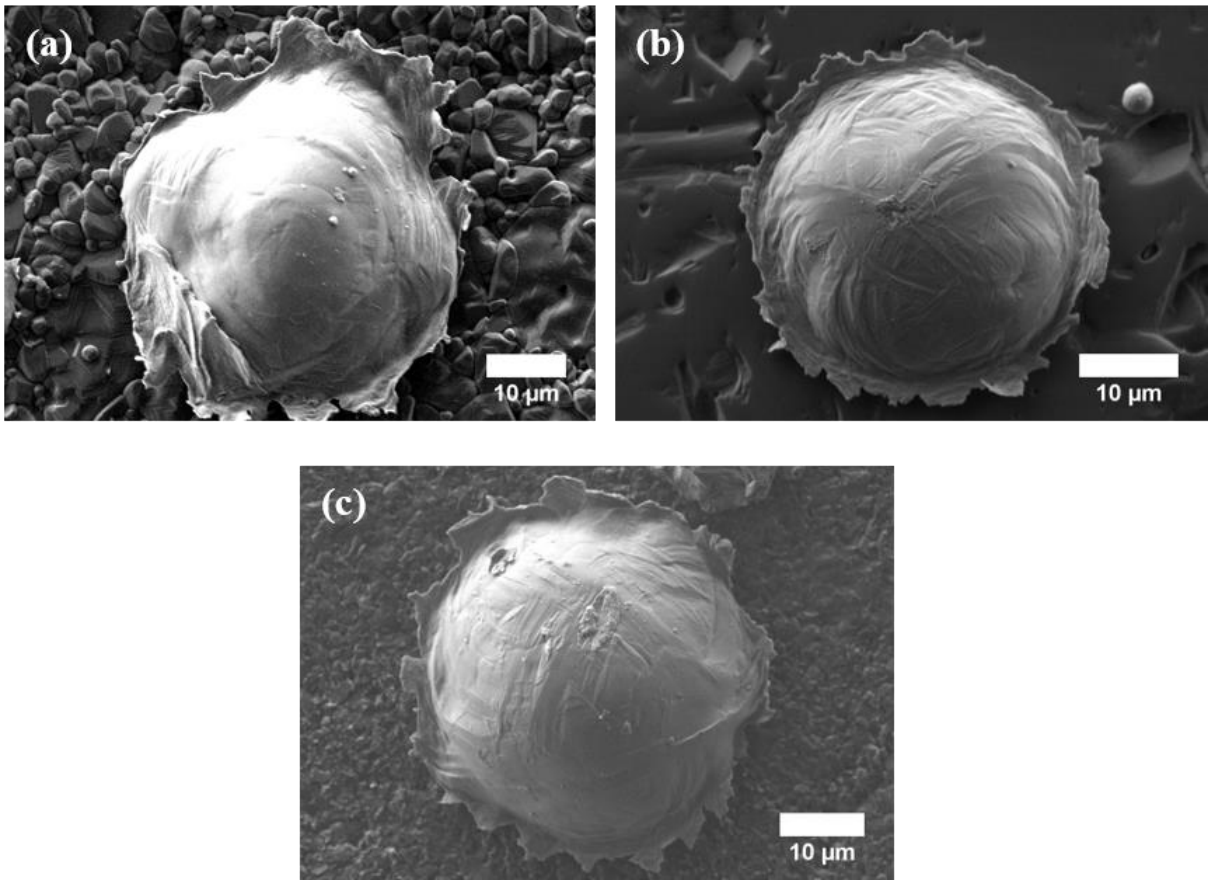

Figure 4.7 Single Ti splat deposited on (a) Al_2O_3 (0.78), (b) Al_2O_3 (0.16) and (c) SiC showing formation of ASI.

Cross-sectional images of single Ti splats deposited on Al_2O_3 (0.78) (Figure 4.8) and SiC (Figure 4.9) showed significant differences despite no observable differences in the plan view splat morphology. Cross-sectional imaging of the Ti splats deposited on Al_2O_3 (0.78) showed a very continuous interface. The Ti was found to follow the morphology of the substrate even within pores. Figure 4.8 (a) shows the interface morphology and Figure 4.8 (b) emphasized the grains of

the Ti powder through ECC. The material which has penetrated within the pores has nanosized grains showing evidence of extensive deformation. When the rougher ceramic surface is impacted, the fine peaks create a zone of higher pressure due to the reduced surface area at the location of initial impact giving localized plasticity within the impacting powder [146]. When the Ti particle impacts on the rougher Al_2O_3 substrate, it is locally deformed around the peaks of the surface, allowing it to penetrate more easily into the pores in addition to the general adiabatic shearing of the particle [146].

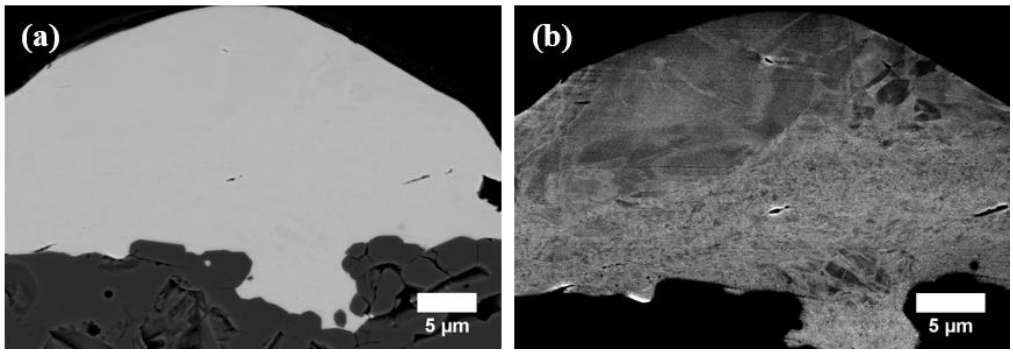

Figure 4.8 Backscattered electron microscopy image of single splat cross-section deposited on Al_2O_3 (0.78) emphasizing (a) interface morphology and (b) grain in the Ti splat.

Mechanical cross-sectioning of single splats on SiC (Figure 4.9) mainly showed gapping between the splat and the substrate with minor mechanical clamping. The weakly bonded particles allowed the epoxy to penetrate the gap between the splat and the substrate (Figure 4.9 (a)). The SiC beneath the splat, in some cases, is more porous than the bulk portion (Figure 4.9 (b)). Microcracking from the impact occurs in this region. The higher hardness of the SiC makes it more brittle than the Al_2O_3. These microcracks cause material beneath the splat to fall during polishing making it appear more porous.

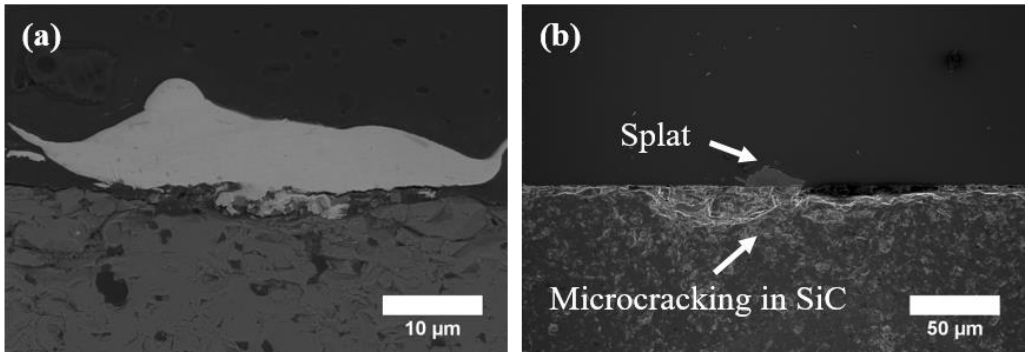

Figure 4.9 Cross-section of Ti/SiC interface showing poor bonding. (a) shows a high magnification image to identify interface features while (b) shows a low magnification image to show cracking in the ceramic substrate.

4.4.2.3 Post-Test Characterization

Failed interfaces from splat adhesion testing revealed traces of Ti on the substrates. The morphology and quantity of the Ti in the failed interface are indicative of the splat's bonding mechanism and strength. Color thresholding of LOM images of the failed interfaces was used to determine the relationship between the amount of Ti on the surface and adhesion strength.

For the Ti/Al_2O_3 (0.16) interface, three cases were observable in post-test characterization. Case 1 is characterized by a circular ring of Ti remaining in the failed interface. The adhering ring of Ti does not significantly protrude from the surface of the substrate. Splats which left a ring on the surface of Al_2O_3 (0.16) impacted areas with minimal porosity. Figure 4.10 shows a representative image of a Case 1 failed interface. Figure 4.10 also shows the linear relation with a coefficient of determination (R^2) of 0.8 between the adhesion strength and the percentage of Ti remaining on the substrate for Case 1.

The surface morphology at the splat level can vary significantly even on the polished substrate due to porosity. Pre-existing porosity in the ceramic substrate or potential induced fracture influenced the morphology of the failed interface. In the presence of large pores, the remaining Ti was found mainly in smooth areas. Figure 4.10 shows a representative image of a failed interface of this type, which is designated Case 2. Also, a linear relation between adhesion strength and the amount of

Ti in the failed interface was found for Case 2 where a fit showed an R^2 value of 0.7. The adhesion strength is influenced by removal of Ti from the pore, potential removal of fractured ceramic and shearing of the Ti. For the same percentage of Ti on the substrate, the adhesion strength is higher for Case 2 than Case 1. In Case 1, the shearing of Ti mainly contributes to adhesion strength.

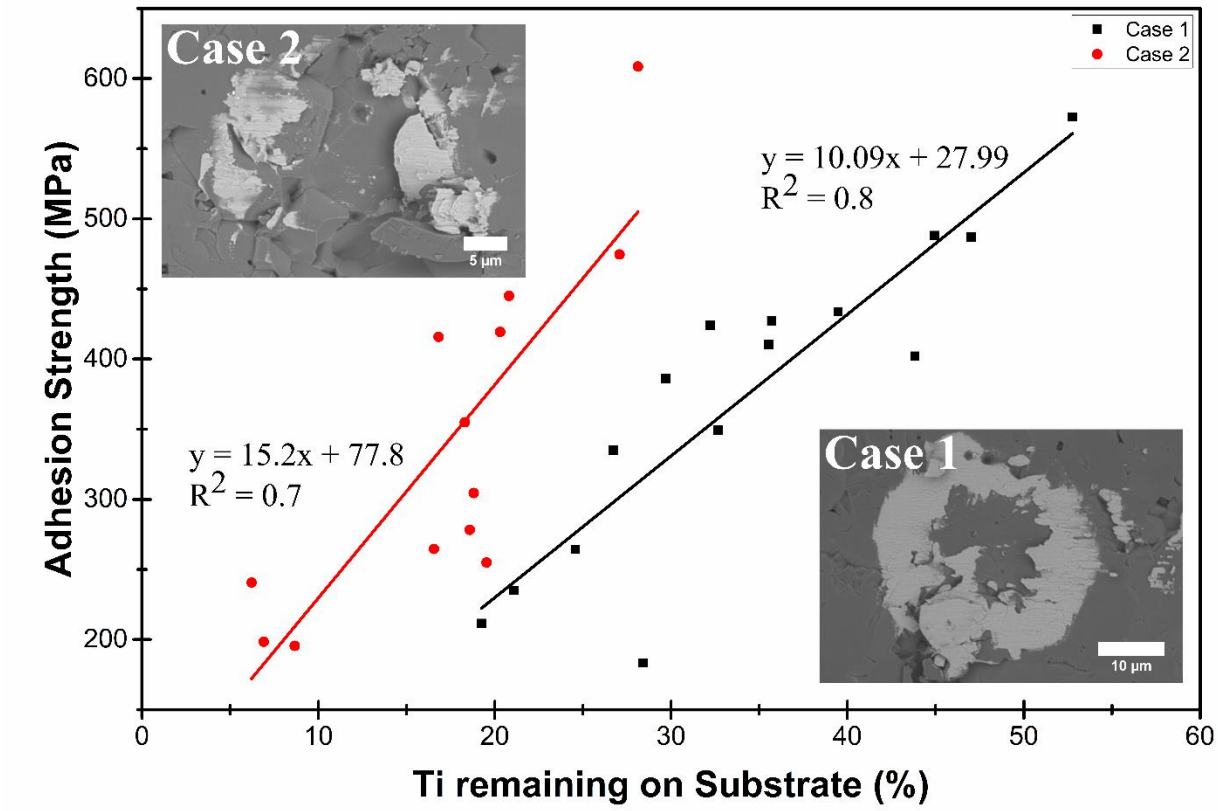

Figure 4.10 Adhesion strength with respect to the percentage of Ti remaining on the substrate following splat adhesion testing with regards to the projected splat area for Cases 1 and 2 on Al_2O_3 (0.16). Representative images of Case 1 and Case 2 failed interfaces on Al_2O_3 (0.16) are also included.

Case 3 is characterized by a series of fine pores on the surface of Al_2O_3 (0.16). Fine, weakly bonded debris of Ti was found to remain on the substrate following splat adhesion testing (Figure 4.11). Only a few tested particles resulted in a Case 3 failed interface. Splats had both high

and low adhesion strengths in Case 3. No relationship could be established between percentage of Ti on the substrate and adhesion strength.

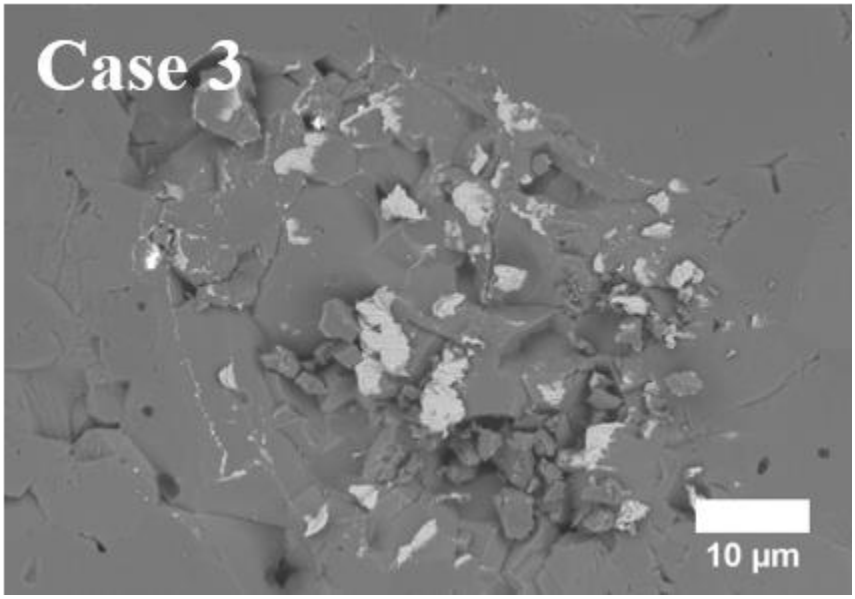

Figure 4.11 Case 3 failed interface between Ti on Al_2O_3 (0.16) following splat adhesion testing.

The amount and characteristics of the remaining Ti on the surface of Al_2O_3 (0.33) and Al_2O_3 (0.78) were similar. Scattered parts of Ti remained on the substrates where the splat was removed, showing evidence of localized bonding. Representative images are shown in Figure 4.12. Ti remaining on Al_2O_3 (0.78) is mainly within the pores and rarely along the surface of the substrate. These failed interfaces differ from those in Case 3 on Al_2O_3 (0.16) as the Ti remaining on the surface appears well bonded and continuous with the grains of the substrate. From the post-test characterization, it can be concluded that adhesion strength between single splats of Ti on Al_2O_3 (0.78) is mainly due to mechanical clamping.

The amount of Ti remaining on the substrate varies significantly from one splat to the other. The adhesion strength with respect to the percentage of the Ti remaining on the Al_2O_3 (0.78) substrate was also plotted in Figure 4.12. It was found that a linear trend with high variance ($R^2 = 0.45$) exists between adhesion strength and quantity of Ti remaining on the substrate. Similarly to Case 2

on the Al_2O_3 (0.16) substrate, the high variance can be attributed to effects contributing to adhesion strength measurements such as the extraction of Ti from within pores or detachment of ceramic grains. The adhesion strength for low percentages of Ti on the substrate is higher than what was observed for the Al_2O_3 (0.16) substrate. However, the splats deposited on Al_2O_3 (0.16) tend to have a higher percentage of Ti remaining on the substrate, following the test, contributing to its overall higher average adhesion.

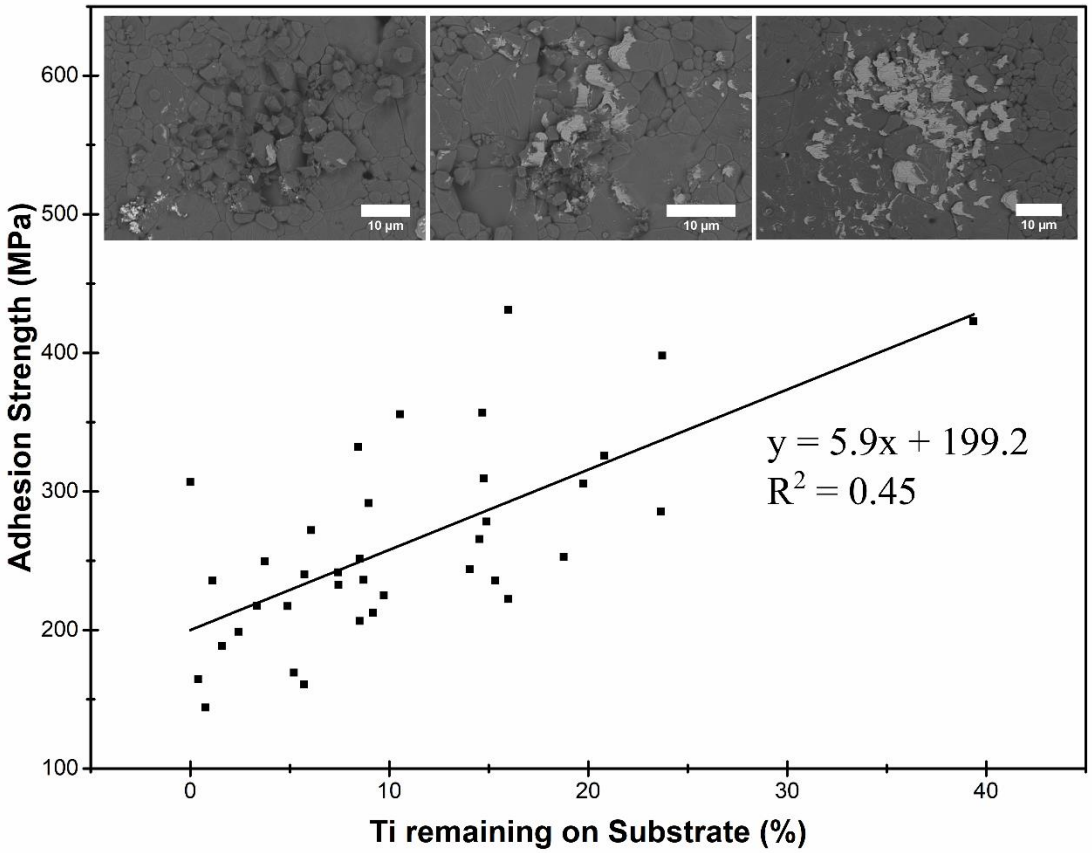

Figure 4.12 Adhesion strength with respect to the amount of Ti that remains on the substrate following splat adhesion testing for the Al_2O_3 (0.78) substrate.

The bonding mechanism of Ti particles sprayed on smooth and rough Al_2O_3 substrates is significantly different. Mechanical clamping appears to play a more significant role in bonding with the rougher surfaces, but mechanical clamping is not necessarily the only bonding mechanism

for cold spraying metal powder on ceramic substrates given the results obtained on the smoother substrates. Bonding also occurs in the zone of ASI, where the temperature is at the highest and deformation is most significant [18, 94]. Hence, ASI is likely a necessary occurrence for bonding on the smooth ceramic substrates.

For the Ti splats deposited on SiC, following splat adhesion testing, there is mainly no evidence of bonding with no Ti remaining on the substrate. Fracture of the substrate is sometimes observable or, in very few cases, a small portion of Ti remained on the substrate (Figure 4.13).

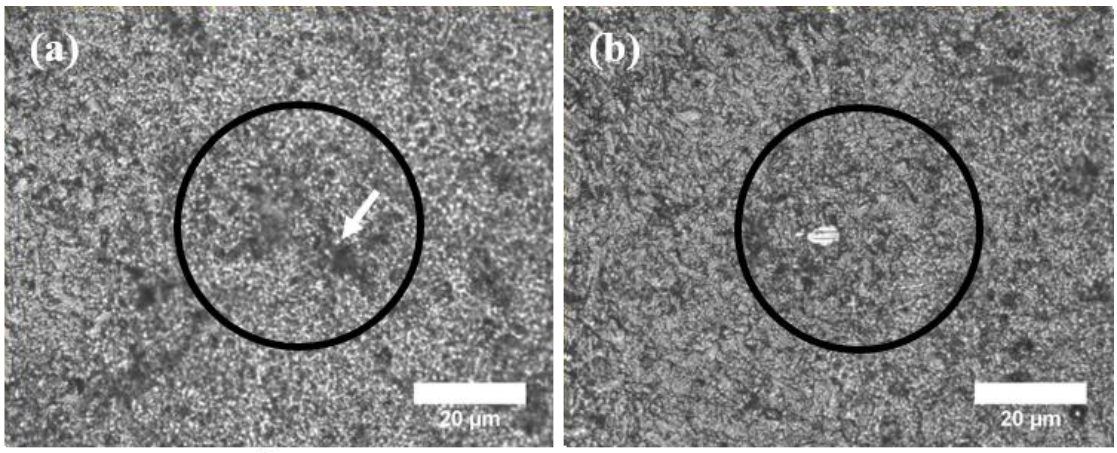

Figure 4.13 Representative LOM image of failed interface on SiC (a) shows a remaining interface with no evidence of Ti and some minor fracturing of the ceramic identified by an arrow, and (b) shows minor evidence of Ti remaining on the SiC.

BSE images revealed traces of Ti on the surface of the substrate from rebounded or weakly bonded particles which fell off of the substrate. A splat that was removed by splat adhesion testing could not be distinguished from a rebounded splat. These fine traces of Ti were not identifiable by LOM. The traces of Ti remaining on the substrate due to rebounded or detached splats are in the shape of a ring (Figure 4.14). Within the ring, the fine traces of Ti appear along the surface and not solely within cracks. This demonstrates that extremely localized bonds are formed within the same area that a complete bond is formed between some Ti splats and Al_2O_3 (0.16) substrate. An example is

marked by an arrow in Figure 4.14. Bonding between Ti and SiC is extremely localized in comparison to Al_2O_3.

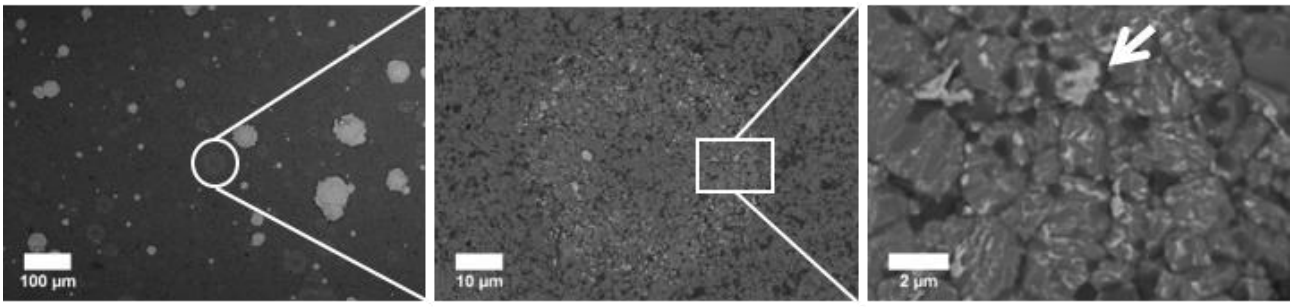

Figure 4.14 Circular ring with traces of Ti appearing on SiC in locations where the particle has rebounded or fallen.

4.5 Discussion

4.5.1 Adhesion Strength

Direct comparisons of splat adhesion test to a bulk coating adhesion test are somewhat difficult due to the different length scales and different loading conditions. Splat adhesion test data provides adhesion at the single splat level while typical tensile testing techniques are intended to characterize full coatings. Goldbaum et al. [36] showed however that splat adhesion tests correlated well to a bulk coating cohesion measurement for cold sprayed Ti. For the Ti/Al_2O_3 and Ti/SiC systems, this work represents the first application of the splat adhesion test. Also, even for bulk tests, there have been no reported bond strength measurements for the Ti/Al_2O_3 and Ti/SiC interface in previous literature.

The bond strength of Ti deposited on Al_2O_3 is comparable or, in some cases, higher than the values reported by Goldbaum et al. for Ti deposited on Ti [36]. The sheared Ti remaining in the failed interface has been highly deformed at impact, and therefore has a higher shear strength than bulk Ti. The Al_2O_3 substrate has a higher hardness than a Ti substrate. Thus, the impact onto Al_2O_3

induces more deformation in the splat than the Ti substrate at impact. This phenomenon can explain the higher adhesion strength measured in certain cases in the Ti/Al_2O_3 interface. Removal of fractured ceramic grains or surface roughness can also influence adhesion in the Ti/Al_2O_3 interface.

For metal/metal splat adhesion testing, where the two metals are of the same material, it is impossible to determine the fraction of metal from the splat remaining on the substrate. However, in the work of Goldbaum et al., they observed that, for their highest adhesion strengths, the test was shearing through the splat very close to the bonded interface [36]. This indicates a very good metallurgical bond and the splat adhesion test at this point measures mechanical properties of the splat itself. From post-test characterization of Ti/Al_2O_3 interfaces, the amount of Ti remaining on the substrate was measured and correlated to the bond strength. Also, the morphology of the remaining Ti provided information with regards to the bonding mechanism. As the tip applies a tangential pressure on the splat, an interface crack spreads leading to the eventual detachment of the splat. The crack spreads through the weakest part of the interface. In the case where crack spreading leaves Ti on the surface of the substrate, it is indicative of a strong bond between the splat and the substrate. The adhesion at the interface is stronger than the cohesion of the splat itself. This was observed when Ti was deposited on Al_2O_3 (0.16). When deposited on Al_2O_3 (0.78), the Ti remained within pores rather than on the surface. The interface was therefore composed of both Al_2O_3 and Ti. When mechanical bonding is the predominant bonding mechanism, shearing of Ti is necessary to remove the splat. Splat adhesion testing in the rough interface therefore provides a measure of how well the particle is mechanically bonded.

4.5.2 Adhesion Rings

Adhesion between single splats of Ti and smooth substrates was not solely dependent on mechanical clamping. Following splat adhesion testing, a ring of Ti remained on Al_2O_3 (0.16) in locations where minimal porosity was observed. Similarly, fine traces of Ti were found in a ring shape when deposited on SiC for rebounded or fallen splats. Various models [18, 21, 94] and

experimental works [36, 164] have shown the link between ASI and adhesion in metallic systems. In splat adhesion testing, a similar ring was previously observed for Ti/Ti and Ti6Al4V/Ti6Al4V interfaces as reported by Goldbaum et al. [36]. While the center of the powder is exposed to the highest hydrostatic pressure, adhesion does not occur. Rather, shear forces within the adiabatically sheared jet are associated with bonding [22, 25, 28, 164]. The presence of a ring of Ti on Al_2O_3 (0.16) and on SiC shows that ASI are significant to bonding in metal/ceramic systems with low surface roughness. Adhesion in the periphery of single splats of Ti deposited onto ZrO_2 due to ASI has also previously been shown [28]. Similarly, adhesion rings were observed for Cu/Al_2O_3 interfaces [10].

Drehmann et al. [8, 75], as well as Wüstefeld et al. [27] and Rafaja et al. [26] also suggested that mechanical clamping is not the sole contributing factor to adhesion in metal/ceramic interfaces created by cold spray. Heteroepitaxy between the metal and ceramic lattices contributes to bonding due to the energy stored in microstructural defects caused during plastic deformation in the metal and heating in the interface [8, 26, 27, 75]. Rafaja et al. extended the concept of heteroepitaxy to polycrystalline Al_2O_3 interfacing Ti, as these materials show a small lattice misfit along multiple planes [26]. On the other hand, Ko et al. attributed adhesion in metal/ceramic systems to atomic intermixing as a result of amorphization due to extreme plastic deformation [133]. Also, Kim et al. suggested that bonding is attributable to the intimate contact between the metal and the ceramic as surface oxides are removed due to ASI [28]. Surface activated bonding is based on the premise that two clean surfaces in intimate contact will form a bond. Clean metal surfaces have a natural tendency to react with oxygen, nitrogen or carbon [183, 184]. Metals and oxides have been shown to bond by this technique in their solid-state [28, 184]. Here, it was shown that adhesion occurs due to ASI in smooth interfaces. ASI are associated to the location of highest temperature. The previously discussed bonding mechanisms such as heteroepitaxy, surface activated bonding or atomic intermixing due to amorphization require atomic motion at the interface. It is therefore consistent that ASI lead to the formation of any of these chemico-physical interactions.

4.5.3 Effect of Surface Roughness

From post-test characterization of single splats deposited on Al_2O_3 with different surface roughness, mechanical clamping is observed when peaks and valleys are present. On the rougher substrate, Ti remained between the grains of Al_2O_3 but for splats on smoother surfaces, a ring morphology was observed showing evidence of a potential chemical interaction. There are only few studies addressing surface roughness in metal/ceramic interfaces created by cold spray. Images of Al splats deposited on Al_2O_3 revealed that mechanical bonding assisted in bond formation on rougher substrate or through porosity on smoother substrates [75]. However, a Ti coating on a smooth sapphire substrate was well-bonded while deposition onto a rougher sapphire substrate resulted in delamination [26].

Some insight can also be obtained from the literature on metal/metal interfaces. Hussain et al. observed that high surface roughness prevented metallurgical bonding in an Al/Cu interface. Mechanical bonding was the main bonding mechanism [92]. Kumar et al. also found that when depositing a soft metal on a hard metal (Al on mild steel), surface roughness influenced adhesion. The bond strength increased with surface roughness until a certain point. For very rough substrates, adhesion decreased. Mixed adhesion mechanisms (metallurgical bonding and mechanical bonding) allowed for high adhesion strength in intermediate surface roughness values [153]. Similarly in this work, roughness highly influenced the adhesion mechanism in the Ti/Al_2O_3 interface. A transition from mechanical bonding to chemical bonding was observable with decreased surface roughness.

4.5.4 Effect of Substrate Composition

Drehmann et al. [8] investigated the effect of the percentage of ionic and covalent bonding in the ceramic on adhesion between the Al and various ceramics in cold spray, as more covalently bonded ceramics tend to be easily wetted by metals. However, higher ionicity of the ceramic did not correlate to higher adhesion strength. For the Ti splats interfacing with Al_2O_3 and SiC, a stronger

bond was formed with the more ionic ceramic further emphasizing that the bond between the cold sprayed metal and the ceramic does not follow the same trend as wetting behaviours between them. Adhesion strength measurements for Al/ceramic interfaces show that the thermal conductivity and thermal effusivity play a significant role in adhesion due to a reduced interface temperature [100]. For Al deposited on Al_2O_3 and SiC, the higher thermal conductivity of SiC allowed for higher adhesion [100]. In the Ti/Al_2O_3 and Ti/SiC interfaces, this trend was not maintained. Ti splats deposited on SiC appear to form highly localized, weak bonds. In fact, several splats were found to rebound. Gaps were found through most of the interface of the deposited single splats. Drehmann et al. also observed significant gapping between a full coating of Al on SiC and single Al splats on Al_2O_3 substrate [8, 75]. This is considerably different to what was observed when depositing single Ti splats on Al_2O_3. The Ti/Al_2O_3 interface appeared continuous and rendered very strong bonds under identical spray conditions to the deposition of Ti on SiC. Potentially, higher velocities are required to deposit Ti on SiC. However, cracking of SiC was observed in cross-sectional images of the Ti/SiC interfaces. This shows that the impact fracture toughness of the ceramic also influences adhesion in cold sprayed metal/ceramic interfaces.

4.6 Conclusion

A better understanding of metal/ceramic interfaces is necessary to optimize metal matrix composites and ceramic metallization created by cold spray. Splat adhesion testing provided insight into bond formation between Ti splats deposited on Al_2O_3 and SiC. The adhesion strength of Ti deposited on Al_2O_3 is shown to be significantly higher than on SiC. The type of ceramic has an important influence on adhesion. The Ti/SiC interface showed microcracking of the ceramic and gapping, while the Ti/Al_2O_3 interface appeared continuous.

The as-received ceramic substrates had significantly different roughness. Al_2O_3 was therefore polished to three final roughnesses of R_{pk} = 0.78, 0.33 and 0.16 µm to investigate the effect of surface roughness on adhesion strength. The bonding mechanism between Al_2O_3 (0.78) and Al_2O_3 (0.16) was significantly different. Splats deposited on Al_2O_3 (0.78) bonded mechanically

with Ti infiltration into surface pores. Splats deposited on non-porous sections of Al_2O_3 (0.16) formed adhesion rings due to ASI. Where large pores on Al_2O_3 (0.16) were present, Ti remained on the substrate in the comparatively smooth areas. Some splats landed in areas with fine pores and left minimal Ti on the surface. For the same amount of Ti remaining in the failed interface, splats landing in large pores had higher adhesion strength given influencing factors such as pull out of ceramic grains or Ti from the pores. The amount of Ti remaining on the substrate following splat adhesion testing influences adhesion strength on all Al_2O_3 substrates.

The failed Ti/SiC interface showed very little evidence of bonding in localized areas. A significant amount of Ti powder rebounded from the substrate leaving rings with fine traces of Ti on the SiC substrate. No traces of rebound were observed on Al_2O_3 substrates. While ASI led to a continuous ring of Ti for many splats on Al_2O_3 (0.16), it led to weak localized bonds in the Ti/SiC interface.

4.7 Acknowledgements

The authors gratefully acknowledge the assistance of Dr. Phuong Vo and Jean-Francois Alarie at the McGill Aerospace Materials and Alloys Design Center (MAMADC) for technical support with the cold spray equipment. They also, thank Thomas Schmitt and Jolanta Sapieha for technical support and access to the scratch tester. This project would also not have been possible without the financial support from the Natural Science and Engineering Research Council (NSERC) Strategic Grants Program.

Chapter 5

Adhesion Strength of Titanium Particles to Alumina Substrate: A Combined Cold Spray and LIPIT Study

Sara I. Imbriglio · Mostafa Hassani-Gangaraj · David Veysset · Maniya Aghasibeig · Raynald Gauvin · Keith A. Nelson · Christopher A. Schuh · Richard R. Chromik

Adapted from a paper of the same title published in *Surface and Coating Technology*, 2019. **361:** p. 403-412

In Chapter 4, the effects of ceramic substrate morphology and of type of ceramic used were examined with respect to the splat adhesion strength. Results showed that Ti forms a significantly stronger bond to an Al_2O_3 substrate than a SiC substrate and that a smoother Al_2O_3 substrate would form a stronger bond. However, the spray conditions were maintained constant throughout the study. In this chapter, we address the effect of velocity and spray conditions on the adhesion strength in a Ti/Al_2O_3 interface. The Ti/Al_2O_3 interface was selected as the focus for this work given its impressively high adhesion strength. While a smooth substrate would render higher

adhesion, in industrialized applications of metal/ceramic interfaces, the use of a smooth ceramic is not always feasible. For instance, when depositing MMCs with ceramic reinforcements, metallic powder is in contact with ceramic powder of various morphologies. In consequence, for a study on the effect of spray conditions and velocity, the as-received ceramic substrate with high surface roughness is used in this chapter.

5.1 Abstract

The cold spray process and laser-induced projectile impact test (LIPIT) are used to deposit Ti powder particles on sintered polycrystalline Al_2O_3. Whereas LIPIT allows real-time observations of single particle impact and measurement of particle impact velocity, cold spray rapidly and simultaneously deposits particles with a wide range of deposition velocities and sizes. By use of these two techniques, the effect of particle velocity and substrate morphology on adhesion strength of single splats is investigated. The critical velocity for deposition is identified to be approximately 580 m/s for the Ti/Al_2O_3 system when using LIPIT and particles of 10 µm. Above the critical velocity, flattening ratio (FR) is also evaluated and observed to be linearly dependent on the particle impact velocity. Splat adhesion testing is performed on LIPIT-deposited as well as on cold spray-deposited powder particles to measure adhesion strength. This analysis shows that adhesion strength is highly affected by local substrate surface morphology, where particles bond more weakly to relatively smooth portions of the substrate. Therefore, mechanical bonding plays a significant role in adhesion. Also, adhesion strength decreases with an increase in FR and therefore velocity. This decrease can be associated with fracture of the ceramic substrate and rebound forces.

Keywords cold spray · impact · metal/ceramic interface · adhesion strength · substrate morphology · impact velocity

5.2 Introduction

Cold spray coatings are formed by high-velocity impact of solid powder particles on a substrate. Metal/metal interfaces between particles or the particles and substrate have the strongest bonding when jetting occurs; jetting leads to metallurgical bonding by creating clean metallic surfaces and/or removing the native oxide layer [18, 21, 89, 92, 109]. Besides metallurgical bonding, mechanical bonding can also lead to particle deposition [92, 109, 153]. For jetting to occur, particles must travel above a critical velocity, which is the minimum particle impact velocity leading to adhesion. This velocity has been estimated for many material systems [22, 185] and it has been recently directly measured through real-time observations [87]. For identical metallic counterparts, critical velocity has been reported to be influenced by melting temperature, mechanical strength, density and powder size [18, 19, 22]. When bonding dissimilar metallic materials, deposition is highly influenced by differences in hardness and density [25, 86].

While metal/metal interfaces created by cold spray are well understood, the necessary conditions for bonding of cold sprayed metal powder particles on ceramic substrates remain unclear [25]. Use of cold spray for metal matrix composite (MMC) coatings with ceramic reinforcement [5] and metal coatings on ceramic substrates [6, 8-10, 26, 27, 75, 100, 133] creates a need to characterize bonding mechanisms and deposition conditions for metal/ceramic systems, especially since no consensus has been established regarding the bonding mechanism in cold sprayed metal/ceramic interfaces. For cold sprayed MMCs, mechanical bonding by deformation of the metal around rigid ceramic particles is a proposed bonding mechanism, which depends on the shape and roughness of the ceramic phase [24]. In the deposition of metal coatings on ceramic substrates, mechanical interlocking has been shown to contribute to bonding when a rough substrate is used in an Al/Al_2O_3 interface [75, 186]. Yet, metal particles have also been successfully deposited on smooth ceramic substrates where mechanical bonding is not possible [8, 10, 12, 26, 27, 29]. Therefore, chemical bonding may also occur in metal/ceramic interfaces created by cold spray. The chemical

interaction between atoms at the interface is attributed to amorphization of the metal and atomic intermixing resulting in a heteoepitaxial relationship [8, 27, 75, 133, 186]. To achieve adhesion, the key parameters identified are the impact velocity as well as the difference in hardness and mechanical properties of the metal and ceramic [186]. Due to a poor understanding of the abovementioned key parameters in forming a chemical or mechanical bond, deposition conditions to achieve adhesion in metal/ceramic interfaces have yet to be identified.

Critical velocity is typically investigated experimentally by two techniques. For example, the deposition efficiency of a full coating under different spray conditions can be compared. Alternatively, single particle impacts can be characterized for specified spray conditions to determine whether particles bonded or rebounded using a wipe test [68]. In neither case is critical velocity directly measured, but rather is back-calculated as a function of process parameters that lead to a certain level of deposition efficiency. In cold spray, particle velocity is varied by either increasing initial gas pressure or gas preheat temperature. An increase in gas preheat temperature results in an increase in thermal softening of the powder prior to impact [25]. Critical velocity also tends to decrease with an increase in gas preheat temperature [187, 188]. In addition, the velocity of the powder in the center of the jet is higher than the velocity near the edges [36, 189]. To avoid these issues in identifying an approximate critical velocity, a laser-induced projectile impact test (LIPIT) is used in this work.

LIPIT is an *in situ* technique used to identify the impact velocity of single particles [87, 190-193]. This technique uses a high-frame-rate camera to image the trajectory of a single particle that has been accelerated from a platform with a laser pulse [87, 194]. From the images, particle velocity is calculated and the adhesion or rebound of a single micron-sized particle is observed [87, 194, 195]. While particle in-flight velocity can be measured using commercially available systems in cold spray, these are not designed to measure impact velocity leading to adhesion. In what follows, LIPIT is used to deposit Ti powder particles onto sintered high purity polycrystalline Al_2O_3 substrates to isolate the effect of impact velocity from other influencing factors in this

metal/ceramic interface. Ti/Al_2O_3 interfaces have been selected as a model metal/ceramic system due to their promising results in previous literature [26, 196]. The critical velocity for deposition of Ti onto the surface of Al_2O_3 is approximated, and by studying the morphology of bonded particles, the effect of velocity on flattening ratio (FR) is identified. Also, the effect of surface morphology on adhesion strength, at similar particle velocities, is investigated where adhesion strength was measured by splat adhesion testing [35]. However, since selective deposition of many particles at certain velocities on certain substrate morphologies is tedious by LIPIT, it is difficult to identify a general trend between adhesion strength and velocity. For this, cold sprayed particles are used to study many particles deposited simultaneously.

5.3 Research Methodology

In LIPIT, micron-sized, commercially pure, spherical Ti powder particles (Grade 1, AP&C, Quebec, Canada) are accelerated from a launch pad composed of a 210 μm thick glass substrate sputter-coated with 60 nm of gold, then coated with an elastomeric polyurea coating about 30 μm thick [87]. Details regarding the LIPIT system [87] and additional characterization of the Ti powder particles [196] have been presented elsewhere. The Ti powder, suspended in ethanol, is spread over the surface of the polymeric coating and is allowed to dry. The laser pulse (Nd:YAG laser pulse of 10 ns and 532 nm wavelength) causes ablation of the gold film and expansion of the polymer. In consequence, rapid acceleration of the Ti powder particle towards the Al_2O_3 substrate (AD-995, CoorsTek, Arkansas, USA) is achieved. Depending on the laser pulse energy, Ti powder particles can be accelerated to velocities between 350 and 995 m/s. A 16-frame high-speed camera (SIMX 16, Specialised Imaging) is used to capture the particle/substrate impact. Velocities are measured by comparing the distance travelled from one frame to the other knowing the interframe time [192].

Powder particles with an average diameter of 10 ± 1 μm are selected and launched. To select powder of a specific size, a secondary CCD camera is used. These powder particles are launched

at Al_2O_3 target substrates cut from large sintered blocks using a diamond blade on a precision cutter to dimensions of approximately 2-3 x 12.5 x 10 mm^3. It is ensured that the edge of 2-3 mm, on which the metallic powder is to be deposited, is not exposed to the blade, and the as-received sintered substrate surface morphology is maintained. The sintered blocks are fabricated with a wide range of particle sizes. This causes local variations in the surface morphology of the substrates. There are granular portions of the substrate with a series of fine peaks and valleys due to small sintered grains and portions that are comparatively smooth and flat with larger grains. In [196], the local heterogeneity of this as-received Al_2O_3 substrate was further characterized and associated to a reduced peak height (R_{pk}) roughness value of 0.78 ± 0.38 µm. Surface features are observable in SEM images as shown in Figure 5.1.

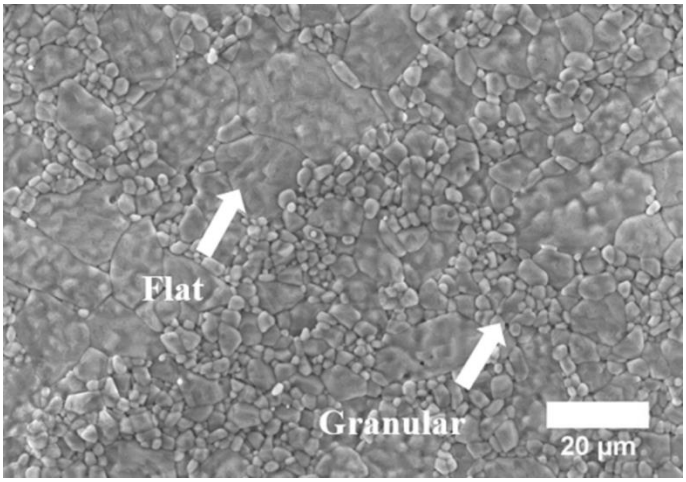

Figure 5.1 Surface morphology of the Al_2O_3 substrate. Portions of the substrate include large grains which make the substrate flatter than areas that include several small grains. Areas with small grains are identified as granular while areas with large grains are identified as flat.

The same as-received Ti powder (with the full particle size distribution) is used for deposition of single particles by cold spray (PCS-800, Plasma Giken, Saitama, Japan) onto the bulk Al_2O_3 substrates. The cold spray gun is mounted on a robotic arm that scans the surface of the substrate during the spray at a traverse speed of 1 m/s. The standoff distance is 30 mm. The maximum initial

gas pressure and gas preheat temperature for this cold spray system are 4.9 MPa and 800°C. For simplicity, throughout the article, gas preheat temperature and initial gas pressure are referred to as gas temperature and gas pressure. To reach a wide range of velocities by cold spray, two cold spray nozzle configurations are used. The "long nozzle" (PG PNFC-012-30, Plasma Giken, Saitama, Japan) geometry renders higher gas velocities and therefore higher powder velocities than the "standard nozzle" (PG PNFC2-010-30S, Plasma Giken, Saitama, Japan) for identical spray conditions (i.e., gas temperature and pressure).

Using the standard nozzle, the initial gas pressure is maintained at 4.0 MPa with a gas preheat temperature of either 400, 600 or 800°C. An increase in gas temperature is known to cause an increase in velocity [197, 198]. The long nozzle configuration is used to investigate the effect of gas temperature on FR and adhesion strength as well as to deposit particles at very high velocities using the highest gas pressure and temperature for this spray system. Using the long nozzle, the maximum gas pressure of 4.9 MPa is maintained for gas temperatures of 450 and 800°C. For each spray conditions, in-flight particle velocity measurements at the standoff distance are taken using a time of flight particle diagnosis system (Coldspraymeter, Tecnar Automation, Quebec, Canada). While this velocity measurement represents the in-flight velocity of the particles, it might not reflect the particle impact velocity due to the bow shock effect, which is the high-pressure region formed near the substrate. The gas pressure and temperature of 4.9 MPa and 450°C using the long nozzle give an average velocity of 695 ± 136 m/s which is effectively identical to the average velocity achieved with the standard nozzle configuration using a gas pressure of 4.0 MPa and gas temperature of 800°C measured at 692 ± 133 m/s. The long nozzle deposition condition of 4.9 MPa and 450°C is specifically selected to deposit the Ti powder particles at the lowest possible temperature while maintaining an impact velocity comparable to that achieved using the standard nozzle with a gas pressure and temperature of 4.0 MPa and 800°C. Increasing the gas pressure is necessary to ensure that the lowest temperature is used. These conditions are used to understand the effect of temperature on measurements of adhesion strength and flattening ratio.

To better understand the role of temperature in the cold spray system, a numerical model was used. Particle temperature (T_p) at the exit of the nozzle is estimated by Eq. 5.1 [67] where the differential equation is solved by the Euler method along the length of the nozzle. In the model, the particle specific heat (c_p) , density (ρ_p) and particle diameter (D_p) are 472 J/(kg K), 4540 kg/m^3 and 29 µm respectively [67].

$$\frac{dT_p}{dt} = \left(T_g - T_p\right)\frac{6h}{c_p \rho_p D_p} \qquad \text{Eq. 5.1}$$

In Eq. 5.1, 'h' is the heat transfer coefficient which can be calculated by a semi-empirical Ranz-Marshall equation which is dependent on Reynolds number and Prandtl's number [67]. The Reynolds number and the Prandtl number are calculated using specific heat, viscosity and thermal conductivity of the gas. These gas properties are found in [199, 200] and are taken at a temperature equivalent to the average temperature of the gas and powder along the nozzle [67]. The gas flow velocity (U_g), pressure (P_g) and temperature (T_g) through the nozzle is obtained numerically by assuming a two-dimensional flow with a gas in a quasi-one-dimensional isentropic semi-perfect state [67]. Additional details regarding the numerical simulation and assumptions made are available in [67]. For the Reynolds number, the particle velocity (U_p), at the exit of the nozzle, is also required and can be solved numerically by Eq. 5.2 [67] where 'ρ_g' is the gas density and 'C_d' is the drag coefficient.

$$\frac{dU_p}{dt} = \frac{3}{4}\frac{C_d \rho_g}{D_p \rho_p}\left(U_g - U_p\right)\left|U_g - U_p\right| \qquad \text{Eq. 5.2}$$

Following deposition, the adhesion strength is measured for all particles deposited by LIPIT and ten or more particles for each cold spray condition. The powder particles deposited by cold spray have a wide range of diameters, but the tests were performed on the particles with approximately an average initial diameter of 29 µm. The initial diameter (D), prior to deposition, can be approximated by Eq. 5.3 [36, 181, 201].

$$D = \sqrt[3]{\frac{d^3}{FR}} \qquad \text{Eq. 5.3}$$

Where 'd' is the splat diameter and FR is calculated by Eq. 5.4 [35, 36]. The height of the splat (h) is measured by recording the height of the microscope when focusing on the top of the splat and subtracting its height when focusing on the substrate. This method is a non-destructive way to measure FR of each splat tested, and in previous work was found to correlate well with measurements from splat cross-sections [35, 36].

$$FR = \frac{d}{h} \qquad \text{Eq. 5.4}$$

The particles studied by cold spray are larger than those deposited by LIPIT but are more representative of the powder size typically used in cold spray, which is also the average size of the powder used in this study. Larger particles could not be deposited by LIPIT to achieve high velocities resulting in adhesion due to limitations in the laser power. A Micro-Combi Scratch Tester (CSM Instruments, Inc, Massachusetts, USA) is used to perform splat adhesion tests [35] on the Ti splats deposited on Al_2O_3. Splats are scratched off the substrate by the flat face of a semicircular specialized tip of 100 μm in diameter. A scratch length of 100 μm and speed of 150 μm/min are used for testing. To ensure that contact is maintained between the tip and the substrate, a normal force of 70-100 mN is used. Throughout the scratch length, the tangential force on the stylus is measured. Results typically show a baseline ($F_{T\ Baseline}$) and peak ($F_{T\ Peak}$) tangential force. The peak force corrected by subtracting the baseline is interpreted as the force required to remove the splat from the substrate. Adhesion strength, calculated by Eq. 5.5, represents the force required to remove the splat from the substrate over the projected splat area [35, 36].

$$Adhesion\ Strength\ [MPa] = \frac{F_{T\ Peak}\ [mN] - F_{T\ Baseline}[mN]}{\pi\left(\frac{d\ [\mu m]}{2}\right)^2} * 1000 \qquad \text{Eq. 5.5}$$

In splat adhesion testing, the material fails at its weakest point. Therefore, failure may occur through the metal, at the interface or through the ceramic substrate. Failure through the metal is associated with a well-adhering interface. Failure at the interface is typically associated with a weak bond strength. Significant failure in the ceramic typically only occurs in the presence of a pre-existing crack in the ceramic. To properly explain and characterize trends observed for different spray conditions and velocities, extensive post-test characterization is conducted. All failed interfaces are observed by light optical microscopy (LOM) following splat adhesion testing. Some splats are imaged by variable-pressure scanning electron microscopy (SEM, SU-3500, Hitachi, Tokyo, Japan) before and after splat adhesion testing. The pressure within the SEM is set to 40 Pa and the accelerating voltage to 5 kV. The low vacuum condition is used to reduce charging within the SEM caused by the non-conductive ceramic substrate [202]. Splat morphologies are compared to better understand the effect of particle impact velocity on deposition. Following splat adhesion testing, the amount of Ti remaining on the substrate and the substrate surface morphology in the failed interface are characterized to understand adhesion strength results.

5.4 Results

5.4.1 Critical Velocity

With LIPIT, impact velocities resulting in bonding and rebounding can be distinguished. Figure 5.2 (a) shows a typical particle impact that resulted in rebounding of the Ti splat from the Al_2O_3 substrate. The particle impacts the substrate with a velocity of 455 m/s between the fifth and sixth frame. Through the sixth to twelfth frame, the particle rebounds at a significantly lower velocity of 37 m/s due to its loss of kinetic energy through deformation. Figure 5.2 (b) shows an impact resulting in adhesion. The particle impacts the substrate at a velocity of 631 m/s. In the fourth frame, the particle has impacted the substrate and is found to remain bonded in subsequent frames.

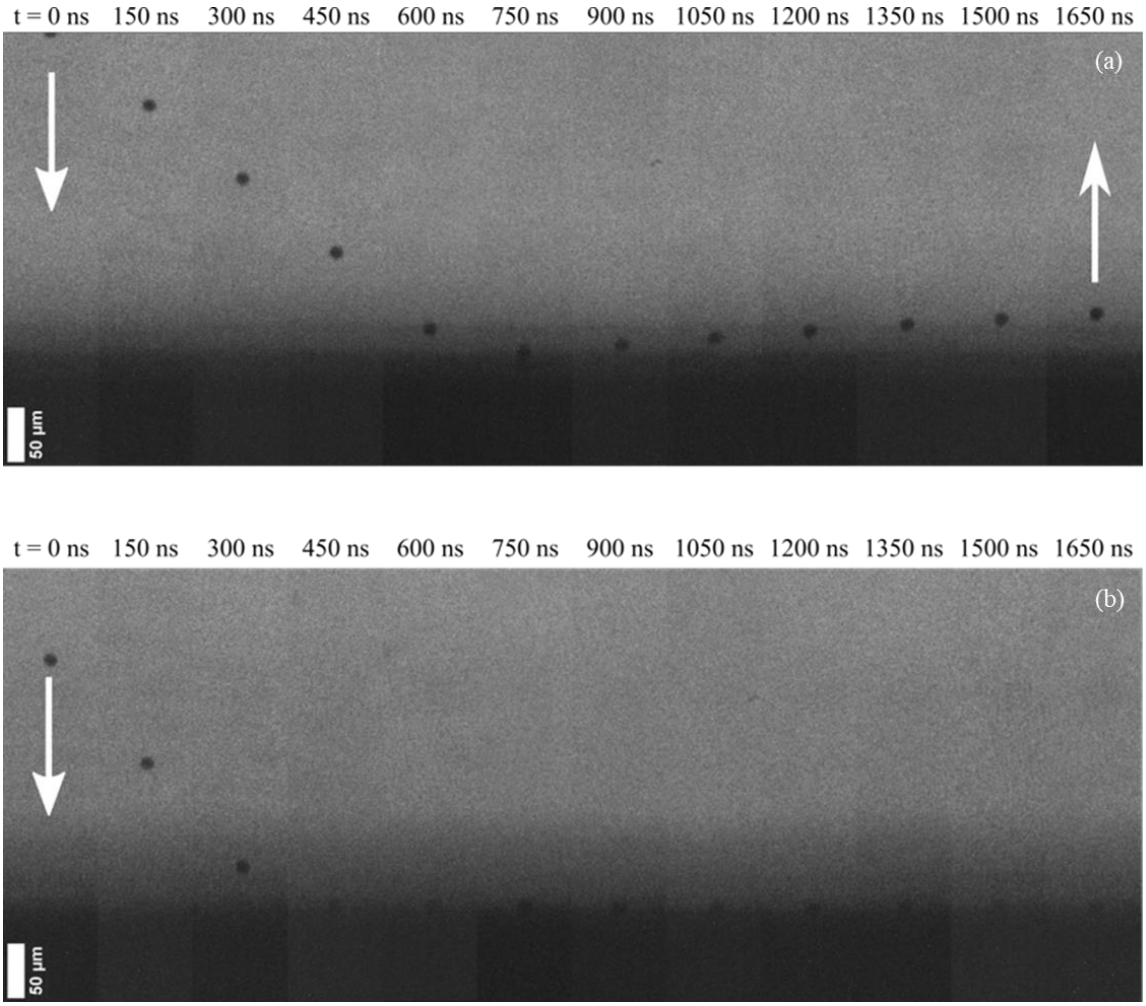

Figure 5.2 12 snapshots captured by the high-frame-rate camera during LIPIT (cropped to emphasize regions of interest) with a 5 ns exposure time depicting the impact of a single micron-sized Ti particle impacting the Al_2O_3 substrate. (a) The powder particle impacts the substrate at a velocity of 455 m/s. Following impact, rebound occurs at 37 m/s. (b) The powder particle impacts the substrate at a velocity of 631 m/s and remains bonded to the substrate.

The coefficient of restitution (COR), which is the rebound velocity divided by the impact velocity, is plotted with respect to impact velocity to identify the critical velocity for deposition of Ti powder on Al_2O_3 (Figure 5.3). COR decreases with increasing impact velocity until adhesion occurs, similar to experiments on matched metallic counterparts by Hassani-Gangaraj et al. [87]. For the

Ti/Al_2O_3 interface, the lowest velocity resulting in adhesion is 580 m/s. The majority of splats impacting above this velocity adhere to the substrate. The highest velocity at which a particle rebounds is 750 m/s.

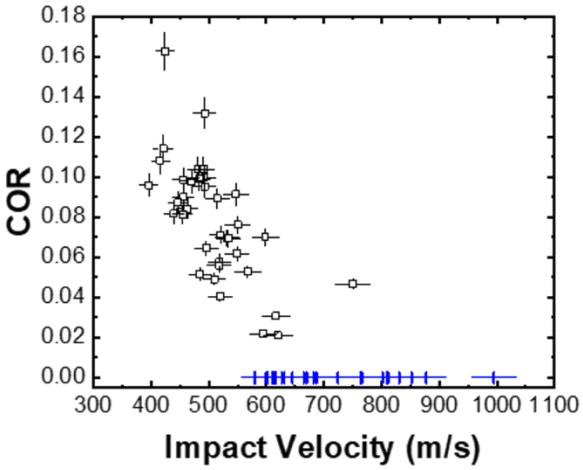

Figure 5.3 Variation of COR with respect to impact velocity for Ti powder particles accelerated towards the Al_2O_3 substrate by LIPIT. Particles begin to bond to the substrate at 580 m/s. Bonded particles are depicted by blue markers on the null COR axis.

5.4.2 Characterization of Bonded Particles

To determine optimal deposition conditions, understanding the effect of an increase in velocity beyond the critical velocity is also necessary. A simple parameter often used in cold spray is FR given in Eq. 5.4. FR is a basic measure of the extent of deformation experienced by a powder particle at impact. Here, for all particles deposited by LIPIT, a linear relation between FR and velocity is identified (Figure 5.4). The equivalent size of the powder particle and substrate surface morphology, also indicated in Figure 5.4, have a minor influence on the FR.

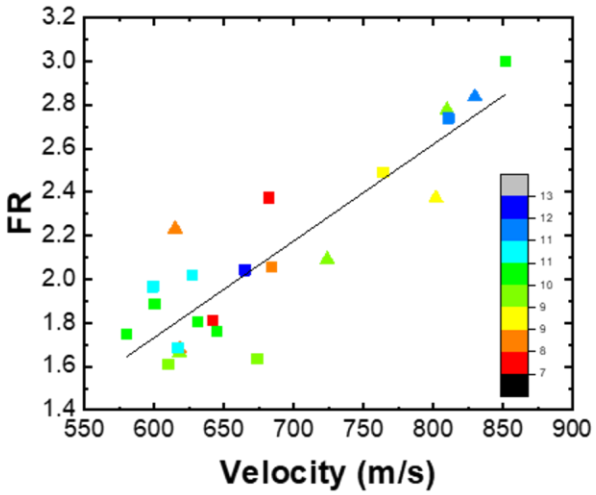

Figure 5.4 Relationship between FR and velocity for Ti powder particles deposited by LIPIT. A color scheme is used to represent the equivalent powder diameter D (in μm) of each bonded particle. Powder particles that have impacted flat portions of the substrate are identified by triangular symbols while powder particles that impacted granular portions are identified by square symbols.

In the LIPIT system, velocity, particle size and substrate surface morphology are the main independent variables, provided that the materials used are not altered, and particle temperature is fixed at room temperature. From our finding in Figure 5.4, FR is strongly dependent on impact velocity with no major influences from diameter or substrate surface morphology, FR could in principle be used to back out a reasonable estimate of the 'effective velocity' of individual powder particles deposited by cold spray, albeit with a mismatch in temperature between those processes, which is expected to be significant. We examine this concept in the following.

Table 5.1 includes the average in-flight velocity of powder particles for the five spray conditions used, as measured by the Coldspraymeter in addition to the numerically simulated temperature of the powder at the exit of the nozzle. For each average in-flight velocity, the average FR of splats is measured. The linear dependence between FR and velocity is shown in Figure 5.5 and is consistent with the trend identified by LIPIT testing (Figure 5.4) and also with numerous

observations of FR increasing with particle velocity in the cold spray literature [18, 35, 36, 203]. For a given velocity, FR measured on cold sprayed splats is consistently larger than FR measured on LIPIT splats. This is due to the different particle sizes used and the differences in temperature of the impacting particles. Interestingly, though, depositing particles at similar velocities using different gas temperatures, by cold spray, does not result in significant differences in FR. For example, FR of particles deposited by using the long nozzle at spray conditions of 4.9 MPa and 450°C are similar to the FR of particles deposited using the standard nozzle at 4.0 MPa and 800°C. These two spray conditions have very similar average particle velocities with very different particle temperatures. Thus, for these experiments, in terms of cold spray, particle velocity can be directly correlated to FR in the same way as for LIPIT. The difference of 295°C in particle temperature and the potential bow shock effect from an increase in pressure at the substrate surface does not appear to have a significant impact on FR.

Table 5.1 Experimental average particle velocity and modeled particle temperature for powder particles deposited by cold spray under different spray conditions.

Nozzle Geometry	Spray Conditions	Experimental Average Particle Velocity (m/s)	Modeled Particle Temperature at Exit of Nozzle (°C)
Standard Nozzle	4.0 MPa, 400°C	491 ± 127	183
Standard Nozzle	4.0 MPa, 600°C	543 ± 133	322
Standard Nozzle	4.0 MPa, 800°C	692 ± 133	459
Long Nozzle	4.9 MPa, 450°C	695 ± 136	166
Long Nozzle	4.9 MPa, 800°C	768 ± 151	343

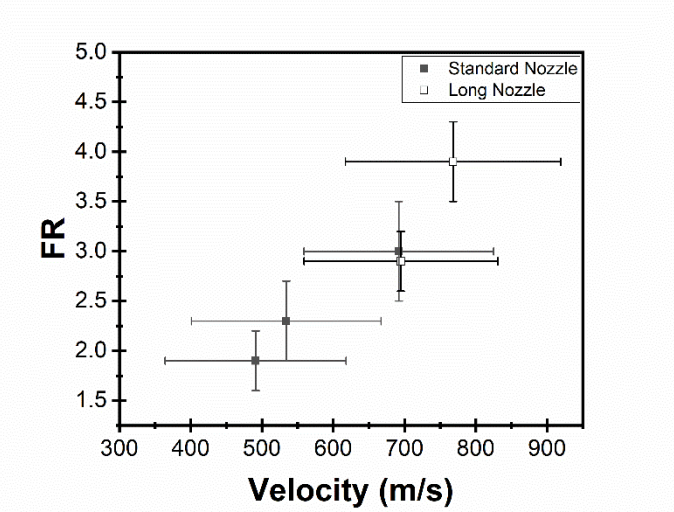

Figure 5.5 The dependence of FR with velocity for powder particles deposited by cold spray.

5.4.3 Splat Adhesion Testing

5.4.3.1 Effect of Substrate Surface Morphology

Particles impacting at similar velocities have relatively similar splat morphologies (Figure 5.6 (a) and (c)), but their bond strength, as measured by splat adhesion testing, can vary significantly. The difference in adhesion strength can be understood by post-mortem observations of failed interfaces. Certain splats landed on the fine granular portion of the substrate, while others landed on the comparatively flat portions. The few splats that landed on smoother portions of the substrates show fine traces of Ti remaining on the substrate and weak bonding (Figure 5.6 (b)). Conversely, particles landing on granular portions of the substrate show more retention of Ti between grains following splat adhesion testing (Figure 5.6 (d)). More retention is associated with higher bond strengths as it is indicative of a continuous interface where Ti has penetrated within the valleys of the surface roughness. The interface bond strength is stronger than the cohesion strength of the Ti. A portion of Ti remaining between grains and having adapted to the surface morphology of the substrate has been identified by an arrow in Figure 5.6 (d).

The granular surface morphology results in several points of contact with the impacting particles. By reducing the contact area, small high stress regions are formed [146]. This improves deformation and also allows the particles to penetrate within pores upon impact. Post observations of the failed interfaces indicate that mechanical bonding significantly contributes to adhesion. The splat adhesion test tip applies a tangential load on the splat. The splats which are strongly mechanically bonded are sheared rather than pulled out from within the grains as this is the weakest point in the system.

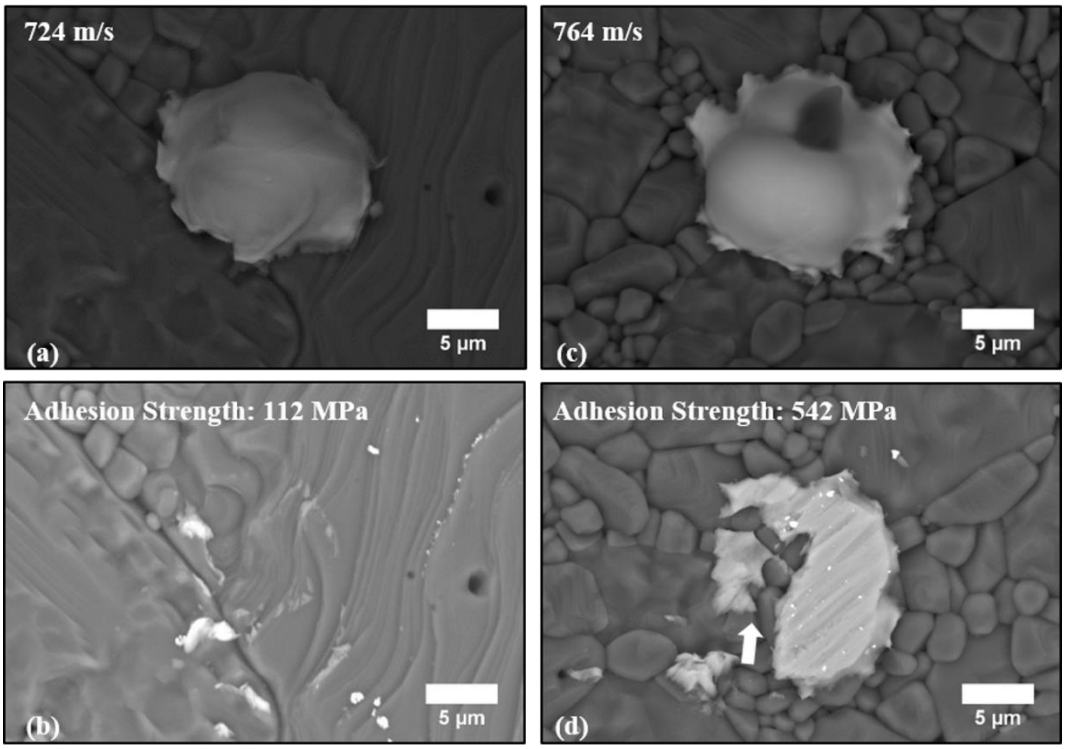

Figure 5.6 A single Ti splat accelerated by LIPIT towards the Al_2O_3 substrate at a velocity of (a) 724 m/s and (b) 764 m/s is shown. The Ti splat shown in (a/b) was removed by splat adhesion testing. The failed interface is shown (b/d).

Tested splats deposited by cold spray have a larger diameter than those deposited by LIPIT. Due to local heterogeneity of the substrate surface morphology, splats with a larger diameter are more

likely to impact portions of the substrate with a combination of flat and granular portions of the substrate. In Figure 5.7, post-test characterization of the failed interface shows about half of the splat on a granular portion of the substrate and the other half on a flat portion. Similar to what was observed for LIPIT splats, there is more retention in the granular portion of the substrate.

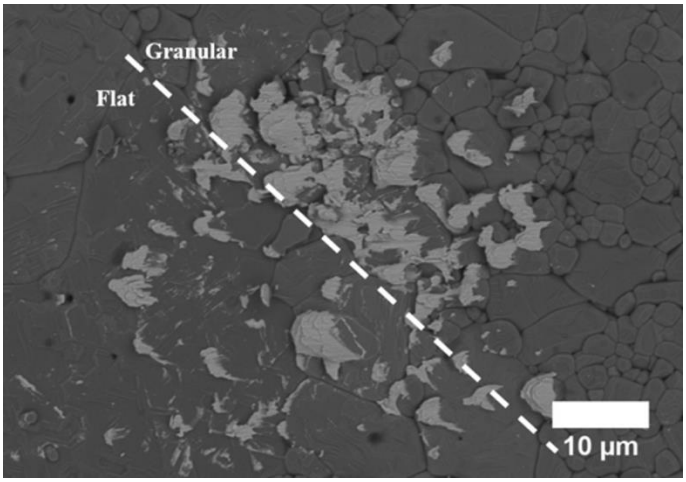

Figure 5.7 Post-test characterization of a single splat deposited by cold spray. The splat landed on both a granular and flat part of the substrate. More Ti remained on the substrate in the region that is more granular.

The above observations correlate residual titanium penetrated into the surface porosity with adhesion strength. A quantitative analysis is required to further confirm the trend for LIPIT splats (Figure 5.8). The area represented by Ti remaining in failed interfaces was analyzed through color thresholding on SEM images, and converted to an area fraction over the projected splat area (Figure 5.8 (d)). The amount of Ti remaining on the substrate is thus representative of the portions of the particles that are strongly bonded mechanically. The increase in adhesion strength with amount of Ti remaining in the failed interface is observable for both the smooth and granular parts of the substrate surface, and is in line with previous similar observations for Ti/Al_2O_3 interfaces created by cold spray [196]. Hence, the present results for Ti/Al_2O_3 interfaces emphasize the importance of mechanical bonding on adhesion strength.

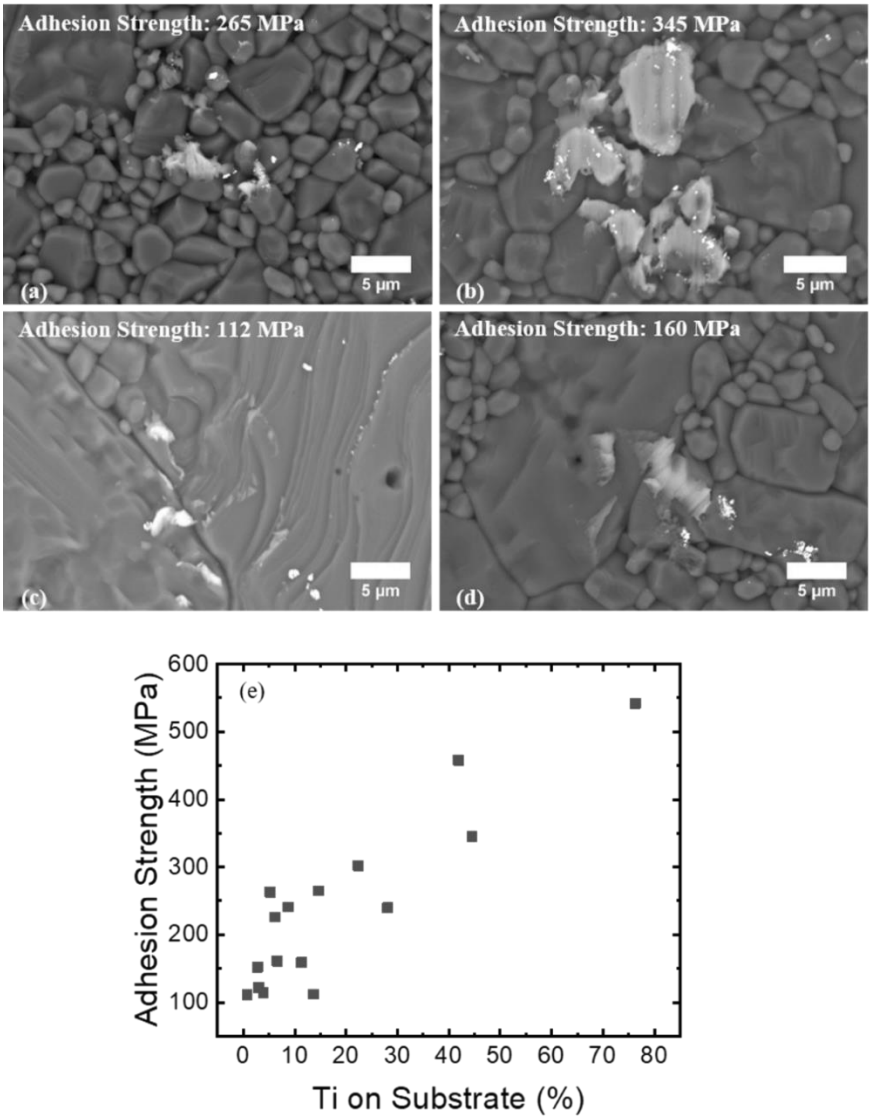

Figure 5.8 Failed interfaces following splat adhesion tests at various velocities for Ti powder particles deposited on Al_2O_3 by LIPIT on (a, b) a granular part of the substrate and (c, d) a flat part of the substrate. (e) The area fraction of Ti remaining in the failed interface with respect to adhesion strength.

5.4.3.2 Flattening Ratio and Adhesion Strength

FR is a characteristic to individual cold spray splats and is linked to their impact velocity per results shown in Figure 5.5 Therefore, while there is significant scatter in in-flight particle velocity at each spray condition (Table 5.1), the relative impact velocity of individual cold spray splats can be approximated by FR to understand its effect on adhesion strength. For this analysis, FR values are grouped into intervals of 0.5 to reduce point-to-point scatter and more accurately investigate broader trends.

It was confirmed that, at similar particle velocities, FR is not strongly influenced by variations in gas temperature but it is also deemed necessary to validate that variations in gas temperature do not significantly affect adhesion strength measurements. Adhesion strength measurements for splats deposited at 4.0 MPa and 800°C using the standard nozzle are compared to values obtained for splats deposited at 4.9 MPa and 450°C using the long nozzle as these represent identical in-flight velocity ranges with different gas temperatures (Figure 5.9). Given high variations in particle velocity for the selected cold spray conditions (Table 5.1), FR varies from 2.5 to 3.5. In both ranges of FR (2.5-3.0 and 3.0-3.5), a t-test shows no significant differences in the average adhesion strength especially considering that the adhesion strength is also influenced by local substrate surface morphology as previously discussed.

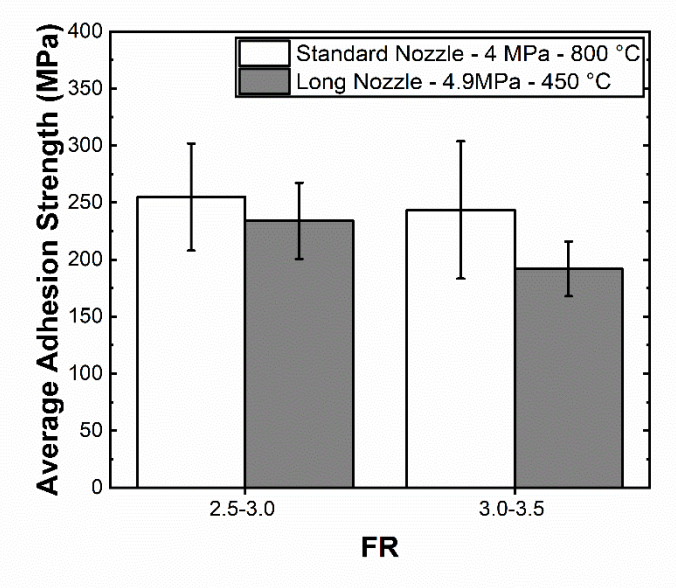

Figure 5.9 Average splat adhesion strength measurements for splats deposited using the long nozzle at 4.9 MPa and 450°C (695 ± 136 m/s) and standard nozzle at 4.0 MPa and 800°C (692 ± 133 m/s) in two FR ranges of 2.5-3.0 and 3.0-3.5.

Given these results, splats from all spray conditions are taken as one dataset and are categorized based on their FR. Figure 5.10 shows the average splat adhesion strengths at various FRs. The splat adhesion strength for Ti splats on an Al_2O_3 substrate decreases with an increase in FR, which is directly proportional to impact velocity. It should be noted that the decreasing trend for adhesion strength with an increase in FR is statistically significant as validated by a t-test.

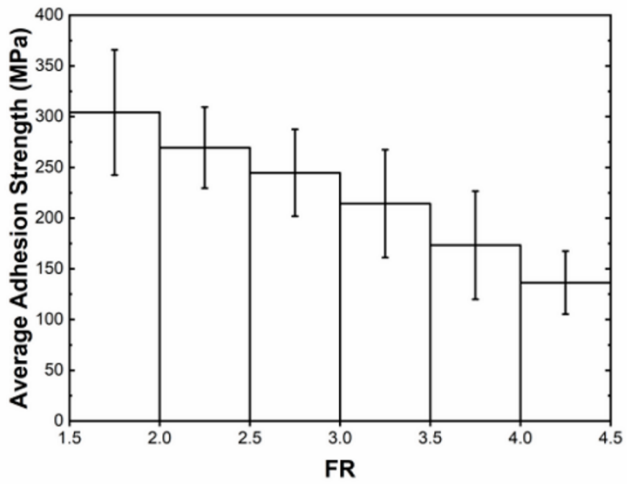

Figure 5.10 Average splat adhesion strength measurements with respect to FR showing a decreasing trend for cold sprayed particles.

In Section 5.4.3.1, the Ti remaining on the substrate is shown to be related to adhesion strength and is highly influenced by changes in substrate surface morphology. Since the percentage of Ti remaining on the substrate is measured following adhesion strength measurements, it is verified that this percentage of Ti is not influenced by velocity and is in fact an independent variable related to substrate surface morphology (Figure 5.11). Despite the decreasing trend observed between adhesion strength and FR, there is no distinguishable trend between the amount of Ti on the substrate and FR between 1.5 and 3.5. For FR between 3.5 and 4.5, there is a weak decrease in the percent Ti remaining on the substrate, but a t-test confirmed that this decrease is not statistically significant.

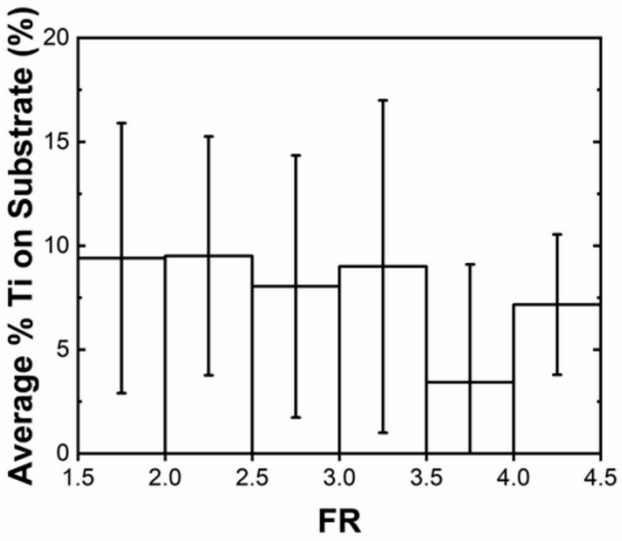

Figure 5.11 Percent bonded of Ti powder particles in post-test characterization of splats deposited by cold spray plotted with respect to FR.

FR values between 3.5 and 4.5 are mainly results of splats deposited at 4.9 MPa and 800ºC using the long nozzle. The slight decrease in the percentage of Ti remaining on the substrate is associated to fracturing of the ceramic beneath the splat in post-test characterization for many splats deposited under these spray conditions (Figure 5.12). While fracturing is observed for some particles deposited at lower velocities, it occurred so infrequently that it is not considered a predominant failure mechanism. Given that the splat adhesion test tip applies a tangential force on the splat, it is unlikely that fracturing occurs due to testing itself. Instead, it is likely that, at this spray condition, the ceramic fractures due to impact of the splat at the high velocity around 768 ± 151 m/s. No fracturing has been observed for splats deposited at similar velocities by LIPIT, however, the particles are smaller than those tested in cold spray. At the same velocities and for the same materials, smaller particles have lower kinetic energy than larger particles, and may thus require higher velocities yet to induce fracture of the substrate.

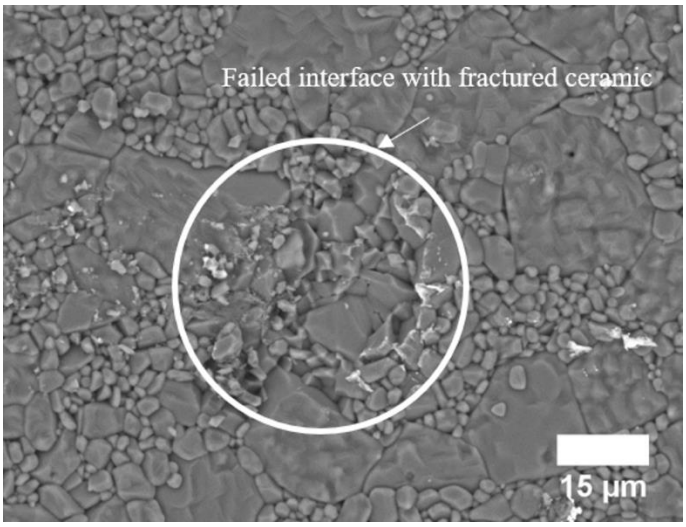

Figure 5.12 Post-test characterization of splats deposited using the long nozzle at 4.9 MPa and 800ºC. That is, splat deposited at the highest velocity in this study. The failed interface shows fracturing of the ceramic.

5.5 Discussion

5.5.1 Ti-Particle Deposition

To identify factors influencing deposition in cold spray, the analysis of single splats is commonly used and often referred to as a wipe test [10, 18, 22, 198]. However, given the large range in particle velocity for individual spray conditions, as notable in Table 5.1, a drawback for wipe tests remains the inability to identify the precise deposition velocity of a single splat. By LIPIT, the deposition velocities of single splats are measured and can be used to identify the critical velocity and factors affecting deposition such as substrate morphology. From Figure 5.3, the critical velocity was identified to be between 580-620 m/s, beyond which most splats bond to the substrate. A single observation of particle rebound occurred at 750 m/s but this may be due to substrate fracture, similar to that observed for splats cold sprayed at high velocity (see Figure 5.12). No prior work has identified the required critical velocity for this material system. While in cold spray the

critical velocity is influenced by particle size [22] and gas temperature [187, 188], the range obtained here, by LIPIT, is a valid first approximation of critical velocity for a Ti/Al_2O_3 interface.

The LIPIT technique also allows for a comparison of FR with velocity identifying a linear trend as expected. To achieve higher velocities in cold spray, options include increasing gas pressure, increasing gas temperature, changing the nozzle geometry or changing the gas type. Here, to achieve a wide range of velocities, the process gas conditions and the nozzle geometry are varied. This approach also has the benefit of using spray conditions with similar in-flight particle velocities at very different gas and particle temperatures. Using the two nozzle geometries, a gas temperature difference of 350°C could be used while maintaining a similar velocity. This gas temperature difference is associated with an approximate difference in particle temperature of 295°C. Comparing first cold sprayed splats to LIPIT splats, thermal softening due to particle impact temperature results in additional powder deformation, which is measurable by FR. For similar velocities, cold sprayed splats generally had higher FR than LIPIT splats. However, when comparing results for cold sprayed splats deposited within the range of temperatures used, between 400-800°C, the effect of temperature on the FR appears to be negligible. That is, while increasing gas temperature for either nozzle results in an increase in particle velocity (see Table 5.1), conditions where the in-flight velocity was the same but with drastically different temperatures resulted in similar FR (Figure 5.5) and adhesion strength (Figure 5.9). Another important observation is the maintained proportionality between FR and particle velocity when using the long nozzle in comparison to the standard nozzle (Figure 5.5). This occurs despite a disproportionate increase in temperature and further confirms that the relationship between FR and particle velocity is likely minimally influenced by the effect of the gas temperature for the Ti/Al_2O_3 interface.

5.5.2 Bonding Mechanism and Adhesion Strength

For proper interpretation of splat adhesion test results, analysis of the failed interfaces is essential [196]. In the Ti/Al_2O_3 interface, the material remaining on the substrate from the splat is clearly identifiable and its footprint can be used to determine factors contributing to adhesion [196]. As previously discussed by Imbriglio et al. [196], splat failure under tangential load occurs through the weakest part of the interface. Low adhesion strengths are typically correlated with interface failure and very little Ti remaining on the substrate. High adhesion strength results typically show a significant amount of Ti on the substrate as the interface adhesion strength is higher than cohesion in the splat. The contribution of sheared Ti in the failure mechanism is particularly important when Ti has infiltrated surface porosity as the interface consists of both Al_2O_3 and Ti [196]. Similar to previous results for this interface [196], the adhesion strengths reported here for many splats, are considered to be relatively high. Near the interface, grain refinement is characteristic of cold spray Ti splats due to extreme plastic deformation at impact [113, 115, 143]. Thus, the mechanical properties near the interfaces are different than the original Ti powder or bulk Ti [113]. When failure occurs, through the Ti, near the interface, grain refinement may contribute to the high adhesion strength measurements [196].

Post-test characterization of failed interfaces and adhesion strength measurements of splats deposited by LIPIT demonstrate the importance of mechanical clamping in the formation of a bond on a rough substrate. These results are consistent with some prior observations of failed interfaces of cold sprayed splats showing that the infiltration of Ti into the surface porosity of as-received polycrystalline Al_2O_3 contributes to adhesion [196]. However, it has also been previously reported that metal powder particles can bond to atomically smooth ceramic substrates by a chemical bond [8, 10, 12, 26, 27]. Imbriglio et al. suggested that chemical bonding is likely the primary bonding mechanism on polished Al_2O_3 surfaces [196]. In such situations the specific state of the surface apparently becomes important: particles impacting on comparatively flat portions of as-received substrates show quite different behavior from well-polished surfaces of the same material.

Whereas polished surfaces show chemical adhesion rings [196], flat portions of as-received substrates are still nanoscopically rough compared to the polished surfaces and do not. Post-test characterization of failed interfaces on flat portions of the substrate shows very little Ti retention on the substrate but adhesion strength measurements still approach ≈ 100 MPa. Therefore, while chemical adhesion rings are not observed, chemico-physical factors may still contribute to the formation of a bond. The possibility of having both mechanical and chemico-physical factors influencing adhesion has previously been discussed by Wüstefeild et al. who observed local heteroepitaxy between Al coatings deposited on polycrystalline AlN substrates and infiltration of Al into the surface porosity of the AlN substrate [27]. These chemico-physical factors may also play a role in high adhesion strength measurements recorded, in this work, for rough portions of the substrate. The interfacial adhesion strength is a result of both crack propagation through chemically bonded portions of the splats and shearing of Ti. Splats bonding to mostly flat portions of the substrate have a smaller contribution from sheared Ti resulting in their lower adhesion strength.

The adhesion strength is also observed to decrease with an increase in FR. An increase in FR results in an increase in the projected splat area, typically expected to form a stronger bond. Yet, the opposite is observed. One factor that is shown to influence adhesion strength is fracture of the ceramic (Figure 5.12). However, fracture of the ceramic during impact is not believed to be the sole contributing factor to the decrease in adhesion strength of single splats with increasing FR. FR was shown to be related to the deposition velocity. As the velocity is increased adhesion and rebound energies act as competing effects. If the rebound energy becomes greater than the adhesion energy at high velocities, particles will not adhere to the substrate. There is an optimal range for deposition bounded by a minimum and maximum critical velocity [85]. While the effect of velocity on adhesion in metal/ceramic interfaces created by cold spray has not been examined in the literature, some authors have attempted to understand this effect in metal/metal interfaces. Wu et al. showed experimentally that as the velocity is increased for deposition of Al-Si powder onto mild steel, the ratio between bonded particles to the total number of deposited particles

reaches a maximum value and then decreases significantly as the velocity is increased due to this rebound phenomenon [85]. In a soft particle/hard substrate interface, the recoverable strain energy increases considerably at higher velocities causing the rebound phenomenon [94]. Within the range where deposition is possible, the ratio between rebound energy and adhesion energy reaches a minimum and then tends to increase. This trend is more pronounced in soft powder (Al)/hard substrate (Mild Steel) interfaces [84]. The rebound phenomenon may cause nanoscopic porosity at the interface rendering lower adhesion strength. In addition to the rebound phenomenon, there is a maximum deposition velocity that, when reached, causes erosion of the interfacing materials [19, 22, 195, 198]. The maximum impact velocity is often referred to as the erosion velocity and defines the maximum boundary of the window of sprayability [22]. The window of sprayability is known to be reduced when using brittle materials [6, 22]. Here, a decrease in adhesion strength is attributed to competing rebound and adhesion energies in addition to fracture of the ceramic at very high velocities. Fracture of the ceramic when depositing powder at 4.9 MPa and 800°C is indicative of the early limit of the window of sprayability. Within the deposition conditions used in this study, only a decrease in adhesion strength was observed. Per LIPIT results, below approximately 580 m/s particles will not adhere. For cold spray, the splats deposited using the lowest gas temperature with the standard nozzle have an impact velocity relatively close to this critical velocity.

5.6 Conclusion

The influencing parameters on the formation of a bond in a metal/ceramic interface by high-speed impact are still unclear in the literature. To better understand some influencing parameters, Ti particles are deposited by LIPIT and cold spray on polycrystalline Al_2O_3 substrates. Specific parameters of interest include identifying critical velocity for this material system, understanding the effect of substrate local heterogeneity when using sintered ceramic substrates and the effect of

velocity on adhesion strength. For the first time, the critical velocity for deposition of Ti onto Al_2O_3 by high-speed impact is identified to be between 580-620 m/s by use of the LIPIT system.

The splat adhesion test is used to measure the adhesion of individual splats. Substrate morphology and deposition velocity of individual splats are identified as influencing parameters on adhesion strength. By knowing the deposition velocity of individual splats when using LIPIT, the effect of substrate surface morphology is isolated from the velocity effect. Splats landing on comparatively smooth portions of the substrates have significantly lower bond strengths than those landing on rough portions of the substrates. The influence of substrate surface morphology on bond strength is important as mechanical bonding is found to contribute significantly to adhesion in this Ti/Al_2O_3 interface. Individual splats also have a characteristic FR related to the particle velocity at impact. The effect of particle velocity on FR is studied for splats deposited by both LIPIT and cold spray. The cold sprayed splats show that adhesion strength tends to decrease with an increase in FR despite the dependence between adhesion strength and substrate surface morphology. This effect can be associated with fracture of the ceramic at very high velocities and competing effects between adhesion and rebound energies.

5.7 Acknowledgement

RRC and SII acknowledge the assistance of Dr. Phuong Vo and Jean-Francois Alarie at the National Research Council Canada for technical support with the cold spray equipment and Drs. Thomas Schmitt and Jolanta Sapieha from Polytechnique Montréal for technical support and access to the scratch tester. This work was supported by the Natural Science and Engineering Research Council (NSERC) Strategic Grants Program.

MHG and CAS acknowledge support from the US Army Research Laboratory, Contract: W911NF-15-2-0034, “Development of Additive Manufacturing and Advanced Materials Processing for the DOD”. DV and KAN acknowledge support from the U. S. Army Research

Office through the Institute for Soldier Nanotechnologies, under Cooperative Agreement Numbers W911NF-13-D-0001 and W911NF-18-2-0048 as well as support for equipment through the Office of Naval Research DURIP Grant No. N00014-13-1-0676.

Chapter 6

Failure Dynamics of Spherical and Irregular Shaped Ti Splats Deposited on Sapphire by Cold Spray

Sara I. Imbriglio · Venkata N.V. Munagala · Thomas Schmitt · Raynald Gauvin · Jolanta E. Klemberg-Sapieha · Richard R. Chromik

Adapted from a paper of the same title published in *Surface Topography: Metrology and Properties,* 2019. **7:** p. 045002

In the previous two chapters, independent variables in the cold spray system from the processing point of view and from the ceramic substrate material and morphology point of view were address. The effect of powder morphology was not considered and is the focus of this chapter. The high adhesion strength between Ti and Al_2O_3, found in chapter 4, remained of high interest and thus the ceramic was not changed in this chapter. The spherical shaped powder used in the previous two chapters is compared to an irregular shaped powder with a coral-like morphology manufactured by the Armstrong process. Two different spray conditions and velocities are used to also characterize the effect of velocity for the irregular shaped powder.

6.1 Abstract

Single splats of commercially pure (CP) Ti are deposited onto sapphire by cold spray under two spray conditions to achieve different in-flight powder velocities. The powders used have two morphologies: spherical powder (SP), manufactured by plasma gas atomization and irregular powder (IP), manufactured by the Armstrong process, with a coral-like morphology. The adhesion strength of the single splats is measured by splat adhesion testing. By use of a specialized *in situ* scratch tester, interface failure during splat adhesion testing is observed through the sapphire substrate. Particle velocity does not significantly influence the adhesion strength and failure mechanism of SP splats. After deposition, the SP splat has an interface pore in its center which acts as an initiation site for crack propagation during splat adhesion testing. After failure, a well-bonded portion of Ti remains on the substrate in the shape of a ring. IP splats deposited at low velocity show similar, well adhering, rings on the surface in localized locations scattered throughout the interface. An increase in velocity for IP splats led to an increase in adhesion strength and a nearly continuous well adhering interface. The behaviour of IP splats is understood by electron channelling contrast images of cross-sections where low velocities resulted in little change in microstructure while high velocities led to a highly deformed microstructure at the interface.

Keywords cold spray · irregular powder · spherical powder · sapphire substrate · titanium powder · metal/ceramic interface

6.2 Introduction

During cold spray deposition, micro-particle impact onto a substrate allows for coating buildup. The microparticles adhering to the substrate are referred to as ‘splats’. Coating properties are

directly affected by cohesion between splats and adhesion of splats to the substrate. Testing of adhesion and cohesion of coatings is typically done by bulk mechanical testing in tension [75, 80, 151, 204, 205]. When investigating new coating/substrate combinations, information pertaining to the ideal deposition conditions and adhesion strength at the interface is sought. Bulk mechanical testing in tensions has several drawbacks for this application including the use of a lot of powder, machining of specific substrate geometries and failure away from the coating/substrate interface [35]. The latter drawbacks are of particular concern when investigating adhesion between metal coatings and ceramic substrates. Interest in metal/ceramic interfaces deposited by cold spray stems from their advantageous properties in metal matrix composite coatings [5] and potential applications in ceramic metallization [6, 9, 10, 27]. With little known regarding the required spray conditions to deposit a dense and well-adhering coating, a lot of wasted powder is expected if using a tensile test. Specific substrate geometries may also be difficult or expensive to manufacture out of ceramic. Failure of the ceramic in tension rather than at the interface may prevent a proper investigation of interface failure. For a more direct study of interface characteristics, Chromik et al. introduced a splat adhesion test which is an experimental technique adapted from the ball bond shear test, typically used to investigate adhesion of solder balls in microelectronics, to quantitatively study the adhesion of single cold sprayed splats [35].

The splat adhesion test has been successful in characterizing adhesion in metal/ceramic interfaces (i.e., Ti/Al_2O_3 and Ti/SiC interfaces) [196, 206]. Post-test characterization using light optical microscopy (LOM) and scanning electron microscopy (SEM) images of failed interfaces provides information regarding factors contributing to adhesion. Substrate morphology and substrate composition have been found to influence the appearance of failed interfaces [196, 206]. Splat adhesion testing of Ti splats deposited on polycrystalline Al_2O_3 revealed differences in bonding mechanism with different substrate morphologies [196]. Ti formed a bond at the periphery of the splat when deposited on polished polycrystalline substrates. On rough substrates the Ti penetrated into the asperities to form a mechanical bond [196]. The bond formed along the periphery of the splat on polished substrates covered a larger contact area than the localized mechanical bonding

on rough substrate rendering an overall higher adhesion strength. It was assumed that the bond formed in the periphery of the splats on polished substrates is from chemico-physical interactions between the metal and ceramic during the formation of adiabatic shear instabilities (ASI) and jetting at impact because no mechanical interlocking could occur in these interfaces [196]. The formation of a bond in the periphery of the splat and a gap at the center is characteristic of cold sprayed spherical powder (SP) and has been observed in many metal/metal [22, 28, 36, 164] and metal/ceramic [10, 28] interfaces. A peripheral bond reflective of that found in Ti/Al_2O_3 interfaces was also observed in post-test characterization of failed interface between Ti splats deposited on a relatively smooth as-received SiC substrate but only in localized regions of the periphery resulting in a weak adhesion strength [196].

Given the high adhesion strength between Ti splats and polished Al_2O_3 substrate or atomically smooth sapphire, these interfaces remain of interest for potential industrial application [26, 196]. Yet, the cost of spherical Ti powder is often prohibitively high. The Armstrong process is a novel technique for manufacturing irregular shaped Ti and Ti alloy powders with a coral-like morphology at a fraction of the cost [139]. Depositing irregular Ti powder onto Ti substrates results in dense coatings at lower velocities than SP [139]. Similar results are observed when depositing Ti6Al4V irregular powder (IP) onto Ti6Al4V substrates [140]. The superior density of coatings deposited using Armstrong powder is attributed to its shape and microstructure which allows for better deformability and higher velocities for a given spray condition as compared to SP [139, 140]. However, their performance in metal/ceramic interface remains unknown. The irregular shape of the powder was previously found to be advantageous in metal/metal interfaces as they promote compaction and mechanical bonding [139-141]. When deposited at low velocities, metallurgical bonding was not achieved as revealed by weak microhardness measurements with debonding between the splats [139]. Jetting and ASI have been observed for these powders but they appear localized as compared to SP [141]. Given the importance of jetting and ASI in forming a strong bond on a smooth ceramic substrate, it is unclear if the irregular, coral-like, morphology of the powder will be advantageous or detrimental to the formation of a strong bond.

In this work, single splats of spherical and irregular Ti powder are deposited onto optical sapphire windows. These powders are compared in terms of their adhesion strength as measured by the splat adhesion test for two different spray conditions. Rather than only relying on post-test characterization to understand the bonding mechanism, the transparent nature of the optical sapphire window allows for the use of an *in situ* splat adhesion test where failure dynamics are characterized as the tip interacts with the splat. Adhesion strength measurements and bonding mechanisms are explained through the failure mechanism, post-test characterization and cross-sectional imaging.

6.3 Experimental Procedure

Single splats were deposited using spherical and irregular shaped, commercially pure Ti powder particles by cold spray (PCS-800, Plasma Giken, Saitama, Japan) onto sapphire (Meller optics, Rhode Island, USA) substrates. To deposit single splats by cold spray, nitrogen, with an initial gas pressure of 4 MPa and preheat temperature of 400°C and 800°C, is used as the carrier gas for both powder morphologies. Hereafter, samples are identified by the gas preheat temperature as pressure is maintained constant in both spray conditions. The in-flight velocity of the powder is measured by a time-of-flight particle diagnosis system (Coldspraymeter, Tecnar Automation, Quebec, Canada). To ensure the deposition of scattered single splats, the gun traverse speed is 1 m/s with the lowest possible feed rate.

The sapphire substrates have a diameter of 11 mm and thickness of 5 mm. The surface of the sapphire substrate has a C-Plane (0001) crystallographic orientation. The SP, with an average particle size of 29 µm, is manufactured by plasma gas atomization and has been characterized elsewhere [196]. The irregular shaped Ti powder (Cristal metals, USA) is manufactured by the Armstrong process and has a coral-like morphology with an average size of 66 µm (Figure 6.1). The IP's coral-like morphology, in the cross-section, shows large, irregularly shaped pores with equiaxed grains. Some grains show minor evidence of deformation (Figure 6.2). The deformation

may be due to ball milling, a post-processing technique used to target specific tap densities and particles size distributions [145]. There is also a large variation in grain size heterogeneously distributed throughout the microstructure of individual powder particles. Grains range from hundreds of nanometers to few microns (Figure 6.2).

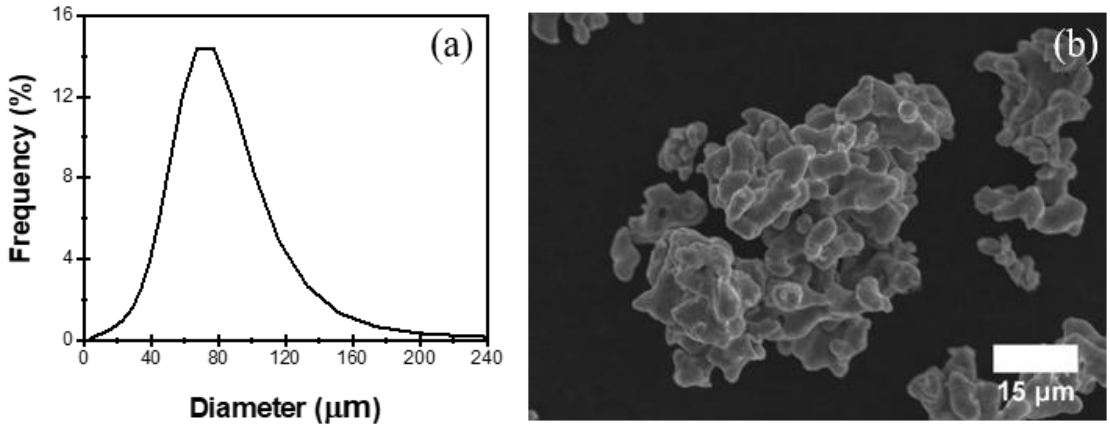

Figure 6.1 The (a) powder size distribution and (b) morphology of the IP manufactured by the Armstrong process.

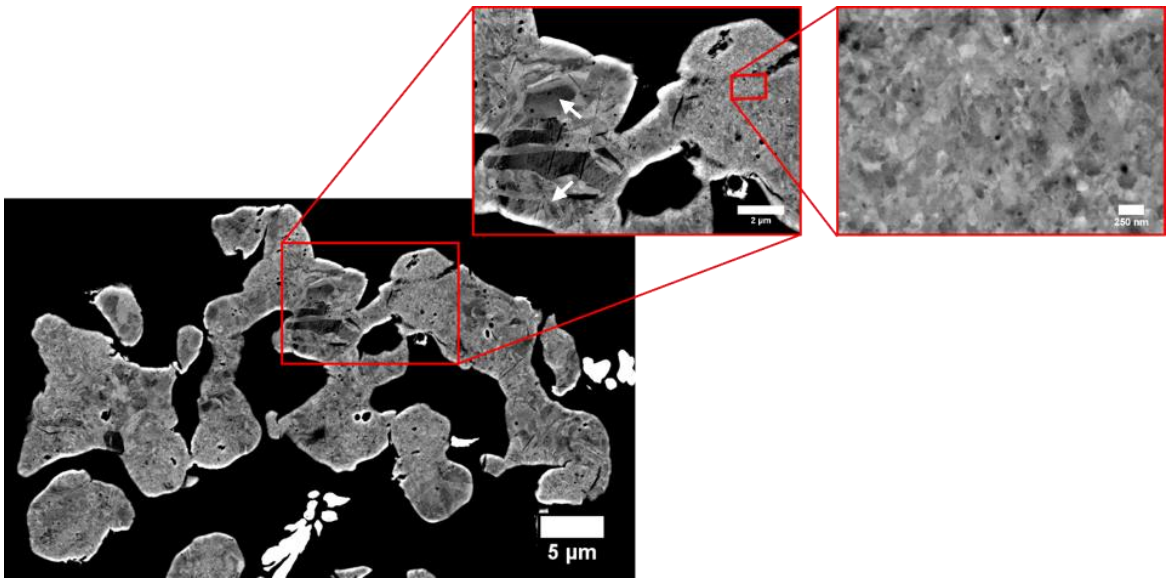

Figure 6.2 The microstructure of the IP manufactured by the Armstrong process. Arrows have been used to emphasize grains showing minor evidence of deformation.

Coating buildup is dependent on initial interactions occurring at the splat level. As such, the study of adhesion of single splats is required to better understand the deposition process. Yet, to date, there is no standardized testing methodology for testing the adhesion of single micron-sized particles. Chromik et al. proposed a technique for testing single splats which is based on the commonly used ball bond shear test for solder balls [35]. This technique has been referred to in previous works as a splat adhesion test [36, 196, 206]. While failure under the applied load is not completely in tension (mode I) or in shear (mode II) as traditional adhesion testing techniques, results from this technique, accompanied by extensive post-test characterization, are useful to characterize the deposition process and bonding mechanism. The splat adhesion testing methodology, used here, is the same as found in Chromik et al. [35]. A tip with a semi-circular cross-section of 100 µm in diameter is used to scratch the single splats. The sliding speed is fixed to 150 µm/min and the normal force is set to 100 or 200 mN for all tests. The higher normal force is only used for IP splats deposited at 800°C as the tip consistently traveled over the splat with a lower normal force. The scratch length varies based on the available space between the splats and

size of the splats tested. As the tip removes the splat, the tangential force on the tip is recorded. The tangential force records a baseline ($F_{T\ Baseline}$) due to friction between the tip and the substrate and a peak force ($F_{T\ Peak}$) when the tip removes the splat. From these results a splat adhesion strength is calculated using Eq. 6.1 [35].

$$Splat\ Adhesion\ Strength\ [MPa] = \frac{F_{T\ Peak}\ [mN] - F_{T\ Baseline}[mN]}{Projected\ Area\ [\mu m^2]} * 1000 \qquad \text{Eq. 6.1}$$

For SP, the projected area is measured using the diameter of the impacted splat prior to each test. The projected area of irregular shaped splats is measured by image processing of LOM images in ImageJ. The tangential force plots with respect to positions and projected areas are also used to calculate splat adhesion energy by Eq. 6.2 [35]. Splat adhesion energy is used to distinguish between a more brittle or more ductile failure of the splats [35].

$$Splat\ Adhesion\ Energy\ [kJ\ m^{-2}] = \frac{\int_{Contact}^{Failure}[F_T(x) - F_{T\ Baseline}]dx\ [mN.\mu m]}{Projected\ Area\ [\mu m^2]} \qquad \text{Eq. 6.2}$$

Splat adhesion testing is completed on both an *in situ* and *ex situ* platform. *In situ* splat adhesion testing is performed on a modified Micro-Scratch Tester (CSM Instruments, Inc, Graz, Austria) with an optical setup allowing for observation of the contact area through the transparent substrate. Details regarding the optical setup used have been presented elsewhere [172]. Between 5 and 10 splats are tested for each spray condition using the *in situ* setup. Experiments completed on the *in situ* setup are used to understand fractography of a splat during splat adhesion testing. To ensure consistency between the data presented here and other work [35, 36, 196], the Micro-Combi Tester (Anton Paar, Graz, Austria) was also used to test at least 15 splats. Results were compared for splats tested with the two equipment. Splat adhesion strength measurements taken with the *in situ* system were higher than the average splat adhesion strength with the *ex situ* system. This difference was due to differences in the measurement of splat area from above (*ex situ*) versus beneath (*in situ*) the splat. When this difference was taken into account, the measurements from the two

systems were consistent with one another. Nevertheless, because all previous reports using this technique are on *ex situ* testing, reported splat adhesion strength measurements and tangential force versus position plots are shown for experiments completed on the Micro-Combi Tester. Alongside these results, observations of splat failure are presented from *in situ* testing.

Splats are imaged prior and post splat adhesion testing by a variable-pressure SEM (VP-SEM, SU-3500, Hitachi, Tokyo, Japan). Charging caused by the ceramic substrate is reduced by maintaining a pressure of 40 Pa and an accelerating voltage of 5 kV in the VP-SEM [202]. Powder cross-sections are imaged by a high-pressure SEM (SEM, SU-8230, Hitachi, Tokyo, Japan). Also, to better understand IP splat adhesion test results, focus ion beam milling (FIB) is used to cross-section single IP splats deposited on sapphire. FIB and imaging for these particles is completed on a FEI Helios NanoLab 660 electron microscope located at the Facility for Electron Microscopy Research at McGill University.

6.4 Results

6.4.1 Cold Sprayed Splats

Consistent with previous literature [139, 140], IP has a higher in-flight velocity than SP for a specific spray condition (Table 6.1). Due to their shape, IP experiences more drag than SP resulting in higher in-flight velocities [140]. In this case, the velocity difference is more pronounced using a gas preheat temperature of 400°C.

Table 6.1 Velocity of IP and SP for each spray condition.

Spray Conditions	Average Particle Velocity (m/s)	
	SP	IP
4.0 MPa, 400°C	491 ± 127	581 ± 80
4.0 MPa, 800°C	692 ± 133	710 ± 91

The morphology of impacted splats is shown in Figure 6.3. SP splats show evidence of jetting along the periphery of the powder (Figure 6.3 (a) and (b)). Jetting is more pronounced for SP splats deposited at 800°C as compared to SP deposited at 400°C. IP splats, deposited at 400°C, show localized evidence of jetting around the splat (Figure 6.3 (c)) while IP splats deposited at 800°C, show more generalized jetting around the splat (Figure 6.3 (d)). The initial morphology of the splat affects the deformation behaviour at impact.

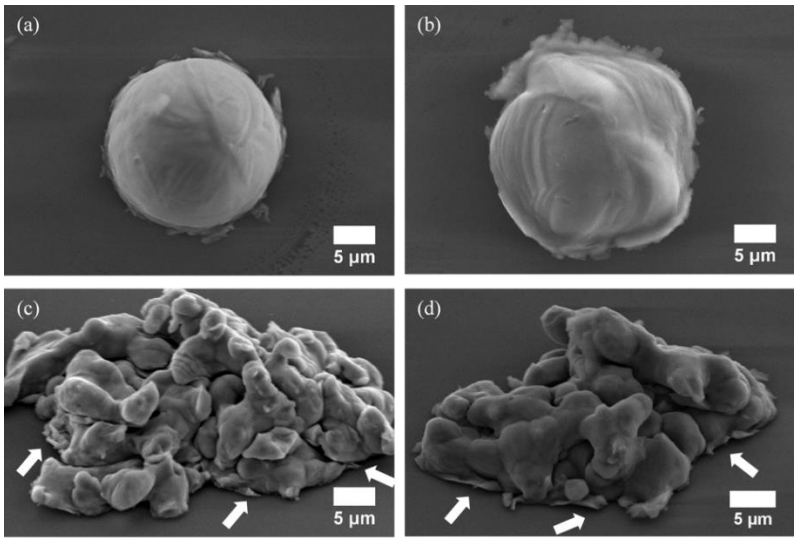

Figure 6.3 Morphology of SP deposited with a gas preheat temperature of (a) 400°C, (b) 800°C and morphology of IP deposited with a gas preheat temperature of (c) 400°C, (d) 800°C. In (c) and (d) arrows emphasize regions of jetting in IP splats.

6.4.2 Splat Adhesion Test

6.4.2.1 Spherical Powder

The splat adhesion strengths for SP are shown in Figure 6.4 (a). There is no statistical difference in splat adhesion strength with an increase in gas preheat temperature as verified by a t-test. SP splats deposited under both spray conditions result in Ti remaining on the substrate along the periphery of the splat (Figure 6.4 (b)) as previously observed when depositing Ti on polished Al_2O_3 [196]. The post-test morphology of Ti remaining on the substrate is referred to as an adhesion ring.

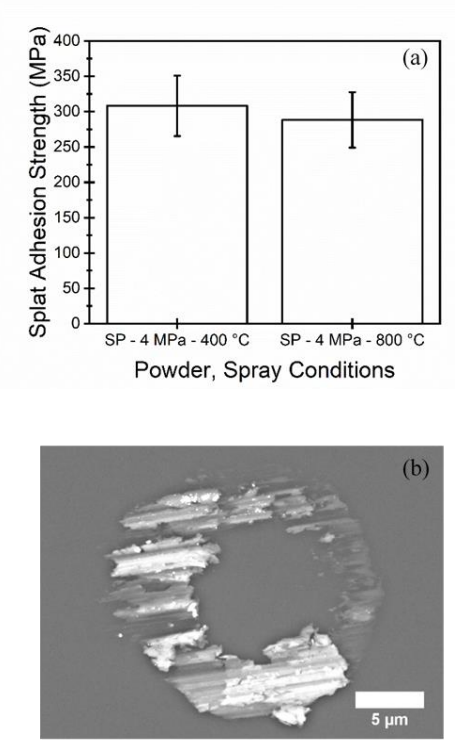

Figure 6.4 (a) Splat adhesion strength of single SP splats deposited at 400°C and 800°C. (b) Failed interface of an SP splat showing an 'adhesion ring'.

Six frames recorded for a single SP splat, deposited at 400°C, during *in situ* splat adhesion testing are shown in Figure 6.5. Observations of failure for SP splats deposited at 800°C (not shown here) are identical to those deposited at 400°C. For this splat, a center interface crack is visible in the first frame by a light contrast at the center of the splat. This center interface crack was repeatedly seen when observing through the substrate. However, due to the resolution of the LOM when recording through the sapphire substrate, the center crack is difficult to see. As the center begins to buckle under the tangential load of the tip, the center interface crack propagates and becomes more visible. Crack propagation continues through frames two to five, from the center outwards, until failure occurs instantly through the Ti (frame six) leaving a ring of material on the substrate. The ring remaining on the substrate is representative of well-bonded material. Crack propagation occurs through the weakest part of the material. Therefore, the strength of the Ti is lower than the interface shear strength between the Ti and sapphire in the adhesion ring.

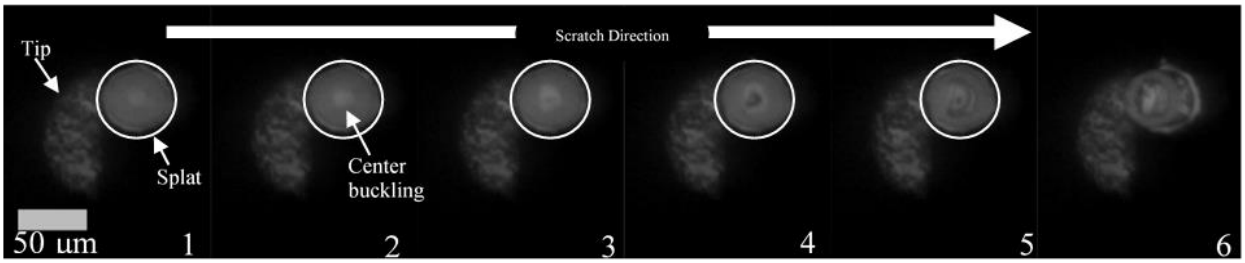

Figure 6.5 Six frames captured during *in situ* splat adhesion testing of a SP splat deposited at 400°C showing the typical failure dynamics in splat/substrate interfaces using SP where failure begins in the center with crack propagation outwards leaving a ring of Ti on the substrate.

Features identified in typical tangential force plots with respect to position (Figure 6.6) match *in situ* observations. When the tip meets the splat, the tangential force increases. The increase is not perfectly linear as plastic deformation and crack propagation starts to occur. There is a sudden drop in the tangential force when splat failure occurs.

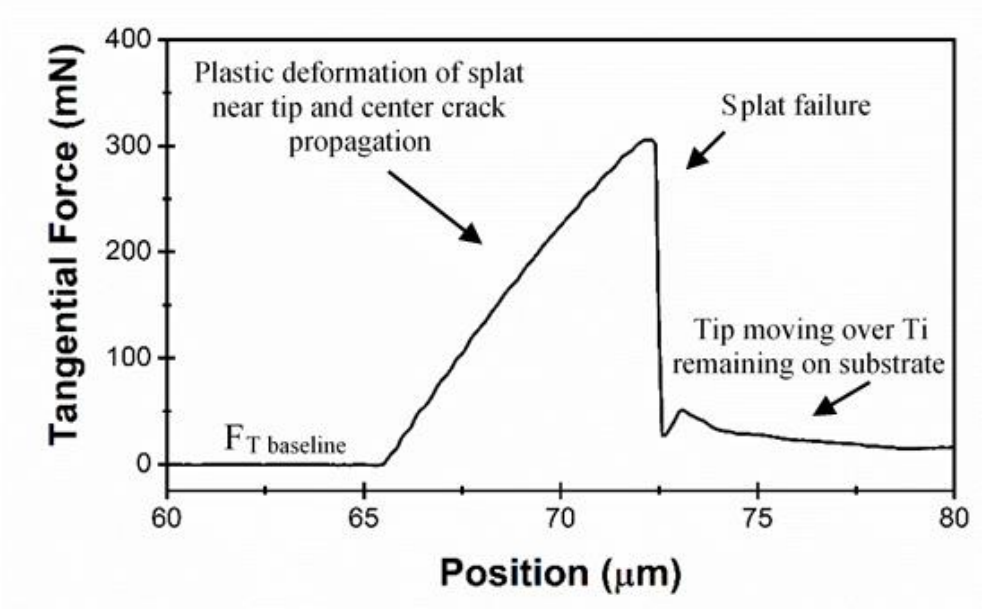

Figure 6.6 A representative tangential force with respect to position plot during splat/substrate failure of SP deposited at 400℃.

6.4.2.2 Irregular Powder

The increase in gas temperature has a more pronounced impact on IP (Figure 6.7). At a gas preheat temperature of 400℃, IP have weak adhesion to the sapphire substrate. Increasing the gas preheat temperature to 800℃ for IP significantly improves adhesion.

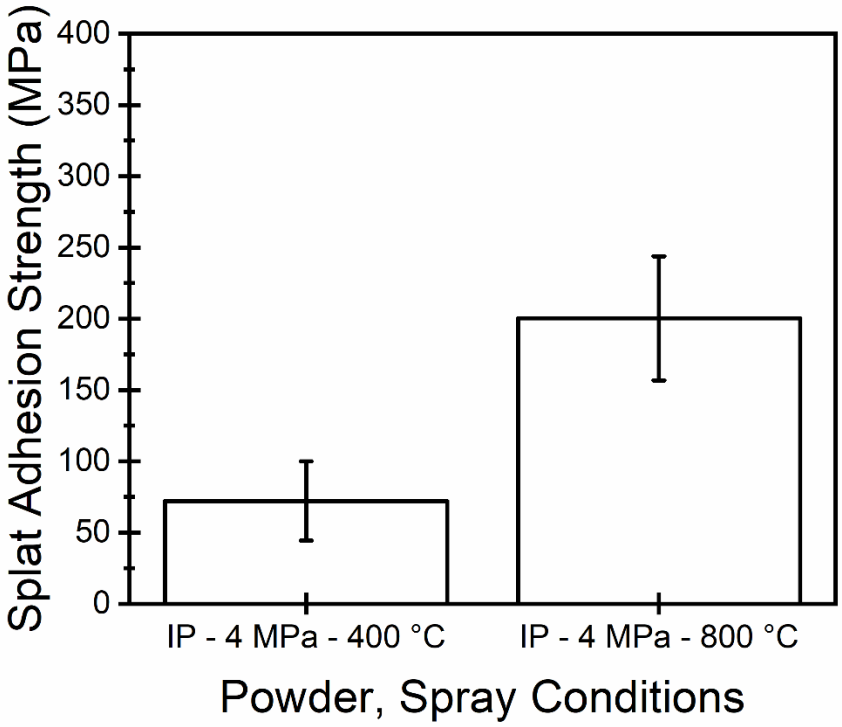

Figure 6.7 Splat adhesion strength of IP splats deposited at different gas preheat temperatures.

The footprint observed in post-test characterization (Figure 6.8 (a) and (b)) is significantly different for both spray conditions. For IP splats deposited at 400℃, failed interfaces show localized adhesion rings (Figure 6.8 (a)). These rings are a result of localized contact between the irregular shaped protrusions and the substrate which form a material jet through ASI similarly to SP. As previously shown (Figure 6.3), IP show localized evidence of ASI which correlates with the localized adhesion rings found on the substrate following the splat adhesion test. In regions where jetting and ASI are formed, the Ti and sapphire form a bond. Due to the large number of interface cracks propagating simultaneously, failure of the splat occurs rapidly (Figure 6.9 (a)). The representative tangential force plot in Figure 6.8 (c) shows a drop shortly after contact with the splat. When testing IP splats, the shape of the peak may be slightly different from one splat to another given the irregular nature of the bond formed. However, general observations as previously mentioned remain valid. This rapid crack propagation is further confirmed by *in situ* observation

of failure during splat adhesion testing for splats deposited at 400°C (Figure 6.9 (a)). Cracks start to propagate in many locations through the interface (frame 2). These cracks continue to propagate until failure of the splat (frames 3 to 5).

For particles deposited at 800°C, only few splats experience interface failure even when increasing the normal force in the splat adhesion test. Failed interfaces include a large amount of Ti remaining on the substrate in the shape of the scratched splat (Figure 6.8 (b)). There is some evidence of interface cracks as identified by arrows in Figure 6.8 (b) but these are less prominent than for SP or IP deposited at 400°C and appear to minimally affect failure. Since failure does not occur in the interface, Ti is sheared near the interface as observed in *in situ* observation of failure (Figure 6.9 (b)). Tangential force plots consistently show a peak with no drastic drop (Figure 6.8 (d)). The particle fails before the tip has traveled over the entire splat. Given that failure occurs through the Ti, the tip continues to shear residual Ti on the surface. Therefore, the tangential force does not return to the baseline after failure. For splat adhesion energy calculations, the area under the curve is taken up to the initial peak drop as it is more representative of the splat failure.

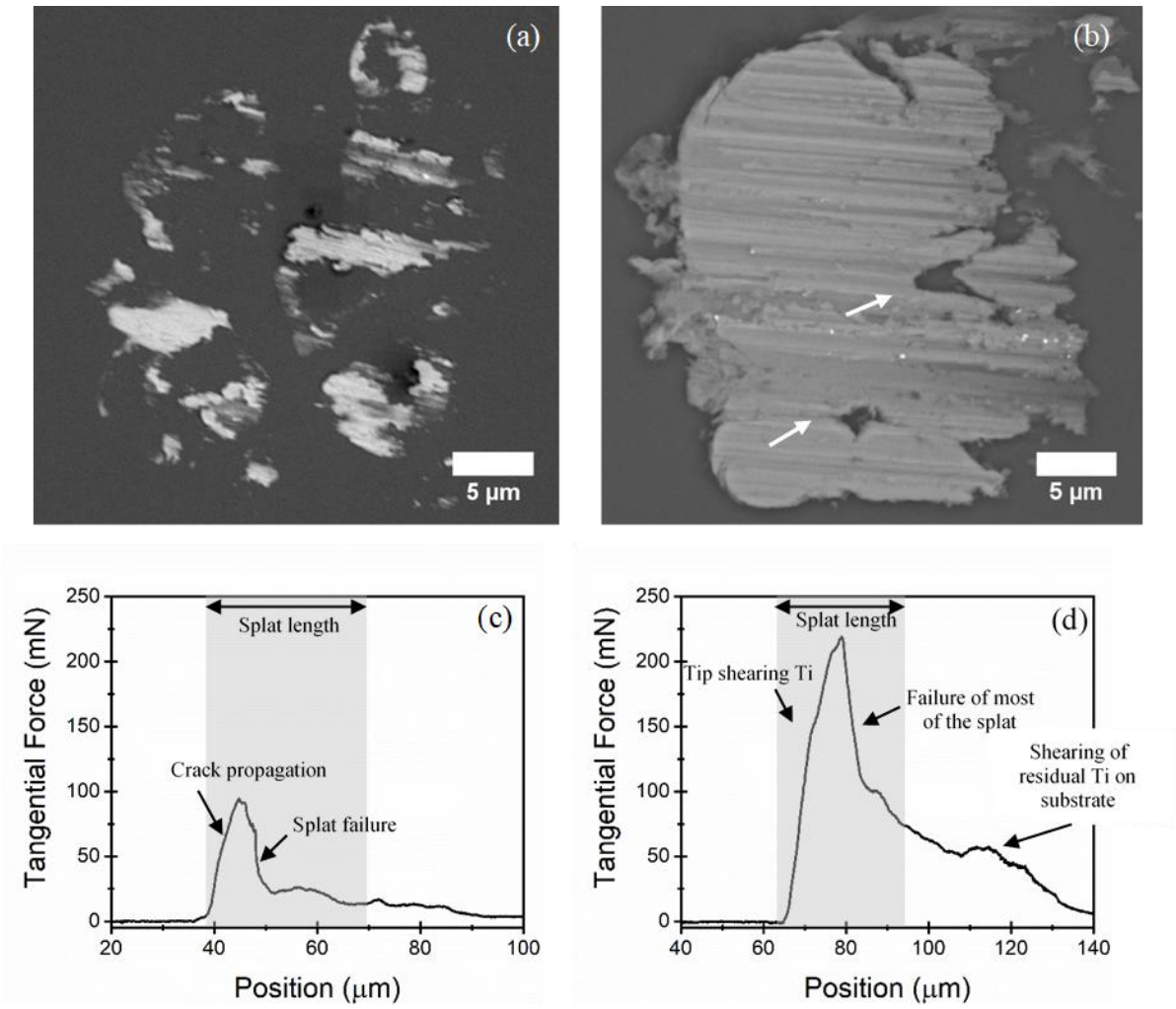

Figure 6.8 Failed interface and tangential force versus position plot for an IP splat deposited at (a, c) 400℃ and (b, d) 800℃.

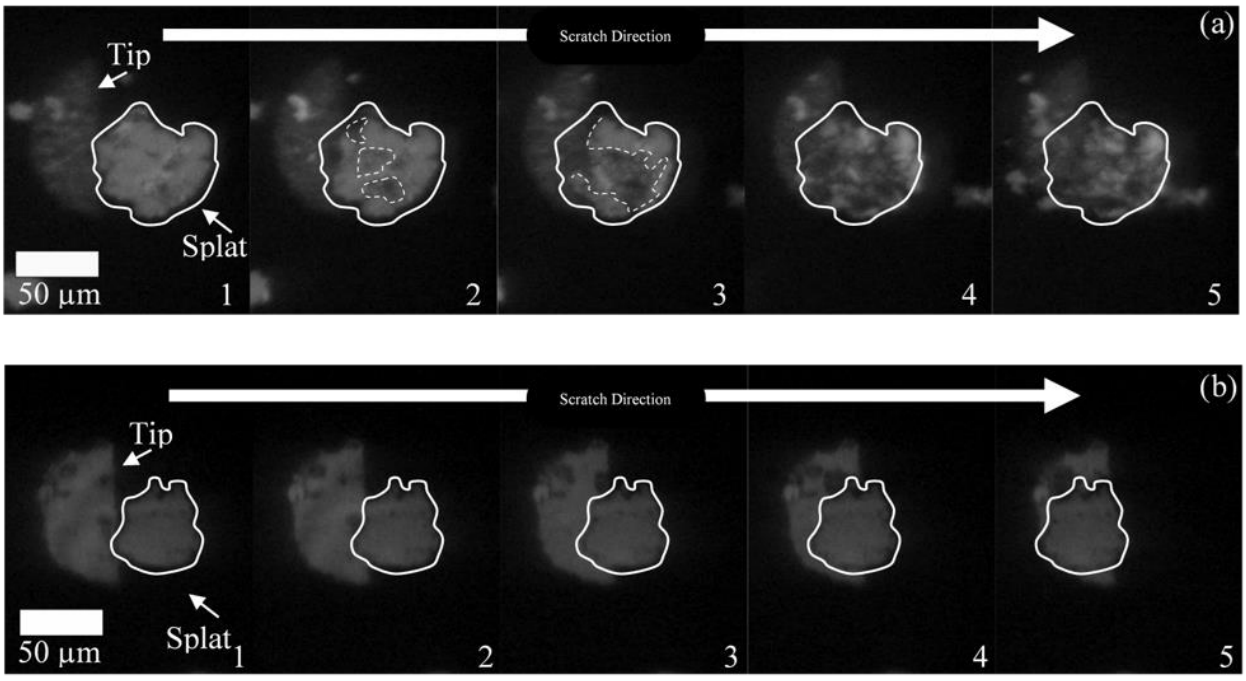

Figure 6.9 Five frames captured through the sapphire substrate during *in situ* splat adhesion testing for IP splats deposited at a gas preheat temperature of (a) 400°C and (b) 800°C showing the failure dynamics of these interfaces.

No crack propagation in the interface between the IP splats deposited at 800°C and the substrate is indicative of a continuous well bonded interface. Given the irregular shape of the powder, at higher velocities, more shear contact may occur in the Ti/sapphire interface resulting in less interface defects. Despite the continuous and well-bonded interface between IP splats deposited at 800°C and the sapphire, splat adhesion strength is lower than SP splats deposited under the two spray conditions. However, the splat adhesion energy is higher for the IP splats deposited at 800°C than that of the SP splats under both spray conditions (Figure 6.10). The higher splat adhesion energy is indicative of a more ductile failure occurring through the Ti. SP splats deposited at both spray conditions and IP splats deposited at 400°C experienced a more brittle failure due to interface crack propagation. Therefore, while IP deposited at 800°C has a lower splat adhesion strength, it has better cohesion to the substrate.

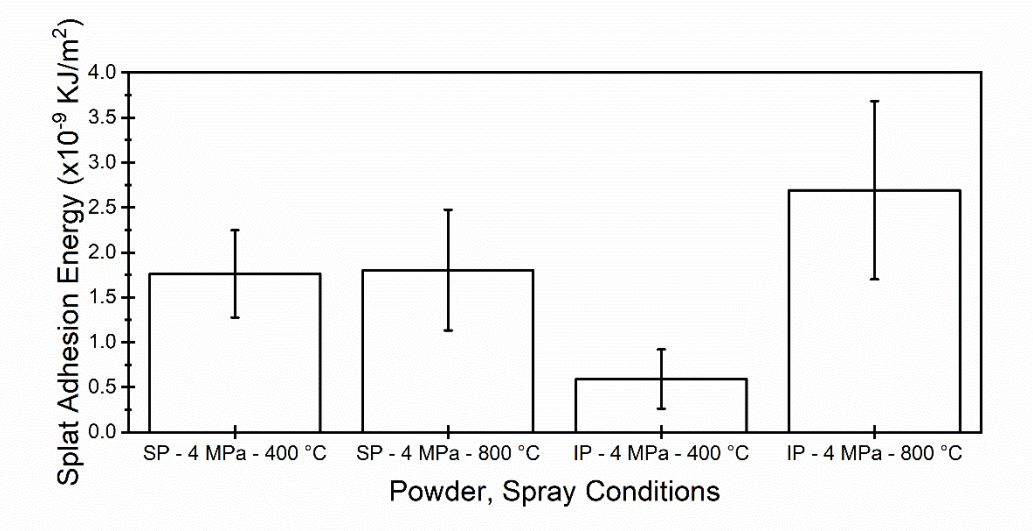

Figure 6.10 Splat adhesion energy for the SP and IP deposited at both spray conditions.

Cross-sectional electron channelling contrast images (ECCI) are captured for the IP splats deposited under both spray conditions to better understand the splat adhesion test results. The IP splats deposited at 400℃ (Figure 6.11) show significantly less deformation than IP splats deposited at 800℃ (Figure 6.12). In both interfaces, there is no evidence of fracture in the ceramic substrate. The IP splats deposited at 400℃ have a combination of fine grains and coarser deformed grains at the interface (Figure 6.11 (a) and (c)). The splat largely retains its initial microstructure but coarse grains near the interface show significantly more deformation. Near the interface, there is also no evidence of the large irregularly shaped pores typically found in the initial powder particles. The pores appear to collapse during impact. In the top portion of the splat, there is less deformation and more porosity.

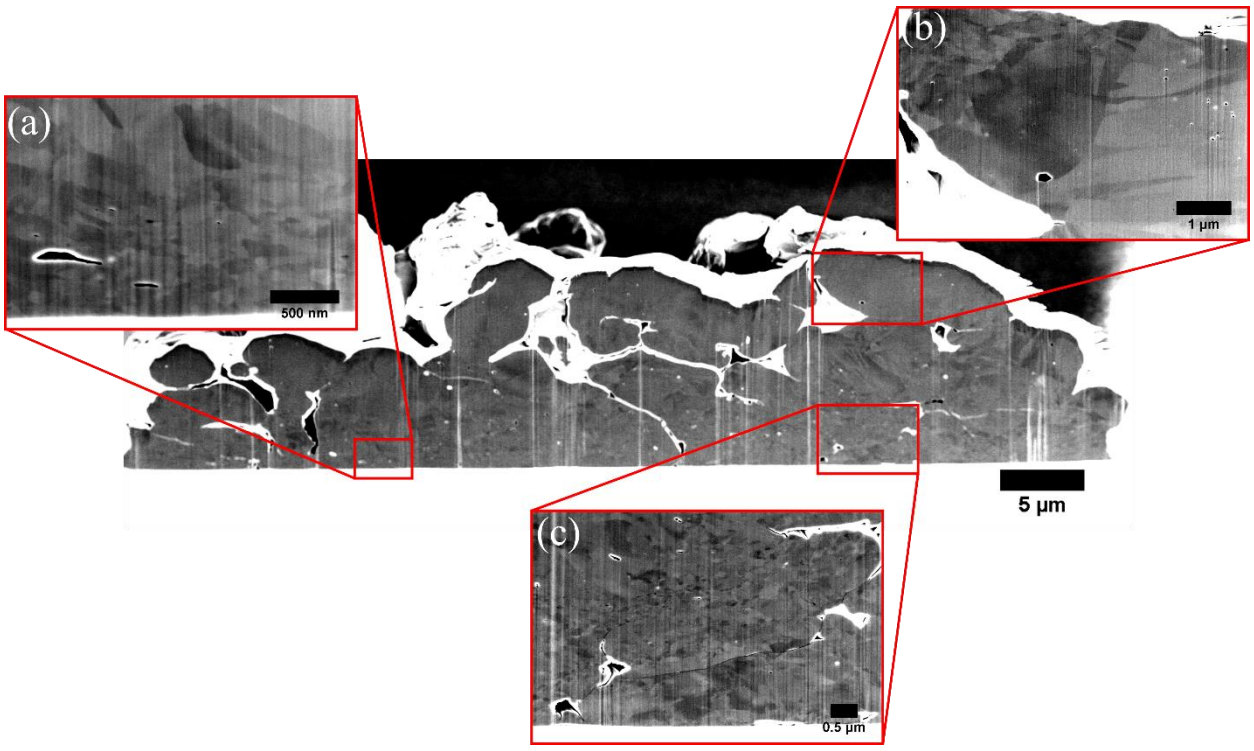

Figure 6.11 Microstructure of the IP Ti splat deposited at 400°C showing (a) fine grains in localized regions near the interface whereas (c) larger grains are also observed in the Ti along the interface. At the top of the splat, (b) large grains reflective of the initial powder microstructure are observed.

For IP deposited at 800°C, there are ultrafine grains along the entire interface with sapphire extending into the particle to a height of 1 ± 0.4 µm. Beyond the ultrafine grains, there is a region of fine grains followed by heavily deformed coarse grains. The splat appears completely deformed with minor evidence of initial powder microstructure at the top region. The amount of deformation in the coarse grains is not reflective of the initial powder. There is also significantly less porosity throughout the splat as compared to the splat deposited at 400°C. The protrusions conform to one another through the entire height of the splat but some fine interface pores between the protrusions are still present. At the interface there are some small pores as expected from post-test characterization results (Figure 6.8 (b)).

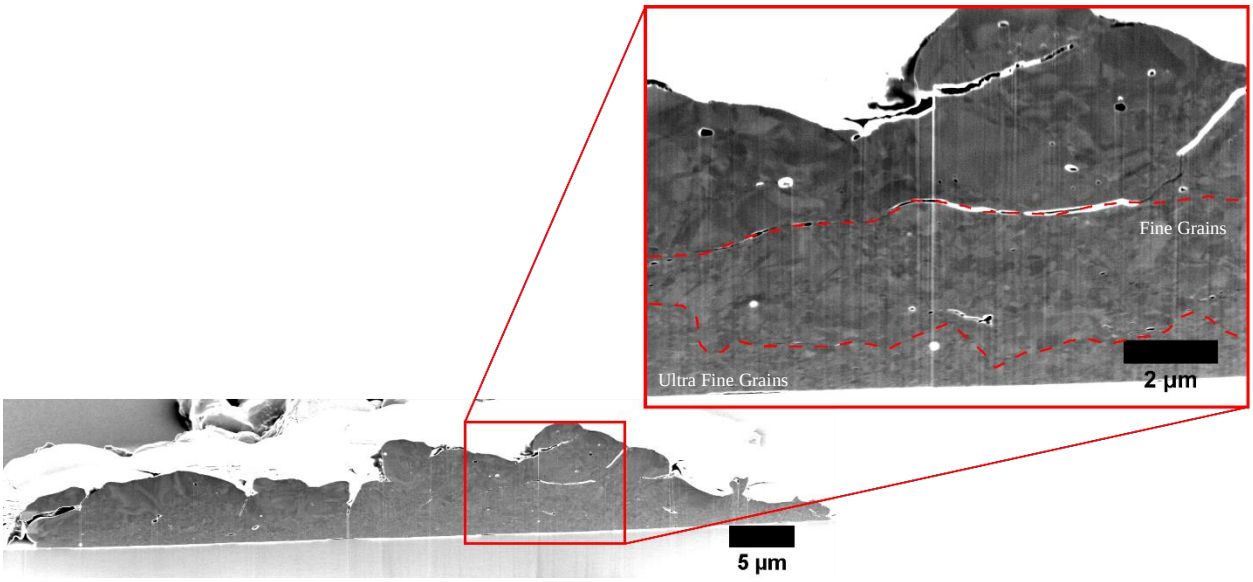

Figure 6.12 Microstructure of the IP Ti splat deposited at 800°C showing ultrafine grains throughout the entire interface that extends into the splat and leads to a region of fine grains. There is minor evidence of the initial microstructure in the top portion of the splat.

6.5 Discussion

6.5.1 Velocity

In this work, powder in-flight velocity was increased by increasing gas preheat temperature from 400°C to 800°C (Table 3.3). Previous work on Ti/Al_2O_3 interfaces showed that temperature has a secondary influence on deformation and splat adhesion strength for the Ti/Al_2O_3 interface while velocity plays a primary role [206]. Deformation and splat adhesion strength are less affected by gas preheat temperature as the contact time between the gas and the powder particles is short which limits heat transfer as previously investigated for Ti by a numerical model [206].

For the nozzle used, the maximum gas preheat temperature is 800°C. As observed previously [139, 140], for a given spray condition, IP achieves higher in-flight velocity than SP. Changes in velocity had very little effect on the splat adhesion strength of Ti/Al_2O_3 interface using SP. While it is

possible to achieve higher velocities with a different nozzle or by using helium as the working gas, many studies on cold spray have shown that splats from SP always have a small unbonded section near the center of the impact [22, 25, 28, 36, 164]. Goldbaum et al. [36] used helium to achieve higher velocities for CP-Ti and Ti6Al4V splats onto Ti substrates. The effect of higher velocities with helium had minimal influence on the splat adhesion strength measured by the same techniques used here. For IP, increased velocity did result in an increase in splat adhesion strength. For the IP sprayed at the highest condition, deformation resulting in nearly full closure of all pores was observed. Higher spray conditions might lead to better adhesion, but previous studies by our group have shown that eventually fracture of the alumina occurs leading to a drop in splat adhesion strength [206].

6.5.2 Impact Induced Deformation and Bond Formation

Above a certain critical velocity, the impact of cold sprayed splats results in jetting and ASI in the periphery of the splat [22, 198]. Jetting and ASI induce microstructural changes in the deformed material [18, 21, 25, 112, 115]. For SP, these microstructural changes have been well characterized in the literature and appear consistent for various material interfaces. The severe plastic deformation, occurring in the material jet, causes an ultrafine grain microstructure near the interface particularly in the periphery of the splat [22, 25, 112, 113]. The ultrafine grains are a combined result of a high dislocation density leading to elongated subgrains in addition to dynamic recovery and recrystallization [112]. ASI formation requires a certain contact angle to induce viscoplastic deformation as understood by experiments on explosive welding. The angled contact is prevented in the nearly parallel contact at the south pole of the splat [25]. Here, it is shown that adhesion for a spherical Ti powder particle deposited on sapphire occurs along the periphery of the splat where ultrafine grains are typically found similarly to metal/metal interfaces. These results are also comparable to those found when spraying Ti on polished polycrystalline Al_2O_3 substrates [196] and zirconia [28]. Grain refinement and potential amorphization which can occur at the interface are associated with a reorientation of interface atoms which can form a

heteroepitaxial bond in the metal/ceramic interface as previously described in the literature [8, 27, 75, 133, 186]. Therefore, the extent of deformation experienced by a single particle is significant to bond formation and is manifested by the amount of grain refinement observed in the splat/substrate interface.

The negligible effect of spray conditions on the splat adhesion strength of SP may be associated with the contact angle required for viscoplastic deformation. This would therefore be a geometric limitation to forming a more continuous bond. By use of geometry (Figure 6.13), the minimum angle required to form a bond between Ti and sapphire can be approximated. The point 'b', where the Ti begins to bond to the substrate, is assumed to be at the required contact angle for adhesion to occur. The arc 'ab' is assumed to flatten as the particle impacts the substrate. As point 'b' comes in contact with the substrate, its angle with the substrate will be approximately 'θ'. The radius of the center pore is approximately equivalent to the length of the arc 'ab' and can be used to calculate the angle 'θ' allowing for adhesion in each splat. Using this methodology for SP splats deposited at 400℃ and SP splats deposited at 800℃, the calculated angles are $30 \pm 4°$ and $27 \pm 3°$ respectively. Given the relatively consistent angle measured despite an increase in velocity, the geometric limitation is believed to be a significant factor affecting the adhesion of single spherical Ti splats. In metal/metal interfaces, the center pore reduces in size as velocity is increased [25]. Potentially, the deformation of the substrate or some surface roughness would render the conditions more favourable to minimizing the size of the center pore when depositing single SP splats of Ti. Here, for the atomically smooth sapphire substrate that shows no evidence of deformation, adhesion appears highly affected by contact angle.

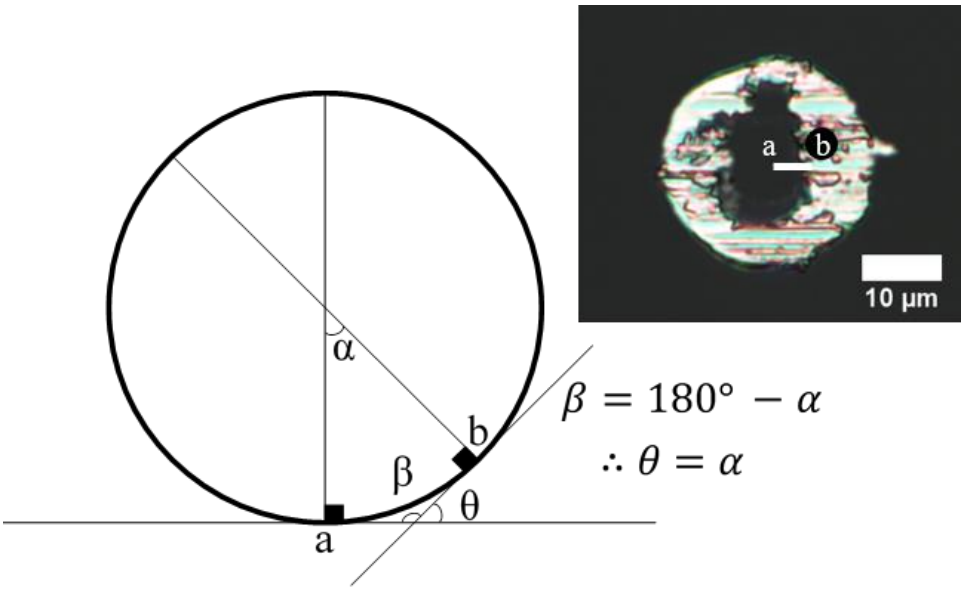

Figure 6.13 Contact angle between specified points on the circumference of the splat and the substrate.

When depositing a full coating, tamping from the impact of succeeding particles reduces porosity in the coatings/substrate interface that may be caused by such geometric limitations [68]. The specifically engineered coral-like morphology of the IP powder particles, used here, causes tamping within individual powder particles at high velocities rendering a continuous bond at the splat level. Geometric limitations in SP are therefore prevented by use of IP manufactured by the Armstrong process. Individual IP particles can be considered as an agglomerated matrix of small powder particles of irregular shape. Protrusions near the interface are initially deformed. The collapse of the powder's initial internal porosity causes tamping of the first layer of protrusions in contact with the substrate. At high velocity, this continued compaction from tamping effects allows for a nearly continuous interface with the substrate.

The behaviour of the IP during impact, described above, is based on the observation of splat cross-sections and splat adhesion results. When deposited at low velocity, the IP splats show deformation near the interface but in the top portion of the splat there is a significant amount of porosity which is reflective of the initial powder's porosity (Figure 6.11). The spray condition used is not adequate

to cause complete deformation of the powder particle. Only protrusions near the interface are deformed and cause localized ASI at the multiple contact points. The localized ASI cause localized, irregularly shaped, adhesion rings in post-test characterization of failed interfaces (Figure 6.8 (a)) allusive to the rings formed in SP splats. For IP splats deposited at a higher velocity, there is a complete collapse of internal porosity (Figure 6.12). The reduced pore size is indicative of the higher strain experienced by the splat at impact. This collapse of internal porosity in the IP splats deposited at higher velocities causes tamping as previously discussed which allows for a complete deformation of the splat near the interface as identified by the ultrafine grains throughout the entire Ti/Sapphire interface.

6.5.3 Splat Adhesion Strength and Fractography

SP splats showed similar splat adhesion strength results at both spray conditions (Figure 6.4 (a)). From *in situ* observation of fracture during the splat adhesion test, the center interface crack acts as a stress concentration site under the applied load of the semicircular tip (Figure 6.5). As the critical stress for crack propagation is reached, the crack begins to propagate along the interface where adhesion is comparatively weak. Farther away from the center where ASI lead to a strong bond, the crack continues to propagate through the Ti. Crack propagation occurs rapidly causing a nearly instant drop in the tangential force plot with respect to distance (Figure 6.6). Similar observations are made for the IP splats deposited at low velocities. However, the reported splat adhesion strength results are significantly lower than those of SP splats (Figure 6.7). The lower adhesion is related to the large number of interface cracks which propagate simultaneously and ultimately lead to failure (Figure 6.9 (a)). In both above-mentioned cases, the presence of interface cracks leads to a more brittle failure of the splat when compared to the IP splats deposited at higher velocities. For these IP splats deposited at higher velocity, a more continuous interface is identified where interface failure under the loading condition is not achievable. While splat adhesion strength measurements show a lower value for IP splats deposited at higher velocities when compared to SP splats, these results cannot be directly compared. The splat adhesion strength result reported

for the high velocity IP splats is the minimum splat adhesion strength limited by the shear strength of the Ti splat. Since failure occurs through the Ti before delamination at the interface, the interesting impact conditions induced by the coral-like morphology of IP splat are considered to render better cohesion between the splat and the substrate as compared to SP when deposited at high velocities. For IP splats deposited at higher velocity, the greater compaction and greater degree of recrystallization would naturally lead to better mechanical properties in a full coating. The mechanism of multiple tamping events due to the coral-like morphology seems to be especially effective for cold spray. These observations are consistent with previous research on full coatings made on metal substrates, where coating made with IP were found to have better mechanical properties than coatings made with SP [139, 140].

6.6 Conclusion

Ti splats of SP and IP were deposited onto sapphire under two spray conditions, differentiated by changes in temperature resulting in changes in velocity. *In situ* splat adhesion testing provided insight regarding the failure mechanism of each splat. The SP splats deposited under both spray conditions showed very similar splat adhesion strengths due to a similar center interface crack propagation. The center interface crack is likely present due to a geometric limitation preventing an angled contact at the south pole of the splat for the formation of ASI. Failed interfaces presented well bonded rings. It was, therefore, confirmed that material jetting and ASI is a prerequisite to adhesion. These rings were also observed in the failed interfaces of IP splats deposited at 400℃. The localized protrusions on IP deform at impact and result in localized jetting and ASI resulting in localized adhesion. These scattered ring formations in the interface caused a low splat adhesion strength due to simultaneous cracks propagating. Increasing the velocity by increasing the gas temperature to 800℃ for IP allows for a higher splat adhesion strength due to tamping induced by the complete deformation of the splat. Deformation of the IP deposited at 800°C occurred through the entire interface while IP deposited at 400°C showed very little deformation as identified by ECCI imaging. Failure of splats deposited at 800°C occurred through the Ti rather than at the

interface. The failure of high velocity IP splats through the Ti allowed for a more ductile failure identified by a higher splat adhesion energy as compared to low velocity IP splats and SP splats. Therefore, the irregular shape of Armstrong Ti powder is conductive to the formation of a continuous interface with sapphire when deposited at sufficiently high velocities. In contrast, with the spray conditions used, SP powder could not form a continuous bond due to the characteristic center interface crack which led to a more brittle failure.

6.7 Acknowledgements

The authors acknowledge the assistance of Dr. Maniya Aghasibeig, Dr. Phuong Vo and Jean-Francois Alarie at the National Research Council Canada for technical support with the cold spray equipment and the contributions of Rene Cooper from Cristal Metals for providing the irregular Ti powder. We also thank Weawkamol Leelapornpisit at the Facility for Electron Microscopy Research of McGill University for help with the FEI Helios NanoLab 660 and Stéphanie Bessette at the McGill Materials Services Electron Microscopy Labs for help with the SU8230. Also, this work was supported by the Natural Science and Engineering Research Council (NSERC) Strategic Grants Program.

Chapter 7

New Insight on Adhesion in Ti/Al_2O_3 Interfaces Created by Cold Spray

Sara I. Imbriglio · Nicolas Brodusch · Boris Nijikovsky · Raynald Gauvin · Richard R. Chromik

This chapter is a manuscript intended for publication. In the previous chapters of this thesis, the experiments performed were targeted towards getting a better understanding of the effect of various process independent variables on adhesion strength at the splat level. However, the mechanisms leading to adhesion remains poorly understood. By use of transmission electron microscopy and scanning transmission electron microscopy, insight regarding the mechanisms leading to adhesion is provided in this chapter. Given the more common use of spherical powder in the cold spray process, spherical powder is used for the analysis. The spherical powder is also sprayed on different orientations of sapphire to investigate the effect of crystal orientation on mechanisms leading to adhesion to further understand the role of heteroepitaxy in the cold spray process.

7.1 Abstract

The mechanisms leading to adhesion between Ti and Al_2O_3 during high-speed impact in the cold spray process are investigated. To determine the role of heteroepitaxy in bond formation, Ti is deposited on three orientations of sapphire. Splat adhesion strength is then measured by the splat adhesion test. Results insinuate that crystal orientation has a minimal effect on bond formation. High-resolution microscopy is used to further understand the effect of severe plastic deformation in microstructural changes leading to adhesion in the Ti/Al_2O_3 interface by use of a rough polycrystalline substrate. Images reveal the formation of an interfacial reaction layer. Imaging combined with energy-dispersive X-ray spectroscopy as well as electron energy loss spectroscopy point towards atomic intermixing in the interaction layer. The interaction layer appears to also have nanosized precipitates forming a new phase.

Keywords cold spray · adhesion · HRTEM · aluminum oxide substrate · titanium powder · metal/ceramic interface

7.2 Introduction

Cold spray is a coating deposition technique by which single micron-sized particles are accelerated to supersonic velocities by a carrier gas flowing through a converging/diverging nozzle. Coating deposition occurs by the high-speed impact of these powder particles onto a substrate [68]. Throughout the whole process, powder particles are generally maintained in their solid state. Adhesion is a result of extreme plastic deformation leading to jetting in the material near the periphery of the powder. Jetting has been demonstrated to be an important factor contributing to adhesion in metal/metal interfaces as it allows the materials to conform and be in intimate contact leading to mechanical interlocking and interatomic bonding [18, 25, 68].

In recent work [196, 207], by use of the splat adhesion test and post-test characterization, the importance of jetting has also been demonstrated for metal/ceramic interfaces by the study of Ti/Al_2O_3 interfaces. For Ti deposited onto Al_2O_3, several conclusions regarding the mechanisms leading to adhesion at the micro-scale were suggested through single particle mechanical tests (i.e., splat adhesion testing). Deposition onto rough substrates shows a significant contribution from mechanical interlocking where failed interfaces showed Ti remaining on the substrate within surface porosity [196, 206]. On smooth substrates, failed interfaces show 'adhesion rings' remaining on the substrate in regions where jetting is prominent. Interestingly, results for spherical Ti powder deposited onto polished polycrystalline substrates (see Figure 4.6 and Figure 4.10) are comparable to those deposited on single crystal sapphire substrates with a (0001) crystallographic orientation (see Figure 4.6). Adhesion on smooth substrates as a result of jetting suggests that a chemico-physical factors contribute to adhesion in the Ti/Al_2O_3 interface [196, 207]. Incomplete adhesion rings observed in the Ti/SiC interface further suggests that the chemical affinity of interfacial elements is critical to adhesion [196]. The abovementioned work only reviews adhesion at the micro-scale and does not address several critical research questions regarding interatomic interaction in the metal/ceramic interface. The microstructural changes which occur during high-speed impact, leading to chemico-physical bonds, remain unclear. Currently, in the literature, only the work by Rafaja et al. [26] addresses interatomic changes which may occur during high-speed impact and which may contribute to adhesion in Ti/Al_2O_3 interfaces. Through high-resolution transmission electron microscopy (HRTEM) imaging of interface cross-sections, these authors suggest that in addition to mechanical interlocking, the dynamic recrystallization accompanying severe plastic deformation allows for an increase in atomic mobility and, in consequence, partial heteroepitaxy (or orientation relationships) at the interface is formed.

In the last decade, there has been a growing interest in metal/ceramic interfaces created by cold spray. These interfaces are investigated for their use in the deposition of metal matrix composite (MMC) coatings with ceramic reinforcements [5] and for ceramic metallization by cold spray [6, 9, 10, 27]. Regarding MMCs with ceramic reinforcements, few have studied the role of chemico-physical factors on adhesion and deposition. For ceramic metallization, following Rafaja et al.'s work, several researchers have continued to investigate chemico-physical bonds formed between

metals and ceramics during high-speed impact [8, 26, 27, 75, 100]. Some suggested methods by which chemico-physical bonds are formed in metal/ceramic interfaces are local heteroepitaxy [8, 26, 27, 75, 100], surface activated bonding [28] and atomic intermixing due to amorphization [133], but no generalized understanding of these interfaces is available to date.

In this work, a new perspective on the mechanisms leading to adhesion in Ti/Al_2O_3 interfaces is described. With heteroepitaxy being frequently identified as present in metal/ceramic interfaces deposited by cold spray, the effect of single crystal orientation of aluminum oxide is investigated at the splat level. Single splats of Ti are deposited on three orientations of sapphire and tested by use of the splat adhesion test. In addition, the potential for the formation of an interaction layer when using a rough polycrystalline substrate is studied by HRTEM, energy-dispersive X-ray spectroscopy (EDS) and electron energy loss spectroscopy (EELS) in the interface.

7.3 Experimental Procedure

To investigate the effect of crystallographic orientation on adhesion strength, single splats of commercially pure Ti powder particles with a spherical morphology are deposited by cold spray (PCS-800, Plasma Giken, Saitama, Japan) onto three orientations of sapphire (Meller optics, Rhode Island, USA and GT Advanced Technologies, Massachusetts, USA) substrates. The surfaces of the single crystal sapphire substrates of 11 mm in diameter and 5 mm thickness have a C-plane (001), A-Plane (110) and R-plane ($1\bar{1}2$) crystallographic orientation. By cold spray, single splats are deposited by use of a 1 m/s gun traverse speed and the lowest possible feed rate. For analysis of the mechanisms leading to adhesion by TEM, a full coating is also deposited onto polycrystalline aluminum oxide. The polycrystalline aluminum oxide substrate is selected in the investigation of adhesion at the nano-scale given its greater potential in cold sprayed metal/ceramic interface. The polycrystalline substrate with a rough morphology more closely resembles the morphology in metal matrix composites with ceramic reinforcements. The as-received polycrystalline aluminum oxide and Ti powder has previously been characterized in [196]. For all cold spray deposits, the initial gas pressure and preheat temperature of nitrogen are maintained at

4 MPa and 400°C. These conditions have been found to be ideal for deposition of Ti on Al_2O_3 [206].

The adhesion strength of single splats is tested by splat adhesion testing [35] on the Micro-Combi Tester (Anton Paar, Graz, Austria) for 15 splats. A detailed description of the splat adhesion test is available elsewhere [35, 36] A semicircular tip of 100 μm in diameter, traveling at a fixed speed of 150 μm/min and a normal force of 70 or 100 mN, is used to scratch and remove single splats from the surface of the substrate while recording the tangential force applied on the tip. The splat adhesion strength is measured (Eq. 7.1) by subtracting the baseline tangential force ($F_{T\ Baseline}$) from the peak tangential force ($F_{T\ Peak}$) and dividing by the projected area measured before each experiment [35].

$$Splat\ Adhesion\ Strength\ [MPa] = \frac{F_{T\ Peak}\ [mN] - F_{T\ Baseline}[mN]}{Projected\ Area\ [\mu m^2]} * 1000 \qquad \text{Eq. 7.1}$$

Analysis of mechanisms leading to adhesion for full Ti coatings deposited by cold spray onto the polycrystalline ceramic substrate requires preparation of a thin cross-sectional TEM lamella at the interface between Ti and Al_2O_3. TEM lamellae are prepared by *in situ* lift-out in a FEI Helios NanoLab 660 electron microscope equipped with focus ion beam milling (FIB) with a Ga ion beam located at the Facility for Electron Microscopy Research at McGill University. Two TEM lamellae are used in this interfacial study. One of the lamellae is sufficiently thin for an EELS analysis of the interface in scanning transmission electron microscopy at 30 kV (SU-9000, Hitachi, Tokyo, Japan). However, this sample has a thin amorphous layer at its surface developed under the effect of the FIB. In consequence this sample rendered blurry HRTEM images. To avoid the formation of an amorphous layer, the methodology suggested by Baram and Kaplan [176] is used in the preparation of a second sample for use in the TEM (Talos, Thermo Scientific, Massachusetts, USA). Analysis in the TEM included both imaging and EDS in scanning transmission electron microscopy mode at 200 kV. However, this sample could not be thinned enough for EELS. The combined results of both samples are included here. TEM image analysis by Fast Fourier

Transforms (FFT) and Bragg filtering of Inverse Fast Fourier Transforms (IFFT) to create a distribution map [208, 209] is done by use of the Digital Micrograph software.

The interface is also studied by interpretation of the energy loss near edge structure (ELNES) found in the EELS spectra. In the scanned interfacial area, some atoms might be unaffected or only partially affected by the presence of the interface causing a significant portion of the spectrum to contain bulk-like characteristics. To extract the interfacial component of the spectrum, a 'spatial difference' method is used [210-218]. By the spatial difference method, EELS spectra must be recorded in the bulk materials and in the interface. In this work, to also identify the location at which changes occur in the material approaching the interface, a line scan of 112.8 nm is used starting in Ti, crossing the interface, and ending in Al_2O_3. The line scan captures 48 EELS spectra at an interspace distance of 2.4 nm. The spatial difference technique is applied only to the Ti ELNES peaks because radiation damage was identified in the Al_2O_3. The O-K edge is known to be particularly susceptible to radiation damage [219]. Radiolysis when using a low electron beam energy is of concern [220]. The bulk signal, taken to be the first spectrum in the line scan, is then subtracted from the 47 remaining EELS spectra (Eq. 7.2) to emphasize interface specific components of the ELNES [211]. Hereafter, the first spectrum is referred to as the reference spectrum. In order to obtain the interfacial specific spectrum intensity (I_{diff}), the reference spectrum is (I_{bulk}) is subtracted from the interface intensity ($I_{Interface}$) as shown in Eq. 7.2. α is a scaling factor for the bulk material intensities [210, 216]. The scaling factor is used due to a difference in bulk atoms contributing to the intensity of the spectrum when recorded in the bulk and in the interface [210, 216].

$$I_{diff} = I_{Interface} - \alpha\, I_{Bulk} \qquad \text{Eq. 7.2}$$

The complexity of this technique stems from determining the scaling factors to be used [210-218]. There are various methods for determining the appropriate scaling factor. Subtraction is completed in accordance with Gu et al. who recommended an orthogonal separation method which involves monitoring the disappearance of a fingerprint feature of the bulk spectrum in the subtraction [221]. The peak intensity of the selected feature is scaled to be equivalent to the interface spectrum

intensity over a narrow range of the energy loss. Rendering the feature component in the spatial difference spectrum null may result in a negative intensity. Therefore, some trial and error is still required. There remains some uncertainty in this technique attributed to the researcher's choice in the fingerprint feature to monitor and in the step size for adjustment. Nevertheless, by this subtraction, changes in peak morphology or overlapping peaks are emphasized [221, 222]. An additional technique has been recommended by Scheu et al. [216] but it requires HRTEM images of the area analyzed in EELS which is not possible on a 30 kV STEM. In consequence the technique proposed by Gu et al. is used here. All EELS data is processed after smoothening the spectra with a Savitzky-Golay method with a 5-point window and a second-order polynomial. Also, the spatial difference spectrum shown have a multiplier of two due to their weak signal after subtraction.

7.4 Results & Discussion

7.4.1 Ti Deposited on Single Crystal Sapphire

In the case of Ti deposited onto Al_2O_3 by cold spray, adhesion tests conducted on single splats show that sapphire orientation has a minimal effect on adhesion strength (Figure 7.1). The results obtained here, at the splat-level, differ from those shown by Drehmann et al. in Al/Al_2O_3 interfaces with different crystal orientations completed at the coating level [223]. These tests are rather difficult to compare given the vastly different nature of the loading conditions. However, results obtained here suggest that near-surface heteroepitaxy may have a less critical role in chemico-physical interaction between Ti and Al_2O_3 when deposited by cold spray.

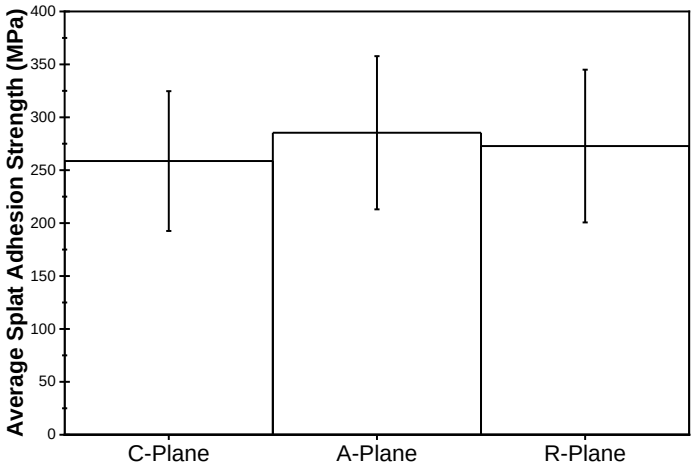

Figure 7.1 Splat adhesion strength of single titanium splats deposited onto single crystal sapphire of C-Plane, A-Plane and R-Plane.

Post-test characterization for all orientations shows that bond formation occurs in the periphery of the splat where jetting occurs. The importance of jetting in metal/ceramic interface was also previously presented by Imbriglio et al. on both polycrystalline smooth substrates and sapphire substrates of a single orientation with two powder morphologies [196, 207]. Jetting is associated with high strain rate viscoplastic deformation causing ultrafine grains near the interface in shear motion relative to the substrate during impact at high pressure [22, 25, 112, 113]. The viscoplastic deformation also generates relatively high temperatures near the interface [18, 21]. The material's behavior in the jetting region is allusive to that found in solids under high-pressure shock compression, accumulative roll-bonding, high-pressure torsion, ball milling and other processes with severe plastic deformation [224]. Interfaces exposed to severe plastic deformation show interesting phenomena including accelerated interdiffusion, atomic intermixing, supersaturated solutions, dissolution of precipitates and amorphization [119-131]. These phenomena may play a significant role in bond formation by high-speed impact during cold spray deposition and have only previously been considered by few [96-99]. The following section further elaborates on the importance of these phenomena.

7.4.2 Ti Deposited on Rough Polycrystalline Al_2O_3

In the case of smooth ceramic substrates, a chemico-physical interaction is the only possible explanation for the high adhesion strengths obtained. Whereas in the case of rough substrates, it is still debated whether adhesion is solely mechanical or whether chemico-physical interactions have a significantly contribution. The abovementioned critical conditions for adhesion are emphasized using a rough substrate where the presence of sharp peaks reduce the contact area causing high-pressure zones and more plastic deformation locally [146]. Surface oxides may remain entrapped on rough substrates, whereas on smooth substrates surface oxides are easily removed from the interface during jetting [92]. Nevertheless, it is necessary to explore the interaction between Ti and polycrystalline rough substrates to further understand the development of metal matrix composites in which specifically oriented and smooth particles of ceramic could not be used. As such, the remaining part of this article focuses on the investigation of Ti/Al_2O_3 interfaces using a rough polycrystalline substrate.

At relatively low magnification, TEM images (Figure 7.2) show a highly heterogeneous interface. In some locations along the interface, one or two interaction layers have been identified. Other locations show no interaction layer between the metal and the ceramic. The cold spray process is highly dynamic and could lead to different pressure, shearing and temperature conditions along the length of the interface. These differences are further emphasized when using a rough substrate due to the localized high-pressure regions. The heterogeneity of the interface may be a consequence of the abovementioned local differences occurring along the interface during impact. The heterogeneity identified within the TEM lamella suggests that, throughout the sample, interfacial mechanisms leading to adhesion may vary significantly. As such, observations are not expected to be found throughout the sample. Adhesion may result from a combination of several mechanisms. While TEM is an effective tool to characterize atomic-scale phenomena leading to adhesion, it can only analyze a very small fraction of the interface at a time; this remains an important limitation to fully characterize the interface produced by a dynamic process like cold spray.

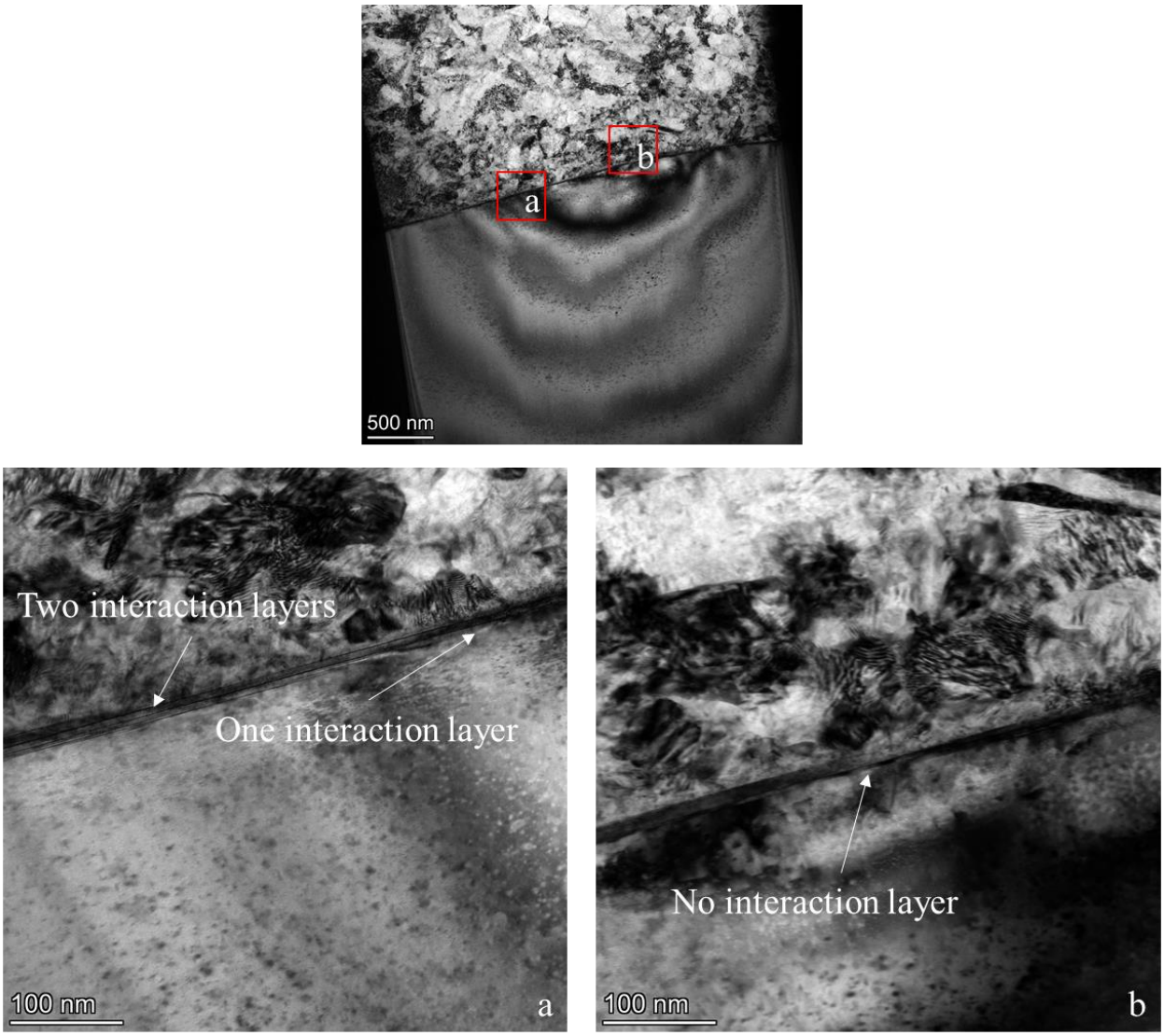

Figure 7.2 TEM images of the interface between Ti and rough polycrystalline Al_2O_3 showing heterogeneity along the interface with two, one or no interaction layers. Higher magnification images correspond to regions identified as (a) and (b).

The region of the interface with no interaction layer spans over about 100 nm. A HRTEM image taken in this section shows nanocrystalline Ti near the interface (Figure 7.3). FFTs taken in a region of interest (ROI) of under 10x10 nm at several regions along the interface, within the Ti, mostly show rings (Figure 7.3 (b) and (d)) indicating that grains are as fine as few nanometers and are not preferentially oriented near the interface. Only in Figure 7.3 (c), a single grain of Ti is

identifiable which spans over approximately 15 nm. Therefore, no specific orientation relationship between the Ti and Al_2O_3 is identified. The small grain size for Ti suggests that if an orientation relationship is formed between the Ti and Al_2O_3, it would be highly localized and not be present along the entire interface.

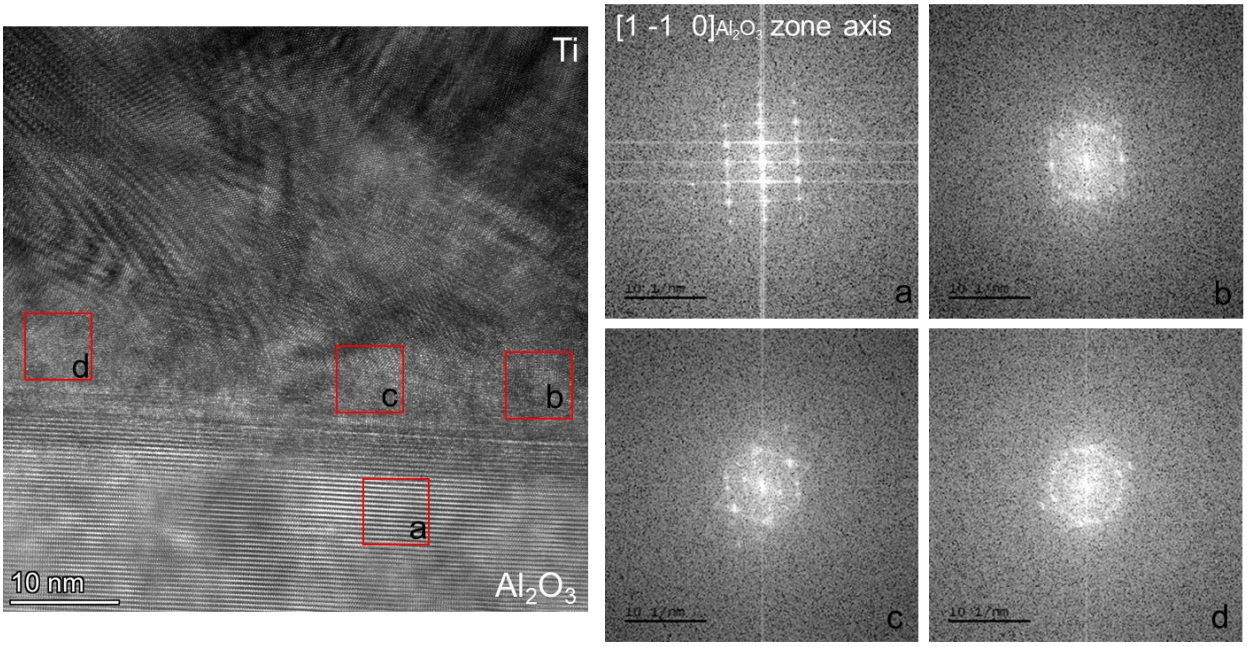

Figure 7.3 HRTEM image focusing on a region with no interaction layer and FFT at four locations along the interface. FFTs correspond to regions identified as (a), (b), (c) and (d).

Of interest is the apparent interaction layer spanning along most of the interface. Figure 7.4 includes a HRTEM image showing the end of a region with two interaction layers leading into a region with one interaction layer. FFTs are taken within the Al_2O_3 (Figure 7.4 (a)) and within each interaction layer (Figure 7.4 (b) and (c)). The FFT taken in the Al_2O_3 is indexed to the [1 $\bar{1}$ 0] zone axis. While the Al_2O_3 substrate is polycrystalline, grains are large, allowing the 3 µm wide cross-section to be within a single grain.

Regarding the interaction layers, the FFT taken in the second interaction layer is very similar to that of Al_2O_3 with minor evidence of additional spatial frequencies identified by arrows in Figure 7.4 (b). The additional spatial frequencies are too weak to characterize. In the first

interaction layer, which spans over a large fraction of the interface, the FFT shows three columns of spatial frequencies originating from the Al_2O_3 planes superimposed on an additional four columns (identified by arrows in Figure 7.4 (c)) of spatial frequencies which may be originating from a new phase. There is a clear orientation relationship between Al_2O_3, and the additional phase or phases present in the interface. A possible explanation for the presence of multiple phases within an FFT is the formation of nanoscale precipitates in the aluminum oxide matrix. Nanoscale precipitates within a matrix have previously been identified as a superimposed signal in an FFT [208].

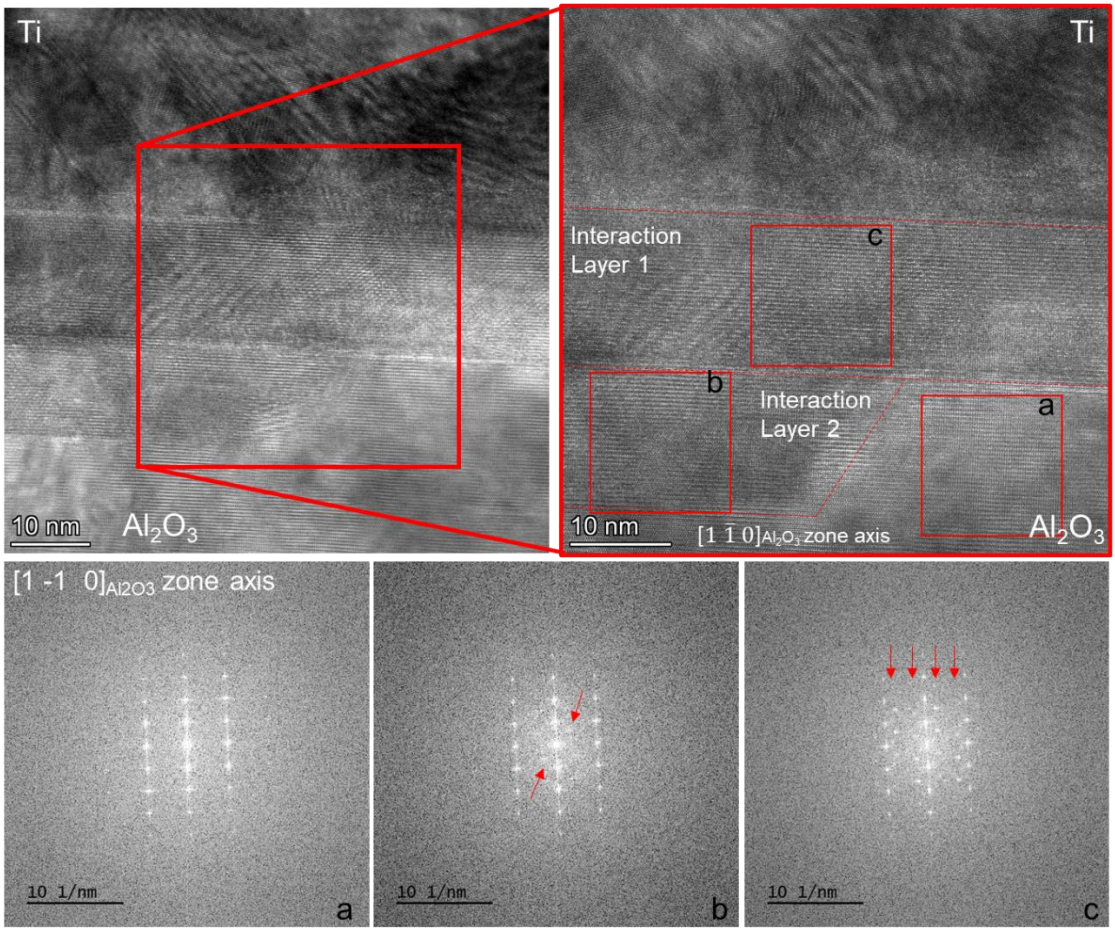

Figure 7.4 HRTEM image focusing on a region at the end of two interaction layers. Half of the image shows a region with a two interaction layers and the other half shows one interaction layer. Interaction layers have been clearly identified by dashed lines. FFTs correspond to regions identified as (a), (b) and (c).

To ensure that the spatial frequencies identified in the first interaction layer are not artifacts and are truly representative of a new phase formed near the interface, a diffraction pattern at the interface is also captured and shown in Figure 7.5. It must be noted that the diffraction pattern captured in the TEM is not at the same scale as used for the FFT. The area analyzed in the diffraction pattern is significantly larger. Therefore, there is signal from Al_2O_3, Ti and from the interaction layer. The signal from the additional phase is weak since it is originating from only a small fraction of the analyzed area and, as will be discussed later, the additional phase is highly localized. Nevertheless, the weak signal identified by arrows in Figure 7.5 is similar to that found in the FFT shown in Figure 7.4 (c).

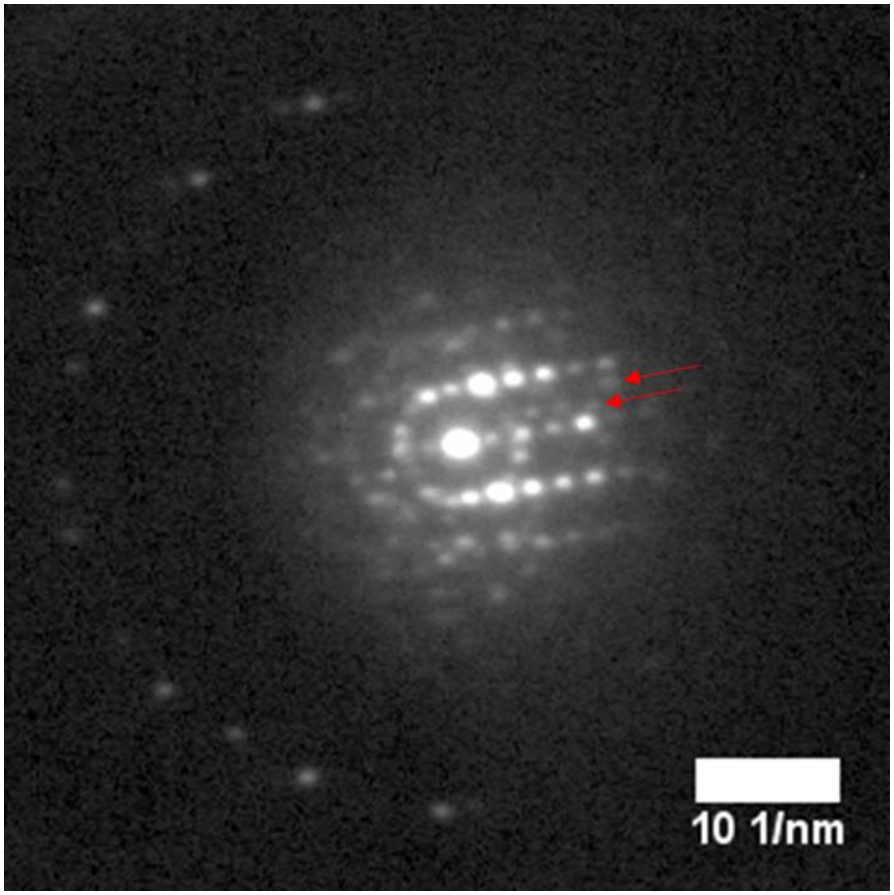

Figure 7.5 Interfacial diffraction pattern with new phase comparable to that shown in the FFT identified.

To further understand the composition of the first interaction layer and possible phases present, EDS elemental mapping in STEM is used (Figure 7.6). The EDS elemental map taken in a region with one interaction layer between Ti and Al_2O_3 confirms atomic intermixing or diffusion. The area corresponding to the first interaction layer in HRTEM images (Figure 7.6) is composed of Al, Ti and O atoms. The phases appearing within the FFT in the interaction layer may correspond to nanoscale clusters of a new compound formed to reduce the interface energy [208]. Given the short contact time in the cold spray process these clusters would not have the time to grow and would remain unevenly distributed within the interaction layer. As such, the EDS signal may consist of a combination of all phases present for which the concentration remains unknown. Therefore, results are qualitative and cannot be used to identify the interfacial compound. Furthermore, in STEM, damage under the effect of the electron beam is of particular concern for oxygen and may contribute to discrepancies in the atomic fraction identified [219].

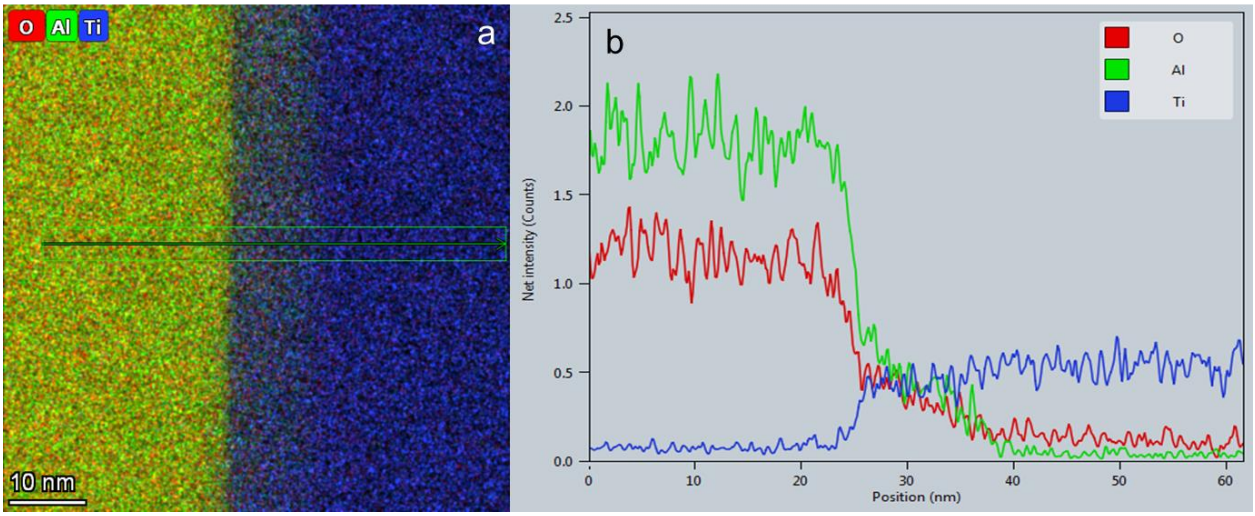

Figure 7.6 EDS results captures by STEM along the interface in a region with one interaction layer. (a) Color mix image of the interface based on EDS data showing where the line scan was captured. (b) The net intensity along the line scan showing that the interaction layer is composed of Al, Ti and O atoms.

Further investigation of the HRTEM images (Figure 7.7), within the interaction layer, reveals local differences in the crystal structure (Figure 7.7 (b)). These local differences further point towards the formation of precipitates in the Al_2O_3 matrix. As identified in Figure 7.7 (e), regions with a

locally different structure are also associated with FFTs including the additional spatial frequencies found through the interaction layer (Figure 7.4 (c)).

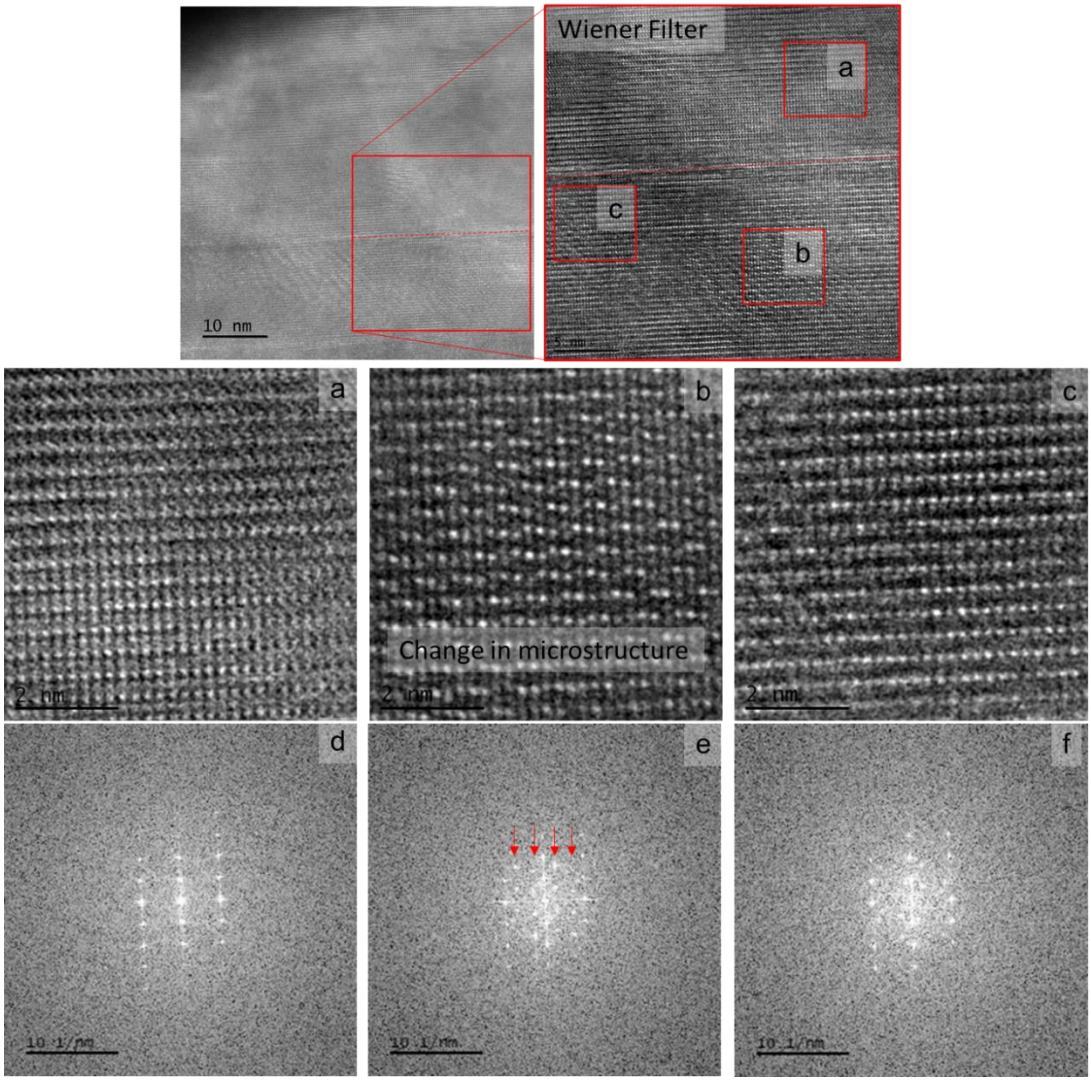

Figure 7.7 Identification of potential precipitates within the interaction layer. FFTs for specific regions (a), (b) and (c) with their respective FFTs identified in (d), (e) and (f) in the image are shown as well as a higher magnification image of that section. The microstructure appears to be different in regions where additional points appear in the FFT (b). A Weiner filter has been applied to reduce noise in the image.

Bragg filtering, using different masks in the FFTs, identified the part of the image from which a majority of the periodicity rendering spatial frequencies in the FFT are located. Local differences

identified in the IFFT are colored and superimposed onto the HRTEM image (Figure 7.8 (b), (d) and (e)) to emphasize the local distribution of precipitates within the matrix. The periodicity associated with the new phase is different than that of Al_2O_3 as compared in Figure 7.8 (c) and (f). Unfortunately, the particular phase could not be indexed with current available databases. It may be a metastable or nonstoichiometric phase formed under non-equilibrium conditions due to the severe plastic deformation. In addition, the new phase may not be in zone axis making it unindexable. EELS data is used to get a preliminary understanding of the phase (Figure 7.9).

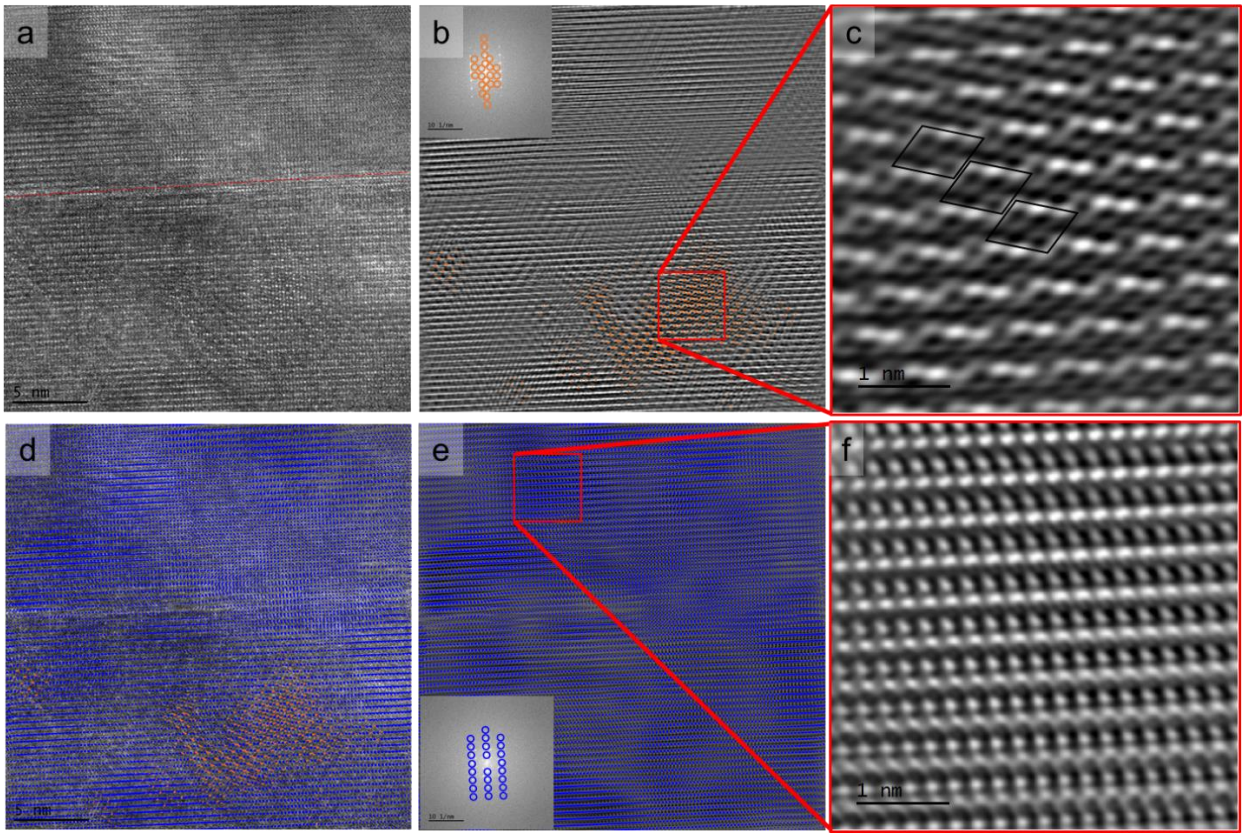

Figure 7.8 IFFT using Bragg filters to identify the precipitates rendering specific signals in the FFT of (a). In (b), the secondary phase signal is masked; the colored region identifies the part in the image where the majority of the periodicity observed the FFT originates. A higher magnification image of this region is provided in (c). Similarly, in (e), a mask was placed on the spatial frequency identified as Al_2O_3 in the FFT highlighting the crystal structure magnified in (f). (d) shows a superimposition of the colored regions in (b) and (e) onto the original image (a).

The Ti peak in the reference EELS spectrum correlates with the position of a Ti peak at 455.5 eV [225]. The 20th spectrum shows a broadening of the peak which persists until the 26th spectrum. The 27th spectrum has minimum signal from Ti indicating that the electron beam has crossed into Al_2O_3. The peak broadening is investigated by the spatial difference technique (Figure 7.9 (c)). Following subtraction, spectra 1 to 19 only show noise with no appearance of a peak. As of the 20th spectrum, a new peak is revealed which appears in spectra 20 to 26. Using spectrum 20 as an example, a closer look into the peak revealed by the spatial difference technique in comparison to the reference spectrum shows a clear peak shift (Figure 7.9 (d)). A higher energy peak shift is characteristic of the formation of a titanium oxide or charge transfer between Ti and the O atoms within the Al_2O_3 as previously reported by Scheu et al. [219]. Given the difficulty in matching the peaks in the FFT with any known titanium oxide, the EELS data may point towards the formation of a metastable titanium oxide, a ternary oxide of Al, Ti and O or a titanium aluminide. Further characterization is required to identify this phase, but these results suggest the presence of an interfacial reaction layer of approximately 15 nm which corroborates well with HRTEM observations. A line scan was also repeated at another location on the sample (not shown here). The peak shift occurred closer to the interface at about 3 nm. These results correlate with the observed heterogeneity near the interface in HRTEM images.

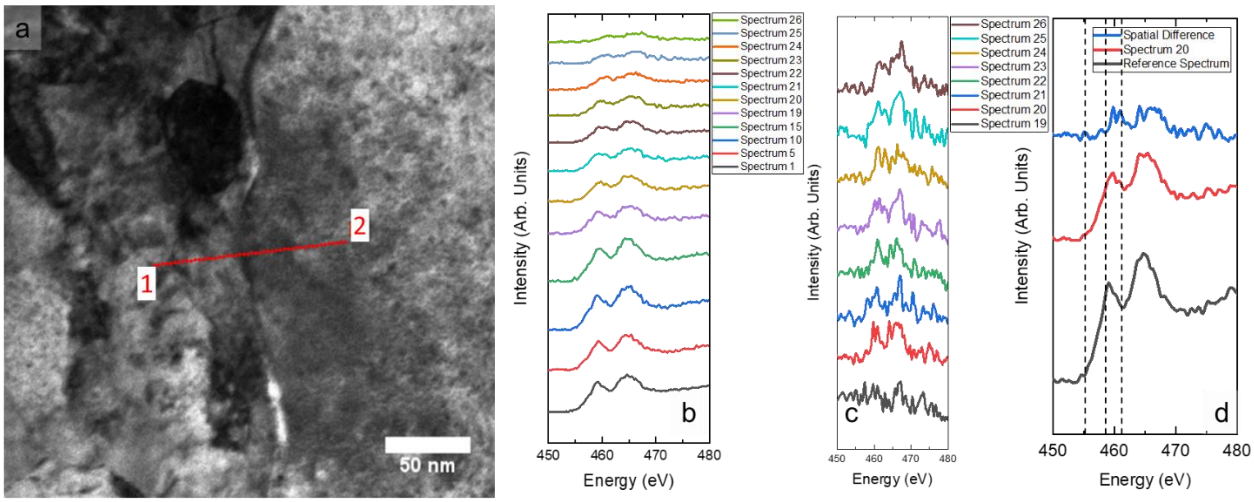

Figure 7.9 EELS data captured along a line scan for which the location is shown in (a). The Ti peak of the EELS spectra is emphasized in (b) on which the spatial difference technique was applied to reveal the newly formed shifted peak in spectra 20 to 26 as shown in (c). The peak shift is emphasized and compared to the reference spectrum in (d).

The process by which an interaction layer can be formed during severe plastic deformation remains unclear. Nevertheless, this is not the first observation of an interaction layer formed by cold spray [96-99]. Interdiffusion is often overlooked given the speed of impact; diffusion rates are considered too slow [21, 97, 109]. However, diffusion rates available in databases do not consider effects occurring under severe plastic deformation. Defect-enhanced solid-state diffusion can cause a drastic increase in the diffusion rate. It has been demonstrated that during severe plastic deformation, diffusion rates are significantly accelerated due to increased atomic mobility [110]. Atomic mobility increases during plastic deformation due to boundary diffusion, lattice diffusion and dislocation assisted lattice diffusion. Furthermore, the associated grain refinement by dynamic recrystallization reduces atomic transport distance [111]. Diffusion time scales with the square of the transport distance rendering significantly higher diffusion rates as grain size decreases. Furthermore, plastic deformation is also associated with an increase in temperature accompanied with vacancy generation which further enhance atomic mobility. For ceramics, dislocations may not be mobile but they contribute to diffusion by the formation of sources and sinks of vacancies or by providing a path for diffusion [111].

In addition to accelerated diffusion rates, some have observed dynamic amorphization which leads to atomic intermixing [97, 99, 132-134]. Dynamic amorphization is also seen in other methods causing severe plastic deformation [121, 123, 124, 126]. Local amorphization may occur to accommodate the high stress accumulated as a result of a large dislocation density caused by plastic deformation, or may occur as a consequence of excessive lattice distortion due to interdiffusion [97, 119]. In the Ti/Al_2O_3 interface studied here, no amorphous region is visible. An amorphous region may not be identified due to crystallization under the effect of temperature [99]. For ceramics, heat localization is more prominent given their insulating properties, therefore, crystallization, which is thermally activated, may be more pronounced and could lead to the formation of crystalline metastable precipitates.

7.5 Conclusion

The deposition of single powder particles onto three orientations of sapphire showed that adhesion strength and well-adhering regions of the interface are uninfluenced by crystallographic orientation. As such, it is suggested that heteroepitaxy is likely highly localized and is of secondary importance in bond formation. Rather, non-equilibrium phenomena occurring through severe plastic deformation appear to contribute to bonding. These phenomena were further investigated by use of EDS and HRTEM imaging within the TEM as well as EELS in a 30 kV STEM in Ti/Al_2O_3 interfaces using a polycrystalline substrate. The EDS data confirmed that the interaction layer observed in HRTEM was composed of a mixture of Ti, Al and O. The Ti peak in the EELS spectra showed a peak shift as revealed by the spatial difference technique. This peak shift demonstrates a change in local bond state which can be associated with the formation of an oxide. By Bragg filtering of the HRTEM images, it was also possible to identify the location and periodicity associated with the crystal structure of the additional phase present in the interaction layer. The abovementioned data all points towards the formation of a secondary phase in the reaction layer. These oxide phases may occur due to atomic intermixing as a consequence of amorphization or diffusion. High temperatures after impact may also lead to crystallization.

However, these observations cannot be generalized for a full cold sprayed metal/ceramic interface due to sample heterogeneity.

7.6 Acknowledgements

The authors acknowledge the assistance of Dr. Maniya Aghasibeig, Dr. Phuong Vo and Jean-Francois Alarie at the National Research Council Canada for technical support with the cold spray equipment. At McGill university, Weawkamol Leelapornpisit at the Facility for Electron Microscopy Research of McGill University must be highlighted for all FIB work. Furthermore, Prof. Christina Scheu, Prof. Wayne D. Kaplan and Priyadrashini Ghosh provided guidance in sample preparation and data analysis. Also, this work was supported by the Natural Science and Engineering Research Council (NSERC) Strategic Grants Program.

Chapter 8

Concluding Remarks

8.1 Global Discussion

Chapters 4, 5 and 6 investigate the effect of various process independent variables on deposition. In early work (Chapter 4), Al_2O_3 and SiC were compared in terms of their adhesion strength along with the effect of surface roughness. For the Ti/Al_2O_3 interfaces, the role of powder velocity on adhesion in addition to surface morphology was investigated (Chapter 5). The effect of powder morphology was then discussed (Chapter 6). Nanoscopic chemico-physical factors contributing to adhesion were subsequently studied (Chapter 7). Each chapter was written as a standalone manuscript. Some interconnections have not been elaborated on and, as such, are included here. For instance, the comparison of Al_2O_3 and SiC interfacing with Ti was not further pursued beyond Chapter 4 due to a significantly stronger bond strength between Ti and Al_2O_3 which became the focus of this thesis. Nevertheless, the knowledge acquired on the Ti/Al_2O_3 interface can be applied to the Ti/SiC interface to better understand the significant difference in bond strength obtained as will be addressed in Section 8.1.1. In addition, recommendations are summarized for the deposition of strong metal/ceramic interfaces in Section 8.1.2.

8.1.1 The Ti/Al_2O_3 Interface Compared to the Ti/SiC

The splat adhesion strength of Ti splats deposited onto SiC rendered a significantly lower bond strength than those deposited on Al_2O_3 with any surface roughness. It had been found that several splats rebounded in the process of depositing onto SiC and in consequence it was not possible to identify the exact location of splats that had been tested by splat adhesion testing. The analysis of Ti remaining on the substrate in regions that were either tested or that had rebounded revealed Ti in the shape of a ring allusive to adhesion rings observed in Ti/Al_2O_3 interface. Therefore, the conditions of high shear, high pressure and high temperature remain of great importance for the Ti/SiC interface. The comparison was made under the same spray conditions, which begs the following questions:

> Would different spray conditions have assisted in the formation of a stronger bond in the Ti/SiC interface?
>
> Is the effect of material properties on critical velocity as prominent in metal/ceramic interfaces as it is in metal/metal interfaces?

LIPIT experiments were also conducted in the Ti/SiC interface. Results were presented in Section 3.2.1 (Figure 3.7). Particles begin adhering to the SiC substrate at 802 m/s. That is a velocity of 1.4 times greater than the initial deposition velocity recorded for the Ti/Al_2O_3 interface of 580 m/s. These results demonstrate that critical velocity is dependent on the specific interface of interest. However, velocity is not the sole critical factor.

The results obtained for the Ti/Al_2O_3 interface in Chapter 5 demonstrated that an increase in velocity beyond the critical velocity is detrimental to the adhesion strength. Beyond the critical velocity, higher velocity causes an increase rebound energy [84] and fracture in the ceramic substrate. However, for deposition of Ti onto SiC, the abovementioned factors are likely of significant importance at deposition considering the high critical velocity.

The spray conditions for SiC used in Chapter 4 (4 MPa, 800°C, standard nozzle) are associated with a powder velocity of 692 ± 133 m/s, as reported in Table 5.1. The critical velocity for deposition onto SiC (802 m/s) approaches the upper limit of this velocity range. This comparison

of spray conditions and critical velocity provides an explanation for the large number of rebounded splats which likely impacted below critical velocity and left traces of Ti on the substrate, as identified in BSE images. The deposited powder particles are likely impacting at velocities corresponding to, or just above critical velocity. Per observations on Ti/Al_2O_3 interface, these powder particles are likely depositing at near-ideal velocity for deposition. Nevertheless, measured splat adhesion strength for Ti/SiC interface was low further suggesting that there is likely also a chemico-physical factor contributing to the low splat adhesion strength in this interface.

A possible explanation for the difference in critical velocity, when comparing Al_2O_3 and SiC, could be their differing Hugoniot Elastic Limits (HEL). In shock compression of solids, the HEL is defined as the point at which a solid under shock loading transitions from elastic to elastic-plastic deformation, showing a fluid-like flow of material [226]. Evidence of jetting in the metal indicates that the metal has reached its HEL. For the ceramic, to accommodate the formation of an intermixed reaction layer with nanoscale precipitates of a new phase, as reported in Chapter 7, there is likely plastic deformation. The HEL is significantly higher for SiC than Al_2O_3 which may explain why higher velocities are required to allow for adhesion in the Ti/SiC interface [227].

8.1.2 Cold Spray of Metal/Ceramic Interfaces

The effects of independent variables found within this thesis can be combined to better understand how to optimally deposit metal/ceramic interfaces by cold spray. In both the deposition of MMCs and ceramic metallization, the ideal spray conditions for the particular interface must be identified. Frequently, different metal/ceramic combinations are compared by use of identical spray conditions [100, 196]. As discussed in Chapter 4 and further elaborated in the previous section, each material combination has a critical velocity for deposition which must be reached. In the deposition of Ti/SiC interfaces, higher velocities would have been required to get a higher splat density. A higher splat density is necessary to ensure the deposition of a full coating. Furthermore, some metal/ceramic interfaces, such as the Ti/SiC interface, may never render a high adhesion strength given the importance of chemico-physical factors contributing to adhesion. Chemico-physical factors also play a role when depositing metal coatings on rough ceramic substrate as demonstrated in Chapter 7. Therefore, these chemico-physical factors are likely present in MMCs

as well, although they are generally not considered. As such, particular attention should be given to the material combinations used. Due to a weak chemical affinity, some ceramics may always have a weak adhesion strength and therefore may render very low ceramic retention in MMCs. The benefits of having even a small quantity of a particular ceramic must be outweighed with respect to its weak adhesion and low deposition efficiency. Otherwise, a ceramic with a better chemical affinity should be selected. What renders better chemical affinity in metal/ceramic interfaces deposited by high-speed impact remains unknown and should be addressed in future work.

Furthermore, results presented in Chapter 6, show an advantage of using powder with a coral-like morphology. The coral-like morphology resembles that of depositing smaller powder particles. These results insinuate that smaller powder particles would experience more tamping during the deposition of a full coating and therefore close interfacial gaps. The closure of interfacial gaps is particularly important when depositing metal/ceramic interfaces due to the limited deformation experienced in the ceramic which does not conform to the shape of the metal particle. It must be noted that the powder particles should not be so small that jetting is not possible. A minimum critical powder size was defined by Schmidt et al. [22].

Regarding surface roughness, in MMCs, where interfaces with a flat smooth ceramic could not be deposited, it would likely be best to increase the surface roughness of the ceramic powder used. That is, use irregularly shaped ceramic powder with high surface porosity. The surface porosity must be accompanied by peaks along the surface to enhance deformation in these highly stressed regions of the interfacing metal powder. Concerning surface roughness, spacing between peaks and valleys must be smaller than the diameter of the metal powder particle to ensure interpenetration [153] causing a combined mechanical and chemico-physical bond. On the other hand, for ceramic metallization, there is an advantage in depositing coatings on smooth substrates, particularly for the Ti/Al_2O_3 interface given the higher bond strength measured on the smooth substrate in comparison to the rougher substrates (Figure 4.6). When metalizing a ceramic with a lower chemical affinity, like SiC, it is rather advantageous to use a rough substrate and promote mechanical clamping. Once again, the surface roughness must be finer than the size of the powder [153].

8.2 Summary and Conclusions

The deposition of metal/ceramic interfaces created by cold spray was mostly investigated by use of a splat adhesion test with post-test characterization. Post-test characterization of the amount and morphology of the Ti remaining on the substrate revealed information regarding the bonding mechanism. Various process independent variables including type of ceramic, powder and substrate morphology, velocity, gas temperature and gas pressure were addressed by verifying their effect on splat adhesion. The objective was to gain a better understanding of these interfaces for use in metal matrix composites and investigate the feasibility of using the cold spray process for ceramic metallization. The bonding mechanism was also further investigated by high-resolution microscopy and spectroscopy.

The splat adhesion of Ti powder particles deposited onto SiC was significantly weaker than when deposited on Al_2O_3, even when the Al_2O_3 substrate was polished to a comparable surface roughness. Deposition of single splats onto Al_2O_3 showed the formation of a complete and continuous adhesion ring while deposition onto SiC showed a fragmented adhesion ring with micro-cracking throughout the interface. These results demonstrated that the type of ceramic used has an influence on the adhesion strength. In consequence, it was concluded that bonding has a chemico-physical component in addition to the mechanical component. Given the weak bonding between Ti and SiC, the remaining part of the thesis focused on the Ti/Al_2O_3 interface which rendered particularly interesting results.

The effect of surface roughness (i.e., substrate morphology) was addressed by depositing single particles on Al_2O_3 substrates with three values of surface roughness as defined by their reduced peak height values (R_{pk} = 0.78, 0.33 and 0.16 µm). Post-test characterization revealed that the bonding mechanism varies greatly when transitioning between the lowest surface roughness to the highest surface roughness. The substrate with the highest surface roughness showed a bonding mechanism which is primarily influenced by mechanical bonding with Ti penetrating into surface porosity. Nevertheless, TEM results obtained later demonstrated that this was in fact a mixed mode bonding mechanism as an interaction layer was formed despite the high surface roughness. The deposition onto the smoothest substrate shows a primarily chemico-physical bond occurring in the

periphery of the splat. Deposition resulted in adhesion rings. It must be noted that smooth substrates still had a high level of porosity. The porosity greatly influenced adhesion. Large pores showed Ti bonding in comparatively smooth regions while finer pores had minimal Ti on the surface. Without the presence of peaks along the surface as found in the high surface roughness substrates, there was no high stress regions to help in deformation and penetration into surface porosity.

Critical velocity for deposition was then investigated by the combined use of the LIPIT technique and cold spray. Critical velocity was identified for the Ti/Al_2O_3 interface to be 580-620 m/s by the LIPIT technique. To further investigate the effect of velocity beyond the critical velocity, the cold spray process was used. Flattening ratio was used to monitor the effect of velocity in the deposited particle given a direct correlation with velocity. The flattening ratio was then used as a relative velocity between particles which showed that an increase in velocity resulted in a decrease in adhesion strength given the rebound phenomenon and fracturing of the ceramic. By cold spray, however, it is not possible to dissociate velocity from gas preheat temperature and initial pressure. Through an analysis comparing similar powder velocities achieved with the standard nozzle and a long nozzle geometry, which requires less heat to accelerate powder particles to higher velocities, it was found that gas preheat temperature does not greatly influence the deformation behaviour.

Given large standard deviations when measuring velocity in the cold spray system, knowing the velocity of individual powder particles by LIPIT also allowed for a more thorough analysis of the effect of local substrate heterogeneity. Deposition on a granular substrate with peaks and valleys finer than the size of the powder particles promote deformation and adhesion.

The effect of powder morphology was also considered by deposition onto a smooth single crystal sapphire substrate. Splat adhesion strength of spherical powder was compared to irregularly shaped powder with a coral-like morphology deposited under two spray conditions. The different spray conditions allowed for the effect of velocity to be considered for both powder morphologies. The transparent nature of the single crystal sapphire substrate allowed for *in situ* splat adhesion testing by which the failure mechanism for each splat morphology was clarified. Spherical powder formed adhesion rings as was previously seen on smooth polycrystalline Al_2O_3 substrate. These adhesion rings form due to a geometric limitation preventing angled contact near the south pole of the splat.

Spherical powder consistently failed by spreading of this center interface crack. These adhesion rings were also formed locally in powder with a coral-like morphology when deposited at lower velocity, which caused very low adhesion strength. An increase in velocity for the powder with a coral-like morphology allowed for internal tamping which formed a well bonded and continuous interface. The interesting morphology of the coral-like powder was therefore advantageous to bond formation.

The abovementioned work allowed for an understanding of bond formation at the microscale, but local microstructural changes at the nanoscale leading to adhesion remained unclear. To investigate the role of local heteroepitaxy in bond formation, spherical powder was deposited on different crystallographic orientations of sapphire to determine the effect on splat adhesion strength. The splat adhesion strength was unaffected by substrate crystallographic orientations, indicating that heteroepitaxy may not significantly contribute to adhesion. The bonding mechanism in a Ti/Al_2O_3 interface was further analyzed using rough polycrystalline substrates. EDS, HRTEM and EELS results pointed towards the formation of an interaction layer as a consequence of severe plastic deformation with either diffusion or atomic intermixing due to amorphization leading to the formation of nanoscale precipitates inside the Al_2O_3 matrix at the interface. The peak shift identified in the Ti EELS spectrum near the interface shows that these nanoscale precipitates are likely a form of Ti oxide, Ti, Al ternary oxide or Ti aluminide. Crystallization of the new phase may be a result of the high temperature localized near the interface in the moments after deposition given the nonconductive nature of the ceramic.

8.3 Contribution to Original Knowledge

1. The splat adhesion test was first introduced in 2010 and had only ever been used for metal/metal interfaces. The work presented in this thesis is the first instance in which the splat adhesion test was used for metal/ceramic interfaces. These tests allowed for new conclusions

regarding bond formation in metal/ceramic interfaces which could not be studied through the deposition of full coatings. For instance:

1.1. The importance of jetting and ASI was identified, for the first time, to highly influence bond formation in Ti/Al_2O_3 and Ti/SiC interfaces.

1.2. The importance of chemico-physical factors contributing to adhesion was also identified for the first time in the comparison between Ti/Al_2O_3 and Ti/SiC interfaces where the use of a SiC substrate resulted in significant rebounding and an interface which was not continuous while deposition onto Al_2O_3 resulted in a continuous well adhering adhesion ring.

1.3. Splat adhesion testing also revealed the effect of substrate surface roughness on bond formation in metal/ceramic interfaces. The effect of local changes in substrate morphology on the rougher substrates was also investigated for particles with a known velocity.

1.4. The effect of crystallographic orientation at the splat level in the Ti/Al_2O_3 interface was studied for the first time and further confirmed the importance of jetting and ASI in bond formation with crystallographic orientation being of secondary importance.

1.5. The effect of an increase in velocity beyond the critical velocity on the deposition of Ti/Al_2O_3 interface was also identified at the splat level.

2. The LIPIT technique was applied to metal/ceramic interfaces for the first time and by use of this testing methodology, it was possible to identify the critical velocity for deposition of Ti on Al_2O_3.
3. The LIPIT technique showed a direct correlation between velocity and flattening ratio for particles deposited at the splat level. For the first time, the use of flattening ratio as a relative velocity between individually deposited splats was proposed.
4. The advantages of using powder with a coral-like morphology as manufactured by the Armstrong process was investigated for the first time on a ceramic substrate. Results revealed that the specifically engineered powder morphology has a geometric advantage as compared to spherical powder since additional interfacial shearing could be achieved when deposited at

sufficiently high velocities due to tamping. Tamping therefore allows for a continuous interface which could not be achieved with spherical powder at the splat level. In this analysis, an *in situ* version of the splat adhesion test was also used for the first time which allowed for a better understanding of the testing methodology.

5. High resolution transmission electron microscopy was used to investigate bonding mechanism in the Ti/Al_2O_3 interface revealing, for the first time, an interfacial interaction layer contributing to bond formation which allows for new insight regarding the bonding mechanism.

8.4 Suggestions and Future Work

1. The work conducted in this thesis was fundamental to gain a better understanding of bond formation. However, to render these results useful in an industrial application, particularly for ceramic metallization, the deposition of full coatings should be studied and analyzed. From the findings shown in this thesis, the velocity required to get good adhesion between the metal and the ceramic is lower than that required to deposit Ti onto Ti. Therefore, full coatings deposited with spherical powder will likely be very porous. The use of the Armstrong powder may be beneficial for full coatings.
2. In the global discussion, the potential importance of the HEL of the ceramic was proposed to understand the large difference in critical velocity when comparing deposition of Ti on Al_2O_3 and SiC. To further elaborate on this concept, the critical velocity for deposition onto other ceramics should be determined and compared to the HEL. In addition, the study of other metals should be investigated to determine the importance of metal material properties on deposition. These results would help in creating a generalized parameter window for deposition of metal/ceramic interfaces.
3. It was mentioned that Ti likely has a chemical affinity for bond formation in the interface with Al_2O_3, creating a continuous interface which could not be obtained in the interface with SiC. To further understand concepts such as chemical affinity, diffusion, atomic intermixing, amorphization and recrystallization and their contribution to bond formation,

molecular dynamic simulations should be used for the study of cold sprayed metal/ceramic interfaces.

4. Some recommendations based on the current knowledge of metal/ceramic interfaces were proposed in the global discussion for deposition of MMCs and ceramic metallization. Possible solutions included the use of highly porous ceramic powder with large peaks and valleys and the use of high substrate surface roughness in the deposition of Ti on SiC or other metal/ceramic interfaces with a low chemical affinity. Some work would be required to investigate these possible solutions for deposition in full coatings.
5. In Chapter 7, per splat adhesion testing, it was stated that crystallographic orientation appears to have a minimal effect on bond formation. It would be interesting to investigate a region of the interface within the adhesion ring by TEM for each crystallographic orientation to better understand the link between jetting and bond formation and how specific crystallographic orientations may or may not play a role in adhesion. Smooth sapphire substrates would also reduce the level of heterogeneity throughout the sample, which may help in gaining a more generalized understanding of metal/ceramic interfaces created by cold spray.
6. In Chapter 7, an interfacial interaction layer was found. A second phase was formed in the form of nanoscale precipitates. It was not possible to index this phase. Atom probe tomography or density function theory may be useful in further characterizing this phase.

Bibliography

[1] M.M. Schwartz, Ceramic joining, ASM International, Materials Park, Ohio, 1990.

[2] B. Basu, K. Balani, Advanced structural ceramics, Wiley, New Jersey, 2011.

[3] P. Kumar, V.A. Greenhut, Metal-ceramic joining, Minerals, Metals & Materials Society, Pennsylvania, 1991.

[4] M.G. Nicholas, Joining of ceramics, first ed., Chapman and Hall, London, 1990.

[5] R.R. Chromik, S.A. Alidokht, J.M. Shockley, Y. Zhang, Tribological coatings prepared by cold spray, in: P. Cavaliere (Ed.), Cold-spray coatings: recent trends and future perspectives, Springer International Publishing, Cham, 2018, pp. 321-348.

[6] K.-R. Donner, F. Gaertner, T. Klassen, Metallization of thin Al_2O_3 layers in power electronics using cold gas spraying, J. Therm. Spray Technol., 20 (2011) 299-306.

[7] D. Dietrich, B. Wielage, T. Lampke, T. Grund, S. Kümmel, Evolution of microstructure of cold-spray aluminum coatings on Al_2O_3 substrates, Adv. Eng. Mater., 14 (2012) 275-278.

[8] R. Drehmann, T. Grund, T. Lampke, B. Wielage, K. Manygoats, T. Schucknecht, D. Rafaja, Interface characterization and bonding mechanisms of cold gas-sprayed Al coatings on ceramic substrates, J. Therm. Spray Technol., 24 (2015) 92-99.

[9] B. Wielage, T. Grund, C. Rupprecht, S. Kuemmel, New method for producing power electronic circuit boards by cold-gas spraying and investigation of adhesion mechanisms, Surf. Coat. Technol, 205 (2010) 1115-1118.

[10] K.R. Ernst, J. Braeutigam, F. Gaertner, T. Klassen, Effect of substrate temperature on cold-gas-sprayed coatings on ceramic substrates, J. Therm. Spray Technol., 22 (2013) 422-432.

[11] M. Floyd, D. Raybould, D. Troller, Cold gas-dynamic spraying method for joining ceramic and metallic articles, US 2007/0215677 A1, 2007.

[12] P.C. King, S. Zahiri, M. Jahedi, J. Friend, Aluminium coating of lead zirconate titanate—a study of cold spray variables, Surf. Coat. Technol, 205 (2010) 2016-2022.

[13] P.C. King, S.H. Zahiri, M. Jahedi, J. Friend, Cold spray electroding of piezoelectric ceramic, Mater. Forum, 31 (2007) 116-119.

[14] I. Botef, J. Villafuerte, Overview, in: J. Villafuerte (Ed.), Modern cold spray: materials, process, and applications, Springer International Publishing, Cham, 2015, pp. 1-29.

[15] V.K. Champagne, 1 - Introduction, in: V.K. Champagne (Ed.), The cold spray materials deposition process, Woodhead, Cambridge, 2007, pp. 1-7.

[16] P. King, M. Yandouzi, B. Jodoin, The physics of cold spray, in: J. Villafuerte (Ed.), Modern cold spray: materials, process, and applications, Springer International Publishing, Cham, 2015, pp. 31-72.

[17] A. Papyrin, V. Kosarev, S. Klinkov, A. Alkimov, V. Fomin, Chapter 1 - Discovery of the cold spray phenomenon and its basic features, in: A. Papyrin, V. Kosarev, S. Klinkov, A. Alkimov, V. Fomin (Eds.), Cold Spray Technology, Elsevier, Amsterdam, 2007, pp. 1-32.

[18] H. Assadi, F. Gärtner, T. Stoltenhoff, H. Kreye, Bonding mechanism in cold gas spraying, Acta Mater., 51 (2003) 4379-4394.

[19] H. Assadi, T. Schmidt, H. Richter, J.O. Kliemann, K. Binder, F. Gartner, T. Klassen, H. Kreye, On parameter selection in cold spraying, J. Therm. Spray Technol., 20 (2011) 1161-1176.

[20] V.K. Champagne, The cold spray materials deposition process fundamentals and applications, Woodhead, Cambridge, 2007.

[21] M. Grujicic, C.L. Zhao, W.S. De Rosset, D. Helfritch, Adiabatic shear instability based mechanism for particles/substrate bonding in the cold-gas dynamic-spray process, Mater. Des., 25 (2004) 681-688.

[22] T. Schmidt, F. Gartner, H. Assadi, H. Kreye, Development of a generalized parameter window for cold spray deposition, Acta Mater., 54 (2006) 729-742.

[23] H.Y. Lee, Y.H. Yu, Y.C. Lee, Y.P. Hong, K.H. Ko, Cold spray of SiC and Al_2O_3 with soft metal incorporation: a technical contribution, J. Therm. Spray Technol., 13 (2004) 184-189.

[24] A. Moridi, S.M. Hassani-Gangaraj, M. Guagliano, M. Dao, Cold spray coating: review of material systems and future perspectives, Surf. Eng., 30 (2014) 369-395.

[25] H. Assadi, H. Kreye, F. Gärtner, T. Klassen, Cold spraying – a materials perspective, Acta Mater., 116 (2016) 382-407.

[26] D. Rafaja, T. Schucknecht, V. Klemm, A. Paul, H. Berek, Microstructural characterisation of titanium coatings deposited using cold gas spraying on Al_2O_3 substrates, Surf. Coat. Technol, 203 (2009) 3206-3213.

[27] C. Wüstefeld, D. Rafaja, M. Motylenko, C. Ullrich, R. Drehmann, T. Grund, T. Lampke, B. Wielage, Local heteroepitaxy as an adhesion mechanism in aluminium coatings cold gas sprayed on AlN substrates, Acta Mater., 128 (2017) 418-427.

[28] K. Kim, M. Watanabe, S. Kuroda, Bonding mechanisms of thermally softened metallic powder particles and substrates impacted at high velocity, Surf. Coat. Technol, 204 (2010) 2175-2180.

[29] P.C. King, S.H. Zahiri, M. Jahedi, Focused ion beam micro-dissection of cold-sprayed particles, Acta Mater., 56 (2008) 5617-5626.

[30] S.Q. Fan, G.J. Yang, C.J. Li, G.J. Liu, C.X. Li, L.Z. Zhang, Characterization of microstructure of Nano-TiO_2 coating deposited by vacuum cold spraying, J. Therm. Spray Technol., 15 (2006) 513-517.

[31] Y.Y. Wang, Y. Liu, C.J. Li, G.J. Yang, K. Kusumoto, Electrical and mechanical properties of nano-structured TiN coatings deposited by vacuum cold spray, vac., 86 (2012) 953-959.

[32] S.V. Klinkov, V.F. Kosarev, Cold spraying activation using an abrasive admixture, J. Therm. Spray Technol., 21 (2012) 1046-1053.

[33] A. Sova, V.F. Kosarev, A. Papyrin, I. Smurov, Effect of ceramic particle velocity on cold spray deposition of metal-ceramic coatings, J. Therm. Spray Technol., 20 (2011) 285-291.

[34] A. Sova, A. Papyrin, I. Smurov, 2009. Influence of ceramic powder size on process of cermet coating formation by cold spray. J. Therm. Spray Technol. 18, 633

[35] R.R. Chromik, D. Goldbaum, J.M. Shockley, S. Yue, E. Irissou, J.G. Legoux, N.X. Randall, Modified ball bond shear test for determination of adhesion strength of cold spray splats, Surf. Coat. Technol, 205 (2010) 1409-1414.

[36] D. Goldbaum, J.M. Shockley, R.R. Chromik, A. Rezaeian, S. Yue, J.G. Legoux, E. Irissou, The effect of deposition conditions on adhesion strength of Ti and Ti6Al4V cold spray splats, J. Therm. Spray Technol., 21 (2012) 288-303.

[37] M. Braccini, M. Dupeux, Mechanics of solid interfaces, Wiley, New Jersey, 2012.

[38] H.-J.r. Butt, K. Graf, M. Kappl, Physics and chemistry of interfaces, Second ed., Wiley, Weinheim, 2003.

[39] W.D. Callister, D.G. Rethwisch, Materials science and engineering: an introduction, eighth ed., Wiley, New Jersey, 2010.

[40] J.M. Howe, Bonding structure and properties of metal/ceramic interfaces, Int. Mater. Rev., 38 (1993) 233-256.

[41] L.F.M. da Silva, A. Öchsner, R.D. Adams, Handbook of adhesion technology, Second ed., Springer, Cham, 2018.

[42] M.W. Finnis, The theory of metal - ceramic interfaces, J. Phys.: Condens. Matter, 8 (1996) 5811-5836.

[43] A.G. Evans, B.J. Dalgleish, The fracture resistance of metal-ceramic interfaces, Mater. Sci. Eng., A, 162 (1993) 1-13.

[44] H.H. Manko, Solders and soldering, fourth ed., McGraw-Hill Professional Publishing, Ohio, 2001.

[45] L.-C. Dufour, C. Monty, G. Petot-Ervas, Surfaces and interfaces of ceramic materials, Springer, Dordrecht, 1989.

[46] K. Suganuma, Y. Miyamoto, M. Koizumi, Joining of ceramics and metals, Annu. Rev. Mater. Sci., 18 (1988) 47-73.

[47] A. Tomsia, Ceramic/metal joining for structures and materials, J. Phys. IV, 3 (1993) 1317-1326.

[48] A. Bauer, J. Ganz, K. Hesse, K. Köhler, Laser-assisted deposition for electronic packaging applications, Appl. Surf. Sci., 46 (1990) 113-120.

[49] S. Schiller, U. Heisig, K. Steinfelder, D. Mehr, B. Thuss, R. Petermann, Metallization of ceramics for electronic components by magnetron-plasmatron coating, Thin Solid Films, 72 (1980) 313-326.

[50] B. Bhushan, Introduction to tribology, Second ed., Wiley, West Sussex, 2013.

[51] A. Anand, M. Irfan Ul Haq, K. Vohra, A. Raina, M.F. Wani, Role of green tribology in sustainability of mechanical systems: a state of the art survey, Mater. Today:. Proc., 4 (2017) 3659-3665.

[52] K. Holmberg, P. Andersson, N.-O. Nylund, K. Mäkelä, A. Erdemir, Global energy consumption due to friction in trucks and buses, Tribol. Int., 78 (2014) 94-114.

[53] K. Holmberg, A. Erdemir, Global impact of friction on energy consumption, economy and environment, FME Trans., 43 (2015) 181-185.

[54] A. Wu, 26 - Ceramic/metal bonding, in: Y. Zhou (Ed.), Microjoining and Nanojoining, Woodhead Publishing, Florida, 2008, pp. 758-785.

[55] K. Suganuma, Chapter 10.1 - Joining ceramics and metals, in: S. Somiya (Ed.), Handbook of advanced ceramics, Second ed., Academic Press, Oxford, 2013, pp. 775-788.

[56] M.G. Nicholas, Ceramic-metal interfaces, in: L.-C. Dufour, C. Monty, G. Petot-Ervas (Eds.), Surfaces and interfaces of ceramic materials, Springer, Dordrecht, 1989, pp. 393-417.

[57] J.-W. Park, A framework for designing interlayers for ceramic-to-metal joints, Doctoral dissertation, Massachusetts Institute of Technology, 2002.

[58] M. Rühle, A.G. Evans, Structure and chemistry of metal/ceramic interfaces, Mater. Sci. Eng., A, 107 (1989) 187-197.

[59] J.T. Klomp, Thermodynamics and chemistry of ceramic-metal interfaces, in: L.-C. Dufour, C. Monty, G. Petot-Ervas (Eds.), Surfaces and interfaces of ceramic materials, Springer, Dordrecht, 1989, pp. 375-392.

[60] J.T.M. De Hosson, W.P. Vellingal, X.B. Zhou, V. Vitek, Stucture-property relationship of metal-ceramic interfaces, in: A. Gonis, P.E.A. Turchi, J. Kudrnovský (Eds.), Stability of materials, Springer, New York, 1996, pp. 581-614.

[61] D.J. Siegel, L.G. Hector Jr, J.B. Adams, Ab initio study of Al-ceramic interfacial adhesion, Phys. Rev. B: Condens. Matter, 67 (2003) 092105.

[62] T. Epicier, C. Esnouf, Benefits of HREM for the study of metal-ceramic interfaces, J. Phys. III, 4 (1994) 1811-1831.

[63] J.T.M. De Hosson, B.J. Kooi, Metal/ceramic interfaces: a microscopic analysis, Surface and Interface Analysis, 31 (2001) 637-658.

[64] D.L. Gilmore, R.C. Dykhuizen, R.A. Neiser, M.F. Smith, T.J. Roemer, Particle velocity and deposition efficiency in the cold spray process, J. Therm. Spray Technol., 8 (1999) 576-582.

[65] C.-J. Li, W.-Y. Li, H. Liao, Examination of the critical velocity for deposition of particles in cold spraying, J. Therm. Spray Technol., 15 (2006) 212-222.

[66] C.-J. Li, H.-T. Wang, Q. Zhang, G.-J. Yang, W.-Y. Li, H.L. Liao, Influence of spray materials and their surface oxidation on the critical velocity in cold spraying, J. Therm. Spray Technol., 19 (2010) 95-101.

[67] K. Sakaki, 7 - The influence of nozzle design in the cold spray process, in: V.K. Champagne (Ed.), The cold spray materials deposition process, Woodhead Publishing, Cambridge, 2007, pp. 117-126.

[68] J. Villafuerte, Modern cold spray: materials, process, and applications, Springer International Publishing, Cham, 2015.

[69] A. Ganesan, J. Affi, M. Yamada, M. Fukumoto, Bonding behavior studies of cold sprayed copper coating on the PVC polymer substrate, Surf. Coat. Technol, 207 (2012) 262-269.

[70] A. Ganesan, M. Yamada, M. Fukumoto, Cold spray coating deposition mechanism on the thermoplastic and thermosetting polymer substrates, J. Therm. Spray Technol., 22 (2013) 1275-1282.

[71] P.C. King, A.J. Poole, S. Horne, R. de Nys, S. Gulizia, M.Z. Jahedi, Embedment of copper particles into polymers by cold spray, Surf. Coat. Technol, 216 (2013) 60-67.

[72] R. Lupoi, W. O'Neill, Deposition of metallic coatings on polymer surfaces using cold spray, Surf. Coat. Technol, 205 (2010) 2167-2173.

[73] D. Zhang, P.H. Shipway, D.G. McCartney, Cold gas dynamic spraying of aluminum: The role of substrate characteristics in deposit formation, J. Therm. Spray Technol., 14 (2005) 109-116.

[74] X.L. Zhou, A.F. Chen, J.C. Liu, X.K. Wu, J.S. Zhang, Preparation of metallic coatings on polymer matrix composites by cold spray, Surf. Coat. Technol, 206 (2011) 132-136.

[75] R. Drehmann, T. Grund, T. Lampke, B. Wielage, K. Manygoats, T. Schucknecht, D. Rafaja, Splat formation and adhesion mechanisms of cold gas-sprayed Al coatings on Al_2O_3 substrates, J. Therm. Spray Technol., 23 (2014) 68-75.

[76] M. Jeandin, H. Koivuluoto, S. Vezzu, Coating properties, in: J. Villafuerte (Ed.), Modern cold spray: materials, process, and applications, Springer International Publishing, Cham, 2015, pp. 107-224.

[77] V.K. Champagne, P.K. Koh, T.J. Eden, D.E. Wolfe, J. Villafuerte, D. Helfritch, Applications, in: J. Villafuerte (Ed.), Modern cold spray: materials, process, and applications, Springer International Publishing, Cham, 2015, pp. 341-376.

[78] G.L. Eesley, A. Elmoursi, N. Patel, Thermal properties of kinetic spray Al–SiC metal-matrix composite, J. Mater. Res., 18 (2003) 855-860.

[79] R.S. Lima, J. Karthikeyan, C.M. Kay, J. Lindemann, C.C. Berndt, Microstructural characteristics of cold-sprayed nanostructured WC–Co coatings, Thin Solid Films, 416 (2002) 129-135.

[80] E. Irissou, J.G. Legoux, B. Arsenault, C. Moreau, Investigation of Al-Al_2O_3 cold spray coating formation and properties, J. Therm. Spray Technol., 16 (2007) 661-668.

[81] E. Sansoucy, P. Marcoux, L. Ajdelsztajn, B. Jodoin, Properties of SiC-reinforced aluminum alloy coatings produced by the cold gas dynamic spraying process, Surf. Coat. Technol, 202 (2008) 3988-3996.

[82] K. Spencer, D.M. Fabijanic, M.X. Zhang, The use of Al–Al_2O_3 cold spray coatings to improve the surface properties of magnesium alloys, Surf. Coat. Technol, 204 (2009) 336-344.

[83] A. Papyrin, Cold spray technology, Elsevier, Amsterdam, 2007.

[84] A. Manap, O. Nooririnah, H. Misran, T. Okabe, K. Ogawa, Experimental and SPH study of cold spray impact between similar and dissimilar metals, Surf. Eng., 30 (2014) 335-341.

[85] J. Wu, H. Fang, S. Yoon, H. Kim, C. Lee, The rebound phenomenon in kinetic spraying deposition, Scr. Mater., 54 (2006) 665-669.

[86] M.R. Rokni, S.R. Nutt, C.A. Widener, V.K. Champagne, R.H. Hrabe, Review of relationship between particle deformation, coating microstructure, and properties in high-pressure cold spray, J. Therm. Spray Technol., 26 (2017) 1308-1355.

[87] M. Hassani-Gangaraj, D. Veysset, K.A. Nelson, C.A. Schuh, In-situ observations of single micro-particle impact bonding, Scr. Mater., 145 (2018) 9-13.

[88] R.W. Armstrong, C.S. Coffey, W.L. Elban, Adiabatic heating at a dislocation pile-up avalanche, Acta Metall., 30 (1982) 2111-2116.

[89] M. Hassani-Gangaraj, D. Veysset, V.K. Champagne, K.A. Nelson, C.A. Schuh, Adiabatic shear instability is not necessary for adhesion in cold spray, Acta Mater., 158 (2018) 430-439.

[90] M. Grujicic, J.R. Saylor, D.E. Beasley, W.S. DeRosset, D. Helfritch, Computational analysis of the interfacial bonding between feed-powder particles and the substrate in the cold-gas dynamic-spray process, Appl. Surf. Sci., 219 (2003) 211-227.

[91] V.K. Champagne, D. Helfritch, P. Leyman, S. Grendahl, B. Klotz, Interface material mixing formed by the deposition of copper on aluminum by means of the cold spray process, J. Therm. Spray Technol., 14 (2005) 330-334.

[92] T. Hussain, D.G. McCartney, P.H. Shipway, D. Zhang, Bonding mechanisms in cold spraying: the contributions of metallurgical and mechanical components, J. Therm. Spray Technol., 18 (2009) 364-379.

[93] Y. Xie, S. Yin, C. Chen, M.-P. Planche, H. Liao, R. Lupoi, New insights into the coating/substrate interfacial bonding mechanism in cold spray, Scr. Mater., 125 (2016) 1-4.

[94] G. Bae, Y. Xiong, S. Kumar, K. Kang, C. Lee, General aspects of interface bonding in kinetic sprayed coatings, Acta Mater., 56 (2008) 4858-4868.

[95] D.A. Porter, K.E. Easterling, M.Y. Sherif, Phase transformations in metals and alloys, Third ed., CRC Press, Florida, 2009.

[96] F. Khodabakhshi, B. Marzbanrad, H. Jahed, A.P. Gerlich, Interfacial bonding mechanisms between aluminum and titanium during cold gas spraying followed by friction-stir modification, Appl. Surf. Sci., 462 (2018) 739-752.

[97] Q. Wang, D. Qiu, Y. Xiong, N. Birbilis, M.-X. Zhang, High resolution microstructure characterization of the interface between cold sprayed Al coating and Mg alloy substrate, Appl. Surf. Sci., 289 (2014) 366-369.

[98] K.H. Ko, J.O. Choi, H. Lee, Intermixing and interfacial morphology of cold-sprayed Al coatings on steel, Mater. Lett., 136 (2014) 45-47.

[99] Y. Xiong, X. Xiong, S. Yoon, G. Bae, C. Lee, Dependence of bonding mechanisms of cold sprayed coatings on strain-rate-induced non-equilibrium phase transformation, J. Therm. Spray Technol., 20 (2011) 860-865.

[100] R. Drehmann, T. Grund, T. Lampke, B. Wielage, C. Wüstefeld, M. Motylenko, D. Rafaja, Essential factors influencing the bonding strength of cold-sprayed aluminum coatings on ceramic substrates, J. Therm. Spray Technol., 27 (2018) 446-455.

[101] D. MacDonald, A. Nastic, B. Jodoin, Understanding adhesion, in: P. Cavaliere (Ed.), Cold-spray coatings: recent trends and future perspectives, Springer International Publishing, Cham, 2018, pp. 421-450.

[102] S. Guetta, M.H. Berger, F. Borit, V. Guipont, M. Jeandin, M. Boustie, Y. Ichikawa, K. Sakaguchi, K. Ogawa, Influence of particle velocity on adhesion of cold-sprayed splats, J. Therm. Spray Technol., 18 (2009) 331-342.

[103] S. Barradas, V. Guipont, R. Molins, M. Jeandin, M. Arrigoni, M. Boustie, C. Bolis, L. Berthe, M. Ducos, Laser shock flier impact simulation of particle-substrate interactions in cold spray, J. Therm. Spray Technol., 16 (2007) 548-556.

[104] A.V. Bolesta, V.M. Fomin, M.R. Sharafutdinov, B.P. Tolochko, Investigation of interface boundary occurring during cold gas-dynamic spraying of metallic particles, Nucl. Instrum. Methods Phys. Res., Sect. A, 470 (2001) 249-252.

[105] G. Bae, S. Kumar, S. Yoon, K. Kang, H. Na, H.-J. Kim, C. Lee, Bonding features and associated mechanisms in kinetic sprayed titanium coatings, Acta Mater., 57 (2009) 5654-5666.

[106] P.C. King, C. Busch, T. Kittel-Sherri, M. Jahedi, S. Gulizia, Interface melding in cold spray titanium particle impact, Surf. Coat. Technol, 239 (2014) 191-199.

[107] C.-J. Li, W.-Y. Li, Y.-Y. Wang, Formation of metastable phases in cold-sprayed soft metallic deposit, Surf. Coat. Technol, 198 (2005) 469-473.

[108] X.-J. Ning, J.-H. Jang, H.-J. Kim, C.-J. Li, L. Changhee, Cold spraying of Al–Sn binary alloy: Coating characteristics and particle bonding features, Surf. Coat. Technol, 202 (2008) 1681-1687.

[109] M. Grujicic, J.R. Saylor, D.E. Beasley, W.S. DeRosset, D. Helfritch, Computational analysis of the interfacial bonding between feed-powder particles and the substrate in the cold-gas dynamic-spray process, Appl. Surf. Sci., 219 (2003) 211-227.

[110] N. Thadhani, Shock-induced and shock-assisted solid-state chemical reactions in powder mixtures, J. Appl. Phys., 76 (1994) 2129-2138.

[111] R.A. Graham, A.B. Sawaoka, High pressure explosive processing of ceramics, Trans Tech Pub., Aedermannsdorf, 1986.

[112] C. Lee, J. Kim, Microstructure of kinetic spray coatings: A review, J. Therm. Spray Technol., 24 (2015) 592-610.

[113] D. Goldbaum, R.R. Chromik, N. Brodusch, R. Gauvin, Microstructure and mechanical properties of Ti cold-spray splats determined by electron channeling contrast imaging and nanoindentation mapping, Microsc. Microanal., 21 (2015) 570-581.

[114] Y. Zou, W. Qin, E. Irissou, J.-G. Legoux, S. Yue, J.A. Szpunar, Dynamic recrystallization in the particle/particle interfacial region of cold-sprayed nickel coating: Electron backscatter diffraction characterization, Scr. Mater., 61 (2009) 899-902.

[115] K. Kim, M. Watanabe, J. Kawakita, S. Kuroda, Grain refinement in a single titanium powder particle impacted at high velocity, Scr. Mater., 59 (2008) 768-771.

[116] Y. Zhang, N. Brodusch, S. Descartes, R.R. Chromik, R. Gauvin, Microstructure refinement of cold-sprayed copper investigated by electron channeling contrast imaging, Microsc. Microanal., 20 (2014) 1499-1506.

[117] C. Borchers, F. Gärtner, T. Stoltenhoff, H. Assadi, H. Kreye, Microstructural and macroscopic properties of cold sprayed copper coatings, J. Appl. Phys., 93 (2003) 10064-10070.

[118] J.Y. Lek, A. Bhowmik, A.W.-Y. Tan, W. Sun, X. Song, W. Zhai, P.J. Buenconsejo, F. Li, E. Liu, Y.M. Lam, C.B. Boothroyd, Understanding the microstructural evolution of cold sprayed Ti-6Al-4V coatings on Ti-6Al-4V substrates, Appl. Surf. Sci., 459 (2018) 492-504.

[119] S. Romankov, Y.C. Park, I.V. Shchetinin, J.M. Yoon, Atomic-scale intermixing, amorphization and microstructural development in a multicomponent system subjected to surface severe plastic deformation, Acta Mater., 61 (2013) 1254-1265.

[120] Y.P. Li, J. Tan, G.P. Zhang, Interface instability within shear bands in nanoscale Au/Cu multilayers, Scr. Mater., 59 (2008) 1226-1229.

[121] M. Atzmon, K.M. Unruh, W.L. Johnson, Formation and characterization of amorphous erbium-based alloys prepared by near-isothermal cold-rolling of elemental composites, J. Appl. Phys., 58 (1985) 3865-3870.

[122] A. Bachmaier, M. Kerber, D. Setman, R. Pippan, The formation of supersaturated solid solutions in Fe-Cu alloys deformed by high-pressure torsion, Acta Mater., 60 (2012) 860-871.

[123] H.J. Fecht, G. Han, Z. Fu, W.L. Johnson, Metastable phase formation in the Zr-Al binary system induced by mechanical alloying, J. Appl. Phys., 67 (1990) 1744-1748.

[124] R.J. Hebert, J.H. Perepezko, Deformation-induced synthesis and structural transformations of metallic multilayers, Scr. Mater., 50 (2004) 807-812.

[125] S.K. Pabi, D. Das, T.K. Mahapatra, I. Manna, Mathematical modeling of the mechanical alloying kinetics, Acta Mater., 46 (1998) 3501-3510.

[126] M. Peterlechner, T. Waitz, H.P. Karnthaler, Nanoscale amorphization of severely deformed NiTi shape memory alloys, Scr. Mater., 60 (2009) 1137-1140.

[127] X. Sauvage, F. Wetscher, P. Pareige, Mechanical alloying of Cu and Fe induced by severe plastic deformation of a Cu-Fe composite, Acta Mater., 53 (2005) 2127-2135.

[128] B.B. Straumal, B. Baretzky, A.A. Mazilkin, F. Phillipp, O.A. Kogtenkova, M.N. Volkov, R.Z. Valiev, Formation of nanograined structure and decomposition of supersaturated solid solution during high pressure torsion of Al-Zn and Al-Mg alloys, Acta Mater., 52 (2004) 4469-4478.

[129] B.B. Straumal, A.A. Mazilkin, B. Baretzky, G. Schütz, E. Rabkin, R.Z. Valiev, Accelerated diffusion and phase transformations in Co-Cu alloys driven by the severe plastic deformation, Mater. Trans., 53 (2012) 63-71.

[130] B.B. Straumal, S.G. Protasova, A.A. Mazilkin, E. Rabkin, D. Goll, G. Schütz, B. Baretzky, R.Z. Valiev, Deformation-driven formation of equilibrium phases in the Cu-Ni alloys, J. Mater. Sci., 47 (2012) 360-367.

[131] A.R. Yavari, P.J. Desré, T. Benameur, Mechanically driven alloying of immiscible elements, Phys. Rev. Lett., 68 (1992) 2235-2238.

[132] T. Liu, J.D. Leazer, L.N. Brewer, Particle deformation and microstructure evolution during cold spray of individual Al-Cu alloy powder particles, Acta Mater., 168 (2019) 13-23.

[133] K.H. Ko, J.O. Choi, H. Lee, The interfacial restructuring to amorphous: A new adhesion mechanism of cold-sprayed coatings, Mater. Lett., 175 (2016) 13-15.

[134] K.H. Ko, J.O. Choi, H. Lee, Y.K. Seo, S.P. Jung, S.S. Yu, Cold spray induced amorphization at the interface between Fe coatings and Al substrate, Mater. Lett., 149 (2015) 40-42.

[135] S.A. Tsukerman, Chapter III - Metal powders, in: S.A. Tsukerman (Ed.), Powder Metallurgy, Pergamon, Oxford, 1965, pp. 17-28.

[136] G. Xu, P. Lu, M. Li, C. Liang, P. Xu, D. Liu, X. Chen, Investigation on characterization of powder flowability using different testing methods, Exp. Therm Fluid Sci., 92 (2018) 390-401.

[137] M. Jeandin, G. Rolland, L.L. Descurninges, M.H. Berger, Which powders for cold spray?, Surf. Eng., 30 (2014) 291-298.

[138] B. Jodoin, L. Ajdelsztajn, E. Sansoucy, A. Zúñiga, P. Richer, E.J. Lavernia, Effect of particle size, morphology, and hardness on cold gas dynamic sprayed aluminum alloy coatings, Surf. Coat. Technol, 201 (2006) 3422-3429.

[139] D. MacDonald, R. Fernández, F. Delloro, B. Jodoin, Cold spraying of Armstrong process titanium powder for additive manufacturing, J. Therm. Spray Technol., 26 (2017) 598-609.

[140] V.N.V. Munagala, V. Akinyi, P. Vo, R.R. Chromik, Influence of powder morphology and microstructure on the cold spray and mechanical properties of Ti6Al4V coatings, J. Therm. Spray Technol., 27 (2018) 827-842.

[141] V.N.V. Munagala, S.I. Imbriglio, R.R. Chromik, The influence of powder properties on the adhesion strength and microstructural evolution of cold sprayed Ti6Al4V single splats, Mater. Lett., 244 (2019) 58-61.

[142] W. Wong, P. Vo, E. Irissou, A.N. Ryabinin, J.-G. Legoux, S. Yue, Effect of particle morphology and size distribution on cold-sprayed pure titanium coatings, J. Therm. Spray Technol., 22 (2013) 1140-1153.

[143] N. Cinca, J.M. Rebled, S. Estradé, F. Peiró, J. Fernández, J.M. Guilemany, Influence of the particle morphology on the cold gas spray deposition behaviour of titanium on aluminum light alloys, J. Alloys Compd., 554 (2013) 89-96.

[144] X.-T. Luo, Y.-J. Li, C.-J. Li, A comparison of cold spray deposition behavior between gas atomized and dendritic porous electrolytic Ni powders under the same spray conditions, Mater. Lett., 163 (2016) 58-60.

[145] K. Araci, D. Mangabhai, K. Akhtar, 9 - Production of titanium by the Armstrong Process®, in: M. Qian, F.H. Froes (Eds.), Titanium powder metallurgy, Butterworth-Heinemann, Boston, 2015, pp. 149-162.

[146] T. Hussain, Cold spraying of titanium: A review of bonding mechanisms, microstructure and properties, Key Eng. Mater., 533 (2013) 53-90.

[147] S. Kumar, G. Bae, C. Lee, Deposition characteristics of copper particles on roughened substrates through kinetic spraying, Appl. Surf. Sci., 255 (2009) 3472-3479.

[148] P. Richer, B. Jodoin, L. Ajdelsztajn, Substrate roughness and thickness effects on cold spray nanocrystalline Al−Mg coatings, J. Therm. Spray Technol., 15 (2006) 246-254.

[149] R. Singh, K.H. Rauwald, E. Wessel, G. Mauer, S. Schruefer, A. Barth, S. Wilson, R. Vassen, Effects of substrate roughness and spray-angle on deposition behavior of cold-sprayed Inconel 718, Surf. Coat. Technol, 319 (2017) 249-259.

[150] S. Kümmel, T. Grund, P. Löschner, B. Wielage, Influence of deposition conditions and heat treatment on tensile strength of cold spray aluminium coatings on Al_2O_3 and AlN substrates, Thermal Spray 2011: Proceedings of the International Thermal Spray Conference, September 26-29, 2011, (Hamburg, Germany), 2011, p. DVS1130-DVS1135

[151] T. Marrocco, D. McCartney, P. Shipway, A. Sturgeon, Production of titanium deposits by cold-gas dynamic spray: Numerical modeling and experimental characterization, J. Therm. Spray Technol., 15 (2006) 263-272.

[152] J. Wu, J. Yang, H. Fang, S. Yoon, C. Lee, The bond strength of Al–Si coating on mild steel by kinetic spraying deposition, Appl. Surf. Sci., 252 (2006) 7809-7814.

[153] S. Kumar, G. Bae, C. Lee, Influence of substrate roughness on bonding mechanism in cold spray, Surf. Coat. Technol, 304 (2016) 592-605.

[154] J. Shockley, Dry sliding wear and high pressure torsion of cold sprayed aluminum-alumina composites, Doctoral dissertation, McGill University, 2015.

[155] W.Y. Li, G. Zhang, H.L. Liao, C. Coddet, Characterizations of cold sprayed TiN particle reinforced Al2319 composite coating, J. Mater. Process. Technol, 202 (2008) 508-513.

[156] M. Yandouzi, P. Richer, B. Jodoin, SiC particulate reinforced Al–12Si alloy composite coatings produced by the pulsed gas dynamic spray process: Microstructure and properties, Surf. Coat. Technol, 203 (2009) 3260-3270.

[157] S. Dosta, M. Couto, J.M. Guilemany, Cold spray deposition of a WC-25Co cermet onto Al7075-T6 and carbon steel substrates, Acta Mater., 61 (2013) 643-652.

[158] M. Couto, S. Dosta, M. Torrell, J. Fernández, J.M. Guilemany, Cold spray deposition of WC–17 and 12Co cermets onto aluminum, Surf. Coat. Technol, 235 (2013) 54-61.

[159] S.A. Alidokht, P. Manimunda, P. Vo, S. Yue, R.R. Chromik, Cold spray deposition of a Ni-WC composite coating and its dry sliding wear behavior, Surf. Coat. Technol, 308 (2016) 424-434.

[160] V.N.V. Munagala, T.B. Torgerson, T.W. Scharf, R.R. Chromik, High temperature friction and wear behavior of cold-sprayed Ti6Al4V and Ti6Al4V-TiC composite coatings, Wear, 426-427 (2019) 357-369.

[161] J.M. Shockley, S. Descartes, P. Vo, E. Irissou, R.R. Chromik, The influence of Al_2O_3 particle morphology on the coating formation and dry sliding wear behavior of cold sprayed Al–Al_2O_3 composites, Surf. Coat. Technol, 270 (2015) 324-333.

[162] M. Yu, W.Y. Li, H. Chen, X.K. Suo, H.L. Liao, Effect of matrix/reinforcement combination on cold sprayed coating deposition behaviour, Surf. Eng., 30 (2014) 796-800.

[163] A.N. Dremin, O.N. Breusov, Processes occurring in solids under the action of powerful shock waves, Russ. Chem. Rev., 37 (1968) 392-402.

[164] M.V. Vidaller, A. List, F. Gaertner, T. Klassen, S. Dosta, J.M. Guilemany, Single impact bonding of cold sprayed Ti-6Al-4V powders on different substrates, J. Therm. Spray Technol., 24 (2015) 644-658.

[165] S. Krebs, F. Gärtner, T. Klassen, Cold spraying of Cu-Al-Bronze for cavitation protection in marine environments, J. Therm. Spray Technol., 24 (2015) 126-135.

[166] M. Entezarian, F. Allaire, P. Tsantrizos, R.A.L. Drew, Plasma atomization: A new process for the production of fine, spherical powders, JOM, 48 (1996) 53-55.

[167] K. Yamada, M. Mohri, Properties and applications of silicon carbide ceramics, in: S. Somiya, Y. Inomata (Eds.), Silicon carbide ceramics—1, Elsevier Science Publisheres, New York, 1991, pp. 13-44.

[168] R.C. Dykhuizen, M.F. Smith, Gas dynamic principles of cold spray, J. Therm. Spray Technol., 7 (1998) 205-212.

[169] Y.T.R. Lee, Development of cold-sprayed boron carbide metal matrix composite coatings for wear resistance applications, Master's thesis, University of Alberta, 2017.

[170] U. Prisco, Size-dependent distributions of particle velocity and temperature at impact in the cold-gas dynamic-spray process, J. Mater. Process. Technol, 216 (2015) 302-314.

[171] H.Z. Li, J. Wang, J.M. Fan, Analysis and modeling of particle velocities in micro-abrasive air jet, Int. J. Mach. Tools Manuf., 49 (2009) 850-858.

[172] T. Poirié, T. Schmitt, E. Bousser, L. Martinu, J.-E. Klemberg-Sapieha, Influence of internal stress in optical thin films on their failure modes assessed by in situ real-time scratch analysis, Tribol. Int., 109 (2017) 355-366.

[173] J. Goldstein, D.E. Newbury, D.C. Joy, C.E. Lyman, P. Echlin, E. Lifshin, L. Sawyer, J.R. Michael, Scanning electron microscopy and x-ray microanalysis, Springer, New York, 2003.

[174] P. Gnauck, V. Drexel, E. Essers, Detector for variable pressure areas and an electron microscope comprising a corresponding detector, US 2005/0173644 A1, 2005.

[175] D.B. Williams, C.B. Carter, Transmission electron microscopy: a textbook for materials science, second ed., Springer, New York, 2009.

[176] M. Baram, W. Kaplan, Quantitative HRTEM analysis of FIB prepared specimens, J. Microsc., 232 (2008) 395-405.

[177] L.L. Hench, S.M. Best, Chapter I.2.4 - Ceramics, glasses, and glass-ceramics: basic principles, in: B.D. Ratner, A.S. Hoffman, F.J. Schoen, J.E. Lemons (Eds.), Biomaterials science, third ed., Academic Press, Massachusetts, 2013, pp. 128-151.

[178] J.B. Brunski, Chapter I.2.3 - Metals: basic principles, in: B.D. Ratner, A.S. Hoffman, F.J. Schoen, J.E. Lemons (Eds.), Biomaterials science, third ed., Academic Press, Massachusetts, 2013, pp. 111-119.

[179] H. Lee, K. Ko, Effect of SiC particle size on cold sprayed Al–SiC composite coatings, Surf. Eng., 25 (2009) 606-611.

[180] Sintered metal materials, excluding hardmetals -- Measurement of surface roughness, ISO 23519:2010, ISO, 2010

[181] K. Kim, M. Watanabe, S. Kuroda, Thermal softening effect on the deposition efficiency and microstructure of warm sprayed metallic powder, Scr. Mater., 60 (2009) 710-713.

[182] B. Samareh, A. Dolatabadi, A three-dimensional analysis of the cold spray process: The effects of substrate location and shape, J. Therm. Spray Technol., 16 (2007) 634-642.

[183] M. Aghasibeig, H. Monajatizadeh, P. Bocher, A. Dolatabadi, R. Wuthrich, C. Moreau, Cold spray as a novel method for development of nickel electrode coatings for hydrogen production, Int. J. Hydrogen Energy, 41 (2016) 227-238.

[184] T. Akatsu, N. Hosoda, T. Suga, M. Rühle, Atomic structure of Al/Al interface formed by surface activated bonding, J. Mater. Sci., 34 (1999) 4133-4139.

[185] T. Stoltenhoff, H. Kreye, H.J. Richter, An analysis of the cold spray process and its coatings, J. Therm. Spray Technol., 11 (2002) 542-550.

[186] A. Viscusi, A. Astarita, R.D. Gatta, F. Rubino, A perspective review on the bonding mechanisms in cold gas dynamic spray, Surf. Eng., 35 (2018) 743-771.

[187] J. Lee, S. Shin, H. Kim, C. Lee, Effect of gas temperature on critical velocity and deposition characteristics in kinetic spraying, Appl. Surf. Sci., 253 (2007) 3512-3520.

[188] W. Wong, E. Irissou, A.N. Ryabinin, J.-G. Legoux, S. Yue, Influence of helium and nitrogen gases on the properties of cold gas dynamic sprayed pure titanium coatings, J. Therm. Spray Technol., 20 (2011) 213-226.

[189] J. Wu, H. Fang, S. Yoon, H. Kim, C. Lee, Measurement of particle velocity and characterization of deposition in aluminum alloy kinetic spraying process, Appl. Surf. Sci., 252 (2005) 1368-1377.

[190] J.H. Lee, P.E. Loya, J. Lou, E.L. Thomas, Dynamic mechanical behavior of multilayer graphene via supersonic projectile penetration, Sci., 346 (2014) 1092-1096.

[191] J.H. Lee, D. Veysset, J.P. Singer, M. Retsch, G. Saini, T. Pezeril, K.A. Nelson, E.L. Thomas, 2012. High strain rate deformation of layered nanocomposites. Nat. Commun. 3, 1164

[192] D. Veysset, A.J. Hsieh, S. Kooi, A.A. Maznev, K.A. Masser, K.A. Nelson, 2016. Dynamics of supersonic microparticle impact on elastomers revealed by realtime multiframe imaging. Sci. Rep. 6, 25577

[193] D. Veysset, A.J. Hsieh, S.E. Kooi, K.A. Nelson, Molecular influence in high-strain-rate microparticle impact response of poly(urethane urea) elastomers, Polym., 123 (2017) 30-38.

[194] M. Hassani-Gangaraj, D. Veysset, K.A. Nelson, C.A. Schuh, 2017. Melting can hinder impact-induced adhesion. Phys. Rev. Lett. 119, 175701

[195] M. Hassani-Gangaraj, D. Veysset, K.A. Nelson, C.A. Schuh, 2018. Melt-driven erosion in microparticle impact. Nat. Commun. 9, 5077

[196] S.I. Imbriglio, N. Brodusch, M. Aghasibeig, R. Gauvin, R.R. Chromik, Influence of substrate characteristics on single Ti splat bonding to ceramic substrates by cold spray, J. Therm. Spray Technol., 27 (2018) 1011-1024.

[197] R. Huang, H. Fukanuma, Study of the influence of particle velocity on adhesive strength of cold spray deposits, J. Therm. Spray Technol., 21 (2012) 541-549.

[198] T. Schmidt, H. Assadi, F. Gartner, H. Richter, T. Stoltenhoff, H. Kreye, T. Klassen, 2009. From particle acceleration to impact and bonding in cold spraying. J. Therm. Spray Technol. 18, 794

[199] W.M. Rohsenow, J.P. Hartnett, Y.I. Cho, Handbook of heat transfer, third ed., McGraw-Hill, New York, 1998.

[200] K. Stephan, R. Krauss, A. Laesecke, Viscosity and thermal conductivity of nitrogen for a wide range of fluid states, J Phys Chem Ref Data, 16 (1987) 993-1023.

[201] P.C. King, M. Jahedi, Relationship between particle size and deformation in the cold spray process, Appl. Surf. Sci., 256 (2010) 1735-1738.

[202] J.I. Goldstein, D.E. Newbury, P. Echlin, D.C. Joy, C.E. Lyman, E. Lifshin, L. Sawyer, J.R. Michael, Special topics in scanning electron microscopy, in, Scanning electron microscopy and X-ray microanalysis, third ed., Springer, New York, 2003, pp. 195-270.

[203] W.-Y. Li, H. Liao, C.-J. Li, G. Li, C. Coddet, X. Wang, On high velocity impact of micro-sized metallic particles in cold spraying, Appl. Surf. Sci., 253 (2006) 2852-2862.

[204] Q. Wang, K. Spencer, N. Birbilis, M.-X. Zhang, The influence of ceramic particles on bond strength of cold spray composite coatings on AZ91 alloy substrate, Surf. Coat. Technol., 205 (2010) 50-56.

[205] K. Spencer, D.M. Fabijanic, M.X. Zhang, The influence of Al_2O_3 reinforcement on the properties of stainless steel cold spray coatings, Surf. Coat. Technol, 206 (2012) 3275-3282.

[206] S.I. Imbriglio, M. Hassani-Gangaraj, D. Veysset, M. Aghasibeig, R. Gauvin, K.A. Nelson, C.A. Schuh, R.R. Chromik, Adhesion strength of titanium particles to alumina substrates: A combined cold spray and LIPIT study, Surf. Coat. Technol, 361 (2019) 403-412.

[207] S.I. Imbriglio, V.N.V. Munagala, T. Schmitt, R. Gauvin, J.E. Klemberg-Sapieha, R.R. Chromik, 2019. Failure dynamics of spherical and irregular shaped Ti splats deposited on sapphire by cold spray. Surf. Topogr. Metrol. Prop. 7, 045002

[208] J. Guo, G. Haberfehlner, J. Rosalie, L. Li, M.J. Duarte, G. Kothleitner, G. Dehm, Y. He, R. Pippan, Z. Zhang, 2018. In situ atomic-scale observation of oxidation and decomposition processes in nanocrystalline alloys. Nat. Commun. 9, 946

[209] H. Zheng, J.B. Rivest, T.A. Miller, B. Sadtler, A. Lindenberg, M.F. Toney, L.-W. Wang, C. Kisielowski, A.P. Alivisatos, Observation of transient structural-transformation dynamics in a Cu_2S nanorod, Sci., 333 (2011) 206-209.

[210] H. Müllejans, J. Bruley, Electron energy-loss near-edge structure of internal interfaces by spatial difference spectroscopy, J. Microsc., 180 (1995) 12-21.

[211] J. Bruley, R. Brydson, H. Müllejans, J. Mayer, G. Gutekunst, W. Mader, D. Knauss, M. Rühle, Investigations of the chemistry and bonding at niobiumsapphire interfaces, J. Mater. Res., 9 (1994) 2574-2583.

[212] J. Bruley, Spatially resolved electron energy-loss near-edge structure analysis of a near Σ = 11 tilt boundary in sapphire, Microsc. Microanal. Microstruct., 4 (1993) 23-39.

[213] J. Bruley, T. Hoche, H.-J. Kleebe, M. Rühle, Recent attempts to detect magnesium in a heavily doped sapphire bicrystal by spatially resolved electron energy-loss spectroscopy, J. Am. Ceram. Soc., 77 (1994) 2273-2276.

[214] R. Brydson, H. Müllejans, J. Bruley, P.A. Trusty, X. Sun, J.A. Yeomans, M. Rühle, Spatially resolved electron energy-loss studies of metal–ceramic interfaces in transition metal/alumina cermets, J. Microsc., 177 (1995) 369-386.

[215] C. Scheu, G. Dehm, H. Müllejans, M. Rühle, Electron energy-loss spectroscopy at Cu/Al_2O_3 and Ti/Al_2O_3 interfaces, Mater. Sci. Forum, 207-209 (1996) 181-184.

[216] C. Scheu, W. Stein, M. Rühle, Electron energy-loss near-edge structure studies of a Cu/(11-20)α-Al_2O_3 interface, Phys. Status Solidi B, 222 (2000) 199-211.

[217] C. Scheu, G. Dehm, M. Rühle, R. Brydson, Electron-energy-loss spectroscopy studies of Cu-α-Al_2O_3 interfaces grown by molecular beam epitaxy, Philos. Mag. A, 78 (1998) 439-465.

[218] S.D. Berger, S.J. Pennycook, Detection of nitrogen at {100} platelets in diamond, Nat., 298 (1982) 635-637.

[219] C. Scheu, Analytische untersuchungen an Cu/Al_2O_3-und Cu/Ti/Al_2O_3-grenzflächen, Doctoral dissertation, Universität Stuttgart, 1996.

[220] O. Ugurlu, J. Haus, A. Gunawan, M. Thomas, S. Maheshwari, M. Tsapatsis, K. Mkhoyan, 2011. Radiolysis to knock-on damage transition in zeolites under electron beam irradiation. Phys. Rev. B: Condens. Matter. 83, 113408

[221] H. Gu, ELNES separation in spatially-resolved analysis of grain boundaries and interfaces, Ultramicroscopy, 76 (1999) 159-172.

[222] H. Gu, Quantification of interfacial parameters in spatially resolved analysis involving ELNES separation, Ultramicroscopy, 76 (1999) 173-185.

[223] R. Drehmann, Haftmechanismen kaltgasgespritzter Aluminiumschichten auf keramischen Oberflächen, Doctoral dissertation, Technische Universität Chemnitz, 2017.

[224] A. Azushima, R. Kopp, A. Korhonen, D.Y. Yang, F. Micari, G.D. Lahoti, P. Groche, J. Yanagimoto, N. Tsuji, A. Rosochowski, A. Yanagida, Severe plastic deformation (SPD) processes for metals, CIRP Annals, 57 (2008) 716-735.

[225] C.C. Ahn, O.L. Krivanek, R.P. Burgner, M.M. Disko, P.R. Swann, EELS atlas: a reference collection of electron energy loss spectra covering all stable elements, Gatan, Inc, USA, 1983.

[226] R.A. Graham, Solids under high-pressure shock compression: mechanics, physics, and chemistry, Springer, New York, 1993.

[227] D. Grady, Shock-wave properties of high-strength ceramics, in: S.C. Schmidt, R.D. Dick, J.W. Forbes, D.G. Tasker (Eds.), Shock compression of condensed matter–1991, Elsevier, Amsterdam, 1992, pp. 455-458.

Appendix A

Numerical Simulation of Powder Temperature in Cold Spray (MATLAB Script)

```
clear all;
close all;
 a
%KNOWN VARIABLES INPUT BY USER

k=1.4;
R1=15/2;%inlet radius [mm]
R2=2.7/2;%throat radius [mm]
R3=6.4/2;%exit radius [mm]
X1=30;%length of the inlet [mm]
X3=130;%length of the exit [mm]
X2=X1+X3;%Total length of the nozzle [mm]
Pi=4*10^6;% stagnation pressure [Pa]
Ti=600;%stagnation temperature [K]
Rg=297;% universal gas constant [m^2/s^2K]
Ugi=10;% initial gas velocity
Rho_g0=Pi/(Rg*Ti); %gas density [kg/m^3]
Dp=20*10^-6;% Powder diameter [m]
Rho_p=8960;% powder density [kg/m^3]
Cp_p=384; %Specific heat of powder particle

%TABLES FROM LITERATURE FILE MUST BE SAVED IN THE SAME FOLDER

Stp=0.1;
x_n=0.1:Stp:X2;%Position along the nozzle
x_c=0.1:Stp:X1;%Position along the inlet
x_d=0.1:Stp:X3;%Position along the exit
T3 = xlsread('Data_ThermalConductivity.xlsx','A2:A49'); %Thermal conductivity
temperatures
K1 = xlsread('Data_ThermalConductivity.xlsx','C2:C49'); %Termal Conductivity
at specific temperatures
DataThermalCond =
table(T3,K1,'VariableNames',{'Temperature','ThermalConductivity'}); %Defining
variables
T1= xlsread('Data_Specificheat3.xlsx','A2:A51');%Specific heat temperatures
Cp1 = xlsread('Data_Specificheat3.xlsx','C2:C51');%Specific heat at specific
temperaturess
```

```
DataSpecificheat =
table(T1,Cp1,'VariableNames',{'Temperature','SpecificHeat'}); %Defining
variables
T2 = xlsread('Data_viscosity2.xlsx','A2:A48');%Viscosity temperatures
MU = xlsread('Data_viscosity2.xlsx','C2:C48');%Viscosity at specific
temperatures
DataViscosity =
table(T2,MU,'VariableNames',{'Temperature','Viscosity'});%Defining variables

%CALCULATIONS FOR INLET AND EXIT SLOPE

S1=(R2-R1)/(X1);%slope of the inlet
B1=R1;
S2=(R3-R2)/(X2-X1); %slope of the exit
B2=R3-(S2*X2);


% NOZZLE CONTOUR (Radius at positions along the nozzle)

    r=zeros(2,(length(x_n)));
    for i = 1:(length(x_n))
        if x_n(1,i)<X1
            R=(S1*x_n(1,i))+B1;
        elseif x_n(1,i)<X1
            R=(S1*x_n(1,i))+B1;
        else
            R=(S2*x_n(1,i))+B2;
        end
        r(1,i)=R;
    end


  figure(1);
  plot (x_n(1,1:end),r(1,1:end));
  title('Nozzle dimensions')
  xlabel('Axial distance, x (mm)')
  ylabel('Nozzle contour, r (mm)')


Pt = Pi*((2/(k+1))^(k/(k-1))); %throat pressure

syms P M

%CALCULATIONS FOR MACH NUMBER ALONG THE NOZZLE

    %Calculating area ratio at different positions along the nozzle with
    %respect to the throat area

    AR=zeros(1,(length(x_n)));
    for i=1:(length(x_n))
```

```
        A= (r(1,i))^2/(r(1,(X1/Stp)))^2; %X1/Stp gives the position
equivalent to the troat since Stp is used to define positions along the
length of the nozzle.
        AR(1,i)=A;
    end

    %Mach number calculation
   m=zeros(1,(length(x_n)));

    %Must go through many iterations to avoid getting a negative mach
    %number for the inlet section.

   for i=1:(length(x_n))
       if x_n(1,i)<X1
        Mach=@(M)(1/M)*((2+((k-1)*M^2))/(k+1))^((k+1)/(2*(k-1)))-(AR(1,i));
        X0=1.5;
        TempSolM=fzero(Mach,X0);
        if TempSolM <1
            SolM=TempSolM;
        else
            X0=0.5;
            TempSolM=fzero(Mach,X0);
             if TempSolM <1
                SolM=TempSolM;
             else
                X0=0.1;
                TempSolM=fzero(Mach,X0);
             end
              if TempSolM <1
                SolM=TempSolM;
              else
                X0=0.01;
                TempSolM=fzero(Mach,X0);
              end
              if TempSolM <1
                SolM=TempSolM;
              else
                X0=0.0001;
                SolM=fzero(Mach,X0);
              end
        end
       else
        Mach=@(M)(1/M)*((2+((k-1)*M^2))/(k+1))^((k+1)/(2*(k-1)))-(AR(1,i));
        X0=1;
        TempSolM=fzero(Mach,X0);
        if TempSolM >=1
           SolM=TempSolM;
        else
           X0=1.5;
           TempSolM=fzero(Mach,X0);
           if TempSolM >1
                SolM=TempSolM;
           else
                X0=2;
```

```
                SolM=fzero(Mach,X0);
            end
        end
       end
       m(1,i)=SolM;
 end


figure(2);
plot (x_n(1,1:end),m(1,1:end));
title('Mach number along axial distance of nozzle')
xlabel('Axial distance, x (mm)')
ylabel('Mach number')

%CALCULATION FOR PRESSURE ALONG THE LENGTH OF THE NOZZLE
p2=zeros(1,(length(x_n)));
for i=1:(length(x_n))
    P2=((1+((k-1)/2)*m(1,i)^2)^(-k/(k-1)))*Pi;
    p2(1,i)=P2;
end
figure(3);
plot (x_n(1,1:end),p2(1,1:end));
title('Pressure along axial distance of nozzle')
xlabel('Axial distance, x (mm)')
ylabel('Pressure, P (Pa)')

%CALCULATION FOR TEMPERATURE ALONG THE LENGTH OF THE NOZZLE
  t=zeros(1,(length(x_n)));
for i=1:(length(x_n))
    T=((1+((k-1)/2)*m(1,i)^2)^(-1))*Ti;
    t(1,i)=T;
end
figure(4);
plot (x_n(1,1:end),t(1,1:end));
title('Temperature along axial distance of nozzle')
xlabel('Axial distance, x (mm)')
ylabel('Temperature, T (K)')

%CALCULATION FOR VELOCITY ALONG THE LENGTH OF THE NOZZLE

v=zeros(1,(length(x_n)));
for i=1:(length(x_n))
    V=sqrt(2*(k/(k-1))*Rg*Ti*(1-(p2(1,i)/Pi)^((k-1)/k))+Ugi^2);
   % V=sqrt(Rg*k*t(1,i))*m(1,i);
    v(1,i)=V;
end

figure(5);
plot (x_n(1,1:end),v(1,1:end));
title('Gas velocity along axial distance of nozzle')
xlabel('Axial distance, x (mm)')
ylabel('Velocity, V (mm/s)')
```

```
  %CALCULATION FOR THE VELOCITY OF THE POWDER PARTICLES

  %calculate gas density

  Rho_g=zeros(1,(length(x_n)));
  for i=1:(length(x_n))
      roh_g=Rho_g0/(1+((k-1)/2)*m(1,i)^2)^(1/(k-1));
      Rho_g(1,i)=roh_g;
  end

%defining additional variables
nu_ref=18.27E-6; % Reference Viscosity, [Pa/s]
Tref=291.15; % Reference Temperature, [K]
C=120; % Sutherland Temp, [K]

%Initialize additional variables

V_p=zeros(1,length(x_d));
V_P=zeros(1,length(x_n));
RE_P=zeros(1,length(x_d));
NU=zeros(1,length(x_d));
MP=zeros(1,length(x_d));
T_p=zeros(1,length(x_d));

V_p(1)=Ugi;

for n = 2:(length(x_n))
 nu=interp1(DataViscosity.Temperature, DataViscosity.Viscosity, t(1,n-1));
 NU(1,n)=nu;
 Re_p=abs(v(1,n-1)-V_p(n-1))*Rho_g(1,n-1)*Dp/nu; %Particle Reynolds number
 RE_P(1,n)=Re_p;
 M_p=abs(v(1,n-1)-V_p(n-1))/sqrt(k*Rg*t(1,n-1)); %Particle Mach number
 MP(1,n)=M_p;
 %Calculate drag coefficient
 C_D=24/Re_p*((1+0.15*Re_p^0.687)*(1+exp(-(0.427/M_p^4.63)-
(3/Re_p^0.88)))/(1+(M_p/Re_p)*(3.82+1.28*exp(-1.25*M_p/Re_p))));
 %Calculate Velocity
 V_p(n)=(V_p(n-1)^2+1.5*(x_n(1,n)-x_n(1,n-1))*(10^-
3)*C_D*Rho_g(1,n)/Dp/Rho_p*(v(1,n)-V_p(n-1))^2)^0.5;
 %V_p(n)=V_p(n-1)+((3/4)*(x_n(1,n)-x_n(1,n-1))*(10^-3)*C_D*Rho_g(1,n-
1)/Dp/Rho_p*(v(1,n-1)-V_p(n-1))^2/V_p(n-1));
end

for i = 1:(length(x_n))
    V_P(1,i)=V_p(i);
end

  figure(6);
  plot (x_n(1,1:end),V_P(1:end), x_n(1,1:end),v(1:end));
  title('Particle velocity along axial distance of nozzle')
  xlabel('Axial distance, x (mm)')
  ylabel('Velocity, V (mm/s)')
```

```
  legend('Particle velocity','Gas velocity')

%CALCULATION FOR THE TEMPERATURE OF THE POWDER ALONG THE LENGTH OF THE
NOZZLE.

%defining additional variables
  T_p(1)=293;
  Q=zeros(1,length(x_n));
  K2=zeros(1,length(x_n));
  Cp2=zeros(1,length(x_n));
  RE_P2=zeros(1,length(x_n));
  Pr2=zeros(1,length(x_n));
  h2=zeros(1,length(x_n));
  NU2=zeros(1,length(x_n));
  TF=zeros(1,length(x_n));

for n = 2:(length(x_n))
 Tf=(t(1,n-1)+T_p(n-1))/2;
 TF(1,n)=Tf;
 K = interp1(DataThermalCond.Temperature,
DataThermalCond.ThermalConductivity, Tf);
 K2(1,n)=K;
 Cp = interp1(DataSpecificheat.Temperature, DataSpecificheat.SpecificHeat,
Tf);
 Cp2(1,n)=Cp;
 nu2= interp1(DataViscosity.Temperature, DataViscosity.Viscosity, Tf);
 NU2(1,n)=nu2;
 Re_p2=abs(v(1,n-1)-V_P(n-1))*Rho_g(1,n-1)*Dp/nu2;
 RE_P2(1,n)=Re_p2;
 Pr=Cp*nu2/K;
 Pr2(1,n)=Pr;
 h=(2+(0.6*Re_p2^0.5*Pr^0.333))*K/Dp;
 h2(1,n)=h;
 c=6*h/(Cp_p*Rho_p*Dp*V_P(n-1));
 Q(1,n)=c;
 T_p(n)=T_p(n-1)+((x_n(1,n)-x_n(1,n-1))*10^-3*(t(1,n-1)-T_p(n-1))*c);
end

figure(7);
  plot (x_n(1,1:end),T_p(1:end),x_n(1,1:end),t(1:end));
  title('Particle Temperature along axial distance of nozzle')
  xlabel('Axial distance, x (mm)')
  ylabel('Temperature, T (K)')
  legend('Particle Temperature', 'Gas Temperature')
```